UNIVERSITÀ DEGLI STUDI DI TRIESTE

UNIVERSITÀ DEGLI STUDI DI TRIESTE

XXXV CICLO DEL DOTTORATO DI RICERCA IN

SCIENZE DELLA TERRA, FLUIDODINAMICA E MATEMATICA.
INTERAZIONI E METODICHE

Understanding deep convective organization: simple stochastic approaches and new metrics to bridge the gaps

Settore scientifico-disciplinare: GEO/12 OCEANOGRAFIA E FISICA DELL'ATMOSFERA

DOTTORANDO
Giovanni Biagioli

COORDINATORE
Prof. Stefano Maset

SUPERVISORE DI TESI
Dr. Adrian M. Tompkins

ANNO ACCADEMICO 2021/2022

UNIVERSITÀ DEGLI STUDI DI TRIESTE
Department of Mathematics and Geosciences
PhD Course in *Earth Science, Fluid-dynamics and Mathematics. Interactions and Methods*
XXXV Cycle

THE ABDUS SALAM INTERNATIONAL CENTRE FOR THEORETICAL PHYSICS
Earth System Physics Research Section

Understanding deep convective organization: simple stochastic approaches and new metrics to bridge the gaps

Scientific disciplinary sector: GEO/12

Supervisor: dr. Adrian Mark TOMPKINS
ICTP-Earth System Physics
e-mail: *tompkins@ictp.it*

PhD Course Coordinator: prof. Stefano MASET
Università degli Studi di Trieste
e-mail: *maset@units.it*

PhD student: Giovanni BIAGIOLI
e-mail: *GIOVANNI.BIAGIOLI@phd.units.it*
gbiagiol@ictp.it

Thesis reviewers:
prof. dr. George C. CRAIG
Ludwig-Maximilians-Universität München

prof. dr. Christopher E. HOLLOWAY
University of Reading

Academic Year 2021/2022
Second Session

A Trieste e alle persone, vicine e lontane,
che mi hanno accompagnato in questo viaggio

Contents

Abstract

Deep convective clouds can be observed in a variety of organizational states, from spatially random distributions to more coherent structures spanning a wide range of spatial scales. One puzzling mode of organization found in idealized numerical studies is the so-called convective self-aggregation, in which the clouds spontaneously transition from a random distribution in space to a regime where they are clustered. This phenomenon can have important implications for tropical climate and its sensitivity, but the problems are that the models do not agree on their representation of it and there is also a lack of consensus on how to best quantify organization in both modeling and observational studies.

To shed light on the discrepancies among models, we introduced a much simpler stochastic reaction-diffusion model of tropical convection, which, in spite of its minimal complexity, is still adequate to reproduce the behavior of full-physics systems and captures the transition to aggregation at parameter values that are a reasonable approximation of the present-day tropical atmosphere. The simplicity of the model allowed us to derive a dimensionless parameter, referred to as the aggregation number, whose value robustly indicates whether a given experimental configuration would undergo aggregation or not at all. The aggregation number incorporates the model key parameters, namely, a tropospheric radiative overturning timescale, the efficiency of horizontal moisture transport and the strength of the convection-vapor feedback, as well as the domain size and the horizontal resolution, in an attempt to explain these latter sensitivities detected in modeling studies. We suggest that this quantity can help understand the differences between full-physics models of the atmosphere.

Regarding the quantification of the organization level of cloud field scenes, to provide a better assessment a new index has been developed that solves many of the drawbacks and weaknesses of existing methodologies. The index categorizes the organization in an absolute sense, is robust to the details of the calculation algorithm and is linear in spatial scale for most used cases, allowing a quantification of the organization level over and also beyond the β-mesoscale. These advantages make it suitable for use in model intercomparison projects and in the analysis of a wide range of observation products.

Chapter 1

Introduction

This thesis deals with some intriguing and fascinating aspects related to atmospheric convection. We all experience convective phenomena in our everyday life. A common example is when we cook some pasta or boil some vegetables: we heat a pot of water from below and, when its base becomes warm enough, we witness the formation of a strange pattern consisting of adjacent cells. This is a very basic and familiar case of convection, known as the *Rayleigh-Bénard convection*. From a physical point of view, what is happening is that the hot water in contact with the pot base gets less dense and starts to rise, overcoming any viscosity that naturally opposes mixing. Cold water at the top tends to sink and a circulation establishes, the visible manifestation of which is precisely the Bénard cells.

Something similar occurs in the atmosphere. When the solar radiation is absorbed by the ground during hot, summer days, warm pockets of near-surface air heated by conduction, called *thermals*, become positively buoyant and rise under conditions of vertical instability. In conjunction, a downward motion generated by colder air being displaced at the top of the thermal develops, thereby creating a circulation cell. If these bubbles of air contain water vapor, it can condense as the air parcel rises and cools, leading to the formation of clouds. Overall, common to these phenomena is the vertical redistribution of energy driven by the mass motion in a fluid, that goes under the name of *convection*. The movement of mass is caused by vertical temperature (hence density) variations within the fluid, which are then acted upon by a mass-dependent field, such as the gravitational one (Emanuel, 1994; Bohren and Albrecht, 1998).

The clouds that we see in the sky are thus a result of convective motions. Depending on the height they reach, convective clouds can be generally classified as *shallow* if their tops lie below the 500 hPa pressure level, *deep* if they extend above the 500 hPa level. This is just a zero-order classification of cumulus clouds; an exhaustive review of the different regimes of moist atmospheric convection is presented in Stevens (2005). In any case, both types of clouds may have strong impacts on the atmospheric state and also on climate and its sensitivity, mainly through effects on radiation budgets and circulations. Our experience of violent storms associated with the towering cumulonimbus clouds

that reach or sometimes even extend above the tropopause (Fig. 1.1) suggests that deep convection can be very effective at transporting mass, momentum, moisture and energy vertically throughout the troposphere.

This thesis will focus on deep convection only. In the following, unless otherwise specified, the term convection will unambiguously refer to such a type.

Figure 1.1: *Mature cumulonimbus over Pula, Croatia, August 2022.*

1.1 Atmospheric deep convection

Let us take a parcel of air and lift it pseudo-adiabatically, i.e., we assume that the parcel is subject to adiabatic cooling while ascending and, once saturated, its excess water vapor condenses and is instantaneously lost as precipitation. At any height in this hypothetical displacement, if the parcel is lighter than its environment it will continue to rise, else it will sink. Since warm, moist air is less dense than cold, dry air, for moist convection an extra source of energy is provided by the release of latent heat of condensation or deposition in the pseudo-adiabatic ascent. This is related to the concept of *conditional instability*: the atmosphere is said to be conditionally unstable if it is unstable to moist saturated ascent but stable to dry unsaturated ascent, and it is exactly the extra supply of buoyancy mentioned above that allows the parcel to rise.[1]

[1] If the environment is unstable to both unsaturated and saturated ascents, the vertical profile is said to be *absolutely unstable.*

Given an unstable environmental profile, when the boundary layer air is particularly energetic, it manages to overcome the atmospheric stable layers that act as barriers to penetration by cumuli (Johnson et al., 1999, grey dashed lines in Fig. 1.2) and keeps rising all the way to the tropopause. Some overshoot past the level of neutral buoyancy (LNB) is possible due to upward momentum of the rising air (①) in Fig. 1.2) and the parcels undergo oscillatory motion which is then damped by friction. What we have just described is the genesis of deep convective clouds. Among other things, these clouds are characterized by large vertical velocities, high precipitation efficiencies and, upon reaching the tropopause, extensive anvils (②) that increase the cloud albedo and trap the terrestrial radiation. Thus the deep convection might have strong impacts on the tropospheric radiation budgets.

1.1.1 Interactions of deep convection with the nearby environment

Deep convection interacts in several ways with its surroundings. It is a local source of free tropospheric water vapor - the main one in fact (Grabowski and Moncrieff, 2004). This supply is partly due to the *detrainment* of saturated air and cloud condensates, mostly taking place around the cloud top level (③). The detrained air and hydrometeors undergo evaporation or sublimation owing to the unsaturated conditions outside the cloud. At the cloud edges, the turbulent mixing with dry, environmental air (*entrainment*) (④) drives the re-evaporation of some condensate, which chills the air and originates the downdrafts (Houze jr., 2014). The downdrafts import cold and dry low-tropospheric air into the boundary layer (⑤), forming the so-called convective wakes or cold pools (⑥). The latter produce strong gustiness and are responsible for the triggering of new convective events through dynamical lifting processes (Rotunno et al., 1988) or thermodynamical mechanisms (Tompkins, 2001b) (⑦).

This moistening effect of convection is not the only one. We all know the ripples that form in a pond or a lake after throwing a rock into it. This wave-like motion propagates over the water body until gravity, the restoring force, has brought the system back to a state of rest. Such ripples are a classic example of gravity waves, internal or interfacial waves that form after the equilibrium has been disrupted somehow, with gravity systematically trying to restore it. The same happens in the atmosphere when the buoyancy perturbations associated with deep convective motions excite gravity waves. These perturbations are rapidly spread out over scales on the order of the Rossby radius of deformation. Analogous to the pond, the troposphere surrounding the convection needs to adjust in response to the associated upward mass flux and heating. The radiation of gravity waves therefore induces a compensatory downward motion, called *subsidence* (⑧), which takes place in the pulses travelling away from the heat source (Bretherton and Smolarkiewicz, 1989; Mapes, 1993). In real cases, when multiple deep convective turrets are present, the horizontal temperature profile is efficiently homogenized and subsidence is widespread. The moisture content of subsiding air parcels is typically low, as it is related to the small upper tropospheric mixing ratios

carried downwards throughout the atmosphere. While descending, these layers of air are warmed by adiabatic compression, which has a stabilizing effect and also acts to reduce the relative humidity.

In conclusion, the convection acts to moisten its local field through detrainment of water vapor and cloud condensate and to dry the far-field through subsidence. The net effect is a drying of the atmosphere.

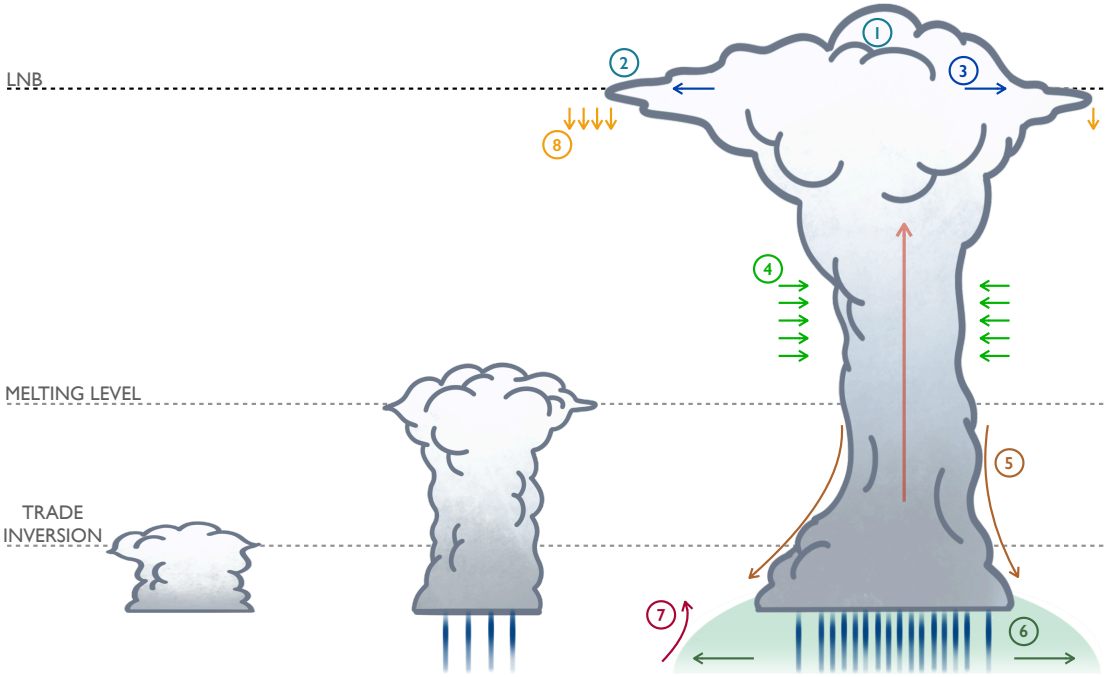

Figure 1.2: *Sketch representing the trimodality in cumulus cloud population in the tropics, including trade wind cumulus, cumulus congestus and cumulonimbus cloud types (left to right), after Johnson et al. (1999). For the cumulonimbus, some phenomenological aspects, physical processes and interactions with the environment are represented and the reader can refer to the text for the numbering. The arrow in the deep cloud interior indicates the upward motion of air parcels within the cloud itself.*

1.1.2 Tropical vs. mid-latitude convection

Deep convection is predominant in the tropics. This is evident from Fig. 1.3: the bright white ring of deep, cold clouds slightly north of the Equator identifies the so-called *Intertropical Convergence Zone* (ITCZ). The ITCZ is essentially a band of deep convective activity that circles the Earth in the tropical regions. It owes its name to the surface convergence of trade winds from both hemispheres. In tandem with the high near-equatorial water and land temperatures, the convergence of the trades helps sustain

the ascent of warm and humid air masses, leading to the development of vigorous convective activity. This rising motion constitutes the ascending branch of the Hadley cell, the low-latitude meridional circulation cell that, together with ocean currents, redistributes the surplus of incoming energy in the Tropics to higher latitudes.

In mid-latitudes we see that similar thermally direct convective processes may prevail especially during summer (Lohmann et al., 2016). In Trieste (45° N) we often experience small-scale and short-lived showers on warm summer afternoons, when the insolation is at a maximum and atmospheric instability can ensue, especially due to elevated heat low effects over nearby steep terrain. Nevertheless, as compared to the tropics, at our latitudes the weather is shaped to a much larger extent by the large-scale dynamics. Extratropical cyclones and the associated frontal systems play a key role, as most of our adverse meteorological conditions are dictated by the passage of synoptic-scale disturbances, responsible for the large-scale uplift of air masses.

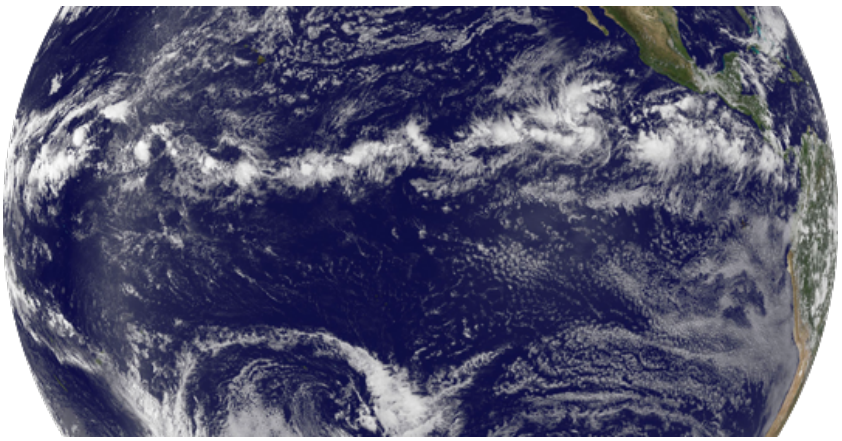

Figure 1.3: *Combination of cloud data over the Pacific from NOAA's GOES-11 satellite. The ITCZ is the band of bright white clouds visible just above the center of the image.*

In this dissertation, we will deal with tropical convection. For modeling purposes, since the interactions of convection with the environment can be very branched out, we would better start with an idealization of the tropical atmosphere, a basic scenario referred to as the radiative-convective equilibrium. In spite of its simplicity, this configuration still retains many fundamental aspects of convective processes and has been used in the past in a variety of studies.

1.2 The paradigm of radiative-convective equilibrium

The simplest energy balance models of the Earth-atmosphere system assume that radiation would be the only mechanism of heat transfer and the surface be an infinite ocean of fixed, uniform temperature. If we approximate the atmosphere as a multi-layer system, not only would this model be inaccurate yielding surface temperatures that much

exceed the present-day ones, but also the resulting vertical temperature profiles would be unstable. Convection is thus allowed to develop.

In other words, the Earth-atmosphere system is not in radiative balance, as is also evident from the observed non-zero net tropospheric cooling rate of $\mathcal{O}(1\ \mathrm{K\,day^{-1}})$, which contradicts the definition itself of radiative equilibrium. A vertical heat transport mechanism must exist to prevent the temperature lapse rate from exceeding some critical value. It is precisely the convection that compensates for radiative cooling and stabilizes the atmospheric column through release of latent heat of condensation and the associated subsidence warming in clear-sky areas. These processes produce a lapse rate that is much smaller than the pure radiative equilibrium one (Hartmann, 2015).

The balance between radiative cooling and convective heating provides the simplest possible description of the climate system and is at the theoretical foundation of the idealization of *radiative-convective equilibrium* (RCE). This paradigm was first employed by Manabe and Strickler (1964) in a study led with a single-column model. In RCE simulations, to keep things simple, any large-scale dynamical forcing is neglected and, in fact, Emanuel et al. (2014) formally defines the RCE state as the statistical equilibrium one that the Earth-atmosphere system would attain in the absence of lateral energy transport.[2] In spite of this, however, the development of internal circulations is still possible, hence interactions between radiation, convection and large-scale dynamics can be analyzed within the RCE framework.

The timescale of adjustment to equilibrium in RCE configurations is set by radiative cooling rates through their control on subsidence velocities in clear-sky regions (Tompkins and Craig, 1998a,b) assuming fixed sea surface temperature (SST). Indeed, in subsidence areas, in the absence of large-scale convergence - as is commonly assumed in RCE - the radiative cooling has to be balanced by subsidence heating (see Section 3.1 for an application of such a balance). This determines a tropospheric overturning timescale that is nothing but the time to equilibrium. If the SSTs are instead interactive, this timescale can be much longer (Cronin and Emanuel, 2013).

Since the real atmosphere is incessantly under the influence of external disturbances, questions arise as to whether RCE is relevant to real-world situations. While this might not be the case locally, on large enough spatial and temporal scales, the tropical climate can be though of as in a state of RCE (Wing and Emanuel, 2014; Hohenegger and Stevens, 2016). The observational study by Jakob et al. (2019) confirmed this hypothesis, showing - perhaps surprisingly - that the tropics as a whole are near RCE even on daily timescales. By extension, the global-mean state of the planet can be assumed to exist in RCE (Stephens et al., 2008). The radiative-convective equilibrium configuration therefore lends itself to be a very accurate and useful idealization to understand tropical weather and climate.

For these reasons, the RCE paradigm has long been adopted in numerical studies of tropical convection (e.g., Held et al., 1993; Tompkins and Craig, 1998a; Bretherton

[2]The definition does not imply that small fluctuations associated with single deep convective events are no longer permitted (Tompkins and Craig, 1998a). Rather, it is over timescales that are long compared to the typical lifetime of convective clouds that the balance holds.

et al., 2005; Wing and Emanuel, 2014). The ordinary radiative-convective equilibrium state of tropical convection is characterized by nearly randomly distributed patterns of cumulus clouds in both space and time (Bretherton et al., 2005; Lebsock et al., 2017). Such a regime is eloquently referred to as the *pop-corn convection*: similar to the corn kernels that puff up, the convection bubbles across the whole computational domain (cf. Fig. 1.4a). A bunch of questions then arise: is this equilibrium climate stable? Is there the possibility that multiple equilibria exist, especially when internal large-scale circulations develop? The mysterious situation depicted in Fig. 1.4b seems to provide an answer...

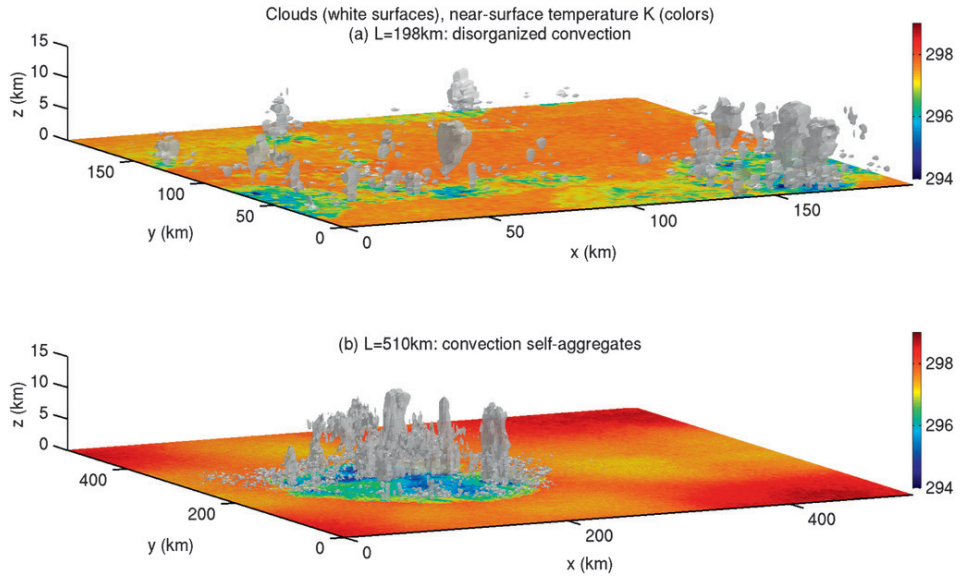

Figure 1.4: *Snapshots of random (a) and self-aggregated (b) convection from cloud-resolving model simulations performed with the System for Atmospheric Modeling (SAM). The experiments employ different domain sizes of* 198 *km (a) and* 510 *km (b). Shown in both panels are the near-surface temperature (units K, colors) and the* 0.4 $g\ kg^{-1}$ *isosurface of the mixing ratio of all liquid and ice condensate species (grey). From Muller and Held (2012).*

1.3 Generalities on the organization of deep convection

In Fig. 1.4b, the clouds are seen to be in close proximity to each other, while in panel (a) they are rather scattered. If we look back at Fig. 1.3, we notice that the ITCZ appears as a unique, very elongated line of convection that spans the entire tropical Pacific. These two images contain textbook examples of convective organization. What do we exactly mean by organization in this context?

Unfortunately, a rigorous, universally accepted definition of convective organization is missing, but a number of attempts have been made. One could define organized

convection as a mode which has a lifetime greatly exceeding that of individual convective events and grows upscale (Craig and Mack, 2013; Windmiller and Craig, 2019), covering an area much larger than the single cells. Or can define organization as the "nonrandomness of meteorological fields in convecting regions" (Mapes and Neale, 2011). Or, perhaps less vaguely, can identify organized states as those marked by spatial and temporal correlations between updrafts, with the correlations induced by the convection itself rather than by external influences, such as mid-latitude cyclones and the associated frontal systems (Windmiller, 2017; Windmiller and Craig, 2019). In this perspective, the ITCZ could be regarded as a planetary-scale manifestation of deep convective organization (Hohenegger and Jakob, 2020).

It is undisputable that convection tends to organize. Cloud fields in the atmosphere can exhibit a variety of organizational regimes. They can be randomly distributed within a given area (Fig. 1.5a) or feature dispersion or clumping. In the first case, the clouds arrange themselves into regular structures (Fig. 1.5b); in the second, they exist in close proximity and are tightly packed together (Fig. 1.5c). The former configuration is referred to as a *regular* one, the latter is said to be *clustered*. These organizational states pertain to all types of convective clouds, both shallow and deep (e.g., Plank, 1969; Sengupta et al., 1990; Zhu et al., 1992; Lee et al., 1994; Nair et al., 1998; Zhao and Di Girolamo, 2007; Tobin et al., 2012, 2013; Holloway et al., 2017; Radtke et al., 2022), but in this work we will only focus on the deep convective organization.

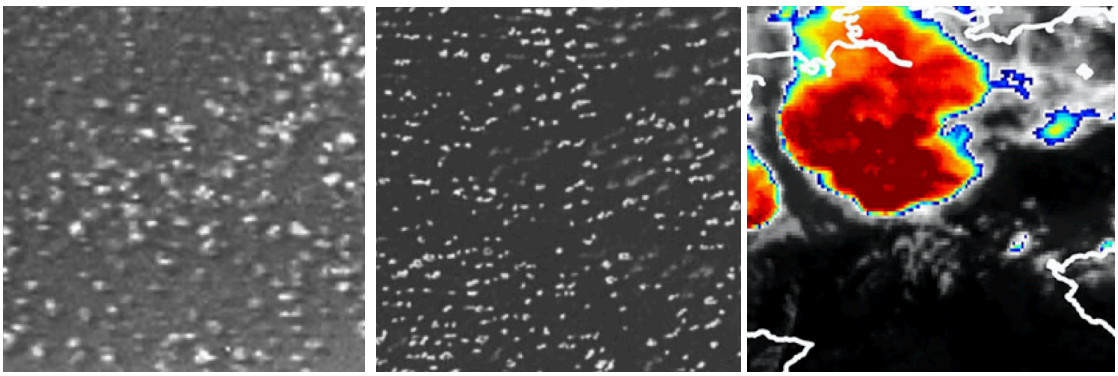

(a) (b) (c)

Figure 1.5: *(a,b) Advanced very high resolution radiometer (AVHRR) imagery, with fair-weather cumulus cloud fields exhibiting randomness (a) and regularity (b). From Nair et al. (1998). (c) Snapshot of infrared brightness temperature from Meteosat Second Generation, with the scene showing a large cluster of deep convective activity over north-western Germany. The red (blue) colors indicate cloud top temperatures on the order of* 210 (240) *K. From Pscheidt et al. (2019).*

Over the last decades, the scientific community has devoted increasing attention to the variety of phenomena falling under the broad category of deep convective or-

ganization. These modes extend over a wide range of spatial scales, from scattered individual thunderstorms to more complex and coherent structures encompassing numerous convective cells. Commonly cited examples include squall lines ($\sim$ 10 km, e.g., Houze jr., 1977), mesoscale convective systems (MCSs, $\sim$ 100 km, e.g., Houze jr., 2004) and the sub-category of mesoscale convective complexes (MCCs, Maddox, 1980), tropical cyclones and hurricanes, up to planetary-scale envelopes like the Madden-Julian Oscillation (MJO, Madden and Julian, 1971).

The interest in these phenomena arose from the fact that they are ubiquitous in the tropical atmosphere, which provides an excellent framework for better understanding the tropical weather and climate. They can be studied to get valuable insights into the mechanisms that lead to tropical cyclogenesis for example, or to give rise to advances in predictability (e.g., MJO is a major source of predictability on intraseasonal timescales, Zhang et al., 2013). Perhaps more importantly, such regimes have interactions with the large-scale environment that are different from those related to ordinary convection and can strongly impact the circulation, the vertical water and energy transport, the tropospheric radiative budgets and the hydrological cycle (e.g., Houze jr., 1982; Hartmann et al., 1984; Machado and Rossow, 1993; Mapes and Houze jr., 1993; Mapes, 1993; Bony et al., 2015). For instance, around 50% of the total tropical rainfall is contributed to by organized systems (Nesbitt et al., 2000; Tan et al., 2013) and recent increases in tropical precipitation have been attributed to changes in the frequency of convective organization (Tan et al., 2015). The occurrence of organized deep convection has also been linked to extreme weather events (Gray and Marshall, 1998; Mathon et al., 2002; Pendergrass et al., 2016; Bao et al., 2017; Rigo et al., 2019). The large-scale impacts of the organization suggest that it can be critical to the present-day and future climates and our assessment of climate sensitivity (Pierrehumbert, 1995; Lindzen et al., 2001; Bony et al., 2015; Mauritsen and Stevens, 2015).

Generally speaking, organized convection can result from mechanisms that are internal to the convection itself or from external factors. Falling into the first category are, e.g., cold pools (Rotunno et al., 1988; Tompkins, 2001b; Haerter et al., 2019), the storm-induced gustiness in convectively active regions (Emanuel, 1987; Neelin et al., 1987) or moisture-convection interactions (Tompkins, 2001c; Grabowski and Moncrieff, 2004). Vertical wind shear (Thorpe et al., 1982; Rotunno et al., 1988; Robe and Emanuel, 2001) or sea-surface temperature gradients (e.g., Waliser and Graham, 1993) instead belong to the second group of mechanisms. In Section 1.4, we will introduce a very special mode of organization found in idealized numerical modeling studies and review the mechanisms that induce it.

The effects of mesoscale convective organization are very rarely reproduced in the representation of convection in current general circulation models (GCMs) due to the coarse resolutions at which they are operated, which requires the use of cumulus parameterizations and thus leads to a misrepresentation of some convective processes (Tobin et al., 2013; White et al., 2018). High priority should therefore be given to a proper representation of organization and its impacts in climate models, owing to the heavy implications for climate variability and change (Tobin et al., 2013).

1.4 Deep convective self-aggregation: dry gets drier, moist gets moister

The intriguing mode of organization shown in Fig. 1.4b is the so-called *convective self-aggregation*. It has been detected in numerical RCE experiments and is in fact quite striking, because sometimes, in spite of homogeneous boundary conditions and zero or time-invariant large-scale forcing, the convection is found to *spontaneously* cluster starting from an initial spatially uniform distribution. This can happen over periods of a few days to several weeks, especially when the domain is large enough (note the difference in domain size between Figs. 1.4a and 1.4b).

The major characteristics of self-aggregated convection are already evident. The end climate is a spatially organized atmosphere with a single, intensely convecting, almost circular, very wet region surrounded by a dry background. For very large domains (Patrizio and Randall, 2019) or long channel geometries (Wing and Cronin, 2016), it has been found that the convection sometimes spreads over multiple clusters, or bands. How do we approach this equilibrium state? Let us have a look at the following Fig. 1.6, which shows the transition to aggregation in terms of the vertically integrated, density-weighted water vapor field. We see that aggregation begins as a dry area that expands (the blue patch in the upper-left corner in panel b) and amplifies, pushing the convection into a limited, increasingly wet region (the red circle in c). This behavior can be encapsulated in the paradigm "dry gets drier, moist gets moister".

From Fig. 1.6c, the evolution towards bimodality in the spatial moisture distribution is apparent, with a dry peak corresponding to the subsiding areas and a moist peak to the convective cluster. However, given the comparatively larger fraction occupied by the former and the fact that saturation limits moisture in convecting areas, the domain-mean state turns out to be much drier. This means that self-aggregation does not produce a spatial redistribution of moisture but has a dramatic impact on the mean climate (Wing et al., 2017). The reduced water vapor absorption in a domain-mean sense also implies that the outgoing longwave radiation (OLR) is much higher compared to the non-aggregated case.

This latter fact means that the system loses energy to space much more efficiently. The implications for climate sensitivity are enormous. Indeed, it has been proposed that self-aggregation can act as a thermostat to regulate tropical climate (Khairoutdinov and Emanuel, 2010; Wing et al., 2017). Moreover, Emanuel et al. (2014) showed that the self-aggregated state could be the preferred equilibrium state of tropical convection under warm SSTs, which implies that global warming may lead to the tropics switching to this regime in future climates. This would provide a negative feedback to global warming itself, referred to as an *iris-like effect* (Mauritsen and Stevens, 2015). In other words, the Earth is proposed to possibly possess an adaptive infrared regulation mechanism, which opens/closes dry regions in response to increasing/decreasing surface temperatures. This action is similar to the enlargement of the eye's iris as the pupil contracts under changes in light intensity, whence the name. However, much uncertainty remains in this respect.

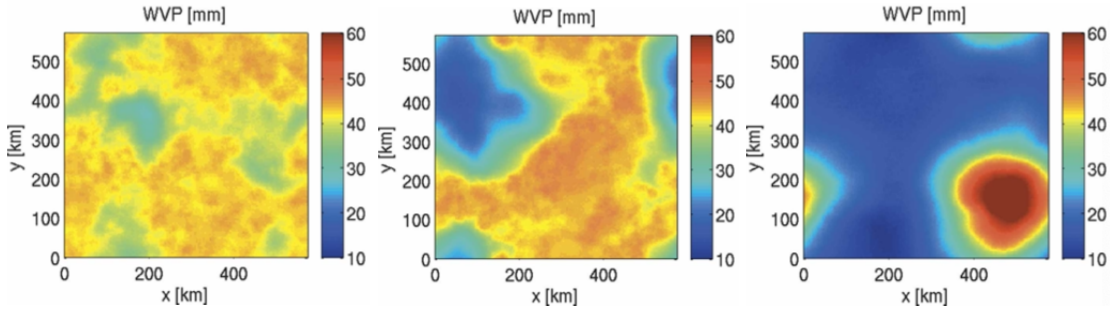

Figure 1.6: *Evolution to self-aggregation in terms of the daily-averaged water vapor path (WVP) for a simulation conducted with the cloud-resolving model SAM. The horizontal maps refer to the field at day 10 (a), day 20 (b) and day 50 (c) of the simulation. From Bretherton et al. (2005).*

Aggregation has been detected in a variety of models, including two- and square-domain three-dimensional cloud-resolving models (CRMs, e.g., Held et al., 1993; Tompkins and Craig, 1998a; Bretherton et al., 2005; Stephens et al., 2008; Muller and Held, 2012; Jeevanjee and Romps, 2013; Wing and Emanuel, 2014; Muller and Bony, 2015; Holloway and Woolnough, 2016; Hohenegger and Stevens, 2016; Tompkins and Semie, 2017; Shamekh et al., 2020; Tompkins and Semie, 2021; Shi and Fan, 2021), elongated-channel three-dimensional CRMs (e.g., Tompkins, 2001c; Stephens et al., 2008; Posselt et al., 2012; Wing and Cronin, 2016) and GCMs with parameterized convection (e.g., Held et al., 2007; Popke et al., 2013; Arnold and Randall, 2015; Reed et al., 2015; Coppin and Bony, 2015; Hohenegger and Stevens, 2016). If the effects of rotation are included, the models feature a behavior resembling spontaneous tropical cyclogenesis (Bretherton et al., 2005; Nolan et al., 2007; Khairoutdinov and Emanuel, 2013).

Overall these studies have identified a series of physical processes responsible for the onset and the maintenance of self-aggregated conditions. This has been accomplished mainly through mechanism-denial/suppression experiments that isolate the effects of some processes. In recent years, however, Wing and Emanuel (2014) introduced an energy budget analysis framework to assess which mechanisms drive a growth of moisture perturbations, based on the fact that self-aggregation is typically accompanied by the amplification of dry and moist anomalies. In particular, they considered the spatial variance of vertically integrated frozen moist static energy (FMSE), which increases as aggregation progresses, and calculated the correlations of the FMSE anomalies with those associated with individual diabatic or dynamical contributions (longwave and shortwave radiative fluxes, surface enthalpy fluxes, circulation terms). In this context, we will say that a physical mechanism provides a *positive feedback* to self-aggregation if it further removes energy from the low-FMSE (i.e., dry) columns and feeds energy into the high-FMSE (moist) columns, thereby favouring the clustering; otherwise, the

process is said to provide a *negative feedback*.

1.4.1 Physical mechanisms

Experiments have shown that a range of internal processes all contribute to convective self-aggregation to various degrees. These include cloud/clear-sky radiative feedbacks, surface flux contributions, advective processes and the relationships between convection and water vapor (e.g., Held et al., 1993; Tompkins and Craig, 1998a; Tompkins, 2001b; Bretherton et al., 2005; Stephens et al., 2008; Muller and Held, 2012; Wing and Emanuel, 2014; Muller and Bony, 2015; Holloway and Woolnough, 2016; Wing et al., 2017). Nonetheless, there is still debate in the literature about which feedback is the most important in driving the aggregation. Most of the feedbacks also change in strength during the simulations and there is not a single leading process throughout the evolution of self-organization (Wing and Emanuel, 2014) to the point that the physical mechanisms that trigger the clustering of convection have been found to differ from those that maintain it once established (Muller and Held, 2012; Muller and Bony, 2015). It is also possible that some processes first favour and then even oppose (or vice versa) the organization, i.e., the feedbacks change in sign between the pre- and post-aggregated states (Wing and Emanuel, 2014; Tompkins and Semie, 2021).

In general, spatial inhomogeneities in diabatic terms have been shown as essential for aggregation to occur. Horizontally homogenizing the radiative heating rates or assuming wind-insensitive surface fluxes indeed prevents the clustering (Tompkins and Craig, 1998a). The importance of differential radiative profiles, with cooling in dry areas and warming due to high anvil clouds in moist areas, has been reiterated by other studies (e.g., Bretherton et al., 2005; Stephens et al., 2008). However, interactive radiative fluxes turn out to be unnecessary for aggregation under some special circumstances, for instance when downdraft and cold pool formation is inhibited, in which case the transition to organization is only driven by feedbacks between moisture and convection (Muller and Bony, 2015; Holloway and Woolnough, 2016).

We now review the main mechanisms responsible for aggregation in more detail. The radiative contributions will be partitioned into a longwave (LW) and shortwave (SW) term.

Longwave radiation

There is a wide consensus in the literature regarding the role that longwave radiative fluxes play in driving the aggregation process. According to Coppin and Bony (2015), the organization in their GCM simulations is initiated by the formation of dry, convective-free regions resulting from random events of large-scale midtropospheric subsidence. Their strong longwave radiative cooling relative to the moister environments amplifies the existing moist static energy (MSE) gradients and induces an expansion like density currents that act to confine deep convection. These dry regions have been termed *radiatively driven cold pools* (Coppin and Bony, 2015).

The one just described is a direct diabatic contribution, but there is also an indirect, circulation-mediated effect. Indeed the efficient LW cooling in non-convective areas, mainly from shallow clouds, has to be compensated for by low-level subsidence heating (cf. Section 1.2), which in turn forces a shallow circulation that exports MSE to the moist regions to satisfy continuity. Such a radiatively driven motion yields net energy loss of the dry patches and therefore reinforces the spatial MSE tendencies, providing a positive feedback to self-aggregation. This upgradient energy transport has been acknowledged as a distinctive feature of organized runs (Bretherton et al., 2005; Muller and Held, 2012; Wing and Emanuel, 2014; Muller and Bony, 2015).

Some aspects are still uncertain. A number of studies have shown that it is mainly the radiative effects from low clouds that are crucial (e.g., Muller and Held, 2012); others instead point to a larger relative importance of clear-sky processes (Wing and Emanuel, 2014). The theoretical work by Emanuel et al. (2014) proposed that, at high SSTs, the rapid increase of lower tropospheric water vapor concentration via the Clausius-Clapeyron relationship leads to a very large clear-sky infrared emissivity, hence significant LW cooling. Thus clustering onset would be driven by direct radiative interactions at warm temperatures. On the other hand, Coppin and Bony (2015) have argued that it is at relatively cold SSTs that the longwave term is the most effective.

Shortwave radiation

Shortwave radiative effects are found to contribute to the self-aggregation process (Wing and Emanuel, 2014; Wing and Cronin, 2016), although in general they are not strictly necessary (Wing et al., 2017). The dry columns favour aggregation because of the reduced water vapor absorption there (Wing and Emanuel, 2014), which yields reduced SW heating and therefore a relative loss of energy. There is no agreement in the literature concerning the sign of the SW feedback in moist regions. Muller and Held (2012) suggested that the reflected shortwave radiation by deep clouds leads to less shortwave heating and therefore opposes the clustering, providing a negative feedback to self-aggregation. By contrast, Wing and Emanuel (2014); Holloway and Woolnough (2016) showed that the SW absorption is highly correlated with the column relative humidity, with the strong positive feedback in moist areas colocated with thick clouds.

Surface fluxes

Similar to shortwave radiation, surface latent and sensible heat fluxes represent another area of disagreement between the models in terms of which processes are fundamental to the aggregation. While some studies have acknowledged their role (Tompkins and Craig, 1998a; Bretherton et al., 2005; Coppin and Bony, 2015; Tompkins and Semie, 2021), others have shown that convection can still cluster if certain conditions are met, regardless of whether surface fluxes are non-interactive (Muller and Held, 2012; Holloway and Woolnough, 2016).

The bulk aerodynamic formulas for latent and sensible heat fluxes suggest that the surface flux feedback contributes through the two competing influences of the wind

speed and the ocean-atmosphere thermodynamic disequilibrium (Wing and Emanuel, 2014). The former effect, sometimes referred to as the *WISHE feedback* (wind-induced surface heat exchange, Emanuel, 1987; Neelin et al., 1987), is stronger in moist areas due to the storm-induced gustiness in the convergence region, which intensifies the heat fluxes around the convective core, providing a positive feedback. Instead the enthalpy disequilibrium effect, which is related to differences in temperature and humidity between the sea and the near-surface air, is larger in dry than in moist areas and acts against the organization. Recently, more sophisticated approaches based on similarity theory have been considered by Tompkins and Semie (2021). These formulations also account for the contribution of boundary layer stability to latent heat flux perturbations, which is shown to be of similar magnitude as the WISHE effect in the pre-onset phase. This impact would be missing from models that only employ bulk aerodynamic formulas.

Large-scale advective processes

The export of MSE by the shallow, radiatively driven circulation that sustains the clustering is an example of the impact of advective processes. However, there is no agreement among the models about whether the large-scale circulations can initiate the organization on their own or intervene to boost pre-existing anomalies (Wing et al., 2017). The sign of the overall circulation feedback is under debate as well: while some studies have found that it favours the clustering during some phases of the evolution to aggregation (Wing and Emanuel, 2014; Holloway and Woolnough, 2016), others have shown that it always opposes the organization (Wing and Cronin, 2016). In general, if aggregation does not occur, it must be due to transport processes, since diabatic effects always act to promote clustering. The GCM experiments by Coppin and Bony (2015) suggest more complex interactions in terms of the spatial exchange of energy. Their total advective tendency provides a negative feedback to self-aggregation, which is consistent with a diffusive (i.e., downgradient) redistribution of moisture; however, there could still be some local upgradient transport.

In this latter respect, Windmiller and Craig (2019) proposed that, if a stochastic representation of convection is adopted, it is reasonable to assume that the transport is purely diffusive, at least in the early stages of self-aggregation. This is in agreement with the initial negative contribution from the advective term found by Wing and Emanuel (2014), but in disagreement with Holloway and Woolnough (2016). A diffusive representation of transport always opposes aggregation.

Water vapor-convection interactions: the moisture-memory feedback

We saw in Section 1.1.1 that convection locally moistens the atmosphere. The moisture-convection interaction is actually two-way, as convection is more likely to erupt in moister environments and is suppressed in dry ones (Mapes and Zuidema, 1996; Sherwood, 1999; Parsons et al., 2000; Raymond, 2000b; Redelsperger et al., 2002; Derbyshire et al., 2004; Grabowski and Moncrieff, 2004). Moist regions thus favour successive

convective activity, enabling a feedback loop in which the moist regions continue to moisten through the generation of new deep clouds (Craig and Mack, 2013).

A moisture-convection feedback, sometimes referred to as the *moisture-memory feedback* (Muller and Bony, 2015), has been proposed and shown as key in organizing the convection (Held et al., 1993; Tompkins, 2001c,a; Grabowski and Moncrieff, 2004). This is primarily due to reduced entrainment of dry air resulting from enhanced humidity in moist areas. The mixing with environmental air in moister environments therefore leads to a reduced cooling of an ascending parcel, which does not largely alter its buoyancy and produces strong and persistent convection. The moisture-memory feedback is sufficient to trigger self-aggregation on its own even in the absence of radiative effects, provided that the re-evaporation of rain at low levels is artificially suppressed (Muller and Bony, 2015; Holloway and Woolnough, 2016). Indeed, without downdrafts injecting dry and cold air into the boundary layer and the associated cold pools that induce efficient low-level mixing, the convection always settles at the same, very wet locations.

Questions may arise as to whether these conditions are realistic to some extent. This could be the case if the boundary layer air is nearly saturated and the precipitation efficiency is around 100% (Wing et al., 2017). Nonetheless, it must be reminded that CRM experiments often simplify the physics of the real atmosphere to a highly idealized representation, and for instance do not impose a mean wind or vertical wind shear, while it has been proved that the latter can shear out incipient moisture anomalies and induce efficient mixing (e.g., Held et al., 1993; Tompkins, 2001c).

Historically the moisture-convection feedbacks have been downgraded as less important with respect to the diabatic interactions. For instance, the theoretical study by Emanuel et al. (2014) suggested that no role is played by the coupling between convection and water vapor in the onset of self-aggregation, even though it may strengthen the otherwise radiatively driven clustering. The GCM simulations by Arnold and Putman (2018) and the mechanism-denial CRM experiments by Yang (2019) further showed that the moisture-convection feedback, although important, is not necessary by itself to drive the aggregation. In particular, Yang (2019) found that convection could still self-organize in the absence of radiative and surface flux feedbacks, rainfall evaporation and virtual effects of water vapor if the moisture profile is relaxed to its horizontal mean. This suggests that the effect on convection of the spatial variability of moisture and their interactions are not essential.

1.4.2 Observational evidence of self-aggregation

The first question you may have come up with when we introduced the concept of self-aggregation earlier has likely been "is this real or just an artifact of the models?". Holloway et al. (2017) provided a detailed answer to this question, suggesting that some promising results and correspondences to the findings of idealized numerical simulations have been documented in observational studies, as later confirmed also by Lebsock et al. (2017); Bony et al. (2020).

The first such studies are those by Tobin et al. (2012, 2013), who explored the interac-

tions of deep convective organization with the atmospheric state over tropical oceans at both the synoptic scale and the mesoscale by means of multisatellite observations and meteorological reanalyses. Statistical relationships were derived by categorizing atmospheric variables by the clustering strength for situations which are similar in terms of convective activity (as measured by domain-averaged precipitation rate), SST and large-scale dynamical conditions. Models and observations agree in several respects: highly aggregated states are accompanied by strong humidity gradients between the convective area and the non-convecting environment, the latter being drier especially in the mid and upper troposphere. This dryness and a prominent reduction in shallow, midlevel and deep convective cloudiness are responsible for large increases in OLR. The decrease in low-level cloud fraction with aggregation is not found in other observational studies (Stein et al., 2017; Lebsock et al., 2017) nor reproduced in models, which rather predict a large increase in low cloud amounts (Wing et al., 2017), even though this can be a result of the relatively coarse resolutions employed that under-resolve shallow convective motions (Wing and Cronin, 2016). As a consequence, while models indicate a strong net tropospheric radiative cooling with aggregation, observations point to a reduced planetary albedo (i.e., less reflected SW), which counteracts the increases in OLR, thereby producing almost no impact on the top-of-atmosphere net radiation budget. Concerning surface flux contributions, models are partially supported by observational analyses. Indeed, Tobin et al. (2012, 2013) found that, at synoptic scales (but not at the mesoscale), the surface heat fluxes are enhanced due to an intensification of near-surface wind speed in the convective regions and ocean-atmosphere thermodynamic contrasts outside.

In their analysis of satellite and radiosonde data over the equatorial Indian Ocean, Kadoya and Masunaga (2018) noticed that the occurrence of organization is characterized by a number of features reminiscent of the self-aggregating RCE experiments. These include the formation and growth of dry areas in the vicinity of intensifying convection (not driven by subsidence though) and the subsequent enhancement of radiative cooling and localization of precipitation. However, some aspects are dissimilar, such as the time to aggregation, which is much shorter in observations than in idealized studies. In this respect, Holloway et al. (2017) argued that the typical timescale for self-organization in models includes the spin-up period of small-scale convective activity, that is, pre-onset periods in which the clustering has not even started. Also, as already noted in Section 1.2, the real atmosphere is constantly subject to external large-scale perturbations, which would end up hindering the establishment and persistence of aggregation and accelerating the disaggregation processes. Bretherton et al. (2005) however suggested that the self-aggregating RCE is supposed to be relevant over the Indian Ocean or the Western Pacific warm pool regions where SST gradients and mean wind shear are weak.

We may also wonder whether the physical mechanisms that induce the clustering in RCE studies are relevant to the real world. CRM simulations conducted under more realistic settings over either small domains or a near-global aquaplanet have shown that this is generally the case, with radiative feedbacks again playing a major role (e.g.,

Bretherton and Khairoutdinov, 2015; Holloway, 2017). In conclusion, although the evidence of self-aggregation in nature is quite limited to date, encouraging signs from observations and more complex modeling frameworks have been found to support the findings of idealized RCE experiments.

1.5 Uncertainties across models and in the assessment of the organization level

Unfortunately much uncertainty remains about the robustness, if not even the existence, of self-aggregation and its relevance to the real world. Even though the models generally agree on the role that diabatic processes play in driving the organization, they show little or no consensus about a series of important aspects. For example, the temperature-dependence of self-aggregation is under debate: while some numerical or theoretical studies have suggested that clustering is favoured by warmer conditions (Held et al., 1993; Khairoutdinov and Emanuel, 2010; Emanuel et al., 2014; Wing and Emanuel, 2014), others have detected the peculiar self-aggregated behavior at temperatures well below the current tropical SSTs (Coppin and Bony, 2015; Holloway and Woolnough, 2016; Wing and Cronin, 2016), even as low as 243 K (Abbot, 2014). This casts doubts on the prospect posed by Emanuel et al. (2014); Mauritsen and Stevens (2015) of self-organization providing a negative climate feedback in future scenarios (Wing et al., 2017).

The most puzzling aspect of self-aggregation is perhaps its strong sensitivity to the specifics of the model configuration and the details of the experimental framework. The occurrence of organization is indeed dependent on the parameterization schemes used, be they radiation, convection, microphysics, boundary layer, subgrid-scale turbulence or mixing schemes (Popke et al., 2013; Wing and Cronin, 2016; Tompkins and Semie, 2017; Shi and Fan, 2021; Huang and Wu, 2022). The condition assigned at the lower boundary is also found to have an impact. In general, the experiments assume an underlying ocean of fixed, uniform SST but, if an interactive lower boundary (i.e., a slab ocean) is prescribed, clustering turns out to be delayed, or even impeded (Bretherton et al., 2005; Hohenegger and Stevens, 2016; Shamekh et al., 2020; Tompkins and Semie, 2021). Another source of concern is represented by the fact that the occurrence of organization is sensitive to the domain size and horizontal grid spacing employed, with large domains and/or coarse resolutions facilitating the aggregation (Muller and Held, 2012). This points to a lack of numerical convergence regarding the clustering. However, the latter sensitivities are found to vanish in some cases when the physics is altered, e.g., if rainfall evaporation (hence cold pool formation) is suppressed (Jeevanjee and Romps, 2013) or ad-hoc vertical profiles of radiative cooling rates are imposed (Muller and Bony, 2015).

1.5.1 Measuring organization

In order to aid understanding of these controversial aspects, efforts have been made to measure the organization in practice. The absence of a unanimously agreed upon definition of deep convective organization (Retsch et al., 2020) implies that it is not straightforward to rigorously identify and measure the clustering, not only in model output but also in the analysis of observational products. This has motivated an extensive body of literature regarding the derivation of *organization indices* (or *metrics*), that reflect different conceptual views and explore a variety of aspects of the organization processes. Such indices can either detect aggregation based on some of its large-scale signatures (e.g., increase in OLR), or essentially tell us how densely deep convective clouds occupy space. In this thesis we present a comprehensive review of the existing methodologies to date. It is not rare that these metrics largely disagree in their assessment of the level of organization across scenes, sometimes even with zero correlations between measures (Wing et al., 2020).

The uncertainties and open questions are summarized by the following Fig. 1.7, which shows the response of aggregation to warming as measured by three organization metrics for a set of models with explicitly resolved convection. This analysis is conducted within a recent model intercomparison study called the Radiative-Convective Equilibrium Model Intercomparison Project (RCEMIP, Wing et al., 2020). The metrics employed are the subsidence fraction f_{sub} (Coppin and Bony, 2015), the organization index I_{org} (Tompkins and Semie, 2017) and the spatial variance of column relative humidity (CRH) σ^2_{CRH} (Wing and Cronin, 2016); for all indices, higher values correspond to more aggregated conditions (Section 5.1). The disparities between the models are confirmed. It is indeed seen that nearly 50% of the models predict net increase of aggregation with warming (dots falling above the horizontal dashed line) and nearly 50% of the models predict net decrease of aggregation with warming. This is true regardless of which metric is used to quantify the organization. However, the lack of consensus among the models is not the only concerning aspect of this analysis: another one is that, even within a given model, there can be no consistent response to warming as indicated by the three indices. This is the case of the UCLA-CRM model, for which σ^2_{CRH} points to an increase in aggregation, while f_{sub} shows the opposite and I_{org} exhibits almost no sensitivity to SST.

1.6 Research objectives and thesis plan

The take-home messages from Fig. 1.7 provide the main motivations to our work, and highlight the uncertainties in our present understanding of convective organization and its implications for weather and climate studies. We will move along two tracks:

- First track: we will aim to construct a simple, diagnostic tool that possibly helps explain the sensitivities of cloud-resolving models and the differences existing between them.

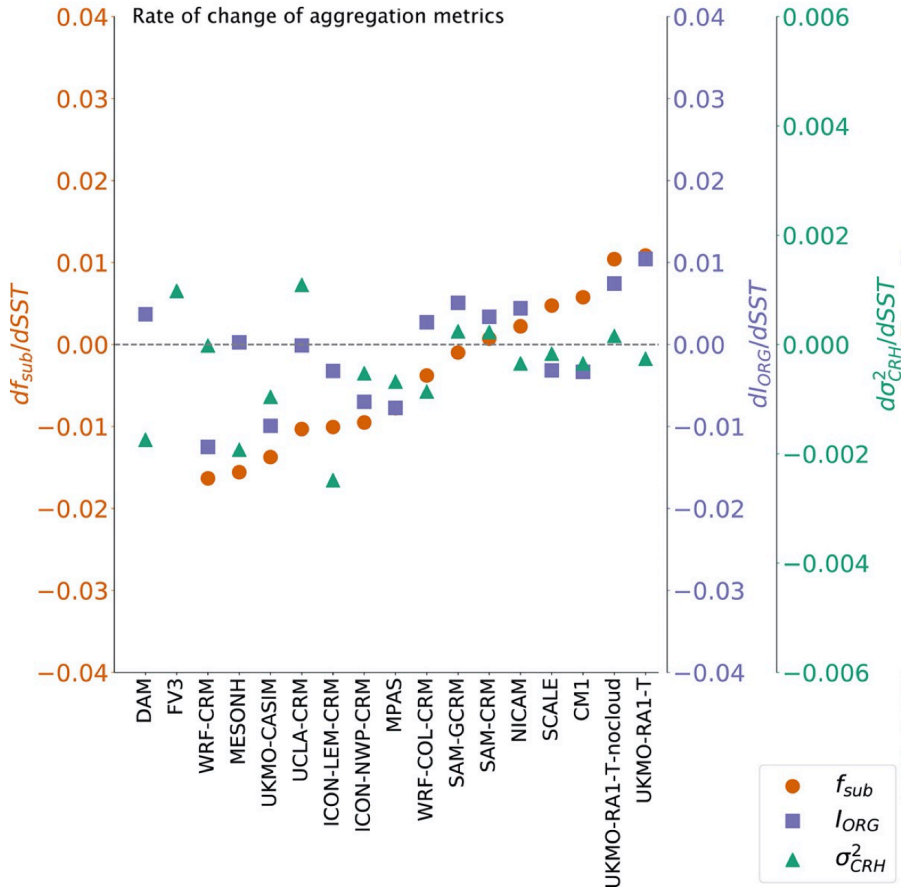

Figure 1.7: *Rate of change of aggregation with warming (per K degree) for a set of models with explicit convection, as measured by three organization metrics f_{sub} (orange circles), I_{org} (purple squares) and σ^2_{CRH} (green triangles), see Section 5.1 for details on these metrics. The response to warming is evaluated by considering the differences between the time-averaged indices corresponding to simulations at* 305 *and* 295 *K surface temperatures, respectively. The models are ordered according to their value of $df_{sub}/dSST$ (for the first two models, f_{sub} could not be calculated due to missing output). From Wing et al. (2020).*

- Second track: we will aim to define a new organization index, suitable for use in model intercomparison studies, that amends as many drawbacks as possible of the previous metrics, leading to robust and objective characterizations of the degree of aggregation.

These two tracks are not parallel but strongly interconnected and point to a better understanding of the self-aggregated convective mode, both in terms of the underlying physical mechanisms (first track) and the practical assessment of the organization degree (second track).

Regarding the first track, we will propose a much simpler model of the tropical atmosphere that, in spite of a minimal complexity in terms of the representation of physics, still retains many aspects of the more complex ones. If such a tool can simulate an evolution to self-aggregation consistently with CRMs, it may be useful to explain their inter-model differences since, unlike CRMs, it lends itself to isolating the effects of different processes and drawing more robust and general conclusions due to its simplicity and less intricate interactions between the physical processes. In the past, approaches of this type have been widely used to shed light on specific aspects of the organization process and understand the fundamental instabilities that govern it (e.g., Nilsson and Emanuel, 1999; Raymond, 2000a; Raymond and Zeng, 2000; Bretherton et al., 2005; Sobel et al., 2007; Craig and Mack, 2013; Emanuel et al., 2014; Windmiller and Craig, 2019; Ahmed and Neelin, 2019; Shi and Fan, 2021; Li, 2021). We therefore introduce a new conceptual model for the humidity budget in the tropical troposphere, which consists of a simple partial differential equation of the reaction-diffusion type. The model is equipped with a stochastic term that makes its representation of convection much more realistic. Details on the model and its numerical solution are given in Chapter 2.

The simple model is found to reproduce many aspects and sensitivities of the more complex ones, posing itself as a valuable candidate to explore the controversial points of CRM simulations. Expanding on a heuristic argument, a dimensional analysis lead us to derive a dimensionless parameter, referred to as the *aggregation number*, which we hypothesize could indicate whether the system organizes or not for a given experimental and model setup. In fact, large ensembles of simulations demonstrate that clustering occurs at a precise critical value of the aggregation number. These findings, and a discussion on their potential relevance for the community, are presented in Chapter 3. The results of Chapters 2 and 3 have been included in a paper that has been published in the American Geophysical Union (AGU) Journal of Advances in Modeling Earth Systems (Biagioli and Tompkins, 2023a).

Chapter 4 examines some further aspects of the simple model that have not been included in the derivation of the aggregation number. Consistent with CRMs, our model exhibits a weak hysteresis, which nevertheless is not particularly strong and thus does not much alter the conclusions of Chapter 3. For a better comparison with more complex numerical studies, a very idealized inclusion of the convective inhibition effects due to cold pools is also discussed.

Regarding the second track of our research, we conducted a comprehensive literature review on the existing organization metrics, which showed that there is not a universally accepted measure of aggregation. This is because distinct indices emphasize different aspects of the organization process and thus possess some relative drawbacks. Taking the perhaps most widely used metric in recent years as a starting point, we introduce new and complementary indices that improve on some of its deficiencies and are much more robust to calculation details. The new metrics prove as useful supplements to measuring convective organization across a range of spatial scales in both model output and observational datasets. These results are presented in Chapter

5 and have been included in a manuscript that has been submitted to the Journal of the Atmospheric Sciences of the American Meteorological Society (AMS) (Biagioli and Tompkins, 2023b).

Chapter 6 concludes with some final remarks and outlines some possible directions for future research.

Chapter 2

An idealized stochastic model of tropical convection

We saw in the introduction that dynamical models of the atmosphere including a detailed representation of microphysics and radiative transfer processes (*full-physics models*) rarely agree on when or how the phenomenon of convective self-aggregation occurs. Attempts have been made in the past to shed light on the areas of disagreement between full-physics models. One possible strategy consists in the development of much simpler models which may serve as useful diagnostic tools. A relatively recent research avenue has led to the derivation of theoretical approaches that interpret the occurrence of self-organization as driven by an instability of the spatially uniform RCE state of tropical convection (Bretherton et al., 2005; Craig and Mack, 2013; Emanuel et al., 2014; Beucler and Cronin, 2016; Li, 2021; Shi and Fan, 2021).

In this chapter, we introduce a new such approach, a stochastic reaction-diffusion model that consists of a single prognostic equation for column total water relative humidity (CRH) and uses CRM-like domain sizes and horizontal resolutions for ease of comparison with full-physics models. Its formulation is largely inspired by the work of Craig and Mack (2013), that is, the model represents the effects of moistening due to convection, horizontal transport and subsidence drying on the tropical CRH budget. Unlike its predecessor, the model is supplemented with a new stochastic term in the representation of convective moistening that makes it suitable to be run at convection-permitting resolutions. This new formulation, however, makes the numerical solution strategy quite challenging, as sharp discontinuities are created in the spatial CRH field. To ensure numerical stability, a solver method was designed, that is also widely introduced in the present chapter.

2.1 Towards the use of highly idealized models

It is a common practice in science to reduce complex problems to much simpler and more tractable ones. This also applies to the puzzling paradigm of convective self-aggregation, whose occurrence stems from intricate interactions between convection, water vapor, radiation, microphysics, turbulence, and so on. The results of mechanism-denial experiments themselves must be interpreted with some caution, as suppressing the effects of a physical process would remove not only its direct, but also indirect, influences. A good way forward could thus be to simplify the physics as much as possible and retain only the absolute essentials.

2.1.1 Simpler models of self-aggregation

Models of the atmosphere that are simpler than the full-physics ones but still able to mimic some of their aspects have long been used in the study of convective self-aggregation.

Under the broad umbrella of self-aggregation are also falling two-dimensional and two-column models featuring a spontaneous symmetry-breaking and instabilities representing the onset of aggregation (Raymond, 2000a; Nilsson and Emanuel, 1999; Raymond and Zeng, 2000), single-column models and two-dimensional CRMs run into the weak temperature gradient (WTG) approximation (Sobel et al., 2001) that exhibit multiple equilibria (Sobel et al., 2007; Sessions et al., 2010, 2015, 2016). These latter studies, together with the two-layer model by Emanuel et al. (2014), hint at a bistability of the atmosphere under certain circumstances. In particular, the single-column experiments by Sobel et al. (2007) demonstrated that two stable equilibria can coexist whose occurrence depends on the initial moisture profile. These results provide a direct link to CRM findings to the extent that the non-convective equilibrium may correspond to the dry patch of a self-organized climate and the moist equilibrium to the deep convective cluster.

In contrast to these column models, other approaches are spatially explicit in that they represent the horizontal variability of convection and/or humidity on spatial grids, but simplify the physics of the system to a highly conceptualized representation. The first model of this type was a two-dimensional stochastic representation of cumulus self-aggregation of Randall and Huffman (1980). More recently, Böing (2016); Haerter (2019) have introduced two-dimensional horizontal idealized models of convective cold pools to show how they could contribute to clustering, while Yang (2021) used a one-dimensional linear shallow-water model to investigate aggregation.

Some conceptual models that are even more basic in terms of their representation of physics were also developed. Within the framework of these minimally simple approaches, the onset of aggregation has been regarded as caused by an instability of the uniformly convecting atmosphere in a state of RCE (the pop-corn state of tropical convection, as we termed it in Section 1.2). A separation of the atmosphere into moist regions with ascent and dry regions with descent then ensues. An early example is the semiempirical ordinary differential equation (ODE) model by Bretherton et al. (2005),

whose derivation follows from their CRM simulations. The aforementioned work by Emanuel et al. (2014) later introduced a two-layer model and showed how an instability due to infrared radiation could occur in warmer, moister atmospheres. More recently, Shi and Fan (2021) proposed a heuristic parametric ODE model of the RCE dynamics. Both Emanuel et al. (2014) and Shi and Fan (2021) described the onset of self-organization in their models as a *subcritical bifurcation* of the spatially homogeneous RCE state of convection.

Including stochastic components

Sometimes highly idealized models have been equipped with stochastic terms to make such models more relevant for the real tropical atmosphere.

In the more general context of tropical convection modeling, stochastic approaches have been used for parameterization purposes and to investigate its impacts on atmospheric spatiotemporal variability (Lin and Neelin, 2000, 2002; Majda and Khouider, 2002; Khouider et al., 2003; Plant and Craig, 2008; Khouider et al., 2010; Khouider, 2014). Another recent research strand has focused on the analogy between the onset of strong precipitation as a function of column water vapor in the tropics and the theory of continuous phase transitions (e.g., Peters and Neelin, 2006), and to this aim stochastic models have been developed that are able to capture the salient features of tropical convection (Stechmann and Neelin, 2011; Hottovy and Stechmann, 2015a,b).

In particular, the model by Hottovy and Stechmann (2015a) considers a single prognostic equation for column water vapor supplemented with both space- and time-uncorrelated noise (white noise) field. Ahmed and Neelin (2019) further elaborated on this model and introduced a more complex formulation in terms of the representation of physics and the addition of a temporal red noise to include the variability induced by the absent processes, which is assumed to possess a temporal auto-correlation. Their model is capable of closely reproducing the observed statistics of tropical precipitation and can also sustain self-aggregation if the radiative feedbacks are strong enough and the amplitude of the stochastic forcing is properly reduced. Their moisture budget equation is of the advection-reaction-diffusion type.

In fact, it is not uncommon to study the intriguing convective self-organization through simple differential problems that can be even more minimal in terms of physical complexity, often consisting of a single reaction-diffusion equation (e.g., Windmiller and Craig, 2019; Li, 2021; Shi and Fan, 2021) or ODE (Bretherton et al., 2005), possibly equipped with stochastic forcing terms.

2.1.2 Our starting point

Another spatially explicit approach of the reaction-diffusion type (Allen-Cahn equation) is a two-dimensional model introduced by Craig and Mack (2013) to examine aggregation of convection. Their model consists of a prognostic partial differential equation for the vertically integrated water budget W in the tropical troposphere, whose derivation follows from arguments by Yanai et al. (1973). The prognostic equation for W

consists of three terms. Convection locally moistens the atmosphere and the moisture is then advected laterally using a diffusive mixing approximation, while the troposphere is subject to subsidence drying (cf. Section 1.1.1 and see cartoon Fig. 2.1). Clustering of convection is driven by a function that dictates greater convective moistening where the atmosphere is more humid, basing this positive feedback on the observed exponential increase of tropical precipitation as a function of W documented in Tropical Rainfall Measuring Mission (TRMM) precipitation data (Bretherton et al., 2004; Rushley et al., 2018).

The model has three physical parameters that describe the efficiency of the horizontal vapor transport, the subsidence drying timescale and a parameter that determines the strength of the convection-water vapor feedback. Starting from a homogeneous state with random fluctuations, Craig and Mack (2013) found that the model reproduces the phenomenon of self-aggregation, termed "coarsening", for most parameter ranges, except for values of the convection-water vapor feedback strength far below those reported by Bretherton et al. (2004); Rushley et al. (2018). They described the conditions for instability in terms of the subsidence timescale and the feedback parameter, but without considering the impact of the horizontal transport. We will show in Chapter 3 that this is also relevant. Their theory also did not incorporate the domain size nor resolution and thus could not explain the sensitivity to these simulation parameters that have been documented in the full-physics CRMs (cf. Section 1.5).

In the next Section 2.2, we will adapt the model of Craig and Mack (2013) to investigate convective aggregation onset in CRM-like experiments which resolve convection and use spatially limited domains of size $\mathcal{O}(10^2\text{-}10^3$ km$)$ with periodic boundaries. In order to do this, the model presented here differs from that of Craig and Mack (2013) in several respects, the key difference regarding the spatial resolution employed. The water budget equation of Craig and Mack (2013) was integrated on a 40 km climate-model-sized grid in which convection was treated deterministically. This means that the convective moistening term operated continuously in all locations, since the coarse resolution implied convection could be always occurring somewhere within a cell at a rate determined by the cell's humidity. Here we instead use a cloud-resolving grid resolution of $\mathcal{O}(1$ km$)$ and treat the spatiotemporal occurrence of convective activity as a stochastic binary process, either on or off. Indeed, the choice of extremely fine grids implies that, at any fixed time, within a single grid box, the presence of convection is "all-or-nothing", i.e., convection is either occurring or not at all, and a deterministic formulation for the moistening term is definitely not appropriate. Using a weighted random variable, a subset of cells will be selected at each time step to develop new convective activity to supplement the existing convection. This stochastic approach with its dependence on grid spacing will allow us to incorporate both the model resolution and the simulation domain size into the theory for aggregation onset presented in Chapter 3.

2.2 The model

As already anticipated, the model introduced here is closely related to the one presented in Craig and Mack (2013). Instead of using W as a prognostic variable, we write the model in terms of the column total water relative humidity, $R = R(\mathbf{x}, t)$, where $\mathbf{x}$ denotes the spatial coordinate(s) and t is time. R is defined as the sum of the density-weighted, column-integrated ice water (q_i), liquid water(q_l) and water vapor (q_v) specific humidities normalized by the column-integrated saturation value (q_s),[1]

$$R = \frac{\int \rho(q_v + q_l + q_i)dz}{\int \rho q_s dz}.$$

Changes in R primarily reflect those in the vertically integrated water content, owing to the horizontal temperature gradients being small in the tropical troposphere (WTG approximation, Sobel et al., 2001). However, R is dimensionless and less sensitive to temperature than W, which shows exponential dependence on temperature through the Clausius-Clapeyron relationship. We also assume time-invariance of temperature, so that the system consists of a single prognostic equation for R.[2]

In our model, as in Craig and Mack (2013), three processes affect R:

$$\frac{\partial R}{\partial t} = R_{\text{conv}} + R_{\text{trans}} + R_{\text{sub}}.$$

The model assumes that column relative humidity is rapidly increased in locations where deep convection occurs (R_{conv}), these moisture sources are subsequently redistributed horizontally by lateral vapor transport (R_{trans}), while subsidence (R_{sub}), that balances the convective mass flux, dries the atmosphere (cf. Section 1.1.1). A sketch of the model representation of physics is presented in Fig. 2.1.

2.2.1 Horizontal transport term

Considering the horizontal transport first, we follow Craig and Mack (2013) in approximating the lateral transport of water vapor by a down-gradient diffusion, $R_{\text{trans}} = K\nabla^2 R$, which is parameterized using a simple fixed value for the diffusivity K. This is an oversimplification as it neglects the enhanced mixing expected near updrafts compared to stably stratified subsidence regions (Tompkins and Semie, 2017) and also neglects temporal variations. However, Windmiller and Craig (2019) demonstrated that a diffusive treatment of lateral transport can reasonably represent the evolution of water vapor at least in the early stages of self-aggregation, as anticipated in Section 1.4.1. The use of a down-gradient mixing implies horizontal transport does not amplify, but rather damps, the existing R anomalies. In other words, by reducing spatial variance of R, the horizontal transport always acts to oppose aggregation.

[1] Although the temperature dependence is not explicitly considered here, our estimate of column cloud water detrainment (see Section 3.1) takes into account the saturation with respect to ice at temperatures colder than 0°C.

[2] If we do not assume time-invariance of temperature, a prognostic equation for temperature would be needed, in spite of the horizontal gradients being negligible in the tropical troposphere.

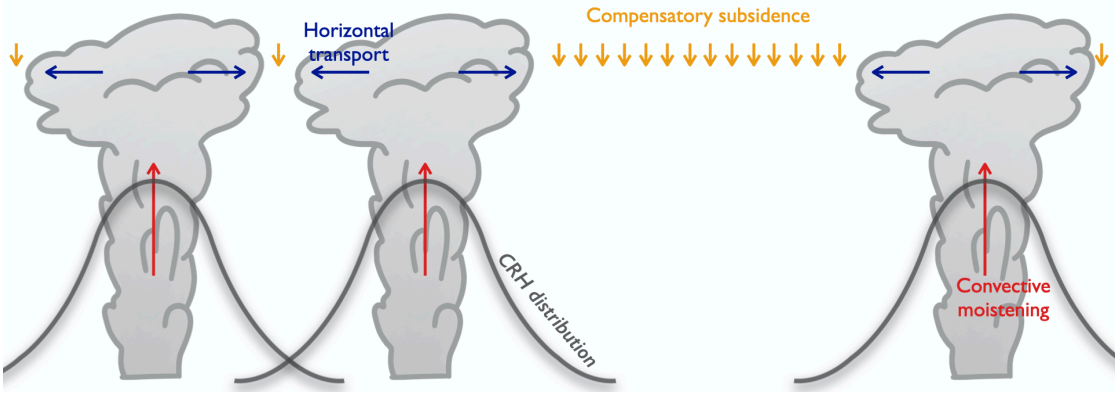

Figure 2.1: *Schematic of the physical processes represented by our toy model, with vertical ascending and descending motions and horizontal transport highlighted (arrows), and impacts on the tropical CRH budget (bell-shaped black curves).*

2.2.2 Subsidence term

The treatment of subsidence also follows Craig and Mack (2013), as subsidence is modeled as a relaxation process towards a completely dry atmosphere, thus $R_{\text{sub}} = -R/\tau_{\text{sub}}$, with a characteristic timescale τ_{sub} set to be uniform throughout the domain. In assuming this, we have implicitly hypothesized that the adjustment due to gravity wave propagation from convective events is instantaneous, which is still reasonable since this propagation is fast relative to other processes and subsidence is a superposition of drying from all convective events. The relaxation representation of subsidence implies that this term will also always reduce spatial variance of R, since it ultimately leads to a homogeneous dry atmosphere.

2.2.3 Convective moistening term

The interesting behavior of the model, namely, its ability to represent convection in both random and aggregated configurations, as we will see in Chapter 3, derives from the specification of the convective moistening term. The key novelty with respect to Craig and Mack (2013) is the adoption of a stochastic treatment for the convective moistening term, so that the model lends itself to be run at convection-resolving resolutions. This is particularly suited to mimic the typical CRM experimental setup, with the modified governing equation integrated on a two-dimensional mesh of grid cells using a $\Delta x \sim \Delta y \sim \mathcal{O}(1\text{ km})$ horizontal resolution and $D = \mathcal{O}(10^2\text{-}10^3\text{ km})$ domain sizes. In some previous idealized modeling studies (Hottovy and Stechmann, 2015a), the grid spacing was chosen to be the minimum scale of a single tropical deep convective cell, but we will not similarly constrain the resolution here.

Convective moistening is modeled as a fast relaxation with characteristic time $\tau_c \ll$

τ_{sub} towards R_c, the total water relative humidity in convective columns, which exceeds unity due to the detrainment of cloud condensate: $R_{\text{conv}} = \mathcal{I}_c(R_c - R)/\tau_c$. This term contains a diagnostic indicator random variable $\mathcal{I}_c = \mathcal{I}_c(\mathbf{x}, t)$ that maps the domain to convecting ($\mathcal{I}_c(\mathbf{x}, t) = 1$) and non-convecting ($\mathcal{I}_c(\mathbf{x}, t) = 0$) locations according to a non-uniform, humidity-dependent probability function $p_c(R(t))$. Thus, unlike the horizontal transport and subsidence terms that operate continuously in all cells, the moistening only occurs in locations occupied by convective updrafts, where $\mathcal{I}_c = 1$. In all other cells $\mathcal{I}_c = 0$ and the convective moisture source is zero (see sketch Fig. 2.2). The moistening term represents the sole stochastic contribution to the humidity budget. The details of the weighted random sampling procedure are outlined in Section 2.2.5.

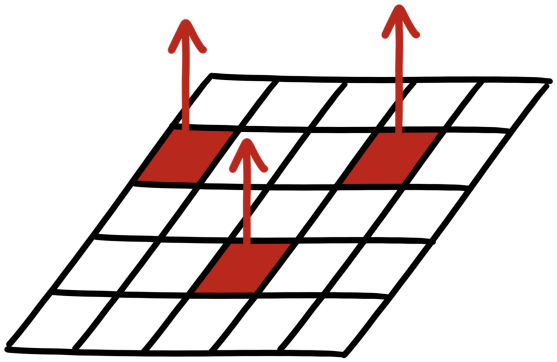

Figure 2.2: *Sketch representing the action of the indicator random variable. Red are the grid cells selected by the underlying weighted random sampling to develop convective activity, where $\mathcal{I}_c = 1$. The white cells are not involved in the convection and within them the dynamics is only governed by subsidence and diffusion.*

2.2.4 Full governing equation

In addition to the previous assumptions and modeling, we impose no large-scale dynamical forcing and exclude the Coriolis effect. Diurnal and seasonal cycle representations are also omitted.

The continuous form of the budget equation for R is thus given by

$$\frac{\partial R}{\partial t} = \frac{(R_c - R)}{\tau_c}\mathcal{I}_c + K\nabla^2 R - \frac{R}{\tau_{\text{sub}}}, \tag{2.1}$$

where the first term on the RHS represents the humidity source associated with convection, the second term expresses the lateral moisture transport, while the third term describes the drying action of subsidence. We recall that the constants τ_c and τ_{sub} denote the characteristic timescales associated with convective moistening and subsidence, respectively, R_c is the convective moistening relaxation target and K represents the horizontal moisture transport efficiency; $\mathcal{I}_c$ is the indicator function of the subset of convective points, which are prescribed at each integration step. To mimic the behavior of

the full-physics models, we will solve this equation on a square discretized grid with periodic boundary conditions of equal resolution in the x and y directions.

In summary, the net effect of convection as represented by the model is to locally moisten around the sites of convection through column saturation and detrainment of cloud condensate and to dry the far-field through compensating subsidence. Note that this treatment is more simplistic than the stochastic model of Ahmed and Neelin (2019) who modelled microphysics processes directly, and also included a treatment of horizontal vapor divergence and large-scale dynamics in addition to local diffusive mixing.

2.2.5 Selection of convective locations

Size of the sampling

To initialize the model a specific number $N_c(t=0)$ of cells are chosen at random to be convective, according to a weighted probability which will be discussed below. There is a memory for convection, and on subsequent time steps, each convective cell has a fixed probability of dying, to give an average convective duration of 30 minutes. Locations are then chosen for initiating new convective events, to ensure that the desired total population size $N_c(t)$, imposed as an external constraint, is maintained.

We require the time-averaged value of convective population size $\overline{N_c}$, and thus also the convective fraction ϵ, be prescribed by a simple mass conservation argument proposed by Tompkins and Craig (1998a). Specifically, continuity requires that the large-scale vertical motion, defined as the weighted average of the mean ascent in active clouds and the mean descent of the environmental air in-between, be

$$\overline{w} \equiv (1-\epsilon)\, w_{\text{sub}} + \epsilon w_c = 0,$$

w_{sub} and w_c indicating the subsidence and the convective updraft vertical velocities, respectively. Assuming the *small area approximation*, i.e., $\epsilon \ll 1$, so that $1-\epsilon \approx 1$, and expressing $\epsilon = \overline{N_c}/N_{xy}$, where N_{xy} is the total number of grid points in the computational domain, yields

$$\overline{N_c} = N_{xy}\frac{|w_{\text{sub}}|}{w_c} = N_{xy}\frac{h}{\tau_{\text{sub}} w_c} = \left(\frac{D}{\Delta x}\right)^2 \frac{h}{\tau_{\text{sub}} w_c}, \tag{2.2}$$

where h is the approximate depth of the troposphere. We emphasize that, as $\overline{N_c}$ is a function of the domain size, horizontal resolution and imposed subsidence rate, it remains invariant throughout simulations.

Rather than imposing a constant convective fraction (i.e., $N_c(t) = \overline{N_c}$), we assume that the temporal variation of $N_c(t)$ follows a Poisson distribution with parameter $\overline{N_c}$, subjected to a running mean with a window length equal to the assumed convective lifetime of 30 minutes, to ensure that the convective birth-rate on any time step is (nearly always) zero or positive. Occasional negative rates are subject to a correction procedure to ensure the time-averaged convective population is precisely $\overline{N_c}$ in

all experiments. We note that increasing the average convective lifetime would make self-aggregation more likely, but this aspect of the model sensitivity is not investigated further.

Weights of the sampling

When choosing the locations for new convective events, all cells in the domain with $\mathcal{I}_c = 0$ are sampled without replacement (i.e., no two convective cells can occupy the same location), using a non-uniform probability distribution $p_c(R(t))$ that depends on the column relative humidity R at current time t. We base the probability of a cell being chosen as convective on the observations of the non-linear moisture-precipitation relationship by Bretherton et al. (2004) and Rushley et al. (2018) using TRMM data, which gives surface precipitation P increasing exponentially with R:

$$P(R) = P_0 e^{a_d R}, \tag{2.3}$$

where P_0 and a_d are constant coefficients quantifying the horizontal mean RCE rain rate and the sensitivity of precipitation to column humidity, respectively. This form was also confirmed independently by Holloway and Neelin (2010).

An increase in precipitation could result from an increase in the occurrence of convective events and/or an increase in precipitation intensity per event. To allow us to use eqn. (2.3) to define the probabilities $p_c(R)$, we make the assumption that the increase in precipitation rate as a function of R is solely due to the more frequent occurrence of convection in moister atmospheres. In other words, we assume that the rainfall intensity per event is constant. This assumption, also adopted by previous idealized modeling studies (Stechmann and Neelin, 2011, 2014; Hottovy and Stechmann, 2015b), seems to be reasonable according to a recent analysis of (mid-latitude) station data by Yano and Manzato (2022) and neglects the limited contribution of increased humidity to increased precipitation efficiency (Narsey et al., 2019). It would be straightforward to include a relationship for this latter effect, but while it would change the critical threshold for aggregation onset, it would not affect the conclusions of the work and is omitted for simplicity.

Making the above assumption means we can apply (2.3) to give the probability of occurrence of *new* convection, associated with the random sampling, as

$$p_c(R_{j,k}) = Z(t) \left(e^{a_d R_{j,k}} (1 - \mathcal{I}_{c_{j,k}}) \right), \tag{2.4}$$

where the subscripts $j, k = 1, \ldots, \dfrac{D}{\Delta x}$ refer to the spatial grid and the relationship is normalized at each time step by $Z(t)$ to ensure the sum of probabilities across all convective-free cells is unity, i.e., $Z(t) = \left(\sum_{j,k} \left(e^{a_d R_{j,k}} (1 - \mathcal{I}_{c_{j,k}}) \right) \right)^{-1}$.[3]

[3]The factor $(1 - \mathcal{I}_{c_{j,k}})$ means that the cells that were already experiencing convection and have not dissipated in the meantime continue to evolve and are therefore excluded from the sampling.

Craig and Mack (2013) modified the fit of Bretherton et al. (2004) by subtracting unity from the exponential (i.e., eqn. (2.3) would become $P(R) = P_0\left(e^{a_d R} - 1\right)$) to give the limit of zero precipitation when $R = 0$. This assumption introduces a second dry equilibrium state as convection can not remoisten a completely dry domain where $R = 0$ everywhere. We instead retain the original form of Bretherton et al. (2004) to allow our model to trigger convection in dry columns. In practice, the difference to Craig and Mack (2013) in the P-R relationship has very limited effect at the values of R found in the domain.

Note that the external constraint on $N_c(t)$ and the specification of the probability law that underlies the weighted random selection process serve to define the indicator function in that they determine the cardinality of the subset mapped by $\mathcal{I}_c$ and the locations where $\mathcal{I}_c$ is activated at time t. This prevents the problem from being underdetermined. Our closure of specifying $\overline{N_c}$ differs from that adopted by Craig and Mack (2013), who instead constrained the domain-mean accumulated precipitation by assuming that the latent heat release balances the radiative cooling above the boundary layer.

2.2.6 The model contains the moisture-convection correlation

The convective term, unlike the transport and subsidence terms, can act to increase or decrease the spatial variance of R, depending on the spatial distribution of R itself and the choice of convective locations. If convection occurs in the moistest regions of the domain, the impact is to increase spatial variance, possibly leading to aggregation. Thus the model will be sensitive to a_d, which describes the observed correlation between convection and water vapor.

Through eqn. (2.4) the model incorporates such a correlation, which some CRM studies associate with the moisture-memory feedback (cf. Section 1.4.1): deep convection moistens its local environment, while enhanced humidity encourages persistence of convection. In addition, as already mentioned in the Introduction (Section 1.4.1), CRM studies have also acknowledged the important role of the radiative and surface flux contributions to the localization of convection. In moist areas, this primarily occurs through enhanced longwave heating and shortwave absorption due to the high infrared opacity and the presence of deep convective cloudiness and through increased fluxes due to the strengthening of the storm-induced gustiness. These effects jointly act to amplify the positive MSE anomalies in the moist patches. In this perspective, the parameter a_d, which describes how likely convection is to occur in the vicinity of previous events, can be thought of as representing the net positive feedback of all diabatic processes driving the aggregation.

In summary, the formulation of the simple model contains the moisture-convection correlation. This correlation can be associated with feedback processes directly involving the water vapor field or can simply represent a diagnostic of other mechanisms (like the diabatic ones) that do not entail a spatial homogeneity of water vapor. The specification of the convective moistening term and, in particular, of the probability function

that underlies the selection of new convective cells can be regarded as a proxy for a number of physical processes, at least those associated with water vapor.

2.2.7 A one-dimensional version of the model

To better visualize the effects of each physical term, a one-dimensional version of the model was also developed, which is identical to eqn. (2.1) except for the fact that the laplacian ∇^2 is to be replaced by the second derivative $\partial^2/\partial x^2$. An animation showing the results of a simulation performed with this one-dimensional counterpart of the model can be found at `http://clima-dods.ictp.it/Users/gbiagiol/animation_1d.mp4`. In this experiment, there is only one convective event at a time, which is anyway consistent with the mass conservation constraint eqn. (2.2). Given its simplicity, this version also lends itself to motivating or checking the findings of some more theoretical studies, which are beyond the scopes of this thesis but will be a topic of future research.

2.3 Numerical treatment

Adequate numerical treatment is needed to ensure the results are not time step sensitive. We will use implicit solution techniques to ensure stability. The time step is set to be uniform. Adaptive strategies could be considered, with a refinement of the time step in the very first, transient phase after the eruption of updrafts. Nevertheless, the local spikes introduced by convection act to continuously perturb the system and in practice the adaptive approach is not viable. In the following, we will provide a full description of the numerical solvers for both the one- and two-dimensional versions of the model and discuss a number of idealized experiments to demonstrate numerical robustness. The code for numerical solution of the two-dimensional model is available on github at `https://github.com/adriantompkins/toy_diffusion` and the version used in this thesis is tagged `v1.1.JAMES`.

2.3.1 The one-dimensional case

For the implicit solution of the full one-dimensional equation, a uniform spatial grid with spacing Δx and a uniform mesh in time with time step Δt are considered. Second-order accurate central difference approximations to the second derivative are employed for the spatial dimension, whereas first-order backward Euler method is applied in time. One may want to adopt the second-order accurate trapezoidal rule for the temporal integration, but it is well known that, when sharp discontinuities are present in a diffusive problem (as is the case here) and a large time step is taken, the solution may contain spurious oscillations, that are then damped with time (e.g., Østerby, 2003). This is directly related to the concept of *L-stability* (e.g., Brugnano and Trigiante, 1998). Moreover, such a treatment would introduce an additional computational burden as a

matrix-by-vector multiplication has to be performed at each time step. For these reasons, the implicit Euler scheme is preferred despite being only first-order in time.

The final discretized equation reads

$$\frac{R_j^{n+1} - R_j^n}{\Delta t} = -\frac{1}{\tau_{\text{sub}}} R_j^{n+1} - \frac{1}{\tau_c}\left(R_j^{n+1} - R_c\right)\mathcal{I}_{c_j}^n + \frac{K}{\Delta x^2}\left(R_{j+1}^{n+1} - 2R_j^{n+1} + R_{j-1}^{n+1}\right),$$

which leads to

$$\alpha_j^n R_j^{n+1} - \beta\left(R_{j+1}^{n+1} + R_{j-1}^{n+1}\right) = R_j^n + \frac{\Delta t}{\tau_c} R_c \mathcal{I}_{c_j}^n, \tag{2.5}$$

where

$$\alpha_j^n = 1 + \Delta t\left(\frac{1}{\tau_{\text{sub}}} + \frac{1}{\tau_c}\mathcal{I}_{c_j}^n + 2\frac{K}{\Delta x^2}\right),\ \beta = K\frac{\Delta t}{\Delta x^2}.$$

In the previous formulation, the subscript j and the superscript n refer to the spatial and temporal discretizations, respectively. It is important to remark that the label α_j^n (rather than just α) is because these elements depend on the spatial and temporal variables through the indicator function $\mathcal{I}_c$. We however recall that the selection of convective locations is performed before the time integration takes place, whence the superscript n.

For each time $n \geq 0$, the set of equations (2.5) can be rewritten in the matrix form

$$A^n \mathbf{R}^{n+1} = \mathbf{b}^n, \tag{2.6}$$

where $A^n \in \mathbb{R}^{N_x \times N_x}$, N_x being the total number of grid points in the x-direction, is the *cyclic tridiagonal matrix*

$$A^n = \begin{pmatrix} \alpha_1^n & -\beta & & & -\beta \\ -\beta & \alpha_2^n & -\beta & & \\ & \ddots & \ddots & \ddots & \\ & & -\beta & \alpha_{N_x-1}^n & -\beta \\ -\beta & & & -\beta & \alpha_{N_x}^n \end{pmatrix},$$

$\mathbf{R}^{n+1} \in \mathbb{R}^{N_x}$ denotes the vector of the unknowns and $\mathbf{b}^n \in \mathbb{R}^{N_x}$ is simply the RHS of (2.5). The structure of the coefficient matrix results from the assumption of periodic boundary conditions which is typically made in CRM studies, i.e., the solution "wraps around itself" at the end of the spatial domain. Note that the matrix is not even circulant due to the presence of the stochastic moistening term.

If A^n were a tridiagonal matrix, the linear system (2.6) could be efficiently solved with the classical tridiagonal matrix (or Thomas) algorithm (TDMA). It is well known that the application of the TDMA to a problem of size N requires $8N - 7$ floating point operations (flops), $3(N-1)$ of which in the LU-decomposition phase of the coefficient matrix and $5N - 4$ in the subsequent solution phase. A condition for TDMA to be stable is the symmetry and positive definiteness of the tridiagonal system matrix (Higham, 2002). Here it is still possible to retain the efficiency of the classical TDMA by adopting

a decomposition of the coefficient matrix based on the *Sherman-Morrison formula* (Golub and van Loan, 2013). This reduces the original problem to the solution of two linear tridiagonal systems.

General case

Let $A\mathbf{x} = \mathbf{b}$ denote a set of equations, with $A \in \mathbb{R}^{N\times N}$ the coefficient matrix, which we assume is cyclic tridiagonal, $\mathbf{x} \in \mathbb{R}^N$ the unknown and $\mathbf{b} \in \mathbb{R}^N$ the RHS. Any cyclic tridiagonal matrix can be interpreted as a rank-one correction of a general (nonsingular) tridiagonal matrix $T \in \mathbb{R}^{N\times N}$, i.e.,

$$A = T + \mathbf{u}\mathbf{v}^{\mathsf{T}}, \tag{2.7}$$

where $\mathbf{u}, \mathbf{v} \in \mathbb{R}^N$ are proper vectors. The choice of T, $\mathbf{u}$ and $\mathbf{v}$ is arbitrary and we will see an example choice for the case of interest below. The Sherman-Morrison formula gives the inverse of A in terms of the inverse of T as

$$A^{-1} = T^{-1} - \frac{1}{1+\lambda}\left(T^{-1}\mathbf{u}\mathbf{v}^{\mathsf{T}}T^{-1}\right), \tag{2.8}$$

under the further assumption $1 + \lambda \equiv 1 + \mathbf{v}^{\mathsf{T}}T^{-1}\mathbf{u} \neq 0$. By means of (2.8), the solution of the original set of equations is reduced to the solution of auxiliary tridiagonal systems

$$T\mathbf{y} = \mathbf{b} \tag{2.9}$$
$$T\mathbf{z} = \mathbf{u}, \tag{2.10}$$

followed by a linear combination of $\mathbf{y}$ and $\mathbf{z}$, to yield

$$\mathbf{x} = \mathbf{y} - \left(\frac{\mathbf{v}\cdot\mathbf{y}}{1+\mathbf{v}\cdot\mathbf{z}}\right)\mathbf{z}. \tag{2.11}$$

Application to our case

In the case of interest, for each $n \geq 0$, the cyclic tridiagonal matrix representation A^n of (2.6) satisfies (2.7) with, e.g.,

$$T^n = \begin{pmatrix} 2\alpha_1^n & -\beta & & & \\ -\beta & \alpha_2^n & -\beta & & \\ & \ddots & \ddots & \ddots & \\ & & -\beta & \alpha_{N_x-1}^n & -\beta \\ & & & -\beta & \alpha_{N_x}^n + \dfrac{\beta^2}{\alpha_1^n} \end{pmatrix} \quad \mathbf{u}^n = \begin{pmatrix} -\alpha_1^n \\ 0 \\ \vdots \\ 0 \\ -\beta \end{pmatrix} \quad \mathbf{v}^n = \begin{pmatrix} 1 \\ 0 \\ \vdots \\ 0 \\ \dfrac{\beta}{\alpha_1^n} \end{pmatrix}. \tag{2.12}$$

Decompositions other than (2.12) can be adopted depending on the first entry of $\mathbf{u}^n$, which is arbitrary: here $u_1^n = -\alpha_1^n$, while, for instance, setting $u_1^n = \alpha_1^n$ will result in

a zero top-left entry in the matrix T^n and in a failure of the LU-decomposition of T^n. The symmetric matrix T^n is strictly diagonally dominant (hence nonsingular) and has strictly positive diagonal entries, thus it is positive definite (Bini et al., 1988). The LU-decomposition process of the matrix T^n is therefore stable.

The computational cost is still massively cut. We notice that, in each update (2.6), in addition to the $10N_x - 8$ flops associated with the solution of (2.9)-(2.10), the computation (2.11) requires $2N_x + 6$ algebraic operations, hence the linear complexity of the TDMA is well retained. Finally, $3(N_x - 1)$ storage units are needed, which introduces insignificant memory overhead.

2.3.2 Towards the solution of the two-dimensional problem

For the numerical solution of the two-dimensional problem (2.1), this kind of approach can not be extended and applied due to the completely different structure of the coefficient matrix resulting from implicit-time discretization. The size of the linear system itself sometimes can be so large that its solution at each time step turns out to be extremely expensive. For instance, the adoption of two-dimensional backward Euler or Crank-Nicolson (CN) schemes yields a block coefficient matrix of dimension $N_xN_y \times N_xN_y$, N_x and N_y being the total number of grid points in the x- and y-direction, respectively. Although sparse, the matrix is not circulant (or at least block circulant with circulant blocks) nor constant with time owing to the triggering of convective events, whose corresponding terms contribute to the entries of the main diagonal. This makes the attempts to solve the problem through implicit procedures almost prohibitive.

On the other hand, the use of explicit schemes is not to be recommended due to severe constraints on the time step to ensure stability. For example, if explicit Euler method is employed to solve reaction-diffusion equations like

$$\frac{\partial R}{\partial t} = K\nabla^2 R - \frac{R}{\tau_{\text{sub}}} \tag{2.13}$$

(eqn. (2.1) with only the diffusion and subsidence terms retained), application of von Neumann stability analysis shows that the scheme is stable provided that $4K\Delta t/\Delta x^2 + 4K\Delta t/\Delta y^2 + \Delta t/\tau_{\text{sub}} \leq 2$, i.e., assuming $\Delta x = \Delta y$, the limit

$$\Delta t \leq \frac{2}{\frac{8K}{\Delta x^2} + \frac{1}{\tau_{\text{sub}}}} \simeq \frac{\Delta x^2}{4K} \tag{2.14}$$

is imposed on the time step, the approximate equality following from the fact that typically $\tau_{\text{sub}}^{-1} \ll 1$. The restriction (2.14) is referred to as the *diffusive stability criterion*. The quantity $\Delta x^2/K$ can be interpreted as a characteristic diffusion time, essentially the time needed for a disturbance to be transmitted by diffusion over a distance Δx (Ferziger and Perić, 2002).

For implicit discretization schemes, there is no longer a critical threshold for stability, yet the limit (2.14) still serves as a measure of accuracy. In fact the unconditionally stable Crank-Nicolson scheme may produce solutions with oscillatory behavior if large

time steps are taken (Ferziger and Perić, 2002), especially in response to sharp discontinuities in the initial conditions. In practice, time steps that widely exceed the constraint (2.14) may be used, the actual limit being often problem-dependent (Ferziger and Perić, 2002), but still caution must be taken in the choice of the time step.

Splitting techniques

A computationally sustainable alternative able to retain the implicitness of the solution method is offered by the adoption of the so-called *splitting strategies*.

Commonly, when a differential problem involves many physical processes, it is not possibly or numerically efficient to attempt the integration of the equations by means of a single solver method. We could then decompose (split) the system into sub-groups of processes and use different suitable and advantageous methods for each group, with tendencies from each treated sequentially in time. Similar techniques can be applied with respect to the spatial dimension. That is, a d-dimensional problem can be broken down into more convenient (sub)problems in lower-dimension spaces, which can be solved more easily/efficiently. These approaches, referred to as *operator* and *dimensional splitting* respectively, may lead to significant simplifications of the overall solution procedure. However, they normally introduce an error, the splitting error, which is investigated in the sequel.

The following discussion focuses on the first type of splitting strategies and is largely based on Hundsdorfer and Verwer (2003). Let $u_t = f(u)$ denote a generic, scalar partial differential equation, where f can be regarded as a spatial partial differential operator. The simplest possible splitting is a two-term splitting, i.e., a two-term additive decomposition of the RHS is assumed,

$$f(u) = f_1(u) + f_2(u). \tag{2.15}$$

Various approaches are considered for the time advancement from t^n to t^{n+1}.

The most intuitive one is the so-called *Lie splitting*, which results in the sequential solution of the problems

$$u_t^* = f_1(u^*),\ t^n < t \leq t^{n+1},\ u^*(t^n) = u^n, \tag{2.16}$$

$$u_t^{**} = f_2(u^{**}),\ t^n < t \leq t^{n+1},\ u^{**}(t^n) = u^*(t^{n+1}), \tag{2.17}$$

and the global solution is set to be $u^{n+1} = u^{**}(t^{n+1})$. The two groups of physical processes are therefore integrated one after the other, with the tendency from the first used as initial condition for the treatment of the second. We can estimate the local truncation error τ^{n+1} associated with the splitting (2.16)-(2.17). This is by definition the error introduced by a single splitting integration step, under the local hypothesis that the exact solution is known at t^n.[4] It obeys

$$\tau^{n+1} = \frac{1}{2}\Delta t^2 \left[\frac{\partial f_1}{\partial u} f_2 - \frac{\partial f_2}{\partial u} f_1\right] u(t^n) + \mathcal{O}\left(\Delta t^3\right),$$

[4]In other words, the local truncation error can be regarded as the residual generated per integration step when the exact solution is plugged into the numerical scheme.

with $\Delta t = t^{n+1} - t^n$. In particular, the splitting is exact only if the term in brackets, called the commutator $[f_1, f_2]$ of the operators f_1 and f_2, is zero, otherwise it provides a first-order approximation as the local error on smooth solutions is $\mathcal{O}\left(\Delta t^2\right)$.

The accuracy can be improved to second order by adopting the so-called *Strang splitting* (Strang, 1968). In this case, rather than taking a full time step with each operator, half a step is performed with the operator f_2, followed by a full step with f_1 and another half step with f_2 (or vice versa), with the tendency from the previous process providing the initial value to the subsequent process(es). In formulae,

$$u_t^* = f_2(u^*), \quad t^n < t \leq t^{n+\frac{1}{2}}, \quad u^*(t^n) = u^n, \tag{2.18}$$

$$u_t^{**} = f_1(u^{**}), \ t^n < t \leq t^{n+1}, \quad u^{**}(t^n) = u^*\left(t^{n+\frac{1}{2}}\right), \tag{2.19}$$

$$u_t^{***} = f_2(u^{***}), \, t^{n+\frac{1}{2}} < t \leq t^{n+1}, \, u^{***}\left(t^{n+\frac{1}{2}}\right) = u^{**}(t^{n+1}), \tag{2.20}$$

and the overall solution is given by $u^{n+1} = u^{***}(t^{n+1})$. The local truncation error introduced by the splitting (2.18)-(2.20) satisfies

$$\tau^{n+1} = \frac{1}{24}\Delta t^3 \left([f_2, [f_1, f_2]] + 2\,[f_1, [f_1, f_2]]\right) u(t^n) + \mathcal{O}\left(\Delta t^4\right),$$

thus revealing second-order accuracy on sufficiently smooth solutions, provided that each subproblem is treated with a method of such accuracy at least.

Splitting techniques are commonly invoked in meteorological applications with multiple timescales (Beljaars et al., 2018). In the case of interest, the subsidence and diffusion components of the full equation (2.1) will be separated from the convective source term. Thus, in analogy with (2.15), we can write

$$\frac{\partial R}{\partial t} = f_1(R) + f_2(R),$$

where $f_1(R)$ is the RHS of (2.13) and $f_2(R) = \tau_c^{-1}\left(R_c - R\right)\mathcal{I}_c$. The convenience of this splitting is immediately apparent: it will not produce any splitting error in the non-convective grid points, where the second operator vanishes - it does not even make sense to talk about a splitting in those locations. On the other hand, in the cells where convection is triggered, the commutator $[f_1, f_2]$ is

$$[f_1, f_2] = K\nabla^2\left(\frac{R_c - R}{\tau_c}\right) - \frac{1}{\tau_{\text{sub}}}\frac{R_c - R}{\tau_c} + \frac{1}{\tau_c}\left(K\nabla^2 R - \frac{R}{\tau_{\text{sub}}}\right) = -\frac{1}{\tau_{\text{sub}}}\frac{R_c}{\tau_c} \neq 0.$$

This requires the use of second-order Strang splitting methods, even though typical values of τ_{sub}, τ_c and R_c (cf. Section 3.1) imply $[f_1, f_2] \simeq 0$ and the convective fraction ϵ is usually $\epsilon \ll 1$ (the small-area approximation, Section 2.2.5).

In conclusion, the numerical solution procedure for eqn. (2.1) consists in solving the differential problem with only the convection term for half a time step, then the problem eqn. (2.13) for a full step and again the former for another half step. Now everything is reduced to finding suitable integration formulas for both subproblems.

2.3.3 Treatment of the convective source term

For the problem involving f_2, the analytical solution is derived, in order to reduce as much as possible any integration error, related to the application of numerical methods, which can be incurred in addition to the splitting error. This exact solution is given by

$$R(t) = \left(R_c + (R(t_0) - R_c)\, e^{-\frac{t-t_0}{\tau_c}}\right) \mathcal{I}_c(t_0).$$

2.3.4 The Alternating Direction Implicit schemes

The numerical solution of the reaction-diffusion equation (2.13) is obtained by means of second-order accurate centered difference approximations of the second derivatives and a properly modified version of the *Alternating Direction Implicit* (ADI) scheme for the temporal discretization.[5] The equation will be integrated on a square mesh with uniform spacing, assumed to be the same in the x and y directions, i.e., $\Delta y = \Delta x$, and on a uniform grid in time with step Δt.

The ADI schemes can significantly reduce the computational cost associated with the application of backward Euler or Crank-Nicolson methods. Nevertheless, they retain all advantages of implicit schemes while also leading to much smaller and generally structured sets of linear systems, which can be easily solved with direct methods. Indeed, the ADI procedures consist in splitting two-dimensional problems into two separate steps, treating implicitly only one spatial derivative at a time and therefore performing line-by-line solution of small, independent sets of equations. Thus the ADI schemes can be interpreted as an example of dimensional splitting approaches (cf. Section 2.3.2).

The classical ADI method, first developed by Peaceman and Rachford (1955) for the numerical solution of the two-dimensional heat equation, can be regarded as a perturbed formulation of the Crank-Nicolson scheme. Applying CN to eqn. (2.13) would yield

$$\left(1 - \beta\delta_x^2 - \beta\delta_y^2 + \omega\right) R_{j,k}^{n+1} = \left(1 + \beta\delta_x^2 + \beta\delta_y^2 - \omega\right) R_{j,k}^{n},$$

where the subscripts j, k, $j = 0, \ldots, N_y$, $k = 0, \ldots, N_x$, refer to the horizontal square grid and the superscript n indicates discrete time steps; $\delta_\bullet^2$ is a second-order difference operator, $\beta = K\dfrac{\Delta t}{2\Delta x^2}$ and $\omega = \dfrac{\Delta t}{2\tau_{\text{sub}}}$. By factoring both sides, the previous equation

[5] In principle it would be possible to derive the analytical solution of eqn. (2.13) (as it is a linear parabolic equation) through separation of variables and the theory of Fourier series. In particular, separation of variables would lead to Sturm-Liouville eigenvalue problems for the spatial components of the solution and to a first-order ordinary differential problem for the temporal part. Nevertheless, numerical treatment is still the preferred approach as future modifications may be made to the model, involving, for example, the inclusion of non-linear terms which necessarily restricts us to the use of numerical schemes.

can be rearranged as

$$\begin{aligned}\left(1-\beta\delta_x^2+\omega\right)\left(1-\beta\delta_y^2\right)R_{j,k}^{n+1} = \left(1+\beta\delta_x^2-\omega\right)\left(1+\beta\delta_y^2\right)R_{j,k}^{n} \\ +\left(\beta^2\delta_x^2\delta_y^2-\omega\beta\delta_y^2\right)\left(R_{j,k}^{n+1}-R_{j,k}^{n}\right).\end{aligned} \tag{2.21}$$

The last term on the RHS is $\mathcal{O}(\Delta t^3)$ as $R_{j,k}^{n+1}-R_{j,k}^{n}\approx\Delta t\partial R/\partial t$ (see below for a complete analysis). In the derivation of the Peaceman-Rachford ADI scheme an analogous third-order term is neglected (the relationship for time advancement is the same as (2.21) with $\omega=0$). This is justifiable when Δt is small, but large errors can be introduced with larger time steps. Methods based on such approximations are called *approximate factorization schemes* (Thomas, 1995).

Our modified version of the conventional ADI method entails the sequential solution of the systems

$$\left(1-\beta\delta_x^2+\omega\right)R_{j,k}^{n+\frac{1}{2}} = \left(1+\beta\delta_y^2\right)R_{j,k}^{n}, \tag{2.22}$$

$$\left(1-\beta\delta_y^2\right)R_{j,k}^{n+1} = \left(1+\beta\delta_x^2-\omega\right)R_{j,k}^{n+\frac{1}{2}}. \tag{2.23}$$

This means that, for a time step $\dfrac{\Delta t}{2}$, the x-derivative is treated implicitly, the y-derivative explicitly and an intermediate solution $\mathbf{R}^{n+\frac{1}{2}}$ is obtained, then the procedure is repeated for a second time step of equal size, with the difference equation (2.23) evaluated implicitly in the y-direction and explicitly in the x-direction.

It is possible to show that the two-step scheme (2.22)-(2.23) is unconditionally stable and second-order in both space and time, hence convergent. For stability, we make use of the von Neumann analysis and take the two-dimensional discrete Fourier transform of both sides of equations (2.22) and (2.23). Labeling ζ, η the transformed coordinates, we see that the symbol (that is, the amplification factor) of the difference scheme (2.22)-(2.23) fulfills

$$\rho(\zeta,\eta)=\frac{\left(1-\omega-4\beta\sin^2\left(\frac{\zeta}{2}\right)\right)\left(1-4\beta\sin^2\left(\frac{\eta}{2}\right)\right)}{\left(1+4\beta\sin^2\left(\frac{\eta}{2}\right)\right)\left(1+\omega+4\beta\sin^2\left(\frac{\zeta}{2}\right)\right)},$$

which is $|\rho|\leq 1$ owing to the positive sign of β and ω. This guarantees that (2.22)-(2.23) is unconditionally stable as a scheme for initial-value problems. Nevertheless, since periodic boundary conditions are assigned, the same conclusions hold for (2.22)-(2.23) now regarded as a method for initial-boundary-value problems (Mitchell and Griffiths, 1980; LeVeque, 2007).

The second-order accuracy can be established by recalling that the ADI scheme differs from CN for the term $-\left(\beta^2\delta_x^2\delta_y^2-\omega\beta\delta_y^2\right)\left(R_{j,k}^{n+1}-R_{j,k}^{n}\right)$. It is well known that the Crank-Nicolson method is second order in time. This order of consistency is inherited

by the ADI scheme as Taylor series expansion of the extra terms yields

$$\left(\beta^2\delta_x^2\delta_y^2 - \omega\beta\delta_y^2\right)\left(R_{j,k}^{n+1} - R_{j,k}^{n}\right) = \frac{K^2}{4}\Delta t^3\left(\frac{\partial^5 R}{\partial t\partial x^2\partial y^2}\right)_{j,k}^{n} + \frac{K}{2\tau_{\text{sub}}}\Delta t^3\left(\frac{\partial^3 R}{\partial t\partial y^2}\right)_{j,k}^{n} + \mathcal{O}\left(\Delta t^3\Delta x^2\right) + \mathcal{O}\left(\Delta t^3\Delta y^2\right) + \mathcal{O}(\Delta t^4).$$

Prescribing periodic boundary conditions leads to circulant tridiagonal systems, which can be easily solved by using Fast Fourier Transform (FFT) algorithms (e.g., Cooley and Tukey, 1965). The matrices resulting from (2.22) and (2.23),

$$A_1 = \text{circ}\left(1 + 2\beta + \omega, -\beta, 0, \ldots, 0, -\beta\right),$$
$$A_2 = \text{circ}\left(1 + 2\beta, -\beta, 0, \ldots, 0, -\beta\right),$$

are strictly diagonally dominant, hence nonsingular.[6] If the mesh points are ordered by lines, in the x-direction in the first stage and in the y-direction in the second one, (2.22) represents a set of N_y independent circulant tridiagonal systems with coefficient matrix A_1 and size N_x each and, similarly, (2.23) constitutes a set of N_x independent circulant tridiagonal systems with matrix A_2 and size N_y. To carry out this procedure, an implicit (transposed) reordering of the CRH data between (2.22) and (2.23) and then again between (2.23) and (2.22) at the new discrete time must be done.

[6] A fundamental property of circulant matrices is that they are diagonalized by the Fourier matrices, the matrix form of the discrete Fourier transform. In formulae,

$$A = F_N^{\mathsf{H}}\Lambda F_N, \tag{2.24}$$

where $A \in \mathbb{C}^{N\times N}$, $\mathbb{C}$ being the set of complex numbers, is a circulant matrix which can also be denoted $A = \text{circ}(a_0, a_1, \ldots, a_{N-1}) = \text{circ}(\mathbf{a})$ in terms of the first column entries; $F_N \in \mathbb{C}^{N\times N}$ is the Fourier matrix of order N which is the Vandermonde matrix of the complex conjugates of the primitive N-th roots of unity, with a multiplicative constant $\frac{1}{\sqrt{N}}$; $.^{\mathsf{H}}$ denotes the Hermitian transpose of a matrix; Λ is the diagonal matrix containing the eigenvalues of A (Davis, 1979). The set of eigenvalues of a circulant matrix can be expressed as

$$\boldsymbol{\lambda} = \sqrt{N}F_N\mathbf{a}. \tag{2.25}$$

For the solution of the circulant system $A\mathbf{x} = \mathbf{b}$, it is seen that, if A is nonsingular, the factorization (2.24) yields

$$\mathbf{x} = A^{-1}\mathbf{b} = F_N^{\mathsf{H}}\Lambda^{-1}F_N\mathbf{b},$$

which implies the sequential solution of the systems

$$\mathbf{y} = F_N\mathbf{b}, \tag{2.26}$$
$$\mathbf{z} = \Lambda^{-1}\mathbf{y}, \tag{2.27}$$
$$\mathbf{x} = F_N^{\mathsf{H}}\mathbf{z}. \tag{2.28}$$

We note that the relationships (2.25), (2.26) and (2.28) represent the Discrete Fourier Transform (DFT) and Inverse Discrete Fourier Transform (IDFT), respectively. Direct evaluation of each of the above expressions would require $\mathcal{O}(N^2)$ flops, precisely N^2 multiplications and $N^2 - N$ additions. The computational burden can be substantially reduced if FFT methods are used, e.g., the Cooley-Tukey algorithm (Cooley and Tukey, 1965). Here the FFT algorithm has to be applied three times, one in (2.26), one in (2.27) via (2.25) and one in (2.28). A proof of numerical stability results for the Cooley-Tukey FFT algorithm, as well as for the solution procedure (2.25)-(2.28), can be found in Higham (2002).

Final remarks and alternative solver methods

Other approaches can be developed for the numerical solution of circulant systems to exploit eventual properties and structures of the coefficient matrix (e.g., Chen, 1987). Alternatively it is still possible to make use of the Sherman-Morrison formula (2.8), especially because the matrix representations of (2.22) and (2.23), hence their decompositions (2.7), do not vary with time. This means that the LU-decomposition of the tridiagonal matrix in (2.7) has to be performed only once and the solution of the linear system (2.10) has to be calculated only at the beginning of the overall integration procedure and then stored. Only the solution of (2.9) would be required in each of the updates (2.22), (2.23). This method was found to be extremely competitive with the FFT one as long as the size of the linear systems resulting from (2.22) and (2.23) stays relatively small (< 100), then the circulant solver is to be preferred.

We agreed upon ignoring the third-order term on the RHS of (2.21), as tests conducted to compare the performances of ADI versus Crank-Nicolson showed that generally the infinity norm $\left\|\mathbf{R}^n_{\mathrm{CN}} - \mathbf{R}^n_{\mathrm{ADI}}\right\|_\infty \equiv \max_{j,k} \left|R^n_{\mathrm{CN}_{j,k}} - R^n_{\mathrm{ADI}_{j,k}}\right|$ of the difference between the respective solutions rapidly goes to zero (not shown). Factorizations other than (2.21) can be used, for example the one adopted by Douglas and Kim (2001) on the basis of a more general formulation of ADI procedures developed by Douglas and Gunn (1964).

Different approaches could be chosen to solve (2.13) by means of implicit methods. For example, one may want to use Crank-Nicolson scheme directly and apply, e.g., the efficient block circulant solver by Chen (1987) to the linear system resulting from the discretization. However, we noticed that the ADI method is able to produce more accurate results than the CN itself for the heat equation with linear source term (2.13) under consideration here. In particular, we saw that, for certain combinations of K, Δt and Δx, the Crank-Nicolson scheme turns out to be overdiffusive, therefore providing inaccurate solutions, whereas the ADI method is not affected by this drawback and smooths spurious oscillations. This feature was already pointed out by other authors (e.g., Sgura et al., 2012).

A further alternative is to use the ADI procedure for the numerical solution of the full equation (2.1), without adopting any operator splitting technique. However, this would lead to the solution of smaller, independent sets of equations which are no longer circulant or constant with time. Obviously it is still possible to employ the Sherman-Morrison formula (2.8) but it would be used for each of the $N_x + N_y$ systems to be solved per time step, for all temporal iterations. Indeed in this case none of the decompositions (2.7) can be stored. Even though the resulting method was still relatively fast, it was not considered further.

2.4 Numerical convergence tests for the two-dimensional case

2.4.1 Numerical convergence of the ADI scheme

The convergence properties of the new ADI solver are assessed against the assumption of initial top-hat or Gaussian profiles. The results of convergence tests under time step and grid refinements are shown in Figs. 2.3 and 2.5, respectively.

Time step sensitivity

In the first case (Fig. 2.3), the problem eqn. (2.13) is considered, with $K = 10^4$ m^{2}s^{-1}, $\tau_{\text{sub}} = 10$ days, over a domain with size $D = 300$ km and spacing $\Delta x = 2$ km,[7] and initial condition given by

$$R_0(\mathbf{x}) = R(\mathbf{x}, 0) = \begin{cases} 1 & \text{for } \mathbf{x} \in [x_1, x_2] \times [y_1, y_2] \\ 0.8 & \text{elsewhere} \end{cases}, \tag{2.29}$$

where $x_1, y_1 = 140$ km and $x_2, y_2 = 160$ km. The top-hat configuration is a good test bench due to presence of very sharp discontinuities. Earlier (Section 2.3.2) we saw that the diffusive stability criterion (2.14) is to be satisfied for the explicit Euler method to be stable, while, for implicit schemes, a limit of this type still serves as a measure of accuracy. Labeling $\xi = 4K\dfrac{\Delta t}{\Delta x^2}$, we impose several time steps corresponding to a range of values of ξ and compute the solutions $\mathbf{R}_\xi$.

Convergence is apparent in the time slices of Fig. 2.3 (dashed and dash-dotted lines), even though the approximation for $\xi = 6$ exhibits a spurious oscillation at the beginning, which is then damped and rapidly disappears. This is also confirmed by a more systematic error analysis which, given the convergence properties, uses the solution corresponding to $\xi = 5 \times 10^{-4}$ ($\Delta t = 0.05$ s) as a reference one, $\mathbf{R}_{\text{ref}}$. For each choice of ξ and time $\{t^n_\xi\}_{n\geq 0}$, the infinity norm of the error $\mathbf{e}$, $\|\mathbf{e}(t^n_\xi)\|_\infty \equiv \max_{j,k} |R_{\text{ref}_{j,k}}(t^n_\xi) - R_{\xi_{j,k}}(t^n_\xi)|$, is computed. The following Fig. 2.4a shows that, in general, the error decays in a few iterations. To evaluate the orders of the magnitude of the errors more precisely, these are charted in terms of time step choice in Fig. 2.4b after $t = 100$ s of simulated time (corresponding to the first iteration for the case $\xi = 1$).[8]

Grid size sensitivity

Spatial convergence properties are examined, as also demanded by a resolution sensitivity study presented in Chapter 3. The results of a grid refinement analysis performed on the problem eqn. (2.13) with $K = 5 \times 10^3$ m^{2}s^{-1}, $\tau_{\text{sub}} = 10$ days and Gaussian initial distribution with $\mu = 150$ km and $\sigma = 5$ km are shown in Fig. 2.5. The horizontal spacing is successively halved ranging from $\Delta x = 2$ km to 250 m, and the time step Δt is

[7] See Section 3.1 for details on the model parameters and setup.

[8] In this dissertation, unless otherwise specified, we will choose the time step such that $\xi < 1$ (see Section 2.4.2).

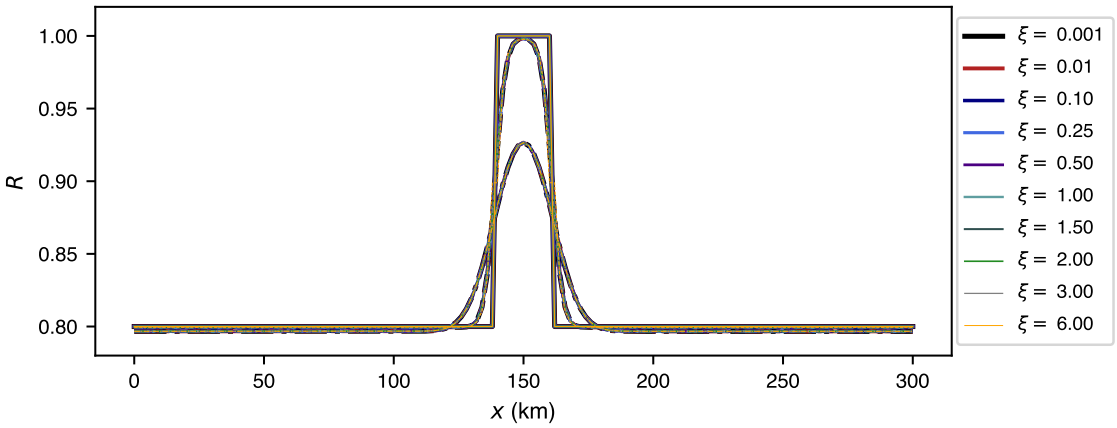

Figure 2.3: *Computed solutions along the section* $y = 150$ *km for the problem* (2.13) *with* $K = 10^4$ m^2 s^{-1}, $\tau_{sub} = 10$ *days,* $R_0(\mathbf{x})$ *as specified in* (2.29). *Shown are the initial profile (solid lines) and the numerical approximations for different time step choices at* $t = 600$ *s (dashed) and* 3600 *s (dash-dotted).* $\xi = 1$ *corresponds to* $\Delta t = 100$ *s.*

such that $\xi = 0.25$ in all cases. At $t = 600$ s (dashed lines), the profiles are almost insensitive to the resolution, then any error is eventually smoothed down and, at $t = 3600$ s (dash-dotted), the curves are nearly indistinguishable.

In case profiles with sharper discontinuities are prescribed, the method is still able to provide reasonably good approximations, despite exhibiting a more pronounced sensitivity to both the time step size and the resolution.

2.4.2 Full solver

In the full system (2.1), the action of convection is to continuously introduce local delta function perturbations into the R distribution, with sharp gradients between the convective points and the surrounding grid cells. This is particularly challenging for the numerics and could possibly amplify numerical errors. Further sets of tests are thus conducted, aimed at quantifying the impact of the errors associated with the operator splitting.

Fig. 2.6 charts the results obtained for different values of K, $K = 10^4$ m^{2}s^{-1} (solid lines) and $K = 2.5 \times 10^4$ m^{2}s^{-1} (dashed lines), and ξ (colors), all else being kept fixed ($\tau_{\text{sub}} = 12$ days, $a_d = 14.72$, $D = 300$ km, $\Delta x = 2$ km, $R_0 = 0.8$). Convergence to the same statistically steady solutions is apparent, even though, in the low-diffusion case, the approximation for $\xi = 3$ ($\Delta t = 300$ s) yields some differences in both the R spatial mean and standard deviation final state. Interestingly, both the transition to equilibrium and the following evolution do not vary monotonically with Δt, and we attribute this effect to the large stochastic component present in the modeled system. The time step dependency almost entirely disappears for higher values of K, as they

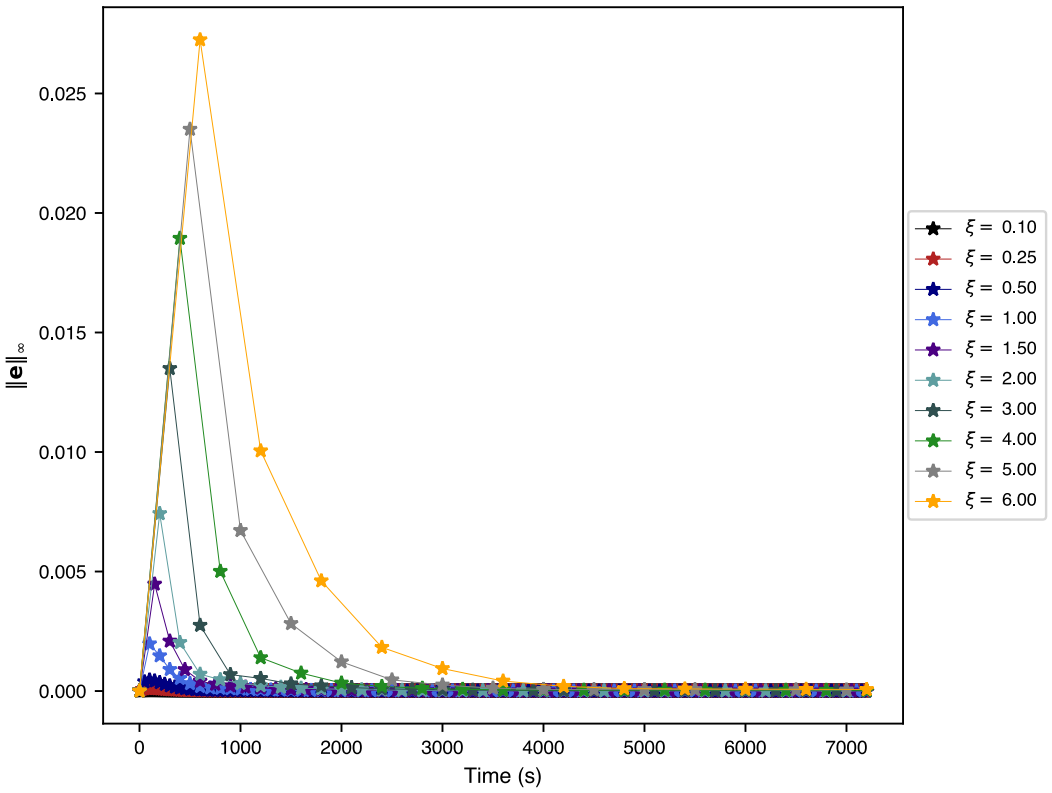

(a)

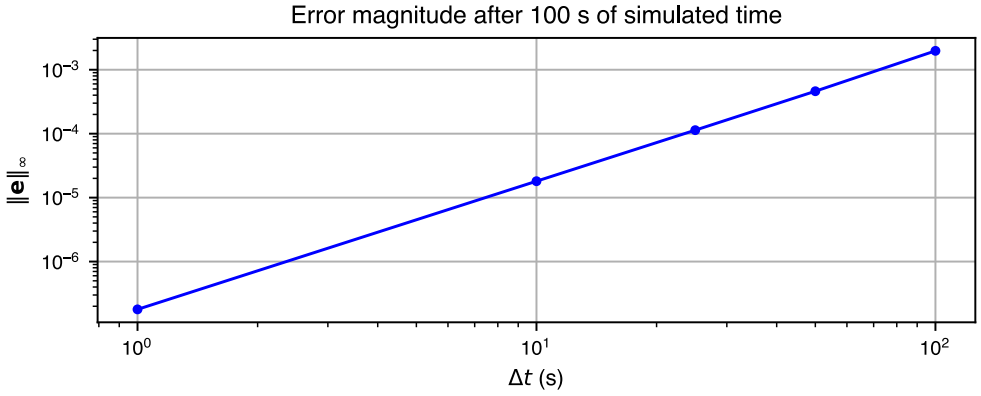

(b)

Figure 2.4: *(a) Time evolution of the infinity norm of the error for numerical solutions of* (2.13) *(with* $K = 10^4\ m^2\ s^{-1}$, $\tau_{sub} = 10$ *days, initial condition as in* (2.29)*) obtained for different time step choices. (b) Infinity norm of the errors at* $t = 100$ *s as a function of time step. The errors are calculated with respect to the solution corresponding to* $\xi = 5 \times 10^{-4}$ *(*$\Delta t = 0.05$ *s).*

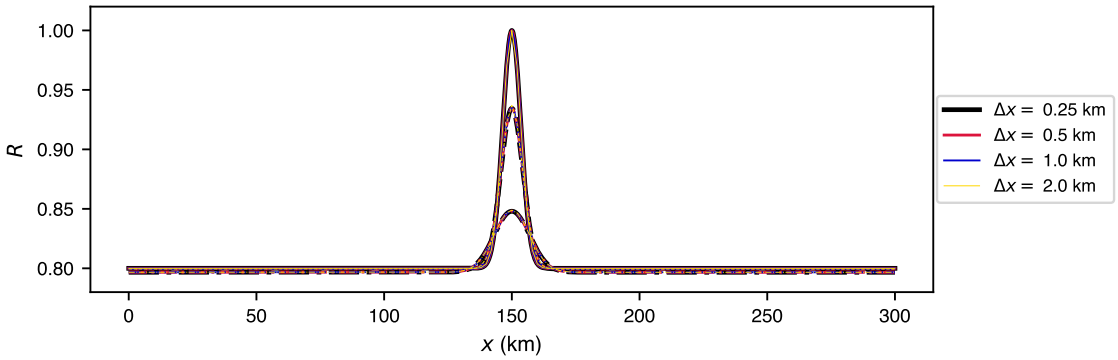

Figure 2.5: *Results of a grid refinement study conducted on the problem* (2.13) *with* $K = 5 \times 10^3\ m^2\ s^{-1}$, $\tau_{sub} = 10$ *days and a Gaussian initialization. Shown are the solutions along the section* $y = 150\ km$, *at times* $t = 0$ *(solid lines)* $t = 600\ s$ *(dashed) and* $3600\ s$ *(dash-dotted).*

require the use of a smaller time step (via eqn. 2.14), which also leads to less severe splitting errors. For the experiments presented in this thesis, in general, the time step is chosen so that $\xi < 1$.

2.5 Summary

In the previous sections, we introduced a simple stochastic lattice model of the reaction-diffusion type which considers the evolution of column total water relative humidity in the tropical troposphere. Due attention was devoted to ensure the model is as insensitive as possible to the specifics of numerical discretization methods, since the grid-point, stochastic representation of the convective moistening term can pose serious problems in this respect.

A number of questions arise, which will be addressed in the next chapter. First, is the model able to reproduce realistic states of random and self-aggregating convection, in spite of being highly idealized? If so, will it allow to draw robust conclusions regarding the onset of the instability that leads to self-aggregation? Is it possible to know in advance which end climate is likely to be approached by the system for a given experimental and model configuration?

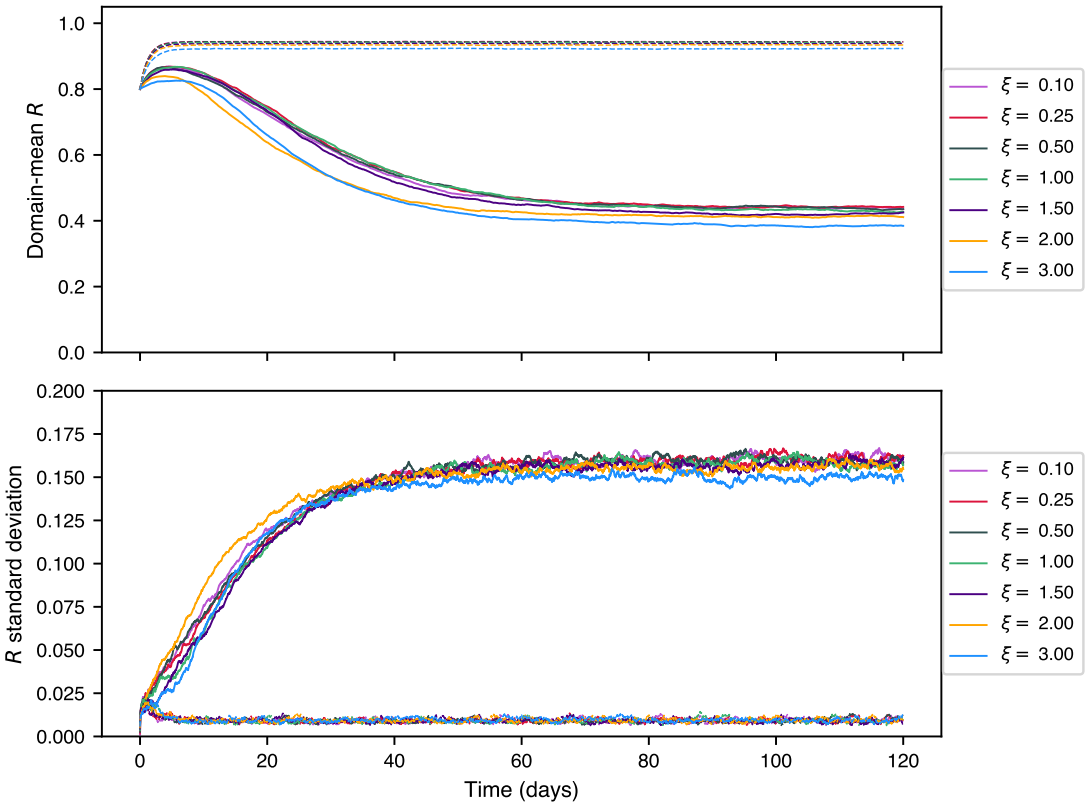

Figure 2.6: *Statistics of the R distribution for different runs of the model in terms of* Δt *in the cases* $K = 10^4\ m^2\ s^{-1}$ *(solid lines),* $2.5 \times 10^4\ m^2\ s^{-1}$ *(dashed lines), with* $\tau_{sub} = 12$ *days and* $a_d = 14.72$. $\xi = 1$ *corresponds to* $\Delta t = 100\ s$ *and* $\Delta t = 40\ s$*, respectively.*

Chapter 3

A dimensionless parameter to predict the onset of convective aggregation

The model introduced in Chapter 2 is minimal-complexity in terms of the representation of physics, but still retains much of the behavior of the models that represent all the key physical processes. In this chapter, we will show that, depending on the chosen parameter and experimental settings, the model can mimic both random and clustered convective states and produces a transition to aggregation at parameter values that are a realistic approximation of the present-day tropical atmosphere. Many other aspects of the full-physics models are reproduced, such as their sensitivity to resolution and domain size, with aggregation more likely using coarser grid sizes and larger domains. The model is therefore a valuable tool to explain these sensitivities in the context of full-physics CRMs, which we attribute to the distribution of inter-convective nearest-neighbor distances in the initial random phase.

The simplicity of the model allows us to investigate its parameter sensitivities. Using dimensional analyses, heuristic scaling arguments and a fit from empirical data, we will derive a dimensionless quantity, called the *aggregation number*, which combines model and experiment configuration parameters and has a predictive power. Analysis of large ensembles of several thousand simulations indeed demonstrates that the transition between random and organized regimes occurs at a critical value of the aggregation number, with convection aggregating when the parameter falls below the critical threshold. The aggregation number ultimately tells us whether a specific model and experiment setup will result in an aggregated or random convective state.

3.1 Choice of the model setup, parameters and constants

We start by describing the model and simulation settings. The governing equation (2.1) is integrated over a square domain which is periodic in both horizontal directions. The simulations examined in this chapter are initialized with column relative humidity field

R assumed to be completely horizontally homogeneous with $R = 0.8$ everywhere. We will see in Chapter 4 that there is sensitivity to the initial conditions with the model exhibiting a weak hysteresis, but this is beyond the scope of the present chapter. No perturbations are imposed to the initial R distribution since stochasticity is already accounted for in the model through the convective location function. All experiments are run for at least 120 days (with some extended to 180 days), a period long enough such that there is a long-term steady state of variables indicating equilibrium has been achieved.

As a metric of clustering or random convection we mostly use the domain spatial standard deviation of R averaged over the last 20 days of simulation, denoted by $\overline{\sigma}_{R,20}$. Low values of $\overline{\sigma}_{R,20}$ indicate random convection while high values indicate convection is aggregated. In addition, we also use the I_{org} parameter of organization described in the appendix of Tompkins and Semie (2017) (see also Chapter 5), a more quantitative metric of aggregation as it allows one to classify scenes as random or aggregated (or even regular, i.e., dispersed, when inter-convective spacing is larger than expected from a random distribution).

Details of the large ensembles with the default values and ranges used for each of the parameters are reviewed below and summarized in Table 3.1. The subsidence timescale τ_{sub} is derived assuming that in subsidence areas, in the absence of large-scale convergence, subsidence heating approximately balances the net radiative cooling, Q_{rad} (cf. Section 1.2):

$$\tau_{\text{sub}} = \frac{h\frac{\mathrm{d}\theta}{\mathrm{d}z}}{eQ_{\text{rad}}},$$

which, inserting characteristic values for the depth of the free troposphere ($h \approx 10$ km), the mean environmental lapse rate of potential temperature $\frac{\mathrm{d}\theta}{\mathrm{d}z} \approx 6.5$ K km^{-1} and the vertically integrated radiative cooling rate $Q_{\text{rad}} \approx 1.5$ K day^{-1}, gives $\tau_{\text{sub}} = 16$ days, with the ensembles spanning 5-40 days. We note that this timescale is much longer than that used in Craig and Mack (2013) of 2 days.

Analysis of TRMM data by Rushley et al. (2018) gave the convection sensitivity factor a_d values of 14.72 and 16.12, depending on the TRMM retrieval version, and our ensembles span values of 10-30. The default values of a_d used here refer to the daily-mean precipitation-R relationships, but the same exponential law eqn. (2.3) applies to the monthly-mean relationship, with a coefficient of 11.4 that was estimated by Bretherton et al. (2004) and employed by Craig and Mack (2013) in their simulations. However we note that this latter value is also included in our experimentation (see Table 3.1).

A reasonable estimate for the horizontal moisture transport efficiency K can be calculated by defining it as a function of characteristic length and velocity scales, ℓ_0 and v_0, associated with convective motions:

$$K = \epsilon \ell_0 v_0,$$

where ϵ is a eddy-size related coefficient set to $\epsilon = 0.1$. Typical scales are the free tropospheric depth, $\ell_0 = 10$ km, and $v_0 = w_c = 10$ m s^{-1} (updraft velocity observed

in convective cores),[1] implying that reliable values for K are on the order of 10^4 m^2 s^{-1}, but our experiments evaluate values from 10^3 to 4×10^4 m^2 s^{-1}.

The convective moistening characteristic time τ_c is set to a very fast timescale of 1 minute to lead to almost instantaneous saturation. We did find some sensitivity of the model to the choice of τ_c but using slower adjustment times did not change the conclusions derived from the model. Finally, we set the convective relaxation target R_c accounting for column cloud water detrainment using estimates from CRM simulations to give $R_c = 1.05$.

To keep the total simulation size tractable while exploring the parameter space, we constructed series of ensembles of $\mathcal{O}(1000)$ members that investigate two parameters while keeping others fixed. Three ensembles of experiments using a domain size $D = 300$ km and resolution $\Delta x = 2$ km cover combinations of τ_{sub} and K for $a_d = 14.72, 16.12$ (results shown in Figs. 3.8, 3.15, 3.18), and K and a_d (Fig. 3.19). An additional ensemble of experiments employed a limited range of fixed values for the three model key parameters, combined with a range of domain sizes ($D = 200, 300, 400, 1000$ km, Fig. 3.4) and spatial resolutions ($\Delta x = 0.5, 1, 1.5, 2, 4$ km, Fig. 3.6), see also Fig. 3.16 and Fig. 3.17. To construct the final analysis exploring the five-parameter space ($K, \tau_{\text{sub}}, a_d, D, \Delta x$), a sub-sampled ensemble of 1160 members was used (Fig. 3.20).

Table 3.1: *Parameters (default and ranges) used in the simulations.*

	Default value	Range
K (m^2 s^{-1})	10^4	$10^3 - 4 \times 10^4$
τ_{sub} (days)	16	$5 - 40$
a_d	14.72 16.12	$10 - 30$
D (km)	300	$200 - 1000$
Δx (km)	2	$0.5 - 4$

The numerical model output is available in netcdf format at `https://samodel.dmg.units.it/`.

3.2 Mimicking cloud-resolving models

3.2.1 Occurrence of self-aggregation and impacts on the mean state

Before analyzing the large ensembles it is useful to demonstrate how the model can produce both random and aggregated convective states depending on the parameter settings chosen. We start by showing two experiments, one with the default values of K,

[1] We recall that the lateral mixing term is a proxy representation of humidity transport by the overturning circulation, i.e. by eddies on the order of the domain size and not by sub-grid-scale eddies determining the mixing between adjacent cells. Thus, by mass conservation, one can derive the scaling with either vertical scales and velocities or those in the horizontal.

τ_{sub} and a_d (CTRL, see Table 3.2) and the second with a reduced value of the horizontal transport efficiency ($0.5K$). Five time slice panels show the evolution of the horizontal R field (Fig. 3.1 and movie available at `http://clima-dods.ictp.it/Users/gbiagiol/regimes.mp4`). In the default experiment (upper panels), the convective sources remain randomly distributed throughout the domain, even on day 180, and the domain-mean R remains moist.

In contrast, halving the strength of the lateral transport of water vapor (lower panels) causes the model to evolve towards a dramatically different state. After an initial period of random convection, the variability of R in the domain increases during the transition towards a spatially organized atmospheric state, characterized by the emergence of a single, almost circular, intensely convecting area surrounded by a dry environment. Close examination shows many examples of localized moist cells caused by the stochastic convective selection in those locations. Once aggregation has established, the dry patch is very rarely disrupted by moistening processes from local sources, but it is not guaranteed that deep convective events necessarily trigger in the wettest cells and occasionally drier cells are chosen (see movie). This behavior would be missing from a deterministic formulation of the model.

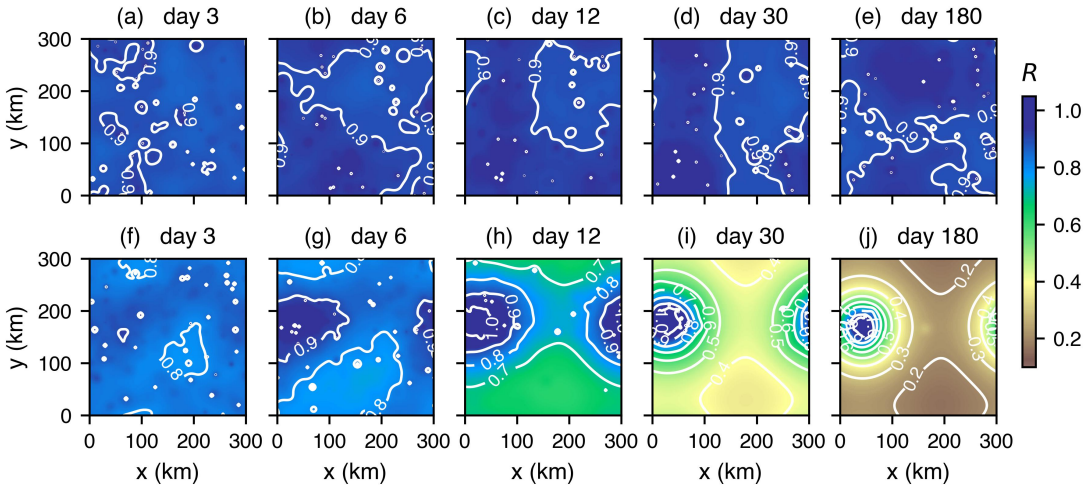

Figure 3.1: *Evolution of the spatial column relative humidity field R (color shading and contours, with intervals of 0.1) for simulations with $K = 10^4\ m^2\ s^{-1}$ (a-e), $K = 5 \times 10^3\ m^2\ s^{-1}$ (f-j), $\tau_{sub} = 16$ days and $a_d = 14.72$. The domain size and the grid resolution are kept at their default values, $D = 300$ km and $\Delta x = 2$ km.*

These experiments highlight the ability of the simple model to mimic both random and aggregated equilibrium states, with results resembling those yielded by more complex, full-physics CRMs, at least from a qualitative point of view (e.g., Bretherton et al., 2005; Muller and Held, 2012). Also in accordance with the full-physics models (e.g.,

Bretherton et al., 2005; Wing and Emanuel, 2014), the mean state is much drier in the aggregated simulation relative to the random case, and column relative humidity has a higher spatial variability, clear from the temporal evolution of the probability density function (PDF) of the spatial moisture field (Fig. 3.2).

In the control experiment with higher horizontal moisture transport efficiency, the PDF stays essentially unimodal throughout the simulation, although a second minor mode corresponding to saturated cells is in evidence and is directly due to the externally imposed constraint (eqn. 2.2) on the number N_c of convectively active columns per time step. The primary unimodal feature of the PDF is to be ascribed to larger diffusive effects (combined with relatively slow drying tendencies), which prevent the domain from developing some drier-than-average background region surrounding moist patches. A transition towards a broader distribution is apparent in the lower diffusion experiment which undergoes aggregation, since the action of moistening processes is able to overcome the counter-gradient smoothing by subsidence and diffusion. As self-aggregation progresses and the dry and humid regions are increasingly separated, a bimodal PDF develops reminiscent of tropical observations (Zhang et al., 2003; Mapes et al., 2018). The dry mode here is linked to the long diffusive tail of the distribution and the moist mode is related to detrainment area, possibly exaggerated by the use of a single detrainment value. This behavior is almost identical to that shown in coarser resolution deterministic experiments of Craig and Mack (2013).

Time series of R show the impact of aggregation on the mean humidity field (Fig. 3.3) in four simulations including the control run (CTRL) and three perturbation experiments, which alter the horizontal transport efficiency ($0.5K$), the subsidence rate ($\tau_{\text{sub}}10$) or the convective-humidity feedback strength ($a_d16.12$) in turn. A brief overview of these runs is reported in Table 3.2. These simulations show that it is possible to generate self-aggregation in the model by reducing the diffusive humidity transport, increasing the subsidence rate or strengthening the convective-moisture feedback. It is interesting to note that the two a_d values corresponding to different TRMM retrieval versions can produce either random or aggregated states, all else being kept fixed.

The existence of two characteristic timescales is apparent, the first associated with the initial fast adjustment on the convective timescale, and the second representing the time of adjustment to equilibrium related to the overturning timescale determined by the subsidence rate (cf. Section 1.2). This is also in agreement with previous CRM experiments using fixed surface temperatures (Tompkins and Craig, 1998b; Cohen and Craig, 2004) although Cronin and Emanuel (2013) highlight that longer timescales are possible if an interactive lower boundary is used. After the equilibrium state is reached, temporal fluctuations in the field are limited to shorter timescale variability associated with the relative position of convective events. The temporal variability is restrained by the condition that the convective population variation in time is limited (see Section 2.2.5). The non-aggregated case, conversely, after the very first transient phase where initial convective events increase the humidity variance, reaches an equilibrium rapidly with a low spatial variance associated with the domain that is moistened throughout by local convective sources.

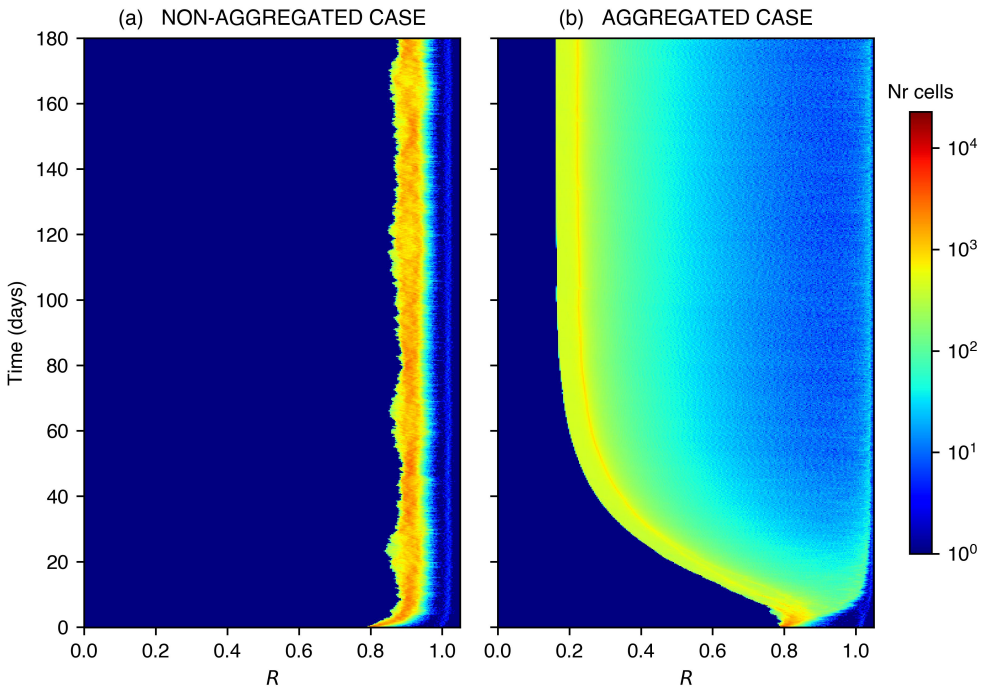

Figure 3.2: *Time evolution of the absolute frequency of occurrence of R values for the simulations reported in Figure 3.1, namely (a) non-aggregating case with* $K = 10^4\ m^2\ s^{-1}$*, and (b) aggregating case with* $K = 5 \times 10^3\ m^2\ s^{-1}$*. The other model settings are* $\tau_{sub} = 16$ *days and* $a_d = 14.72$*.*

The time evolution of the organization index I_{org} introduced by Tompkins and Semie (2017) shows that the convection remains random in the control run, with a time-average value of 0.5, while in the three perturbation experiments it increases towards values exceeding 0.9, indicating highly aggregated conditions.

Table 3.2: *Summary of the simulations of Figure 3.3.*

Simulation name	Parameters		
	K (m^2 s^{-1})	τ_{sub} (days)	a_d
CTRL	10^4	16	14.72
0.5K	5×10^3	16	14.72
τ_{sub}10	10^4	10	14.72
a_d16.12	10^4	16	16.12

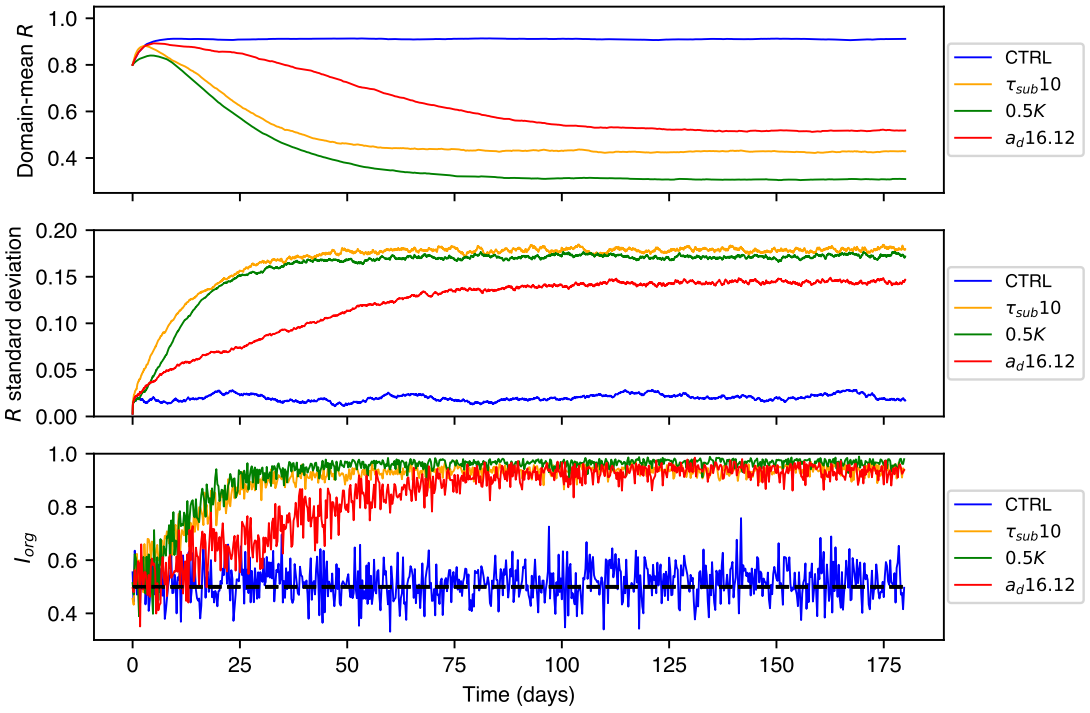

Figure 3.3: *Temporal evolution of the spatial R distribution, in terms of domain mean (upper panel) and standard deviation (middle panel), and the organization index I_{org} (lower panel) for the simulations CTRL (blue line), 0.5K (green line), $\tau_{sub}10$ (orange line), $a_d16.12$ (red line). The dashed line in the I_{org} plot marks $I_{org} = 0.5$, which is the value for a random distribution of convective cells. For details on the experimental setup, refer to Table 3.2.*

3.2.2 Sensitivity to domain size

CRM simulations show that self-aggregation is facilitated by large domains, with abrupt transition to clustered convection taking place when the domain size D exceeds a certain threshold, typically $D \gtrsim$ 200-300 km (Bretherton et al., 2005; Muller and Held, 2012; Jeevanjee and Romps, 2013; Muller and Bony, 2015; Patrizio and Randall, 2019). Li (2021) provided an analytical argument to explain the domain-size dependence of self-aggregation within the framework of a conceptual, two-dimensional, stochastic reaction-diffusion model for the column moist static energy (CMSE) budget. In particular, such a dependence is found to result from the competing influences of vertical and horizontal advective transports on the CMSE anomalies.

Here too the occurrence of aggregated states is found to be sensitive to the domain size (Fig. 3.4; another example is shown in a movie available at `http://clima-dods.ictp.it/Users/gbiagiol/dom_size.mp4`). Convection in the smallest domain of size

$D = 200$ km remains in a random state for these parameter choices (see caption). For $D = 300$ km, there is no aggregation, but some variance of moisture over the scale of the domain is apparent, and the moist patch is elongated. This simulation was extended to 150 days which confirmed that this state is a quasi-stationary equilibrium. Extending the domain to 400 km results in aggregation with a single center.

The largest domain with $D = 1000$ km exhibits an interesting behavior in that the convection originally organizes into two distinct convective clusters that last until around day 20, at which point the larger of the two centers starts to dominate and the first center dies out (Fig. 3.5). This behavior is reminiscent of the two-dimensional simulations of Held et al. (1993) which show two competing centers of convection for a period of time before collapsing to a single convective center, although this was on smaller domains. In our simple diffusive model, we hypothesize that the convection will always collapse to a single center due to the fact that the subsidence term is treated as a uniform relaxation towards zero R and does not account for the location of convection events, in contrast to the transport term which diffuses moisture out from the centers. In the real atmosphere, the subsidence occurs through the propagation of gravity waves from the convective centers (cf. Section 1.1.1), and thus the aggregated convective clusters would be separated by a Rossby deformation radius determined by the Coriolis effect off the equator and by diffusive dissipation, which would give a cluster spacing on $\mathcal{O}(1000$ km) scales, on the equator (Bretherton and Smolarkiewicz, 1989).

Wing and Cronin (2016) offered an alternative mechanism for both the cluster separation distance and the spatial scale of aggregation based on boundary layer recovery through surface fluxes, which would also be a physical process missing in this simple model, that does not account for surface fluxes. Yang (2018) proposed that the characteristic horizontal scale of self-aggregation is determined by the boundary layer height and the density variations between moist and dry regions in the boundary layer, the latter owing to the virtual effect of water vapor. Additionally Beucler and Cronin (2019) recently used a new diagnostic to interpret the role of different diabatic forcings on the spatial scale of aggregation. In any case it remains that the formulation of the simple model presented here will always lead eventually to a single convective center in the cases where aggregation occurs.

3.2.3 Sensitivity to horizontal resolution

Aggregation in CRM studies is also resolution sensitive, with coarser grids favouring the occurrence of clustered convection. For instance, Muller and Held (2012) found that, for spacings $\Delta x < 2$ km, self-aggregation never develops when starting from homogeneous initial conditions (but, when an aggregated initial profile is prescribed, it manages to persist even at resolutions as fine as $\Delta x = 500$ m if the domain size is sufficiently large, namely $D \gtrsim 200$ km).

Similar results are found here, examining the atmospheric states at day 120 for simulations with the numerical grid successively refined (halved), with parameters K, τ_{sub}, a_d and D invariant (Fig. 3.6, animation available at `http://clima-dods.ictp.it/`

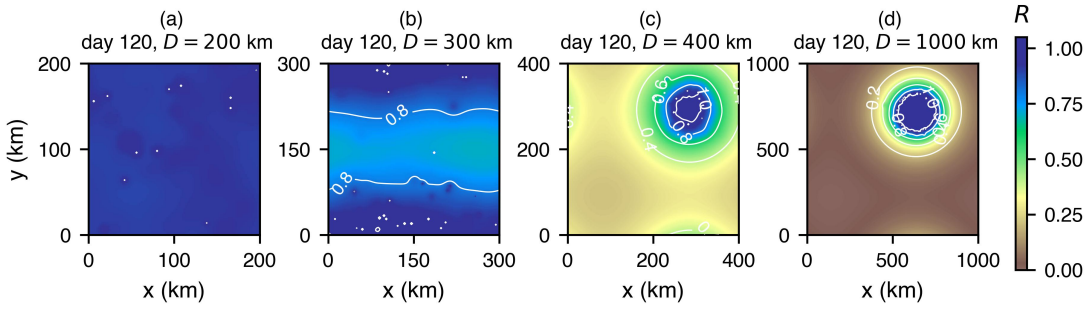

Figure 3.4: *Plan views of the spatial field of column relative humidity R (shading and contours, interval* 0.2*) after* 120 *days of simulated time for runs with* $K = 10^4\ m^2\ s^{-1}$, $\tau_{sub} = 16$ *days,* $a_d = 14.72$ *and domain sizes* $D = 200$ *km (a),* 300 *km (b),* 400 *km (c),* 1000 *km (d).*

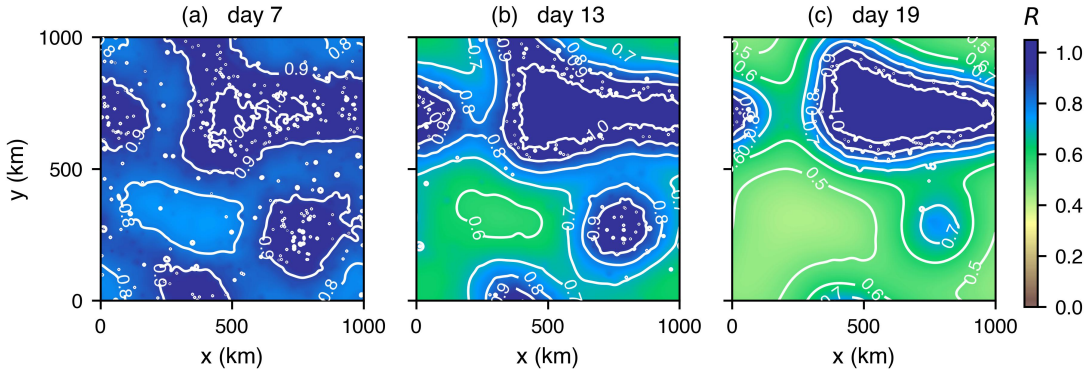

Figure 3.5: *Horizontal maps of R (shading and contours every* 0.1*) after 7 (a), 13 (b) and 19 (c) days in the experiment with domain size* $D = 1000$ *km.*

`Users/gbiagiol/hor_res.mp4`). For a grid resolution of 4 km and 2 km, the convection aggregates into a single center. Refining the resolution to 1 km, the aggregated state takes on the form of an elongated band, instead of the usual circular shape, spanning one horizontal dimension entirely, while using a resolution of 500 m leads to random convection that does not undergo aggregation at all.

Holloway and Woolnough (2016) provided a geometric argument to explain the preferred shape taken by self-aggregated convection in doubly-periodic RCE simulations, suggesting the structure of wet patches is such as to minimize their perimeter-to-area ratio, because lateral mixing acts to reduce any horizontal moisture gradient. In particular, if the area $A_{\rm cl}$ of the cluster is $A_{\rm cl} > A_{\rm cl,\,crit} \equiv D^2/\pi$ (i.e., the moist patch occupies roughly more than one third of the computational domain), then a band-like

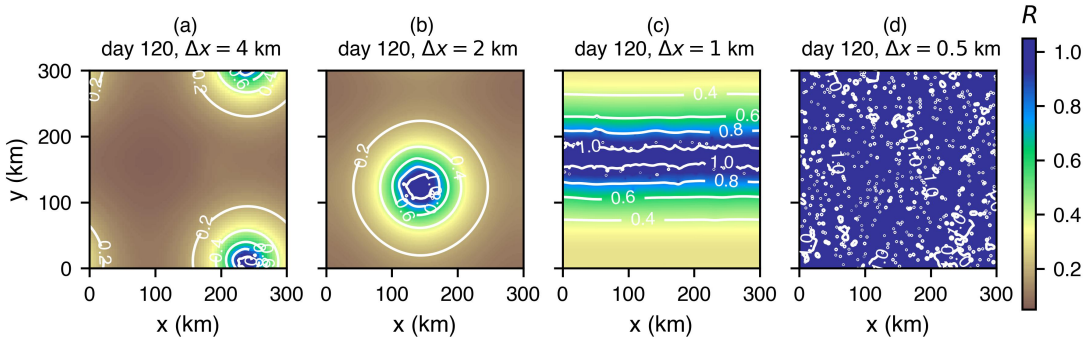

Figure 3.6: *Snapshots of the R field (shading and contours, interval of* 0.2*) after* 120 *days of simulation in the case* $K = 5 \times 10^3\ m^2\ s^{-1}$, $\tau_{sub} = 10$ *days,* $a_d = 14.72$, *with* $D = 300$ *km,* $\Delta x = 4$ *km (a),* 2 *km (b),* 1 *km (c),* 500 *m (d).*

arrangement is likely to appear, as observed in the first three-dimensional simulations of radiative-convective equilibrium by Tompkins and Craig (1998a), which only used a 100×100 km domain. In extremely large domain experiments, however, Patrizio and Randall (2019) actually show a transition from circular clusters towards elongated bands in the largest $\mathcal{O}$(6000 km) domain experiments. For smaller ratios, and indeed over an infinite plane, the preferred form would be a circle in all cases, as in the seminal study of Bretherton et al. (2005).

For $\Delta x = 2$ km and $\Delta x = 4$ km, the time series of the spatial R mean show contrasting behavior at the simulation outset, with the initial adjustment in the R-mean profile completely absent in the 4 km case (Fig. 3.7, top panel), as the initial phase involves the development of larger, but fewer, convection cells, while most columns start to be progressively dried by subsidence. This prevents R from increasing at the beginning of the 4 km simulation when starting from these relatively moist initial conditions.

The 1 km simulation was repeated three times to ascertain any eventual, additional stochastic contribution to the final self-aggregated shape and indeed the results of the multi-run ensemble simulation, shown in Fig. 3.7 (orange solid line and dashed lines), manifest various evolutions. For the same parameter set and experimental design, the simulation may end up either with the usual spatial pattern typical of convective clustering, marked by a pronounced reduction in domain-mean R and a slightly lower variance, or with convective centers being aligned in a band. This indicates proximity to a critical cluster area $A_{\mathrm{cl,\,crit}}$ beyond which the wet spot arranges itself in a banded structure, and whether or not the corresponding radius is reached depends on the large stochastic effects present in the modeled system. The temporal evolution of one run (green dashed line in Fig. 3.7) even shows an initial banded equilibrium state, which transitions to a circular cluster around day 40-45. Wing and Emanuel (2014) found similar behavior in their CRM simulations, pointing out that, in some runs, convection was

confined to a single band maintained for tens of days before collapsing into a circular clump, the evolution of the spatial orientation of the cluster being thus attributed to the largely stochastic nature of self-aggregation.

For $\Delta x = 500$ m, the profile is extraordinarily moist from the very beginning and so it persists throughout the run (Fig. 3.6d and 3.7, blue line).

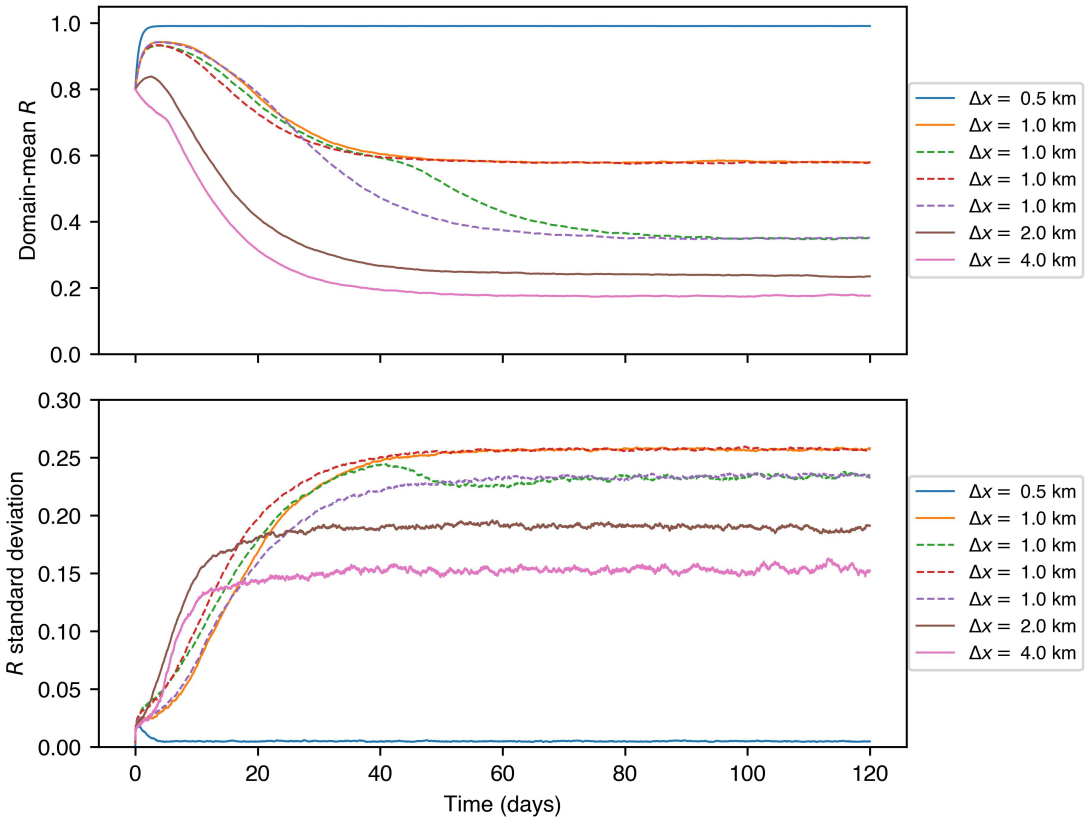

Figure 3.7: *Time evolution of spatial R mean and standard deviation for the simulations presented in Figure 3.6 (solid lines), with a 4-member ensemble performed in the case $\Delta x = 1$ km (orange solid line and dashed lines).*

3.3 Predicting the transition to aggregation

In the previous section we showed that the occurrence of aggregation is sensitive to the settings of the three model key parameters, K, τ_{sub} and a_d, representing the efficiency of the horizontal transport, the strength of the subsidence drying and the sensitivity of convection to humidity, respectively, as well as the domain size D and resolution Δx.

Here we wish to derive a method to predict when aggregation will occur as a function of these five parameters. As a first step, we will use dimensional analysis to empirically derive a dimensionless quantity that predicts the onset of aggregation. We discuss the five parameters in turn to understand their impact on aggregation, and then construct the dimensionless parameter.

3.3.1 Sensitivity to K and τ_{sub}

The occurrence of the self-aggregated state is sensitive to the value of the horizontal moisture transport efficiency K and subsidence strength τ_{sub}. In this model, convection locally moistens its environment while drying the far-field instantaneously through subsidence. Thus the onset of aggregation will depend on how quickly moisture sources are communicated relative to the subsidence drying. Stronger diffusive transport reduces the spatial variance of humidity and makes aggregation less likely. Indeed, in the limit of infinite diffusion, convective moisture sources would be communicated instantaneously throughout the domain resulting in random convection. Likewise, stronger subsidence drying would act to promote aggregation. The competing influences of subsidence and horizontal transport are fundamental.

On dimensional grounds, the subsidence timescale (units s) and the horizontal transport efficiency ($\text{m}^2\ \text{s}^{-1}$) can be combined together to give an area of influence ($K\tau_{\text{sub}}$) on the moisture field of an individual convective cell. Such a quantity (or related ones) would naturally appear in the context of reaction-diffusion problems. For example, the stationary solution $\overline{R}(x)$ of the one-dimensional heat equation with linear sink term

$$\frac{\partial R}{\partial t} = K\frac{\partial^2 R}{\partial x^2} - \frac{R}{\tau_{\text{sub}}},\ x > 0,\ t > 0,$$

with conditions $R(0,t) = R_c$ and $\lim_{x\to\infty} R(x,t) = 0$, is given by

$$\overline{R}(x) = R_c e^{-\frac{x}{\sqrt{K\tau_{\text{sub}}}}},$$

which shows that $(K\tau_{\text{sub}})^{\frac{1}{2}}$ is the e-folding length scale of the steady-state R in this simple problem. Therefore, the area of influence can be intuitively viewed as a measure of the potential (rather than the actual, due to the finite cloud lifetime) maximum area impacted by an individual deep convective event (cf. Fig. 2.1).

As highlighted by the sensitivity studies (Fig. 3.4 and movie `http://clima-dods.ictp.it/Users/gbiagiol/dom_size.mp4`), when the diffusion-based communication of moisture from the sources acts over scales comparable to the domain size, aggregation may be easily prevented. This is consistent with results from previous literature. The stability analyses conducted by Shi and Fan (2021) proved that, if the diffusive tendencies are strong, large-scale humidity perturbations would be required to destabilize the spatially homogeneous state of tropical convection, up to completely inhibiting the clustering. By means of a conceptual model, Li (2021) analytically determined a threshold domain size below which the homogenizing effect of diffusive transport

dominates, thereby preventing incipient CMSE anomalies from amplifying and leading to self-aggregation.

Thus one could scale $K\tau_{\text{sub}}$ by the area of the computational domain, D^2, which would provide a dimensionless quantity. This quantity does not yet account for the dependence of the resolution or the convective sensitivity to the moisture field, which will be considered below, and is in any case not adequate to predict the onset of self-aggregation. This is clearly shown in Fig. 3.8, which refers to the evaluation of the ensemble of experiments that vary K and τ_{sub}, assuming the default values for a_d, domain size and resolution ($a_d = 14.72$, $D = 300$ km, $\Delta x = 2$ km, see Section 3.1). The figure shows contours of $\overline{\sigma}_{R,20}$ and isopleths of $K\tau_{\text{sub}}/D^2$. The region of dense contour lines marks the abrupt transition between those experiments that result in aggregated convection (high values of $\overline{\sigma}_{R,20}$) and those with random convection (low $\overline{\sigma}_{R,20}$) equilibrium states. Below the transition zone, on the left, the pronounced curvature of the contours is due to increasingly weak diffusive effects that encourage convection to (re)develop in a very restricted number of points, thus limiting the size of the cluster (hence the variance of the spatial R distribution). Importantly, the profile of the transition regime in the parameter space is not parallel to the isopleths of $K\tau_{\text{sub}}/D^2$, which means that there is no specific threshold value of $K\tau_{\text{sub}}/D^2$ that captures the transition between random and aggregated convective states. This departure is particularly evident in the limit of small τ_{sub}.

The key is that the sensitivity of the occurrence of self-organization to τ_{sub} is more subtle, because the mean number $\overline{N_c}$ of convective points active at each time step introduces an additional dependence on the subsidence characteristic time through eqn. (2.2). Since the number of updraft centers is inversely proportional to the subsidence timescale τ_{sub}, stronger subsidence, while reducing the area of influence $K\tau_{\text{sub}}$, also increases the density of convective events within the domain, reducing the mean inter-convective spacing. This means that experiments with different values of K and τ_{sub}, but the same product $K\tau_{\text{sub}}$, may exhibit different behavior; experiments with larger K and smaller τ_{sub}, and hence higher number of convective cells, are more likely not to organize.

An animation available at `http://clima-dods.ictp.it/Users/gbiagiol/npts.mp4` shows the impact of the density of events in two simulations with $K = 3 \times 10^4 \text{m}^2\ \text{s}^{-1}$, $\tau_{\text{sub}} = 5$ days and average number of convective sources $\overline{N_c} = 78$ and $\overline{N_c} = 39$.[2] The above arguments and the evolution shown in the movie undoubtedly motivate the necessity of including N_c in the dimensional analysis, either explicitly or implicitly. It seems reasonable to represent the contribution from N_c in terms of the distribution of spatial distances between convective towers, recalling that convection is initially randomly distributed prior to aggregation (or remains random in non-aggregating experiments).

[2] In the second case, the relationship (2.2) is violated, as $\overline{N_c} = 39$ would correspond to $\tau_{\text{sub}} = 10$ days.

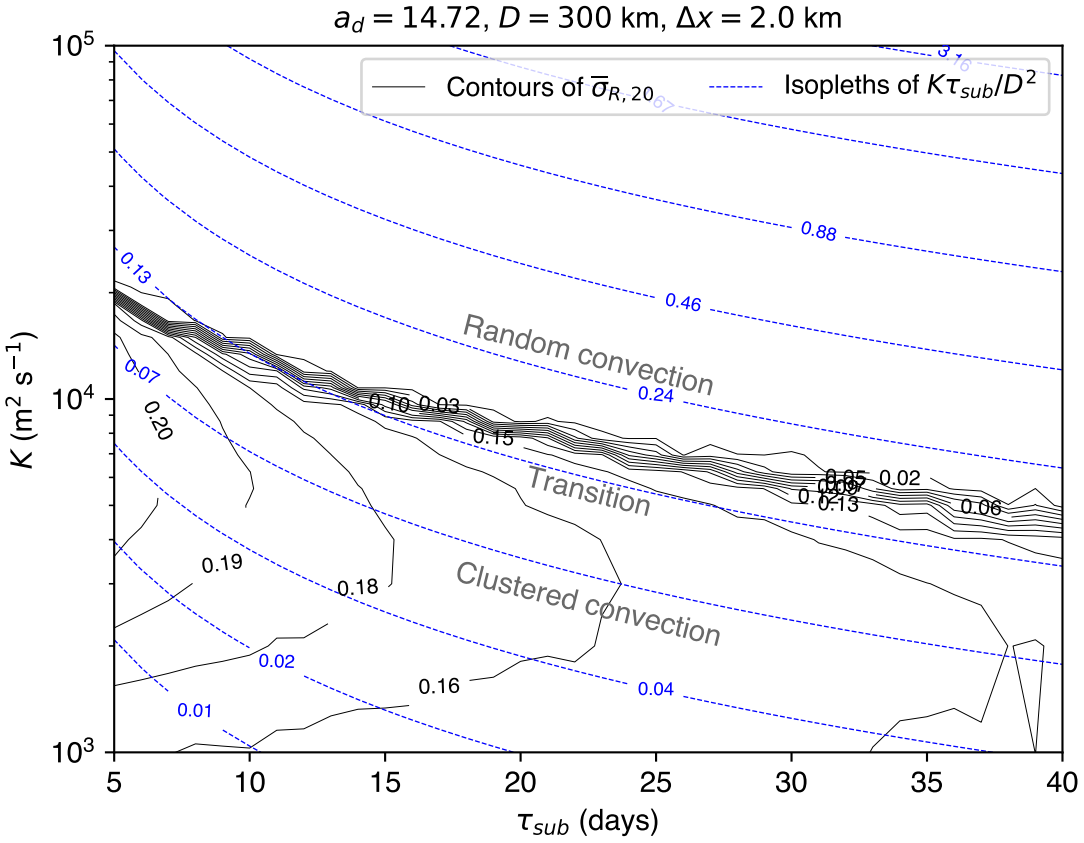

Figure 3.8: *Contours of $\overline{\sigma}_{R,20}$ (black solid curves) along with the isopleths of $K\tau_{sub}/D^2$ (blue dashed curves) for single realizations of the system in a large set of simulations with different K and τ_{sub} and fixed a_d, D and Δx.*

3.3.2 Sensitivity to resolution and domain size

Regarding first the domain-size sensitivity, it is intuitive that small domains may prevent aggregation especially when the moisture diffusion starts to act over scales on the order of the domain size, as already anticipated. Conversely, for large domains, even though the number of grid points occupied by convection increases accordingly as specified by the argument eqn. (2.2), the maximum inter-convective distance will also increase as expected with a Poisson process.

In the construction of the dimensionless parameter therefore, we shall heuristically argue that the key quantity is a measure of the expected maximum distance from the nearest convection, i.e., a measure of the largest convective-free area, which will determine the magnitude of the spatial humidity variance in the pre-aggregated state. Larger distances from convection imply greater dry perturbations and humidity vari-

ance in the domain, more likely to lead to aggregation through the indicator random variable.

The choice of this distance metric as a relevant one to the clustering onset is motivated by the evolution observed in the simple model (cf. Fig. 3.1 and movie `http://clima-dods.ictp.it/Users/gbiagiol/regimes.mp4`) and also by the findings from previous literature, which, unless very few exceptions (Holloway and Woolnough, 2016), documents the formation, expansion and amplification of a dry patch with suppressed convection to be crucial in initiating the aggregation (e.g., Wing and Emanuel, 2014; Coppin and Bony, 2015, see also Section 1.4.1).

Considering the resolution dependence, while the prominent sensitivity of self-aggregation to the horizontal resolution might be attributed to numerical artifacts, for instance the possibility of lateral mixing being resolution-dependent, grid refinement studies conducted to evaluate the spatial convergence properties of the numerical solver excluded this eventuality (cf. Fig. 2.5). Instead, the resolution sensitivity here is a direct result of the number of convective sources.

The scaling closure eqn. (2.2) only constrains the cumulus *fraction* ϵ and not the number nor the size of convective points, and, as the resolution is refined, the convective fraction is the result of more convective centers. Put another way, with a resolution of 2 km, the minimum convective size is 4 km^2, but if Δx is halved, that same area now consists of four separate convective towers of 1 km^2 in different locations, since the model does not impose a horizontal scale on the updraft (Fig. 3.9). This reduces the maximum distance between the convective cores and makes convective aggregation less likely. If a fixed area were set for a single convective updraft core, in order to avoid that the convection centers could become unrealistically small when moving to finer resolution below $\mathcal{O}$(1 km), we predict that no sensitivity to horizontal resolution would be found.

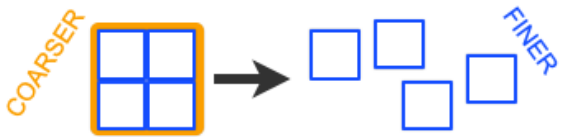

Figure 3.9: *Sketch representing the impact of decreasing grid spacing on the number and positions of updraft cores with the convective fraction ϵ being kept fixed.*

Although this explanation for resolution sensitivity seems simplistic, it is supported by recent experiments using an ensemble of CRM simulations of an MCS at different resolutions (Prein et al., 2021). The study shows that the updraft dimension decreases monotonically with decreasing grid spacing and has still not converged even when the horizontal resolution reaches 250 m. Additionally, Sueki et al. (2019) show that the nearest-neighbor distance between updraft cores reduces with finer resolutions and no convergence is reached at 200 m, directly supporting the hypothesized mechanism for grid size sensitivity represented in the simple stochastic model down to these resolu-

tions. Note that some stochastic approaches instead impose a specific fixed scale for convective events and would not exhibit this facet of resolution sensitivity (Showman, 2007; Yang, 2021; Fu and O'Neill, 2021).

3.3.3 A distance scaling in a discrete domain

The above findings further motivate the definition of a relevant distance for aggregation, which will account for the contribution from N_c and will also allow the incorporation of the resolution and domain size into the theory for aggregation onset. In particular, in the discussion of the resolution and domain size dependence, it was heuristically argued that a relevant distance would be one that describes the largest distance from convection within the domain, which would determine the magnitude of the driest perturbation.

If the initial R distribution is horizontally homogeneous, as prescribed in all the experiments presented in this chapter, the convection locations are random at the simulation outset. In an infinite domain with a homogeneous planar Poisson point process, the cumulative distribution function (CDF) of nearest-neighbor distances between points (NNCDF) is given by the *Weibull distribution* (Stoyan et al., 2013; Weger et al., 1992) as

$$F(r) = 1 - e^{-\lambda \pi r^2} \tag{3.1}$$

where λ is the mean number of events per unit area (the density of points) and r is a radius (the nearest-neighbor distance), $r \geq 0$. However, this approach is not appropriate here, as we need to consider the finite nature of the periodic domain, and treat convection as a binary occurrence on a discrete grid, i.e., we consider cells to be either convective or non convective (cf. Fig. 2.2).

During the entire pre-onset phase, the positions of the updraft centers can still be regarded as the restriction of a Poisson process Φ to a compact set W, the computational domain, and it is well known (e.g., Stoyan et al., 2013; Illian et al., 2008) that the resulting process obeys a binomial law. In detail, assuming that precisely N_c objects of Φ belong

to W, the (conditional) probability that $0 \leq k \leq N_c$ elements lie in a subset B of W is

$$\begin{aligned} p(\Phi(B) = k | \Phi(W) = N_c) =& \frac{p(\Phi(B) = k, \Phi(W) = N_c)}{p(\Phi(W) = N_c)} \\ =& \frac{p(\Phi(B) = k, \Phi(W \setminus B) = N_c - k)}{p(\Phi(W) = N_c)} \\ =& \frac{p(\Phi(B) = k) p(\Phi(W \setminus B) = N_c - k)}{p(\Phi(W) = N_c)} \\ =& \frac{\dfrac{(\lambda \nu(B))^k}{k!} e^{-\lambda \nu(B)} \dfrac{(\lambda \nu(W \setminus B))^{N_c - k}}{(N_c - k)!} e^{-\lambda \nu(W \setminus B)}}{\dfrac{(\lambda \nu(W))^{N_c}}{N_c!} e^{-\lambda \nu(W)}} \\ =& \binom{N_c}{k} \left(\frac{\nu(B)}{\nu(W)} \right)^k \left(\frac{\nu(W \setminus B)}{\nu(W)} \right)^{N_c - k} \\ =& \binom{N_c}{k} \left(\frac{\nu(B)}{\nu(W)} \right)^k \left(1 - \frac{\nu(B)}{\nu(W)} \right)^{N_c - k}, \end{aligned} \tag{3.2}$$

where $p(\cdot)$ denotes the probability, $\nu(\cdot)$ the area, and the fourth and third equalities follow from the hypothesis of Poisson process and the related independence property, respectively.[3]

For a finite domain consisting of discrete cells we consider the probability, $p_{\text{clr}}(n, N_c)$, of not finding any of N_c convective events within a square window B of size $n\Delta x$ (consisting of n^2 grid boxes), centered on an arbitrary non-convective cell in the domain. This is termed *void probability* and is obtained by imposing $k = 0$ and $\nu(W) = D^2$ in the previous relationship (3.2). It can be approximated by

$$p_{\text{clr}}(n, N_c) \approx \left(1 - \left(\frac{n\Delta x}{D} \right)^2 \right)^{N_c}, n \in \mathbb{N}, n \leq \frac{D}{\Delta x}, \tag{3.3}$$

with $\mathbb{N}$ denoting the set of non-negative integers. If the base point has instead been chosen as convective, the void probabilities would simply be $p_{\text{clr}}(n, N_c - 1)$. Owing to the imposed periodicity, no corrections are required if the central cell is in proximity to the edges of the domain. This relationship is an approximation since we should account for the fact that the sampling of convective grid boxes is *without* replacement (i.e., we

[3] By definition, a process Φ on the plane $\mathbb{R}^2$ is termed *homogeneous Poisson* if

(i) the distribution of point counts in a bounded set B is Poisson with parameter $\lambda \nu(B)$, i.e.,

$$p(\Phi(B) = k) = \frac{(\lambda \nu(B))^k}{k!} e^{-\lambda \nu(B)},$$

where λ, the mean density of points, is termed the *intensity* of the Poisson process.

(ii) the random variables describing the number of points of Φ lying in disjoint sets are independent.

should consider $(n^2-1)\,(\Delta x/D)^2$ in place of $n^2\,(\Delta x/D)^2$ in the previous formula), but this is negligible if the convective fraction is small (that is, $N_c \ll N_{xy} = (D/\Delta x)^2$) as is the case here.

We consider two related metrics of the spacing of convective cells relevant to the onset of aggregation, which are illustrated in a schematic (Fig. 3.10). The first distance metric is the size $d_{\text{max,clr}}$ of the largest convective-free box, which would describe the greatest dry perturbation. The second metric instead considers a measure of the largest inter-convection nearest-neighbor distance, specifically the dimension $d_{\text{max,nn}}$ of the maximum box centered on a convective cell that is devoid of further convective sources. The behavior of these two length scales is anti-correlated over the long term as convection starts to aggregate, since the size of the maximum convective-free region grows with the onset of aggregation, while the maximum inter-convective nearest-neighbor spacing reduces, as shown comparing the left and right panels of Fig. 3.10. This is also confirmed diagnosing the two quantities directly from the model simulations in Fig. 3.11 for the same set of experiments presented in Fig. 3.3.

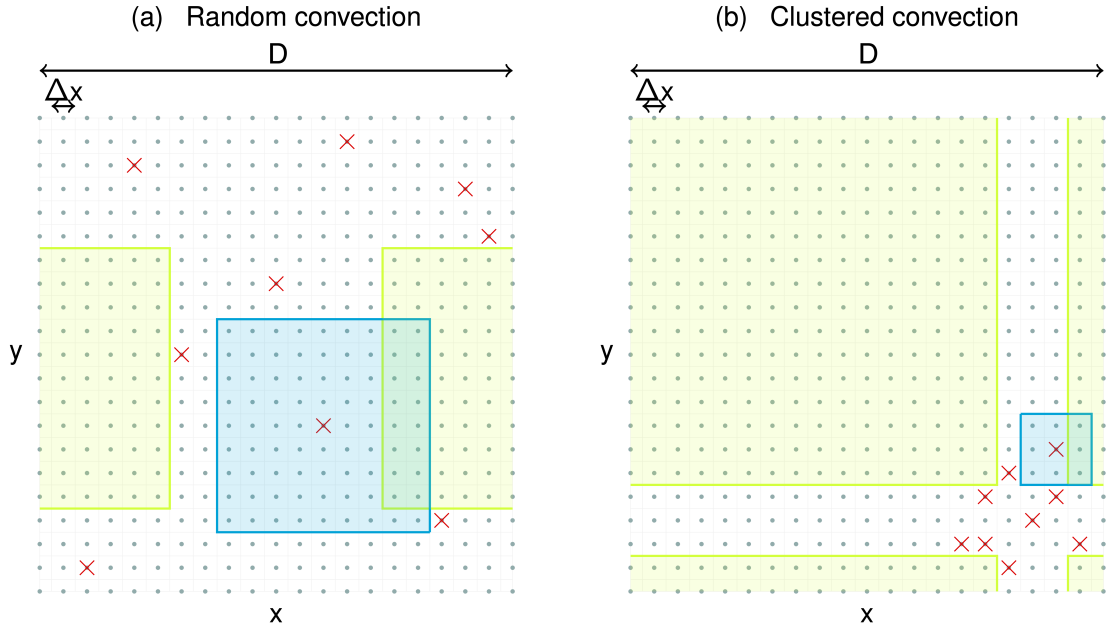

Figure 3.10: *Sketch of two potential metrics of convective spacing relevant for aggregation onset, namely the size of the largest clear-sky, convective-free box ($d_{\text{max,clr}}$, green boxes) and the maximum inter-convective nearest-neighbor spacing ($d_{\text{max,nn}}$, blue boxes), in a random convective situation (left) and highly aggregated situation (right). The cell centroids are represented as grey dots, the convective grid boxes as red crosses and the doubly-periodic nature of the domain is accounted for.*

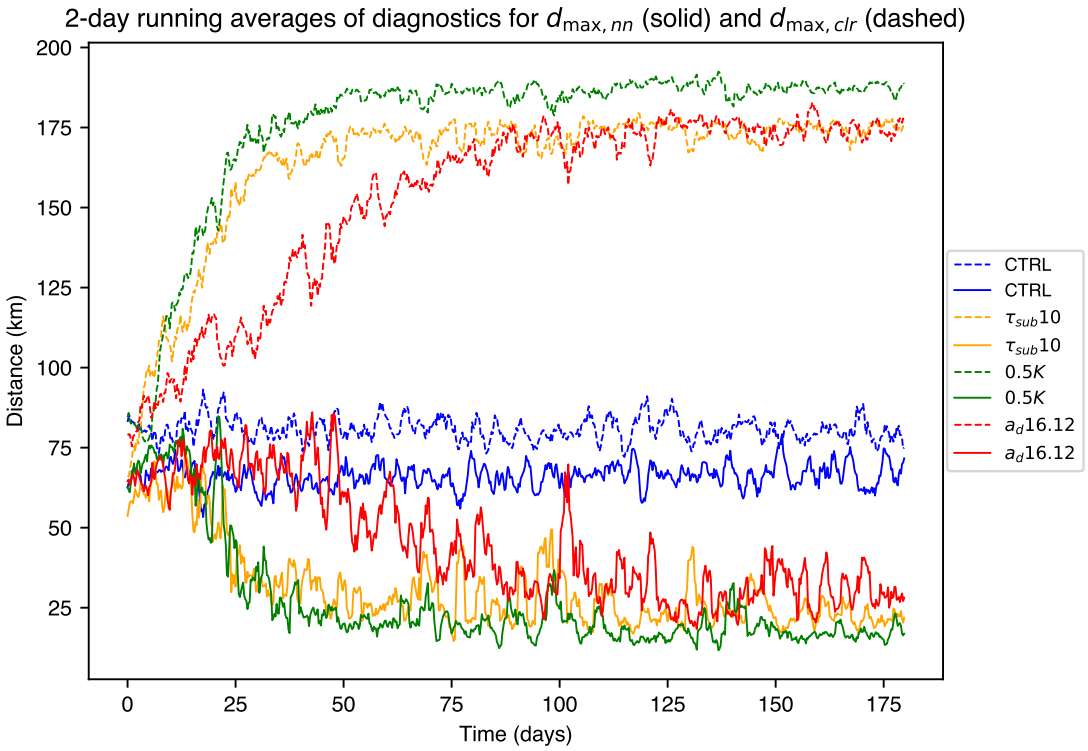

Figure 3.11: *Evolution of the maximum inter-convection nearest neighbor distance (solid lines) and the largest distance from a non-convective to the nearest convective grid cell (dashed), as diagnosed from the numerical model, for the runs of Figure 3.3. A 2-day running mean has been applied.*

Using (3.3), we can derive the distribution of $d_{\max,\mathrm{nn}}$, by considering the central point of the search box to be each of the convective cells in turn. In this respect, we note that $p_{\mathrm{clr}}(n, N_c - 1)$ represents the probability that the convection-free box centered on an arbitrary point of the pattern has size $> n\Delta x$. Therefore the probability that the maximum size of convection-free box centered on a convective tower is less than $n\Delta x$ is given by

$$\begin{aligned} p(d_{\max,\mathrm{nn}} \leq n\Delta x) &\approx \binom{N_c}{N_c} \left(p_{\mathrm{clr}}(n, N_c - 1)\right)^0 \left(1 - p_{\mathrm{clr}}(n, N_c - 1)\right)^{N_c} \\ &= \left(1 - p_{\mathrm{clr}}(n, N_c - 1)\right)^{N_c} \\ &= \left(1 - \left(1 - \frac{n^2\Delta x^2}{D^2}\right)^{N_c - 1}\right)^{N_c}, n \in \mathbb{N}, n \leq \frac{D}{\Delta x}. \end{aligned} \tag{3.4}$$

Eqn. (3.4) defines a cumulative distribution function, from which it is straightforward

to calculate the percentiles and the expected value, $\overline{d}_{\text{max,nn}}$, which represents, for a given density of randomly distributed convective sources, the average dimension of the maximum box centered on any tower that is free from further events:

$$\overline{d}_{\text{max,nn}} = \sum_{i=1}^{\frac{D}{\Delta x}} i\Delta x \left(\left(1 - \left(1 - \frac{i^2 \Delta x^2}{D^2} \right)^{N_c - 1} \right)^{N_c} - \left(1 - \left(1 - \frac{(i-1)^2 \Delta x^2}{D^2} \right)^{N_c - 1} \right)^{N_c} \right). \tag{3.5}$$

The results of 70000 artificially generated random convective scenes with varying N_c show that the theoretical estimate for $\overline{d}_{\text{max,nn}}$ presented in eqn. (3.5) fits the numerical data perfectly (Fig. 3.12).

One might consider the metric $d_{\text{max,clr}}$ to be a more relevant metric related to the spatial variance of water vapor in the initial random convection phase, and thus to aggregation onset. An approximation for this metric is given by

$$p(d_{\text{max,clr}} \leq n\Delta x) \approx (1 - p_{\text{clr}}(n, N_c))^{N_{xy} - N_c}, n \in \mathbb{N}, n \leq \frac{D}{\Delta x}. \tag{3.6}$$

However, this analytical formula somewhat over-estimates the size of the maximum clear-sky square when tested with numerical data as it considers the test at each cell in the domain to be independent, which is not the case. The trials can instead be safely assumed independent in the derivation of (3.4) due to the constraint $N_c \ll N_{xy}$. Additionally, the fact that N_{xy} is very large can lead to precision issues in the calculation of (3.6).

In any case, during the very early phase (first day) of the simulations, when convection is still random, an analysis of scene snapshots from the large ensembles shows that $d_{\text{max,clr}}$ and $d_{\text{max,nn}}$ are strongly linearly related (Fig. 3.13), and thus either can be used in the scale analysis. We therefore choose to use $d_{\text{max,nn}}$, also because it relates more closely to the more familiar nearest-neighbor metrics adopted in the derivation of the widely used I_{org} aggregation index (cf. Chapter 5). In the sequel, $\overline{d}_{\text{max,nn}}$ will be referred to as $\overline{d}$ for brevity.

3.3.4 Initial dimensional analysis

Combining the above considerations, we introduce the following dimensionless parameter to explain the transition between homogeneous and aggregated regimes:

$$\gamma = f(a_d) \frac{K\tau_{\text{sub}}}{D^2} \frac{D}{\overline{d}} = f(a_d) \frac{K\tau_{\text{sub}}}{D\overline{d}}, \tag{3.7}$$

where $\overline{d}$ is given by eqn. (3.5). The parameter γ consists of the normalized area of influence divided by the expected maximum inter-convective nearest-neighbor distance, rescaled by the domain size D. Low values of γ (in turn corresponding to either lower K or τ_{sub} or larger D or $\overline{d}$) are supposed to represent aggregated states.

In addition to the four factors of domain size, resolution, horizontal transport efficiency and subsidence rate that were discussed above, we have also incorporated

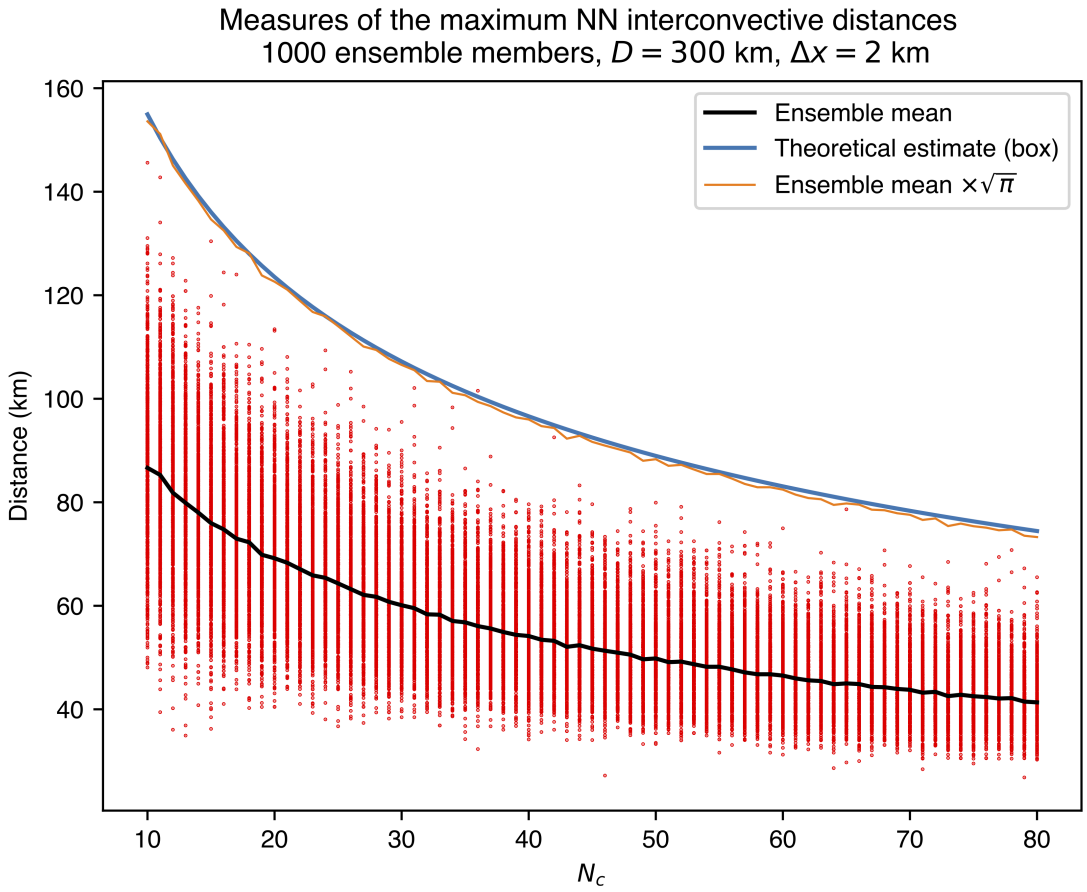

Figure 3.12: *Comparison between the results of a multi-run ensemble of experiments and the theoretical estimate* (3.5). *Red dots illustrate the maximum nearest neighbor distances between* N_c *objects thrown onto a* 300×300 *km domain with* 2 *km resolution, whereas the black line represents the ensemble mean distance. Examining nearest-neighbor distances implies that there are no events within a radius* r *of the base point, whereas the theory here involves the void probabilities for a square box of size* d*. Imposing equal areas gives* d *as* $d = \sqrt{\pi}r$*, and multiplying the ensemble mean by this factor (orange line) reproduces exactly the theoretical curve for* $\bar{d}_{\max,nn}$ *(blue line).*

the sensitivity of convection to water vapor through a generic function $f(a_d)$, where f expresses the (unknown) functional dependence on a_d. As a_d is dimensionless, the functional form of f will be derived empirically using an ensemble of numerical experiments.

However, treating a_d and the other parameters in (3.7) separately seems reasonable since we speculate that the evolution to aggregation requires the generation of R

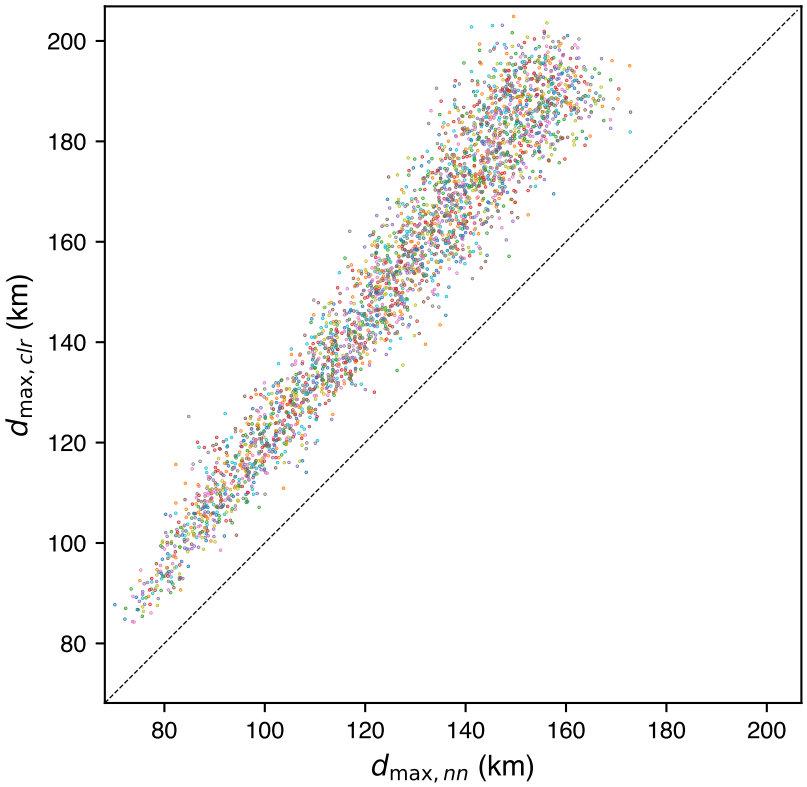

Figure 3.13: *Scatter plot of daily averaged diagnostics for $d_{\max,nn}$ versus $d_{\max,clr}$ from hourly snapshots of scenes taken from a large ensemble in the first day of each experiment when convection is still randomly distributed. The identity line is shown as a black dashed line for better visualization.*

anomalies in the initial random phase, which are then magnified by the indicator function. As discussed earlier, the formation of R anomalies is favoured by large convection-free areas and results from the subsequent interplay between subsidence and horizontal transport, while a_d does not contribute at the beginning and its role can be decoupled from the rest of the analysis. Indeed, if we decompose the column humidity field as $R(\mathbf{x},t) = \overline{R}(t) + R'(\mathbf{x},t)$, $\overline{R}(t)$ and $R'(\mathbf{x},t)$ being the domain-mean R and the local departure from the mean, respectively, it is apparent that $e^{a_d R(\mathbf{x},t)} = e^{a_d \overline{R}(t)} e^{a_d R'(\mathbf{x},t)} \approx e^{a_d \overline{R}(t)}$ if $\overline{R}(t) \gg |R'(\mathbf{x},t)| \approx 0$, as is the case prior to aggregation onset. At this stage, the weights of the selection process are dominated by the uniform term $e^{a_d \overline{R}(t)}$. Conversely, if substantial R anomalies are created, they are easily amplified by the exponential shape of the convection-vapor feedback.

In this respect, we note that the exponential form of the moisture-convection feedback is not necessary for aggregation to occur, but a nonlinear relationship is still needed

to retain the key behavior of the model. The following Fig. 3.14 presents the results of a grid refinement study conducted with different functional forms of the convection-vapor feedback, with K, τ_{sub}, a_d and D invariant. In particular, we replaced the relationship (2.3) with a linear form $P(R) = P_0 a_d R$ (top panels) and a piecewise linear function resulting from the linearization of (2.3) around $R_{RCE} = 0.603$ (Bretherton et al., 2004), i.e., $P(R) = P_0(1 + a_d(R - R_{RCE}))\mathcal{H}(1 + a_d(R - R_{RCE}))$, $\mathcal{H}$ denoting the Heaviside function (bottom panels). These experiments show that the exponential shape of the feedback is not essential for the bimodal solution to exist and a piecewise linear relationship can still capture the key aspects of the organization; however, a linear functional form does not produce clustering, even at coarse resolutions. Nonetheless, in this latter case differences across the end climates do exist, likely due to the fact that coarser resolutions lead to larger values of $d_{\text{max,clr}}$. The larger convection-free patches that ensue are more likely subjected to efficient subsidence drying.

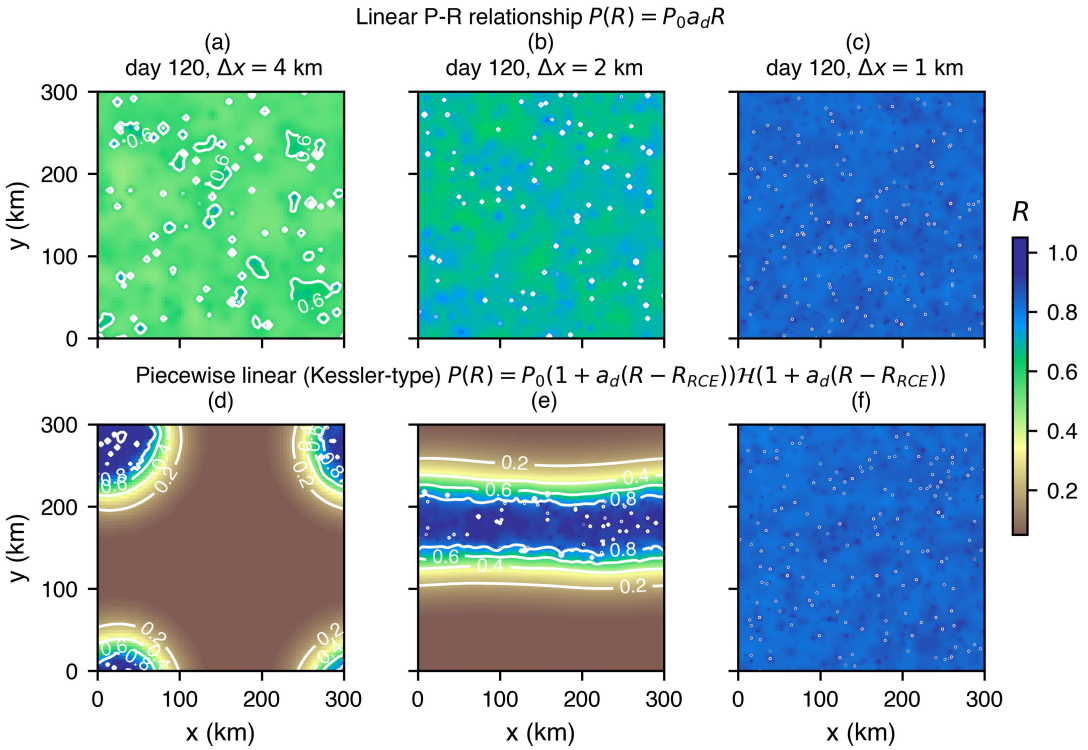

Figure 3.14: *Results of grid refinement studies conducted with different shapes of the convection-moisture feedback function, all else being equal. Shown is the column relative humidity field R (shading and contours, interval* 0.2*) at the end of the integration procedure.*

Thus, setting aside the functionality f for the moment and assuming $a_d = 14.72$, and using the default domain size and resolution ($D = 300$ km, $\Delta x = 2$ km), we again evaluate the ensemble experiments that vary K and τ_{sub} to see if the dimensionless quantity

(3.7) correctly predicts the final state to be clustered or random. Like the previous Fig. 3.8, Fig. 3.15 shows contours of $\overline{\sigma}_{R,20}$, which we recall is the spatial standard deviation of R in the last 20 days. In this case, the slope of the transition zone in (τ_{sub}, K) space is almost exactly parallel to the isopleths of $K\tau_{\text{sub}}(D\bar{d})^{-1}$ (recalling that a_d is fixed here), represented as red dashed curves.

Further sets of simulations from the grand ensembles were examined for other values of D and Δx, with the fit still holding for fixed a_d, and the critical threshold value is the same as in this default case $D = 300$ km, $\Delta x = 2$ km (Figs. 3.16 and 3.17). This means that there is a critical value that predicts the onset of aggregated convection. The critical isopleth that fits the transition will depend on a_d and thus the final task is to determine the functional dependence on a_d in the specification of γ.

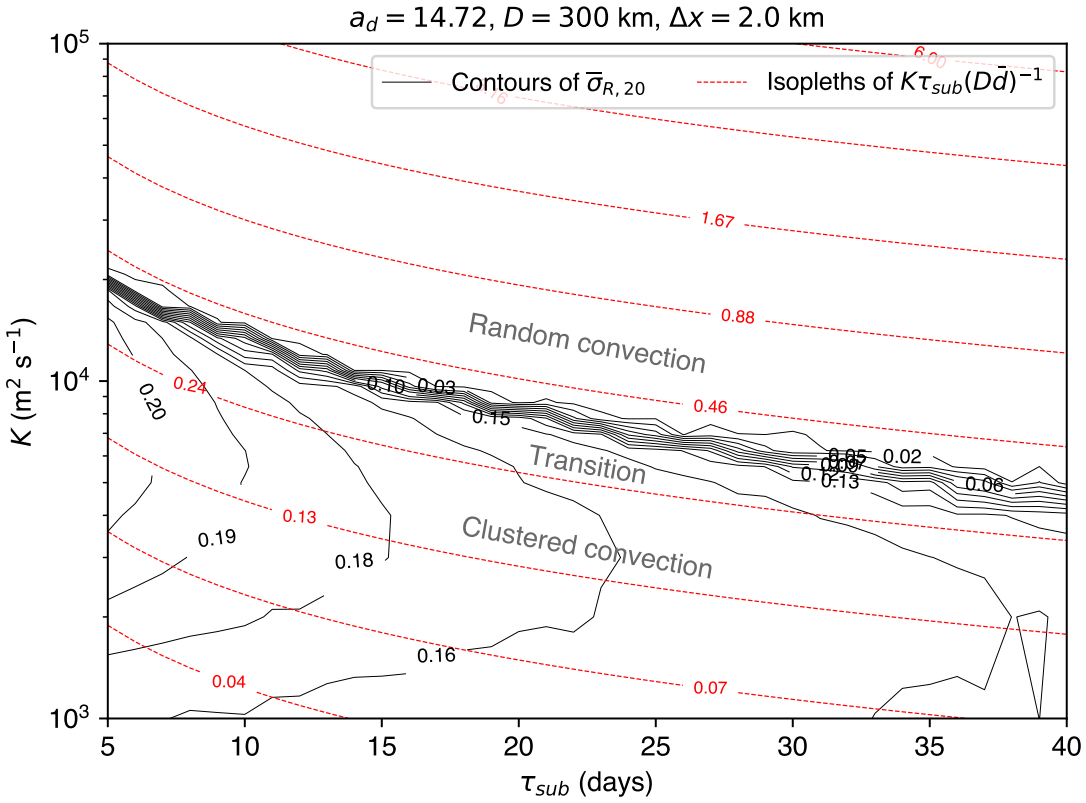

Figure 3.15: *Contours of $\overline{\sigma}_{R,20}$ (black solid curves) and isopleths of $K\tau_{sub}(D\bar{d})^{-1}$ (red dashed curves) for single realizations of the system in a large set of simulations with varying K and τ_{sub} and fixed a_d, D and Δx.*

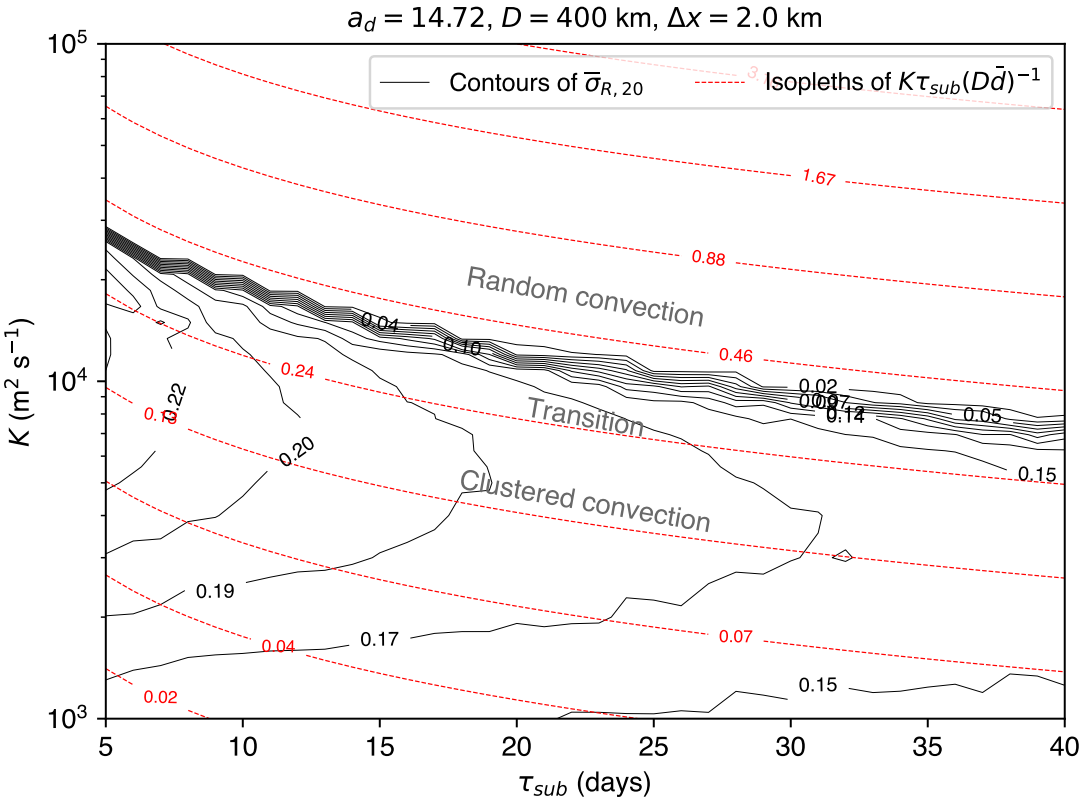

Figure 3.16: *As in Figure 3.15 but with larger domain, $D = 400$ km.*

3.3.5 The role of the parameter a_d

Intuitively, the relationship eqn. (2.4) may strongly impact the aggregation of convection, via the steepness a_d of the exponential function, which governs the choice of convective locations: low values of a_d indicate that convection is very insensitive to water vapor anomalies and stochasticity of the convection choice may dominate, whereas high values produce organization as essentially only the moistest columns are likely to be selected after the initial perturbations are introduced in the water field. In fact, in the limit $a_d \simeq 0$, eqn. (2.4) is homogeneous in the interval $[R_{\text{min}}, R_{\text{max}}]$, R_{min} and R_{max} being the minimum and maximum R values throughout the domain, and convection is rendered completely random by definition. It is thus expected that, as a_d increases, the critical isopleth will be shifted upwards in the (τ_{sub}, K) space, as the range of parameters for which the aggregated climate exists as a stable equilibrium state is broadened. This is exactly seen in Fig. 3.18 changing a_d to 16.12, which corresponds to TRMM retrieval version 5 (Rushley et al., 2018).

The functional dependence of the transition on a_d is determined empirically (Fig.

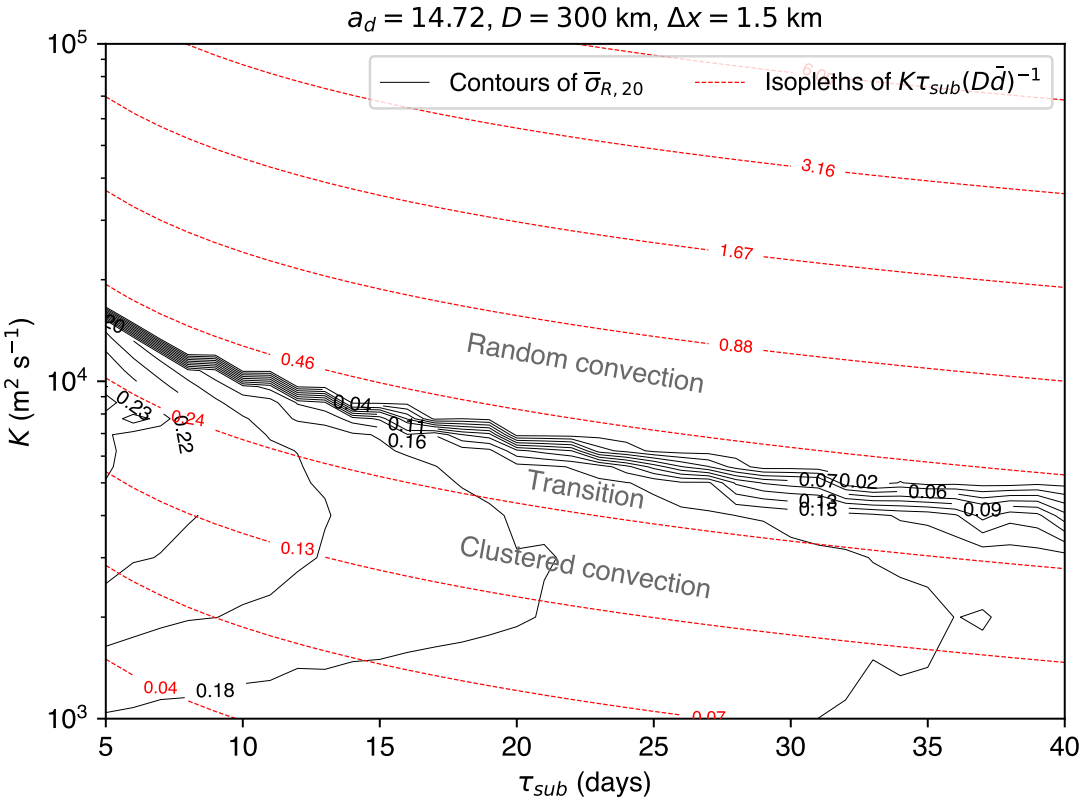

Figure 3.17: *As in Figure 3.15 but with higher resolution, $\Delta x = 2$ km.*

3.19), using $\overline{\sigma}_{R,20}$ for simulations performed with a range of values of K and a_d and fixed τ_{sub}, D and Δx. The fit from empirical data shows that the position of the transition regime in the parameter space increases quadratically with a_d. The changes of $\overline{\sigma}_{R,20}$ for the simulations with aggregated convection are due to the absence of monotonicity of $\overline{\sigma}_{R,20}$ with a_d. Indeed, for organized runs, the size of the moist, convectively active region is reduced for high values of a_d. Owing to the increasingly steep shape of the exponential function eqn. (2.4), the larger a_d gets, the more likely is for convection to reactivate at the same spots (which are the moistest ones), thus shrinking the wet patch, enlarging the area occupied by subsiding air and therefore reducing the spatial R variance beyond the onset point of aggregation.

This nonlinear behavior of $\overline{\sigma}_{R,20}$ in the clustered state seen in Figs. 3.15-3.19, with the spatial variance of humidity increasing sharply with aggregation onset but reducing as the degree of aggregation strengthens, implies that humidity variance can be used to determine whether aggregation has occurred or not, but is not an effective metric of the degree of aggregation for model inter-comparison studies such as Wing et al. (2020).

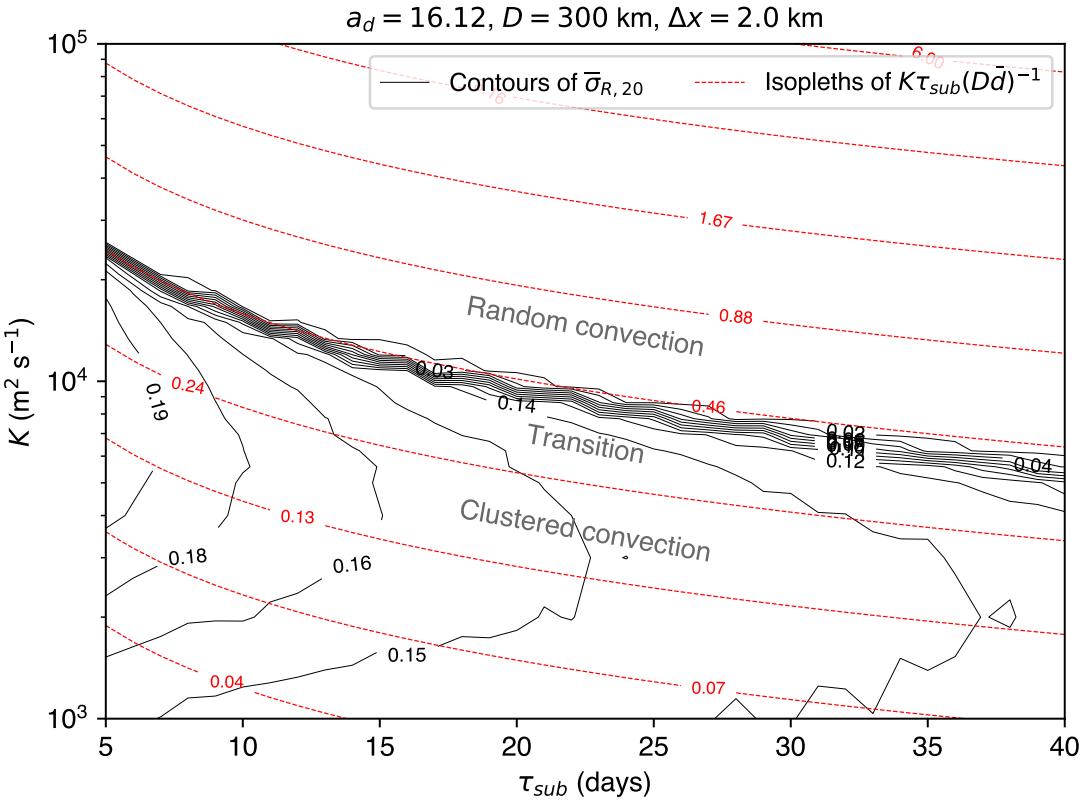

Figure 3.18: *As in Figure 3.15 but with* $a_d = 16.12$.

3.4 The aggregation number

Knowing the quadratic dependence of a_d allows us to construct the full dimensionless quantity that incorporates all three model parameters and the experiment domain size and resolution, which will be referred to as the *aggregation number* N_{ag}. This is given by

$$N_{\text{ag}} = \frac{K\tau_{\text{sub}}}{a_d^2 D\bar{d}}. \tag{3.8}$$

We make an evaluation of the final dimensionless parameter (3.8) using a complete ensemble of experiments which investigate the full five-dimensional parameter space of changing K, τ_{sub}, a_d and the domain size D and resolution Δx. The resulting scatter plot in Fig. 3.20 shows that **the transition between random and aggregated states occurs at a precise critical value of the dimensionless quantity** N_{ag} as specified in eqn. (3.8). This means that N_{ag} **is able to predict almost exactly if a particular model and experiment setup will lead to clustering**, with convection found to aggregate when

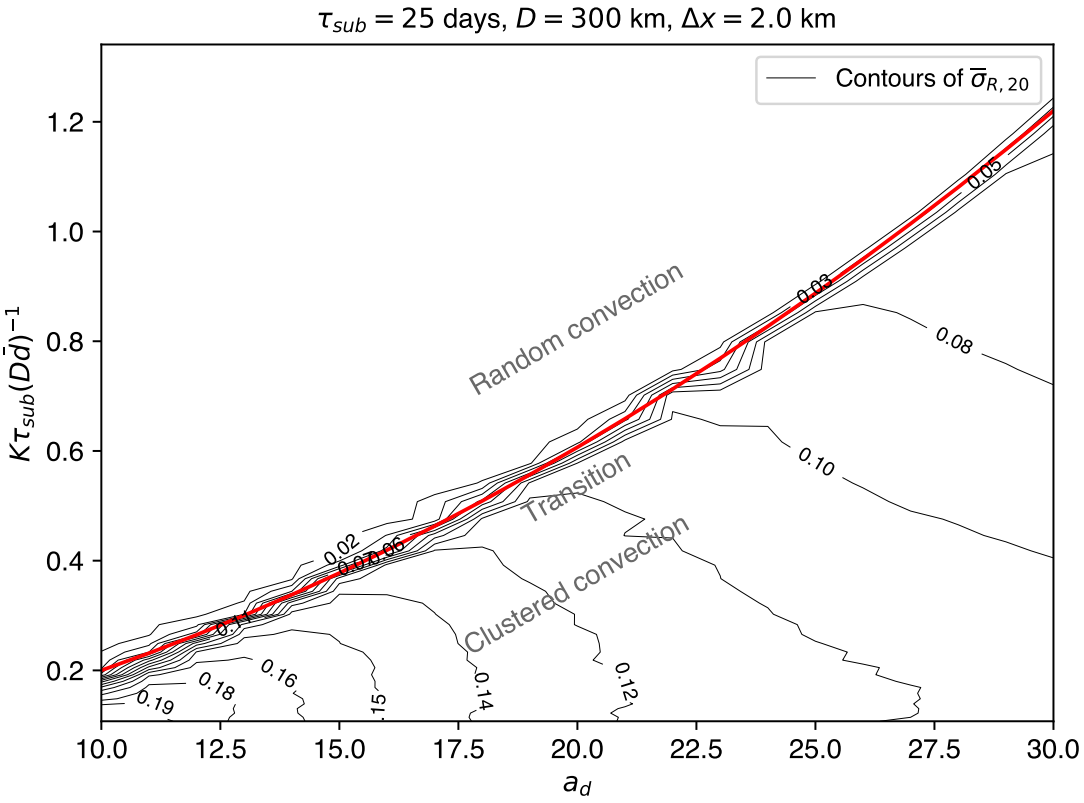

Figure 3.19: *Contours of $\overline{\sigma}_{R,20}$ (black solid curves) for an ensemble of runs carried out with different values of $K\tau_{sub}(D\bar{d})^{-1}$ (here obtained varying K and keeping τ_{sub}, D and Δx fixed) and a_d. The red solid line represents the polynomial (quadratic) empirical fit for the transition regime.*

the combination of the five parameters gives a N_{ag} value below the critical threshold, $N_{\text{ag,crit}}$, of approximately 1.72×10^{-3}. This estimate (that is, the vertical line in Fig. 3.20) has been obtained with an iterative procedure which yields equal number of misses on either sides of the vertical line itself. A threshold of $\overline{\sigma}_{R,20} = 0.05$ was imposed to distinguish between aggregated and non-aggregated runs. There is some variation in the transition zone which we attribute to the stochastic nature of the model. Indeed, repeating some of the experiments with configurations such that $N_{\text{ag}} \sim N_{\text{ag,crit}}$, with small initial random perturbations, showed that these could end up in either a random or aggregated state.

The significance and possible implications of these findings will be discussed in detail in Chapter 6.

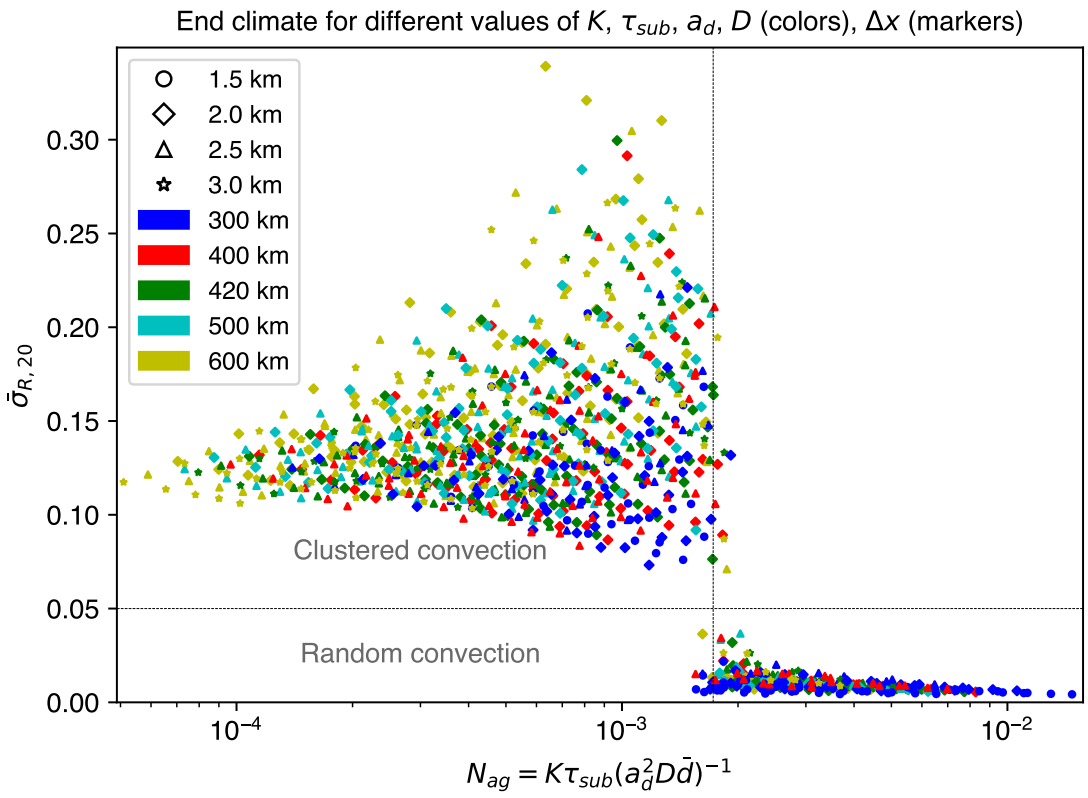

Figure 3.20: *Scatter plot referring to a collection of simulations with different values of the parameter N_{ag}, as defined in* (3.8)*, each associated with the corresponding value of $\overline{\sigma}_{R,20}$. The horizontal dashed line $\overline{\sigma}_{R,20} = 0.05$ separates aggregated and non-aggregated runs, the vertical dashed line represents the threshold value of N_{ag} obtained as specified in the text.*

Chapter 4

What is missing from the aggregation number?

The aggregation number (3.8), while hopefully useful, does not tell the complete story and the toy model of tropical convection introduced in Chapter 2 has some further, unexplored features. For instance, the experiments conducted in Chapter 3 all start from identical homogeneous moist conditions of 80% relative humidity, but, similar to CRM studies, the simple model is also found to be sensitive to the initial conditions, with aggregation more likely starting from drier and/or more heterogeneous conditions. Otherwise said, the model displays a hysteresis that, although very weak, can not be captured by the dimensionless parameter N_{ag}.

We saw that the physics of the model is highly simplified and many processes are neglected. For instance, there is no explicit treatment of advection, unlike in Ahmed and Neelin (2019), or radiation and surface fluxes, and the diabatic effects are implicitly included in the indicator random variable. Another effect that is missing from the model in its present formulation - and hence from the aggregation number - is the one of cold pools, which inhibit new convection in their stable interiors. A first, very basic attempt to account for cold pool exclusivity effects is discussed, and some preliminary results are presented, along with some considerations regarding the impact of cold pools on the localization of convection in the simple model.

4.1 Sensitivity to initial conditions

One of the most striking features encountered in CRM simulations of self-aggregation is the tendency of convection to lock itself into the aggregated state, once established. It is difficult for convection to disaggregate, and the clustered state can be maintained even without the feedbacks necessary to initiate it from homogeneous conditions. That is, the system exhibits hysteresis (Khairoutdinov and Emanuel, 2010; Muller and Held, 2012). The importance of hysteresis lies in that this property extends the parameter

range over which the aggregated regime exists as a stable equilibrium state of tropical climate. Wing et al. (2017) argue that the robustness of clusters to changing environmental conditions hints at the possibility of tropical climate system being intransitive (or almost intransitive).[1]

We now want to see if the simple model of tropical convection introduced in Chapter 2 exhibits hysteresis. A series of runs with different initial conditions were performed to ascertain to which extent the initial state can impose a memory to the system. The following Figs. 4.1, 4.2 and 4.3 refer to simulations initialized with a range of horizontally homogeneous R profiles. The diffusivity K and the parameter a_d have been kept fixed at $K = 10^4$ m^2 s^{-1} and $a_d = 14.72$, respectively, while $\tau_{\text{sub}} = 10$ days (Fig. 4.1), 16 days (Fig. 4.2) and 20 days (Fig. 4.3).

It is apparent that, in the first case, the system always attains the same mean state, regardless of the initial value R_0: sooner (low R_0) or later (large R_0), the wet spot peculiar of spatially organized atmospheres emerges. In particular, when the environment is initially fully saturated, i.e., $R_0 = R_c = 1.05$, the humidity field stays quasi-homogeneous at the simulation outset and the choice of convective locations is nearly random. Then, when the first heterogeneities are created, mainly through the action of subsidence drying, they are rapidly amplified through the convective indicator function. This progression is similar to that of other runs for $R_0 \geq 0.9$. In other words, the moister the domain, the less impact convection has on the moisture field, i.e., it dries by compensating subsidence but does not locally moisten, and the precipitation efficiency would be much higher. For low values of R_0, instead, the transition towards the aggregated state is extremely fast, as shown in the lower panel of Fig. 4.1. Indeed, for the chosen set of parameter values, even though the initial R field is spatially uniform, a cluster is formed at the very beginning in practice - if $R_0 \leq 0.4$, generally within the first day of simulation.

To understand this behaviour in more detail, let us consider an extreme case where the initial humidity content of the environment is close to zero, i.e., $R_0 = 0.01$. The columns first selected for developing convection become dramatically moister than the others owing to the fast relaxation time τ_c. Due to the large contrasts in humidity content between convecting and non-convecting cells, new convection is likely reactivated in the previous spots and/or initiated in the vicinities of pre-existing sites, especially when diffusion is not efficient at moistening the far-field. As in the domain size sensitivity study presented in Chapter 3, one of the ensuing convective centers rapidly prevails and the others shrink. Essentially this is equivalent to initializing the experiment with the typical end climate of the organized case. The simulations performed with low values of R_0 can thus be considered as linked to the runs conducted by Muller and Held (2012) to test for hysteresis. They initialized some of their simulations with a moist bubble in the center of the dry domain, thus featuring large contrasts in humidity content.

[1] In the sense of Lorenz (1968). Essentially, a system is *intransitive* when it possesses more than one stable equilibrium state depending on the initial condition and *almost intransitive* when it is in a stable state for a certain period of time and flips to an alternative one and then oscillates between the two.

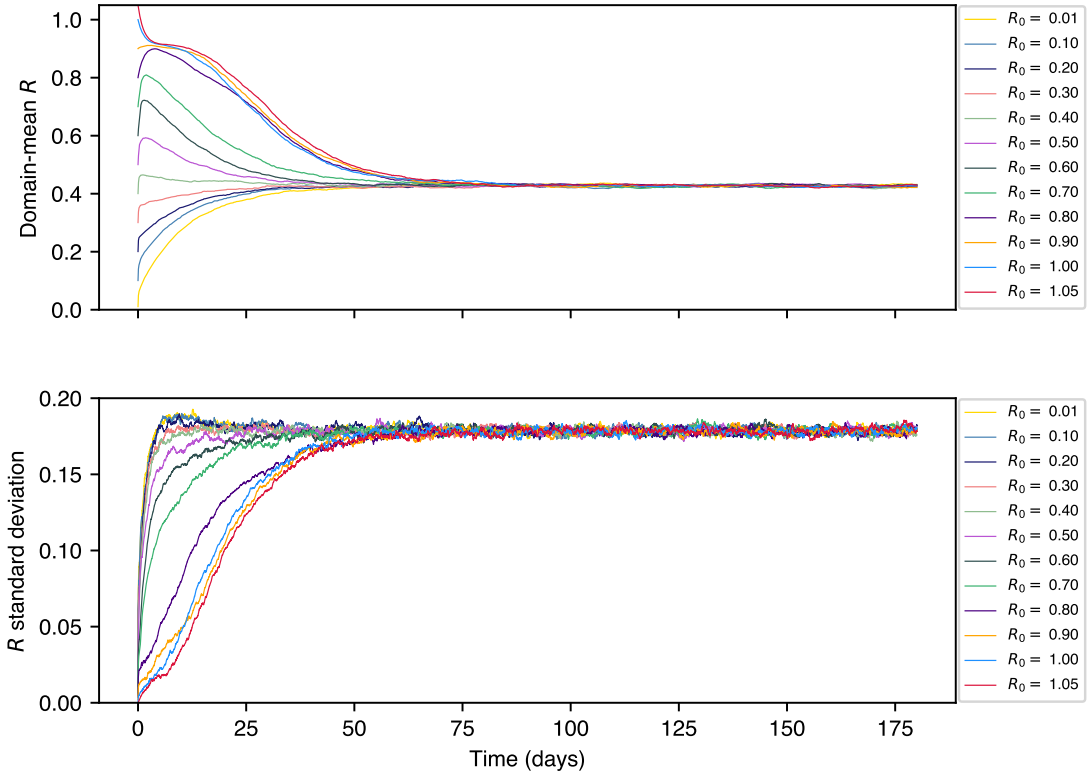

Figure 4.1: *Time evolution of the mean and standard deviation of the spatial R field for simulations with* $K = 10^4\ m^2\ s^{-1}$, $a_d = 14.72$, $\tau_{sub} = 10$ *days,* R_0 *as reported in the legend. Runs are conducted over a doubly-periodic square domain with size* $D = 300$ *km and horizontal resolution* $\Delta x = 2$ *km.*

Fig. 4.2 refers to the same parameter set as above except for $\tau_{\text{sub}} = 16$ days, but looks quite different. Two equilibria exist in this case and the initial condition is seen to have an influence on the nature of the end climate. In other words, the system exhibits hysteresis. Convection organizes only for a range of R_0 values, $R_0 \leq 0.6$. Visual inspection of the scenes however suggests that the region surrounding the moist cluster is not as dry as in the experiments discussed in Chapter 3, with the humidity content there not less than 40%. Aggregated states are instead never obtained when starting from relatively moist environments. In principle, we can not exclude that the two equilibria in the upper panel of Fig. 4.2 would collapse into a single one or further evolve, but extending the simulations past day 180 confirmed this not be the case. Therefore, once clustering is established, it is not altered. A large stochastic component is visible in the lower panel of Fig. 4.2 for the disorganized runs: there is no monotonicity with R_0 and the curves are continually intertwining. Contrary to the case of Fig. 4.1, for $R_0 \leq 0.4$,

the R variance timeseries show a notable decrease after reaching a peak. This is because, after the initial outbreak of convection and the net separation between the moist and dry phases, the moistening due to convection and the ensuing diffusive transport are now opposed less efficiently by subsidence.

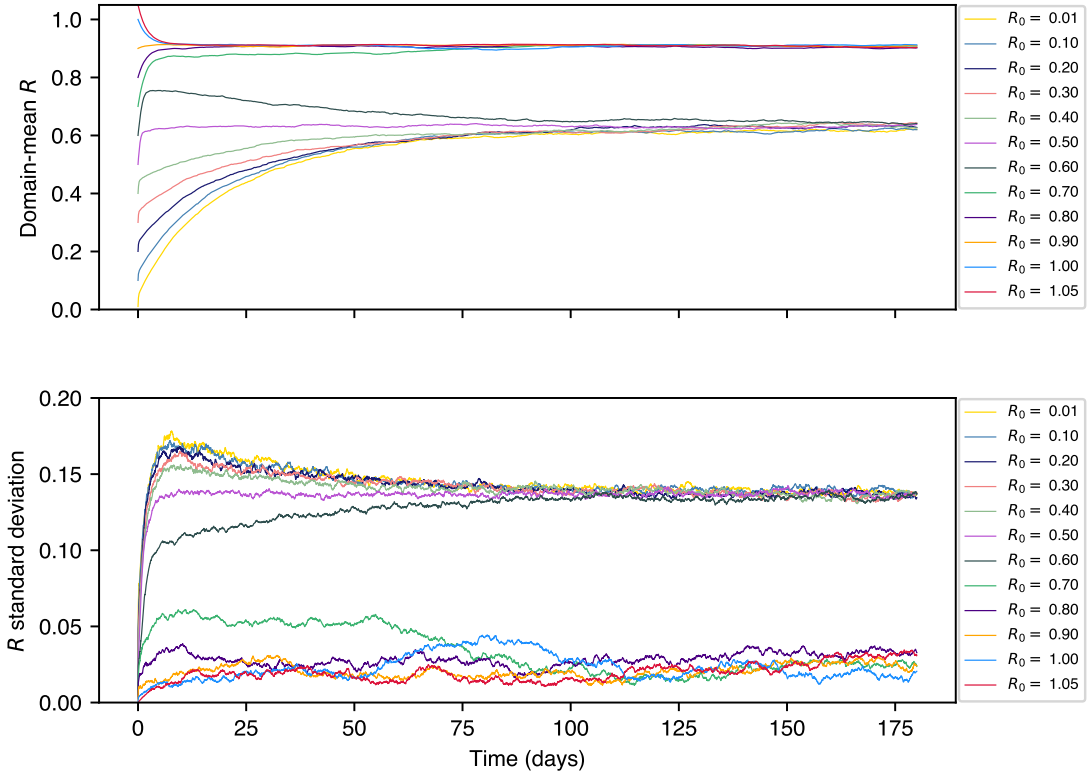

Figure 4.2: *As in Figure 4.1 but with* $\tau_{sub} = 16$ *days.*

This latter effect per se is not sufficient to destroy the clustering. However, if τ_{sub} is further increased, aggregation does not persist, as the enlargement of the moisture halo around convective events forces the active cells to be no longer localized but scattered, even for very low values of R_0 (Fig. 4.3). This is particularly evident in the R standard deviation profile (lower panel). There is again one single statistically steady equilibrium state available for domain-mean R, which corresponds to a quasi-homogeneous spatial distribution of convection.

4.1.1 Existence of hysteresis loops

The hysteresis behavior also manifests itself if K is varied and τ_{sub} held fixed. We show this by conducting a different test, which exhibits the existence of a hysteresis loop.

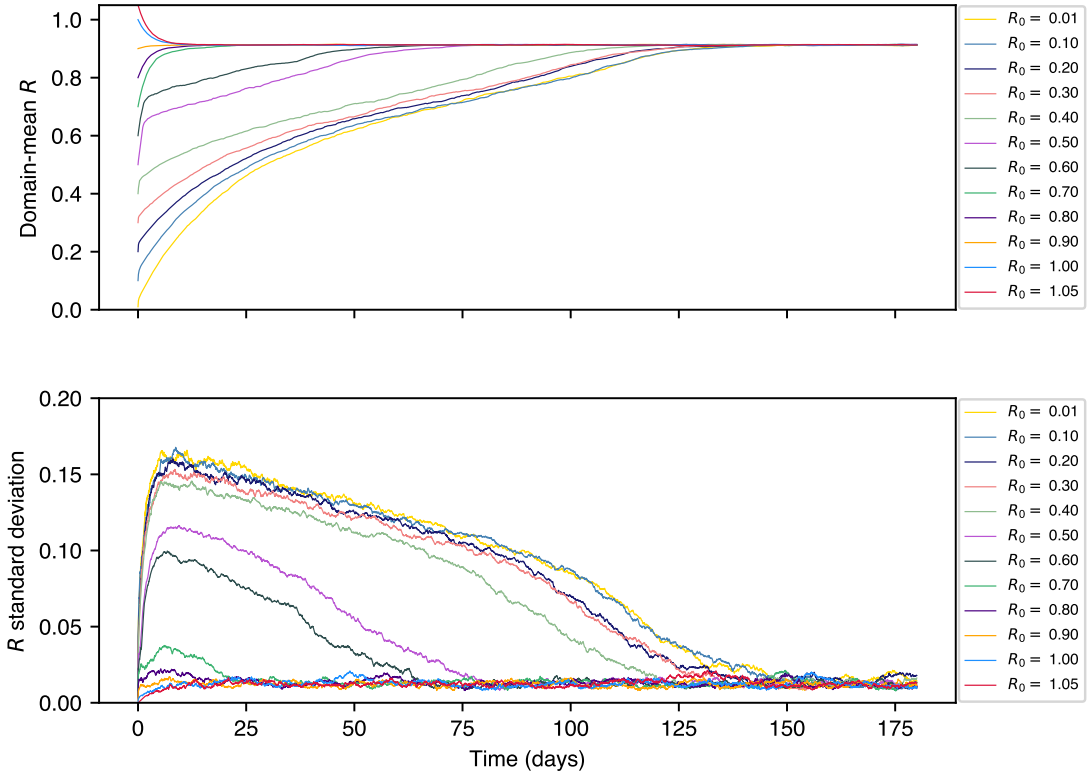

Figure 4.3: *As in Figure 4.1 but with* $\tau_{sub} = 20$ *days.*

Specifically, we start from $R_0 = 0.8$ for $K = 5 \times 10^3$ m^2 s^{-1} and perform a sequential set of simulations by increasing K by 10^3 m^2 s^{-1} at a time, with the initial state of each run given by the end state of the preceding one. When $K = 1.5 \times 10^4$ m^2 s^{-1}, the diffusivity is reversed back. Since τ_{sub} is kept constant at 15 days, the time-averaged convective population size is the same according to the argument (2.2). The results of this sequential multi-run experiment are presented in Fig. 4.4, which shows the spatial R standard deviation averaged over the last 20 days (out of 200) of each simulation, i.e., when equilibrium has been reached, for different values of K. The selected period is long enough to ensure that a stable equilibrium state has been reached by the system at the end of the integration procedure. The hysteresis loop is rather modest and not particularly strong, yet evident.

Overall these experiments revealed that **there is a limited window in the parameter space in which the initial condition imparts a strong memory to the system**; elsewhere, the initial state does not play any role and the conclusions of Chapter 3 well hold. Nonetheless, it would be advisable to conduct some more systematic analysis to see if the hysteresis loop is stronger for other parameter settings, for example changing

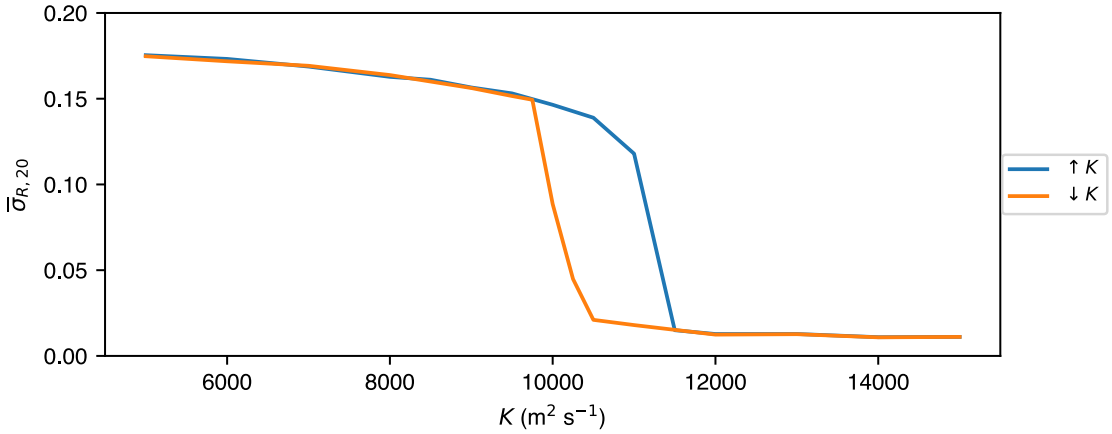

Figure 4.4: *Sequential series of experiments for different values of K,* $\tau_{sub} = 15$ *days and* $a_d = 14.72$*, each simulation being initialized with the end climate of the previous one. The first run has* $R_0 = 0.8$*. At* $K = 1.5 \times 10^4$ m^2 s^{-1}*, the diffusivity is turned back down. K is increased (blue solid line) or decreased (orange) by* 10^3 m^2 s^{-1} *at a time. Shown is* $\overline{\sigma}_{R,20}$*, the standard deviation of the horizontal column humidity distribution averaged over the last* 20 *days, out of* 200 *of simulated time.*

the convection-vapor feedback strength a_d.

4.1.2 Hysteresis behavior at very high resolutions

Another experiment was performed to understand if a spatially organized atmosphere can be disrupted by a finer grid spacing. CRM studies have investigated this facet of the resolution sensitivity, with Muller and Held (2012) showing that, when the simulations are initialized as organized, the clustered regime is maintained even at resolutions as fine as $\Delta x = 500$ m if the domain is large enough. This would suggest that the ability of organized states to persist seems to be less sensitive to resolution than the ability of aggregation to be instigated from homogeneous conditions. Otherwise said, the existence of the aggregated state exhibits less sensitivity than the self-aggregation process itself.

The following Fig. 4.5 refers to the same case of Fig. 3.6d (namely, $K = 5 \times 10^3$ m^2 s^{-1}, $\tau_{\text{sub}} = 10$ days, $a_d = 14.72$, $D = 300$ km, $\Delta x = 500$ m), but with the initial condition given by $R_0 = 0.1$, which, as discussed above, leads to an early establishment of the aggregated state. Here, at day 2 (Fig. 4.5a), the cluster is already fully formed. It then grows in size, mainly due to diffusive transport, but later stabilizes, as suggested by the snapshots at days 50 (b) and 120 (c) that look almost identical. The findings of our simple model are therefore once more consistent with those of CRMs and the model poses as a useful tool to explore also this aspect of the resolution dependence of self-aggregation.

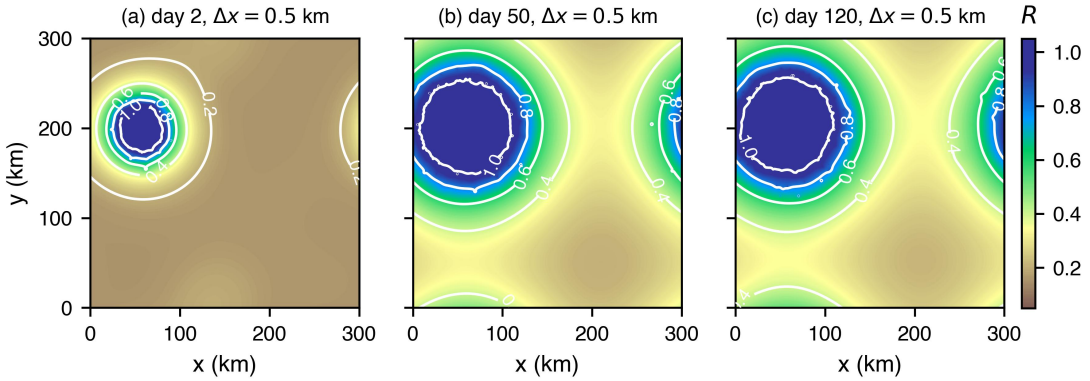

Figure 4.5: *View of the spatial R field at days* 2 *(a),* 50 *(b) and* 120 *(c) of simulation, for a run with the same parameters and setup as in Figure 3.6d, except for* $R_0 = 0.1$ *(*$K = 5 \times 10^3$ m^2 s^{-1}, $\tau_{sub} = 10$ *days,* $a_d = 14.72$, $D = 300$ *km,* $\Delta x = 500$ *m).*

4.2 Inclusion of cold pools

We saw in the Introduction that, when deep convection establishes, the subcloud layer is cooled and moistened by evaporation of precipitation that falls through a subsaturated environment. The cooling introduces a negative buoyancy perturbation and also explains the lag between temperature and humidity drops that has often been documented in observations (Tompkins, 2001b). Later, in the mature stages, the entrainment of dry, environmental air at the cloud edges causes some hydrometeors to evaporate, which cools the air and generates the downdrafts (Houze jr., 2014). These are accelerated by the frictional drag of falling precipitation, which results in some surrounding air being carried down within the downdraft itself. The downdrafts inject cold and dry air of much lower buoyancy into the boundary layer and, upon hitting the surface, the air mass is spread away from the source as a density current (cf. sketch Fig. 1.2). The moist air below the cloud base is replaced and pushed at the edges of the newly formed cold pool, thus, unlike the temperature signal, the vapour depression has limited extent, with the periphery of the cold pool often (but not always, e.g., Kruse et al., 2022) consisting of a ring of very moist air (Tompkins, 2001b). Cold pools suppress convection in the immediate neighborhood of pre-existing towers (inhibition effect), but can initiate it by providing mechanical lifting to the warmer environmental air nearby or by thermodynamic triggering mechanisms (Tompkins, 2001b; Torri et al., 2015).

As a first attempt, we tried to include cold pools in a very idealized way. It consists in modifying the probabilities underlying the weighted random sampling that selects the locations for new convection. Specifically, we account for the inhibition effect due to cold pools by requiring convection to not redevelop in the cells formerly experiencing it, and in their vicinities. To accomplish this, we introduce a new variable

$C(\mathbf{x}, t) \in [0, 1]$, representing the likelihood of convective inhibition, with $C(\mathbf{x}, t) = 1$ corresponding to full suppression of convection at point $\mathbf{x}$ and time t.[2] We then select a radius r_{cin} surrounding each convective point and representing the distance over which convection is not allowed to erupt. That is, C is assumed to be identically one for each point $\mathbf{x}$ within distance r_{cin} off any convective point, while in the field far from convection it is reasonable that $C = 0$. We impose the spatial C distribution be smooth, avoiding discontinuity jumps at the edge of discs of radius r_{cin} centered at the convective points. We thus require C satisfies a reaction-diffusion equation of the type

$$\frac{\partial C}{\partial t} = K_{\text{cin}} \nabla^2 C - \frac{C}{\tau_{\text{cin}}}, \tag{4.1}$$

where K_{cin} and τ_{cin} represent the efficiency of the spreading of high density air, hence of inhibition, and the relaxation time to $C = 0$, i.e., to a complete removal of convective inhibition. The former can be interpreted as due to the cold pool propagation, the latter as the wake lifetime before the recovery of thermodynamic anomalies by surface fluxes and environmental mixing takes place. We note that this approach neglects a wide variety of phenomena, for instance the fact that, at the convergence lines between colliding cold pools, convection can be easily triggered because the dynamical uplift of boundary layer air is at a maximum there. The choice itself of fixed uniform values for K_{cin} and τ_{cin} is also a simplification, as, e.g., K_{cin} should eventually be a function of virtual temperature anomalies. Similar to the concept of area of influence introduced in Chapter 3 for the moisture halo around convective towers, the maximum cold pool size is controlled by K_{cin} and τ_{cin}.

The eqn. (4.1) can be solved numerically on the discrete grid through the ADI scheme presented in Chapter 2. Once the solution is known, it is used to define the non-uniform probabilities of the sampling procedure that determines the triggering of new convection. These probabilities are no longer based on eqn. (2.4), but we impose that

$$p_{c_{j,k}} \equiv p_c(R_{j,k}; C_{j,k}) = Z(t)(1 - C_{j,k}) e^{a_d R_{j,k}}, \tag{4.2}$$

where the subscripts j, k again refer to the grid and $Z(t)$ is a normalizing factor. The relationship eqn. (4.2) means that, if in principle $C_{j,k} = 1$, $p_{c_{j,k}}$ would be zero regardless of the value of $R_{j,k}$ and convection could not redevelop in the moistest grid points. In practice, however, values of $C = 1$ are never attained because of the relaxation term in eqn. (4.1). The extent to which the probabilities are modified by the inclusion of cold pools in both random and aggregated situations is apparent from Fig. 4.6. It is seen that, in the former configuration, the most notable differences are in the areas surrounding the updrafts (red dots) and in the vicinities of pre-existing ones, where full recovery of the inhibition has not yet occurred. The differences are instead extremely evident in the second case, not only within the moist patch typical of self-aggregated states, but also in the far-field. The probabilities here are anyway lower than in the vicinities of

[2] Here $[0, 1]$ denotes the unit interval, the left- and right-closed interval of real numbers between zero and one.

updrafts because of the huge difference in the R content, yet they differ almost by a factor of 100 with respect to the case without cold pools included.

4.2.1 Choice of parameters and constants

For the radius r_{cin} of convective inhibition from a tower we use the value of $r_{\text{cin}} = 8.6$ km corresponding to the mean maximum cold pool radius found by Tompkins (2001b) in his CRM study. The cold pool lifetime τ_{cin} can be thought of as the time taken by surface heat fluxes to aid the recovery of moisture and temperature anomalies, even though more complex processes, such as turbulent entrainment of air from above the boundary layer, can be at play. Numerical and observational studies indicate that this characteristic time ranges from 2, 2.5 to 3 h (Tompkins, 2001b; Ross et al., 2004; Kruse et al., 2022) and here we set τ_{cin} to 2.5 h.

Finally, to provide accurate estimates of K_{cin}, we recall that the motion of the cold pool is largely dictated by its head, a region of relatively deep fluid located in proximity to the gust front. Under the assumption of incompressible and inviscid flow regime for the density current, which allows to neglect viscous effects, the radially spreading velocity of the head, u, is given by the *von Kármán equation* (Benjamin, 1968; Huppert and Simpson, 1980):

$$u = \mathsf{Fr}\sqrt{g'H}, \tag{4.3}$$

where Fr is the *Froude number*, a constant expressing the ratio between inertial and buoyancy forces; $g' = \frac{\rho - \rho_0}{\rho_0} g$ is the *reduced gravity* that expresses the density contrast between the current (ρ) and the ambient fluid (ρ_0); H is the characteristic thickness of the current. Here we follow Kruse et al. (2022) in setting $\mathsf{Fr} = 0.7$ and in approximating the relative density variation in the reduced gravity with the relative temperature variation $\frac{T - T_0}{T_0}$. Taking $T - T_0 = -2$ K, $T_0 = 298$ K, and assuming H be approximately 500 m, if we combine the resulting value of u with the choice of r_{cin}, we obtain an estimate for K_{cin} on the order of 3×10^4 m^2 s^{-1}.

4.2.2 Impacts on aggregation

It is apparent that the inclusion of cold pools acts against organization, as it weakens the feedback between convection and water vapor, favouring the maintenance of uniformly distributed convection. The following Fig. 4.7a-e is to be compared with Fig. 3.1f-j, as the model and experiment setup is the same except for the cold pool convective inhibition effect accounted for in this case. It is seen that aggregation never establishes in Fig. 4.7.

For simulations that aggregate, cold pools enlarge the wet patches and also delay the clustering onset. This is shown in Fig. 4.8, which compares the evolution of two simulations with the model key parameters invariant and cold pools included (orange line) or not (blue). The final equilibrium states feature aggregation in both cases, but with some remarkable differences. Indeed, the reduced size of the wet region without cold pools accounted for translates into a much lower domain-mean R and R standard

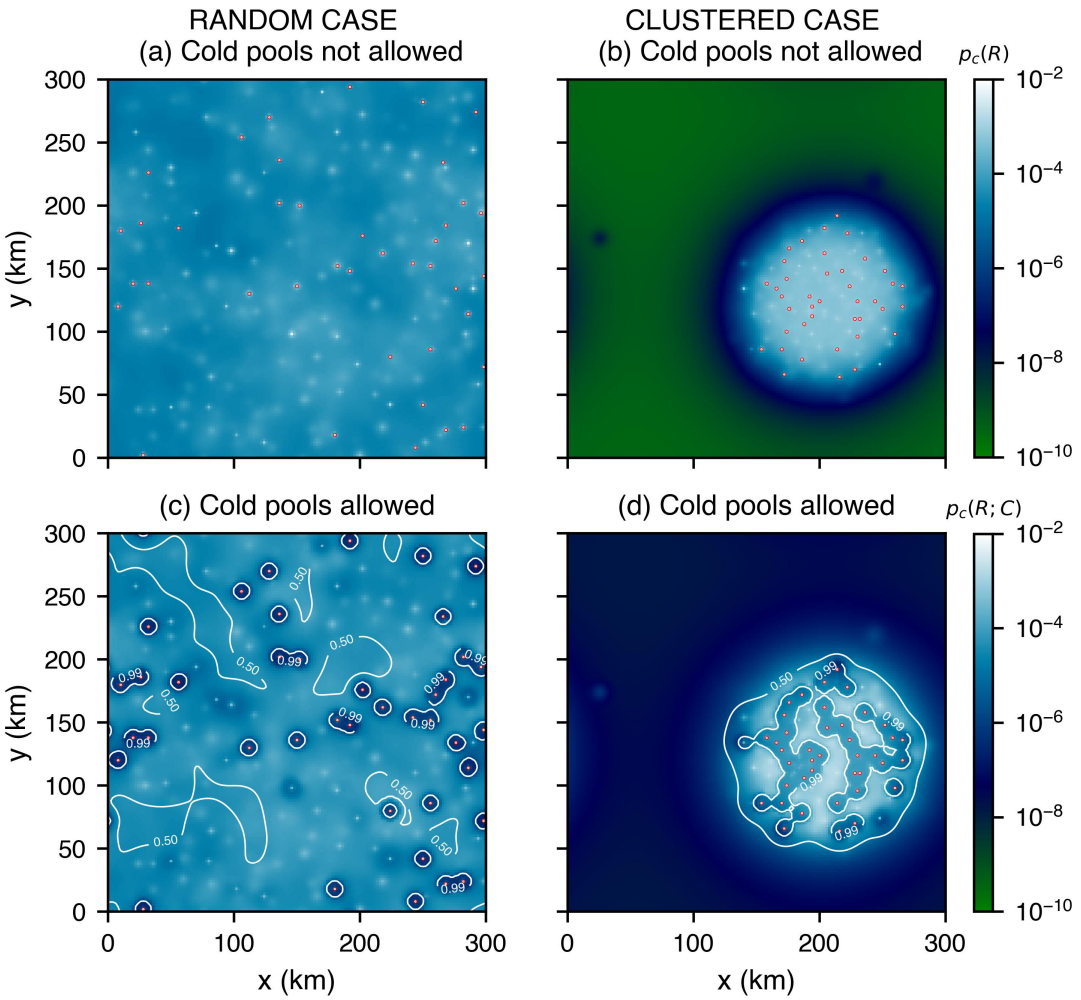

Figure 4.6: *Impact of cold pool convective inhibition effect on the probabilities (color shading) underlying the weighted random sampling to locate new convection. Shown are random (a,c) and clustered (b,d) convective states, both with (c,d) and without (a,b) cold pools included. Convectively active cells are represented as red dots, while the contours in (c,d) refer to the convective inhibition C.*

deviation and a much higher value of I_{org}, indicating very strong clustering. In case cold pools are included, I_{org} shows some tendencies towards regularity at the simulation outset, which was expected because of the inhibition effects that induce dispersion in the cloud field. The time of adjustment to equilibrium is also much longer. Another example is shown in an animation available at `http://clima-dods.ictp.it/Users/gbiagiol/CPs.mp4`.

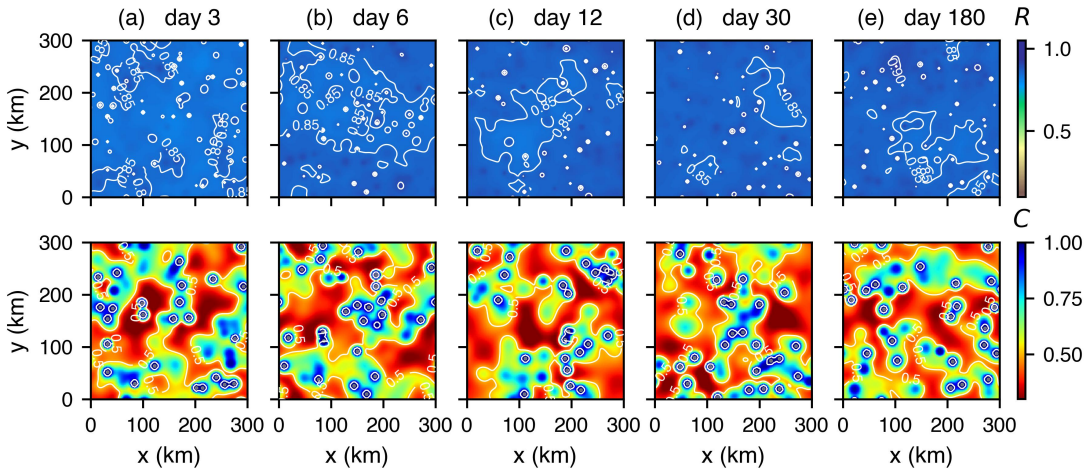

Figure 4.7: *Snapshots of the spatial R (a-e) and C (f-j) fields for a simulation with the same parameters and setup as experiment 0.5K (see Table 3.2), but with cold pool exclusivity effects accounted for and* $r_{cin} = 8.6\ km$, $\tau_{cin} = 2.5\ h$, $K_{cin} = 3 \times 10^4\ m^2\ s^{-1}$. *In panels (f-j), the active cells are marked as grey dots.*

It would be interesting to see whether in this case arguments similar to those used in Chapter 3 apply in order to derive a modified version of the aggregation number N_{ag}. Since the impact of cold pool exclusivity effects is in the probabilities to locate new convection, we expect some of the previous arguments still hold and modifications are possibly to be made with particular regard to the assessment of the role of the indicator random variable. We argue that the concept of area of influence and the assumption of homogeneity for the Poisson point process representing the updraft locations in the pre-onset phase should not be completely unreasonable, the latter at least in a time-averaged sense. A more systematic analysis is however to be conducted, which will be a topic of future work.

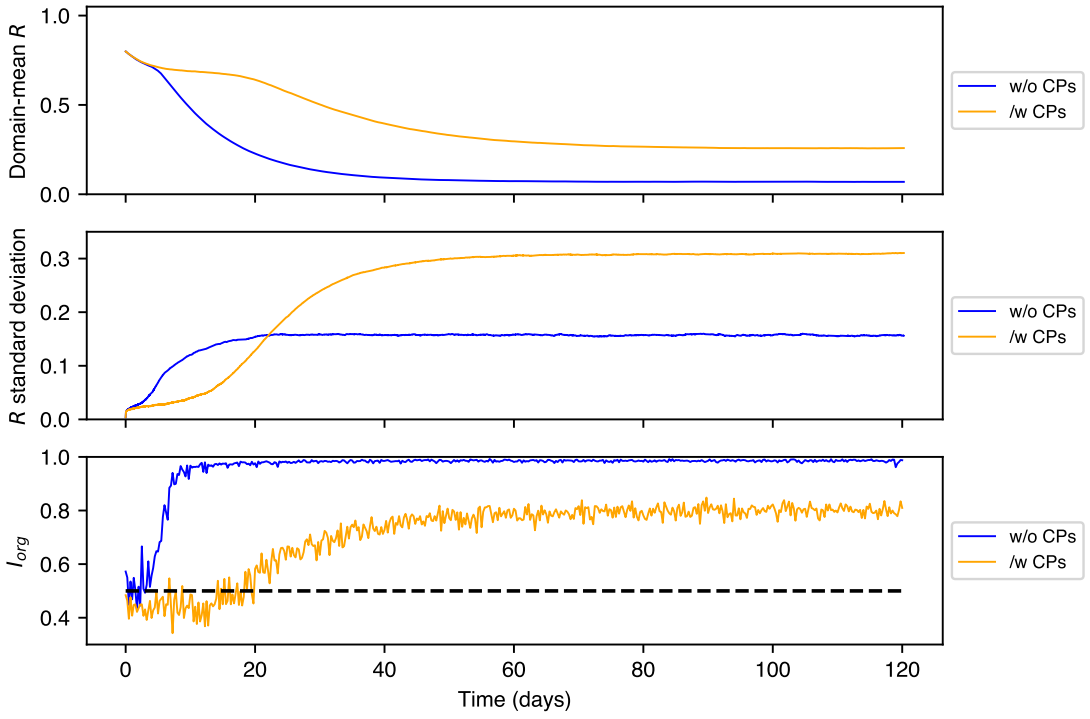

Figure 4.8: *Time evolution of the spatial R distribution, in terms of domain mean (upper panel) and standard deviation (middle panel), and the organization index I_{org} (lower panel) for two simulations with (orange line) and without (blue line) cold pool inhibition effects accounted for. The dashed line in the bottom panel marks $I_{org} = 0.5$, which is the value for a random distribution of convective cells. Here $K = 10^3\ m^2\ s^{-1}$, $K_{cin} = 3 \times 10^4\ m^2\ s^{-1}$, $\tau_{sub} = 10$ days, $\tau_{cin} = 2.5\ h$, $a_d = 14.72$ and $r_{cin} = 8.6\ km$, domain size and horizontal resolution are kept at their default values, $R_0 = 0.8$.*

Chapter 5

A revised index to measure the organization of deep convection

The focus of the previous chapters was on the phenomenon of deep convective self-aggregation, which may appear as an artifact of the models at a first glance. Parallel efforts to provide observational evidence of it have been made, but the problem is that, to detect and quantify its strength not just in observations but also within the models themselves, proper metrics are required. More generically, there is no consensus on what constitutes deep convective organization in practice, which means that there is little agreement in the literature on how to best measure it. This has led to the flourishing of a variety of aggregation metrics. They explore different aspects and signatures of the organization processes, not infrequently exhibiting opposite behavior and trends between each other.

In this chapter, we will first conduct a comprehensive review of the existing methodologies in an attempt to summarize the family of indices used to assess organization. Some of their drawbacks are highlighted, with the vast majority measuring organization only in a relative sense. One widely used metric in recent years, I_{org} (Tompkins and Semie, 2017), addresses this issue, but we will show that it is totally blind to organization beyond the β-mesoscale (20-200 km) and very contingent on the details of the implementation method, a source of concern for the analysis of present-generation precipitation or cloud retrievals.

We thus introduce a new and complementary metric based on all-pair (rather than nearest-neighbor) distances between convective clouds, which also measures organization in an absolute sense and accounts for inter-cluster spacings beyond the mesoscale. Additionally, the new index, L_{org}, is much more robust to the calculation details than I_{org}. Its use, demonstrated with idealized synthetic configurations as well as model output and satellite rainfall retrievals, suggests that the new metric can act as a useful supplement to the existing family of indices for measuring convective organization.

5.1 Review of previous contributions

In our literature review, we will divide the indices used to assess organization broadly into two genera. The first genus contains those metrics devised to account for the large-scale impacts of the organization, i.e., they focus on the evolution of relevant meteorological fields as aggregation progresses. Examples include analyzing the spatial variance of the column water vapor in some way, or the mean top-of-atmosphere OLR. A second genus of indices instead comprises object-based approaches, whose derivation involves the location of cloud entities or updrafts within a given field to then provide a measure of the extent to which these objects can be interpreted as scattered or clumped. In both cases, the indices are usually calculated from snapshots of a given variable(s), and their temporal evolution is considered. Since the first group detects the indirect impacts of aggregation rather than the direct measurement of convective clustering, we will refer to the two genera as *indirect* and *direct* organizational indices, respectively.

The indirect metrics are summarized in Table 5.1. They are intended to reflect some clear signatures of the self-aggregation process, such as the growth of dry patches with suppressed convection at the expense of moist ones and the ensuing transition towards a much larger variability in the spatial moisture field (cf. Fig. 3.2). We further divide this category to consider the humidity-related species as distinct from those based on other markers, e.g., OLR and large-scale vertical velocity. Note, however, that the derivation of metrics based on vertical velocity profiles may entail the analysis of three-dimensional fields which - moreover - are not directly available in observations. All these indices, with the exceptions of the interquartile ratio of WVP, the AFs, $F_{0.8\overline{P}}$ and ARH, take on higher values for more aggregated conditions.

One commonality of all of the indirect metrics is that they are all *relative*. They gauge relative aggregation comparing two scenes, classifying one as more or less clustered relative to the other. Taking the spatial variance and interquartile humidity ranges as an example, it might in theory be possible to derive the expected values associated with a random Poisson process in the distribution of updraft locations, but this would depend on the assumed physics such as convective precipitation efficiency and mixing, and thus in reality is not achieved. Without a theoretical random benchmark to compare to, it is not therefore possible with such metrics to classify scenes as regular, random or clustered.

These metrics are also affected by other factors in addition to the degree of convective organization, which implies that some of the indices may fail even in the task of measuring organization in a relative sense. For example, spatial humidity variability will also be a function of the mean atmospheric temperature and the local surface temperatures. This means that it is not straightforward to use such metrics to compare organization between two model experiments that use different sea surface temperatures SSTs for instance, or indeed between two different models as humidity variance will be impacted by details of their respective sub-grid parameterizations such as those for turbulence and microphysics in addition to their convective arrangements. These drawbacks mean the vast majority of such metrics have only been applied to model

simulations (not observations) to compare situations with identical boundary conditions.

A third weakness of some of these methods is their strong nonlinear behavior as a function of aggregation. For example, a pronounced increase in spatial variance of column humidity or moist static energy is frequently used to mark the onset of aggregation from random conditions (cf. Fig. 3.3). However, we demonstrated in Chapter 3 that, once aggregation is established, further enhancement of the clustered state leads to a reduction of variance. This nonlinear behavior and the non-existence of a 1-1 relationship between these variance metrics and aggregation implies that they are inappropriate to intercompare organized states between models for example.

Table 5.1: List of some indices related to the self-aggregation impacts on climate.

HUMDITY-BASED INDICES		
Index (name/acronym/symbol)	Definition/description	References
WVP interquartile ratio	Ratio of WVP in the driest quartile to WVP in the moistest quartile of grid columns	Bretherton et al. (2005)
Metric for intensity of aggregation σ	Difference in mean CRH between the moistest and driest quintiles of columns	Arnold and Randall (2015)
var$(\hat{h})$	Spatial variance of column-integrated frozen moist static energy	Wing and Cronin (2016)
var$(\mathcal{H})$	Spatial variance of CRH	Wing and Cronin (2016); Wing et al. (2020)
Column water vapor (CWV) interquartile range (IQR)	Difference between the 75^{th} and 25^{th} percentiles of horizontal CWV distribution	Holloway and Woolnough (2016); Holloway (2017)
CWV upper-quantile range (UQR)	Difference between the 95^{th} percentile and the median of horizontal CWV distribution	Holloway and Woolnough (2016); Holloway (2017)
Domain-mean vertical-average relative humidity (ARH)	Spatial mean of vertically-averaged, density-weighted relative humidity	Bao et al. (2017)
Degree of aggregation α	Coefficient of variation of CWV	Lebsock et al. (2017)
Degree of zonal convective clustering $S_\lambda(P)$	Zonal standard deviation of the meridionally (6S-6N) averaged precipitation, normalized by the mean 6S-6N precipitation	Popp and Bony (2019)
Convective organization index BLW	(Reciprocal of the) ratio of the length of the moist margin (separation boundary between moist and dry regions) to a theoretical minimum length	Beucler et al. (2020)
INDICES REPRESENTING OTHER SIGNATURES		

Index (name/acronym/symbol)	Definition/description	References
Mean outgoing longwave radiation (OLR)	Domain-mean OLR	Wing and Emanuel (2014)
Subsiding fraction (SF)	Area fraction of the domain covered by midtropospheric (500 hPa) descending motion	Coppin and Bony (2015); Wing et al. (2020)
Ascending fraction #1 (AF1)	Area fraction of the domain with midtropospheric vertical velocity $>$ domain-mean positive vertical velocity	Bao et al. (2017)
Ascending fraction #2 (AF2)	Area fraction of the domain with net upward mass-weighted vertical integral of vertical velocity	Bao et al. (2017)
Wavelet-based organization index (WOI) and local WOI (LWOI)	Analysis of wavelet energy spectra of rain rates to assess prevailing spatial scales, intensity and anisotropy of precipitation structures	Brune et al. (2018, 2020, 2021)
$F_{0.8\overline{P}}$	Minimum area fraction that accumulates 80% of total precipitation in the band 6S-6N	Popp and Bony (2019)

The second genus of direct metrics require the identification of cloud objects within a given scene and then making an assessment of the spatial relationship between these identified objects as summarized in Table 5.2. In theory, these approaches are versatile, as they can be applied to a range of meteorological variables that can identify cloud positions in either model simulation output or observational datasets. Deep convective entities can be located by imposing arbitrary thresholds on relevant fields used as proxies, such as OLR (White et al., 2018; Wing et al., 2018), infrared brightness temperature T_b (Tobin et al., 2012, 2013; Kadoya and Masunaga, 2018; Pscheidt et al., 2019; Bony et al., 2020), radar reflectivity (Pscheidt et al., 2019; Retsch et al., 2020; Radtke et al., 2022), precipitation (Pendergrass et al., 2016; Holloway, 2017; Bao et al., 2017), updraft velocities (Tompkins and Semie, 2017; Cronin and Wing, 2017), cold cloud optical depth and pressure (Xu et al., 2019).

However, in practice the challenge lies with the definition of distinct events. In models, high updraft velocity can discern convective cores, but updraft velocities are not available from present-generation satellite observations. Using proxies such as OLR or visible imagery can mean cloud overlap causing a merging of distinct convective events and thus confound the statistics, especially as some approaches use recursive algorithms based on four-connectivity (or eight if diagonals are included, e.g., Jin et al., 2022) clustering, that is, contiguous model/observation pixels meeting a given threshold are considered a single entity. Bony et al. (2020) tried to avoid this when identifying convective centers from observed T_b by using the local cold maxima if they were below 240 K with a filter applied to remove the impact of gravity waves.

From the direct indices, the precursor has been the Simple Convective Aggregation Index (SCAI) by Tobin et al. (2012, 2013), which takes into account the number of deep

convective objects within the domain and their degree of clumping. Its formulation is provided in Table 5.2 and lower values of SCAI represent higher degrees of aggregation, reflecting the view of the authors that convective organization intuitively corresponds to a small number of cloud systems that exist in close proximity to one another. One objection made to SCAI is the fact that it does not account for the size of the cloud objects (e.g., White et al., 2018; Xu et al., 2019; Retsch et al., 2020).

Several proposals have amended this: some, like the Modified Convective Aggregation Index (MCAI, Xu et al., 2019), are a variant of SCAI; while others are based on different principles and conceptual views of the organization process. In particular, inspired by the mathematical form of the gravitational interaction potential associated with a distribution of objects, White et al. (2018) defined the convective organization potential (COP) index as the arithmetic mean of the interaction potentials between all possible pairs of convective points in the scene. High values of COP, in turn resulting from small amounts of large, close-by objects, would represent more aggregated conditions. However, both Retsch et al. (2020) and Jin et al. (2022) pointed out that the definition of COP might not properly emphasize the size of the objects, proposing modifications to COP to assign greater weights to larger cloud elements, introducing the Radar Organization Metric (ROME) and the area-based COP (ABCOP), respectively.

Finally I_{org} was introduced that allows specific and quantitative categorization of scenes. Possibly due to this ability, it is perhaps the most widely used organizational index since its introduction for both model and observation studies. The index is based on the nearest-neighbor distances (NNDs) between convective events, and is broadly revisited in the following Section 5.2.

Table 5.2: List of some object-based organization metrics.

Index (name, acronym)	Formulation	Variable and threshold (references)	Remarks and pros/cons

Simple Convective Aggregation Index (SCAI)	$\boxed{\text{SCAI} = \frac{N}{N_{\max}} \frac{D_0}{D} \times 1000}$ N nr of clusters, D_0 geometric mean distance between cluster centroids, $N_{\max}$ half of total nr of pixels, D characteristic domain length.	$T_b \leq 240$ K (Tobin et al., 2012, 2013); Daily precipitation $P \geq P_{95}$ 95$^{\text{th}}$ percentile (Bao et al., 2017).	• Considers number of clusters and their grouping. • Geometric mean distance may not emphasize smaller inter-convective distances (White et al., 2018). • Variability in SCAI might reflect that of N (Tobin et al., 2013; White et al., 2018; Kadoya and Masunaga, 2018; Brune et al., 2018; Jin et al., 2022). • For fixed N, it might classify as less organized scenes with larger objects (Xu et al., 2019; Retsch et al., 2020). • Ill-defined for $N < 2$. • Size of the objects not accounted for.
Precipitation-based SCAI (SCAIP)	Same as SCAI.	Daily precipitation $P \geq 1.49$ mm day^{-1} (Holloway, 2017).	• Not suitable for comparing situations with significantly different domain-mean rainfall (Holloway, 2017).
Convective Aggregation Index (CAI)	$\boxed{\text{CAI} = \frac{ND_1}{T}}$ N nr of clusters, D_1 arithmetic mean distance between cluster centroids, T average event duration weighted by event size.	Daily precipitation $P \geq P_{99}$ 99$^{\text{th}}$ percentile (Pendergrass et al., 2016).	• Incorporates event duration. • Precipitation-based index (not OLR-based), which is preferable when analyzing global warming simulations.
Modified Convective Aggregation Index (MCAI)	Same as SCAI but with the arithmetic mean edge-to-edge cluster distance D_2 in place of D_0.	Cloud optical depth $\delta \geq 10$ and cloud top pressure ≤ 440 hPa (Xu et al., 2019)	• The modified measure of distance accounts for object sizes. • Very weak sensitivity of the aggregation level to the object sizes for fixed N (unlike SCAI). • Behaves as SCAI for small object area ranges, as COP for large object area ranges. • Largely dependent on N for tropical convective scenes at synoptic scales (Jin et al., 2022).

Convective Organization Potential (COP)	$$\mathrm{COP} = \binom{N}{2}^{-1} \sum_{i=1}^{N} \sum_{j=i+1}^{N} \frac{r_i + r_j}{d_{ij}}$$ N nr of clusters, r_i, r_j object area-equivalent radii, d_{ij} inter-centroid distance.	OLR, double thresholding approach (non-max suppression method), with 150 W m^{-2} and 175 W m^{-2} thresholds (White et al., 2018).	• Addresses some of the deficiencies of SCAI. • Assumes circular elements, which might not be the case in real situations (Brune et al., 2018). • It is self-similar (Retsch et al., 2020): COP does not change if size of convective entities and their separation distances are multiplied by a scalar value. • Ill-defined for $N < 2$. • Weak sensitivity to N (Xu et al., 2019). • Tends to overestimate the organization level for small N, to underestimate it for large N (Jin et al., 2022). • Strongly sensitive to the addition of small isolated objects (Jin et al., 2022).
Area-based COP (ABCOP)	$$\mathrm{ABCOP} = \sum_{i=1}^{N} \max_{\substack{j=1,\dots,N \\ j \neq i}} \frac{\frac{A_i + A_j}{2} \frac{1}{D^2}}{\frac{d_{2_{ij}}}{D}}$$ N nr of clusters, A_i, A_j object areas, $d_{2_{ij}}$ edge-to-edge distance (minimum value set to 1), D domain size.	Hourly precipitation data from IMERG (Jin et al., 2022).	• More sensitive than COP to object sizes. • Properly handles small, noisy isolated objects. • Highly organized configurations are those with large object surrounded by many satellite ones. • Application to a range of domain sizes: captures well known synoptic convective phenomena and works well for small domain scenes. • Defined also in cases with $N = 1$, but it could be unreasonably small. • Caution when comparing situations over domains with very different sizes. • Possibility of unphysical behavior for small domains.

Radar Organization Metric (ROME)	$$\mathrm{ROME} = \binom{N}{2}^{-1} \sum_{i=1}^{N} \sum_{j=i+1}^{N} \max\{A_i, A_j\} + \min\left\{1, \frac{\min\{A_i, A_j\}}{A_{d_{ij}}}\right\} \min\{A_i, A_j\}$$ N nr of clusters, A_i, A_j object areas, $A_{d_{ij}}$ area in-between	Radar reflectivity with the adoption of the Steiner et al. (1995)'s algorithm (Retsch et al., 2020).	• Defined also in cases with $N = 1$, in which ROME $= A_1$. • Good correspondence with intuitive concepts of organization (the presence of vast regions of convective activity is a sign of clustering). • Effective at reproducing the observed diurnal cycle of convective precipitation intensity in the tropical wet season months.
Organization index I_{org}	$$I_{\mathrm{org}} = \int_0^1 \hat{F}(F(r))\, dF$$ F and $\hat{F}$ cumulative distribution functions of the cloud-to-cloud nearest-neighbor distances for a homogeneous Poisson point process (eqn. (3.1)) and for the cloud field scene under consideration, r distance.	Vertical velocity w at 730 hPa > 1 m s^{-1} (Tompkins and Semie, 2017); cloud top temperature < 235 K (Cronin and Wing, 2017); hourly averaged w at 500 hPa > 0.5 m s^{-1} (Cronin and Wing, 2017); OLR < 173 W m^{-2} (Wing et al., 2018); precipitation $P \geq 2$ mm h^{-1} (Brune et al., 2018).	• Quantification of the organizational regime for each individual situation. • Size of the objects not accounted for. • Level of organization underestimated for configurations with large aggregates (Retsch et al., 2020; Jin et al., 2022). • No information about number, sizes and shapes of cloud objects (Pscheidt et al., 2019). • Noisy and difficult to interpret for small N (Brune et al., 2018; Pscheidt et al., 2019). • Strongly sensitive to noisy isolated convection (Jin et al., 2022).
Morphological Index of Convective Aggregation (MICA)	$$\mathrm{MICA} = \frac{\sum_{i=1}^{N} A_i}{A_{\mathrm{c}}} \frac{D - A_{\mathrm{c}}}{D}$$ N nr of clusters, A_c area of the minimum rectangle enclosing all cloud objects, D domain size.	$T_b \leq 240$ K (Kadoya and Masunaga, 2018).	• Although object-based, it accounts for clear signatures of self-aggregation, such as the presence of large clear-sky areas. • It performs well if clusters are concentrated in one single part of the domain. • It may not work properly with outliers existing far from the main group of aggregates (Kadoya and Masunaga, 2018) or with broadly scattered objects, as in tropical organization scenes at synoptic scales (Jin et al., 2022).

I_{shape}	$$I_{\text{shape}} = \frac{1}{N}\sum_{i=1}^{N}\frac{P_{\text{eq}_i}}{P_i}$$ N nr of clusters, P_i perimeter of i-th object, P_{eq_i} circumference of area-equal disc.	Radar reflectivity $\geq$ 30 dBz; $T_b \leq$ 240 K (Pscheidt et al., 2019).	• Gives the average 2D shape (more elongated/circular) of cloud objects within the scene. • To be used in combination with other indices to better characterize the organizational state.
Information entropy of maps of convective occurrence $\mathcal{H}$	$$\mathcal{H} = -\sum_{i=0}^{\mathcal{L}^2} p_i \log_2 p_i$$ $\mathcal{L}^2$ total number of grid points in a domain, p_i probability that in a scanning subdomain of i^2 points other (binary) values agree with the entry in the upper-left corner.	$T_b \leq$ 245 K + $\geq$ 1 pixel with $T_b \leq$ 220 K (Sullivan et al., 2019).	• Allows to concisely quantify the response of organized convection to dominant modes of climate variability (e.g., ENSO).

Since each index is designed to capture some specific aspect of the organization process, Pscheidt et al. (2019) suggested the use of a combination of indices to fully characterize the organizational state, for example distinguishing aggregated scenes with fewer but larger objects from those with more numerous but smaller objects, which could be the case of oceanic compared to continental organized convection (e.g., Xu et al., 2019; Jin et al., 2022). In this regard, Brune et al. (2018, 2020, 2021) characterized the degree of aggregation through discrete wavelet decomposition of rain rate fields and introduced indices, called the wavelet-based organization index (WOI) and the local WOI (LWOI), which inform about the dominant spatial scales and orientation of precipitation patterns and their spectral energies.

5.2 Revisiting I_{org} and relative I_{org}

5.2.1 Definition of I_{org} and RI_{org}

I_{org} has its roots in the work of Weger et al. (1992); Zhu et al. (1992); Lee et al. (1994); Nair et al. (1998), who analyzed the clouds in visible imagery and classified their organization based on the cumulative distribution function of nearest-neighbor distances between identified cloud "objects". The identification process of an "object" is very dependent on the type of field used and especially the spatial resolution. For very fine resolution vertical velocity fields from model simulations, or satellite imagery, in which a deep convective event may be very well resolved, horizontally adjacent convective cells must be counted as a single entity by using (often recursive) algorithms to identify connected updraft cells (e.g., Wielicki and Welch, 1986; Zhu et al., 1992; Machado and Rossow, 1993; Tompkins and Semie, 2017). This would not be advisable for scenes with coarser resolution that under-resolve convective events, for instance the $\mathcal{O}(10\,\text{km})$ Global Precipitation Measurement (GPM) rainfall retrievals (Huffman et al., 2020) or global climate models. Moreover, if the whole systems (i.e., including anvils) are identified for example using OLR retrievals, there can be superposition between individual

deep convective clouds. This can be avoided by imposing stringent selection criteria on relevant variables as the use of warm thresholds may even entail the risk of including unrelated cloudiness as belonging to the cluster (Roca et al., 2017; White et al., 2018; Sullivan et al., 2019; Bony et al., 2020).

Given a cloud field, the NNCDF derived from the distribution of objects in the scene, referred to as the observed or simulated NNCDF, $\hat{F}$, is determined by calculating, for each updraft center, the distance to the closest object. If cyclic boundaries are imposed, as is the case in CRM simulations of RCE, the classical euclidean metric has to be replaced by a toroidal one. These observed NNCDFs are compared to a reference theoretical NNCDF expected from the theory if the same number of objects were *randomly distributed* within the domain. Similar analyses of the joint distributions were also carried out by Benner and Curry (1998); Craig and Cohen (2006).

The homogeneous Poisson point process reference model for the location of updraft cores implies that the cumulative distribution function of the nearest-neighbor distances between convective points follows the Weibull distribution (3.1). Given a point of the pattern, $F(r)$ is the probability of the nearest object falling within a circle of radius r centered at the base element. Alternatively, one could also employ the point-to-neighbor statistics, in particular the point-to-cloud cumulative distribution function (PCCDF), which obeys the same law as (3.1) (Weger et al., 1992) due to the memoryless property of the exponential (Moltchanov, 2012), but this approach will not be considered here.

If the graph of the theoretical versus simulated NNCDFs lies on the 1-1 identity line, the observed distribution matches the one that would be expected if the objects were randomly arranged, hence the cloud centers are deemed to be perfectly randomly distributed over all spatial scales (Fig. 5.1a). If the graph of the joint NNCDF lies above the identity line, the corresponding process is designated as clustered, because for a given value of NND there are more pairs than expected with the Poisson process, hence the observed nearest-neighbor distance distribution function will be larger than eqn. (3.1) (Fig. 5.1b). Vice versa, if the joint NNCDF graph lies below the 1-1 line, the scene is regular since, for a given NND, there are less nearest-neighbor pairs than expected for the Poisson distribution and the observed NNCDF is smaller than eqn. (3.1) (Fig. 5.1c). The joint NNCDF can provide information concerning the spatial scales of convection, for example, Tompkins and Semie (2017) showed convection was regular at spatial scales inferior to 16-18 km, and clustered over larger scales.

Tompkins and Semie (2017) then converted the joint NNCDF into a single index I_{org} by integrating the area under the joint NNCDF graph:

$$I_{\text{org}} = \int_0^1 \hat{F}(F(r))\, dF.$$

The index was preceded by the analysis of trade-wind cumulus fields in large-eddy simulation experiments by Seifert and Heus (2013), who examined the integral departure of the observed NNCDF relative to the theoretical one. We therefore term the

unnamed metric proposed by Seifert and Heus (2013) the *relative* I_{org}, or RI_{org}, which is

$$RI_{\text{org}} = \int_0^1 \left(\hat{F}(F(r)) - F(F(r))\right)\, dF = \int_0^1 \hat{F}(F(r))\, dF - 0.5 = I_{\text{org}} - 0.5.$$

For these indices, the integration is performed numerically, by means of the trapezoidal rule. $RI_{\text{org}} = 0$ corresponds to randomly distributed clouds (Fig. 5.1a, equivalent to $I_{\text{org}} = 0.5$), while $RI_{\text{org}} > 0$ refers to clustering ($I_{\text{org}} > 0.5$), and $RI_{\text{org}} < 0$ to regularity ($I_{\text{org}} < 0.5$) as shown in Fig. 5.1b,c. In conclusion, analogous to the other object-based indices, the calculation of I_{org} and RI_{org} takes as input a two-dimensional binary matrix (entries equal to 1 in the convective pixels, 0 elsewhere) resulting from the application of specific selection criteria, and outputs a value that measures the organization level. For ease of comparison with the new index developed in Section 5.3, we shall show RI_{org} hereafter, but the conclusions made about spatial scales and drawbacks of the index are obviously identical for both I_{org} and RI_{org}.

When the number of cloud objects is small, deviations from complete spatial randomness (CSR) must be tested for statistical significance in order to validate whether any regularity or clustering signal suggested by the joint CDF is relevant. In the following, we therefore generate a large number (400) of realizations by means of a random number generator with the same sample size as in the observed case, and then compute the 2.5^{th} and the 97.5^{th} percentiles of $\hat{F}$ for each r within the range of NNDs. The upper and lower bounds of this 95% confidence envelope serve to indicate where significant clustering or regularity begins; if, for each r, the sample statistic lies within the confidence interval, then the corresponding scene cannot be differentiated from randomness.

5.2.2 The organization irregularity index, OII

The fact that RI_{org} is an integrated quantity means that the organization at specific scales can not be determined. $RI_{\text{org}} = 0$ does not guarantee that the convective activity is randomly distributed in space over all scales; rather, it might result from the superposition of, e.g., regular and clustered sub-distributions (Fig. 5.1d). It is not uncommon to have real cloud fields that manifest the coexistence of multiple categories of organization, because clouds of different sizes may exhibit different spatial structures (Weger et al., 1992; Zhu et al., 1992). This is the case of boundary layer cloudiness, i.e., fair weather cumulus (Zhu et al., 1992; Weger et al., 1993; Nair et al., 1998) and stratocumulus cloud distributions (Lee et al., 1994). In our synthetic example, a crossover of the diagonal is clearly visible in the NNCDF plot (Fig. 5.1d, right panel), with clustering at small scales and regularity at large scales, despite the mean index value of zero. The value of RI_{org} should be supplemented by careful analysis of the joint NNCDF. To summarize the departure from randomness, we introduce a second index, the organization irregularity index (OII), which is defined as the root-mean-square error (RMSE) of $\hat{F}$ with respect to F:

$$OII = \sqrt{\int_0^1 \left(\hat{F}(F(r)) - F(F(r))\right)^2 dF}.$$

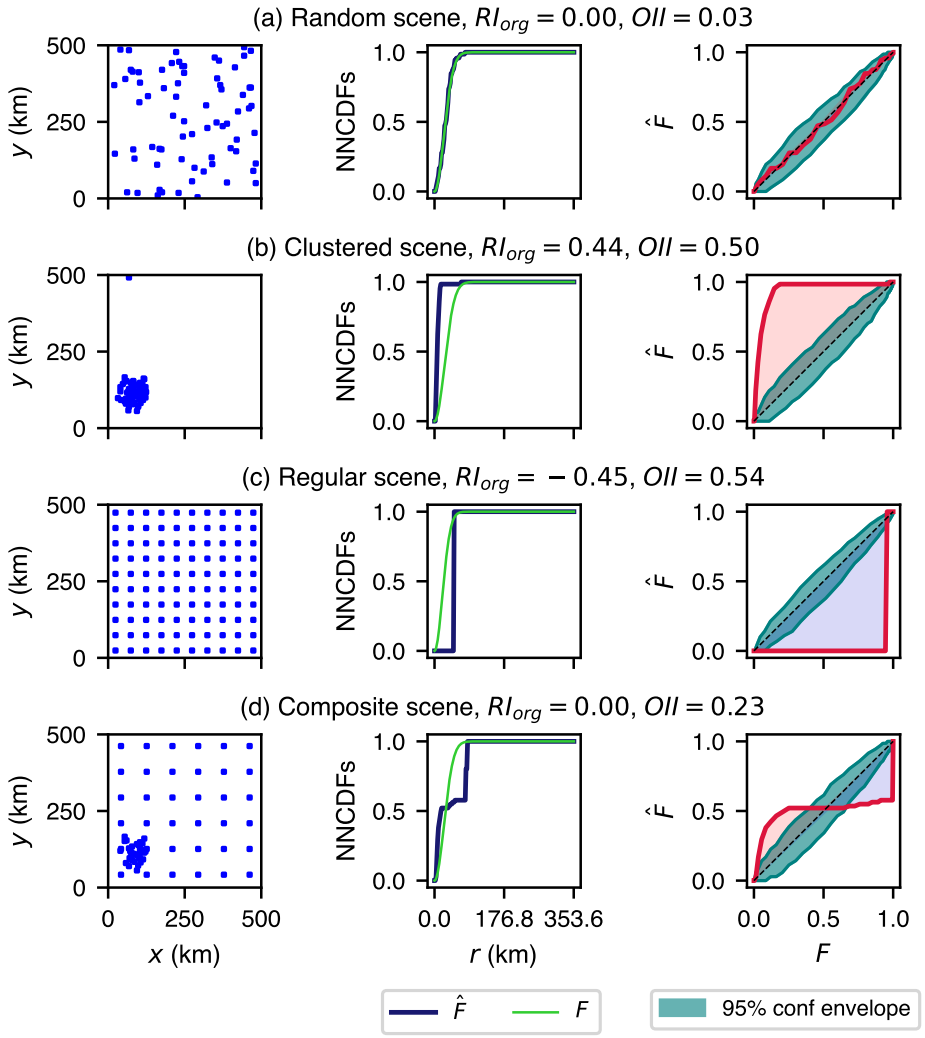

Figure 5.1: *Series of synthetic configurations with cloud centers showing random (a), clustered (b), regular (c) spatial structures and a clustered subregion embedded in a regular background (d), along with the related nearest-neighbor distance distribution functions (blue lines in the middle column) compared to the reference of random organization for the same number of points of the process (that is, eqn.* (3.1)*, green line). For each scene, the corresponding plot of Weibull vs simulated NNCDF is included (red line), with the identity line represented as a dashed line in the right panels. The cyan shading refers to the* 95% *confidence envelope for CSR. The red and blue shaded areas count as positive and negative integrals respectively in the calculation of* RI_{org}*. In (a) and (d), the value of the organization irregularity index (OII) is provided (see Section 5.2.2 for details). The domain is* 500×500 km^2*, with cyclic boundaries and resolution* $\Delta x = 2$ *km, while the number* N_c *of points is* $N_c = 72$ *(a,b,d),* $N_c = 100$ *(c).*

OII can take values from zero (distribution is random at all spatial scales) to $1/\sqrt{3}$ (distribution's departure from randomness is maximum). Thus RI_{org} and OII effectively describe two moments of the organization, summarizing the mean and a measure of the variance of the organization across spatial scales, respectively.

5.2.3 Inhibition effects

The choice of modeling the cloud field spatial structure as a point process, as assumed in the derivation of RI_{org} may lead to inaccuracies. In both numerical simulations and satellite/radar imagery, the deep convective entities are finite-size rather than punctiform, and this poses a constraint on the minimum inter-convective distance r_0 (Stoyan et al., 2013). Such a constraint is the more severe the larger the total fractional cloudiness ϵ, related to either increased cloud number and/or cloud size, because the possible positions over which the constituent objects of the pattern can be located are reduced. This inhibition effect is particularly pronounced for the nearest-neighbor statistics, as it can alter the cumulative probabilities for small NNDs (Fig. 5.2b), impairing any possible interpretation of the NNCDF plot. Indeed, while $\hat{F}(r) = 0$ for $r < r_0$, $F(r) = 0$ if and only if $r = 0$. A strong regularity signal is imposed (Fig. 5.2c), with the joint curve (red) lying irreversibly below the identity line (dashed), instead of being coincident. The distortion can be significant even when the cumulus fraction is about 1% (not shown).

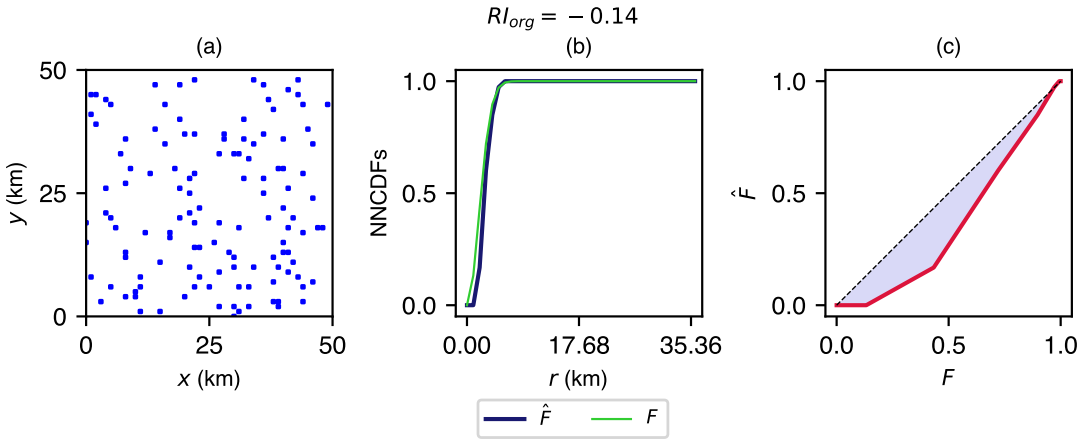

Figure 5.2: *(a) Generation of a scene with $N_c = 125$ randomly distributed points over a doubly-periodic square domain with size $D = 50$ km and resolution $\Delta x = 1$ km ($\epsilon = 0.05$). (b, c) Inhibition effects due to finite cloud sizes. In (c), the blue shaded area represents the integral deviation $\hat{F} - F$ that gives RI_{org}.*

To reduce this effect, one may treat the objects as discs and consider the edge-to-edge rather than inter-centroid distances between them, as suggested by Weger et al. (1992); Nair et al. (1998); Pscheidt et al. (2019). This would also make the nearest-

neighbor index sensitive to the size of the objects, somehow addressing the most important criticism made against it (e.g., Retsch et al., 2020; Jin et al., 2022). Indeed the index can provide a counterintuitive indication of low degrees of organization for patterns featuring the presence of large aggregates, since their centroids might be further apart. However, if the edge-to-edge distances are considered, a theoretical model for the random case is no longer available and the Weibull NNCDF (3.1) has to be replaced by an estimated one, resulting from the generation of configurations in which the same objects as in the observed scene are randomly distributed. For this lack of theoretical null, we prefer not to use this approach here.

5.2.4 Spatial scales of $RI_{\mathbf{org}}$

The NND statistics that underlie the calculation of RI_{org} can provide information concerning the spatial scales over which convection is clustered, random or aggregated. However, due to the exponential form of the Weibull CDF (3.1), RI_{org} does not assess organization linearly across spatial scales (Fig. 5.3) and no mathematical derivation has been provided for the mean scale that RI_{org} measures organization over. Bony et al. (2020) analyzed statistics of NNDs of tropical deep convection identified in T_b and inferred that the nearest-neighbor connectivity metric measures clustering on the $\mathcal{O}(100\,\text{km})$ β-mesoscale, according to the subdivision of scales by Orlanski (1975). One of the aims of this section is to derive the mean spatial scale of RI_{org} analytically.

We denote the mean spatial scale associated with a point pattern when analyzed in terms of the relationships of each object to its close neighborhood by $\lambda_{RI_{\text{org}}}$. If a random variable X is distributed according to a Weibull law, let Y be the truncated variable with support limited to $[0, r_{\max}]$, i.e., $Y = X|(0 \leq X \leq r_{\max})$, $r_{\max}$ being the maximal nearest-neighbor distance within a domain of characteristic length D. This is the case encountered in practical applications, in which finite study areas are considered and $r_{\max} = D/\sqrt{2}$ if periodic lateral boundary conditions are applied, $r_{\max} = D\sqrt{2}$ if open lateral boundary conditions are assigned. The definition of conditional probability implies that the probability density function $f_Y(y)$ obeys $f_Y(y) = \dfrac{f_X(y)}{p(X \leq r_{\max})}$, where $p(\cdot)$ denotes the probability of an event. Let $\mathbb{E}(Y)$ be the expectation of Y, then $\lambda_{RI_{\text{org}}} = \mathbb{E}(Y)$ and

$$
\begin{aligned}
\lambda_{RI_{\text{org}}} &= \left(1 - e^{-\lambda\pi r_{\max}^2}\right)^{-1} \int_0^{r_{\max}} r 2\lambda\pi r e^{-\lambda\pi r^2}\, dr \\
&= \left(1 - e^{-\lambda\pi r_{\max}^2}\right)^{-1} \left(-r e^{-\lambda\pi r^2} \Big|_{r=0}^{r=r_{\max}} + \int_0^{r_{\max}} e^{-\lambda\pi r^2}\, dr \right) \\
&= \left(1 - e^{-\lambda\pi r_{\max}^2}\right)^{-1} \left(-r_{\max} e^{-\lambda\pi r_{\max}^2} + (\lambda\pi)^{-\frac{1}{2}} \int_0^{\sqrt{\lambda\pi} r_{\max}} e^{-t^2}\, dt \right) \\
&= \left(1 - e^{-\lambda\pi r_{\max}^2}\right)^{-1} \left(-r_{\max} e^{-\lambda\pi r_{\max}^2} + (4\lambda)^{-\frac{1}{2}} \operatorname{erf}\left(\sqrt{\lambda\pi} r_{\max}\right) \right),
\end{aligned}
\tag{5.1}
$$

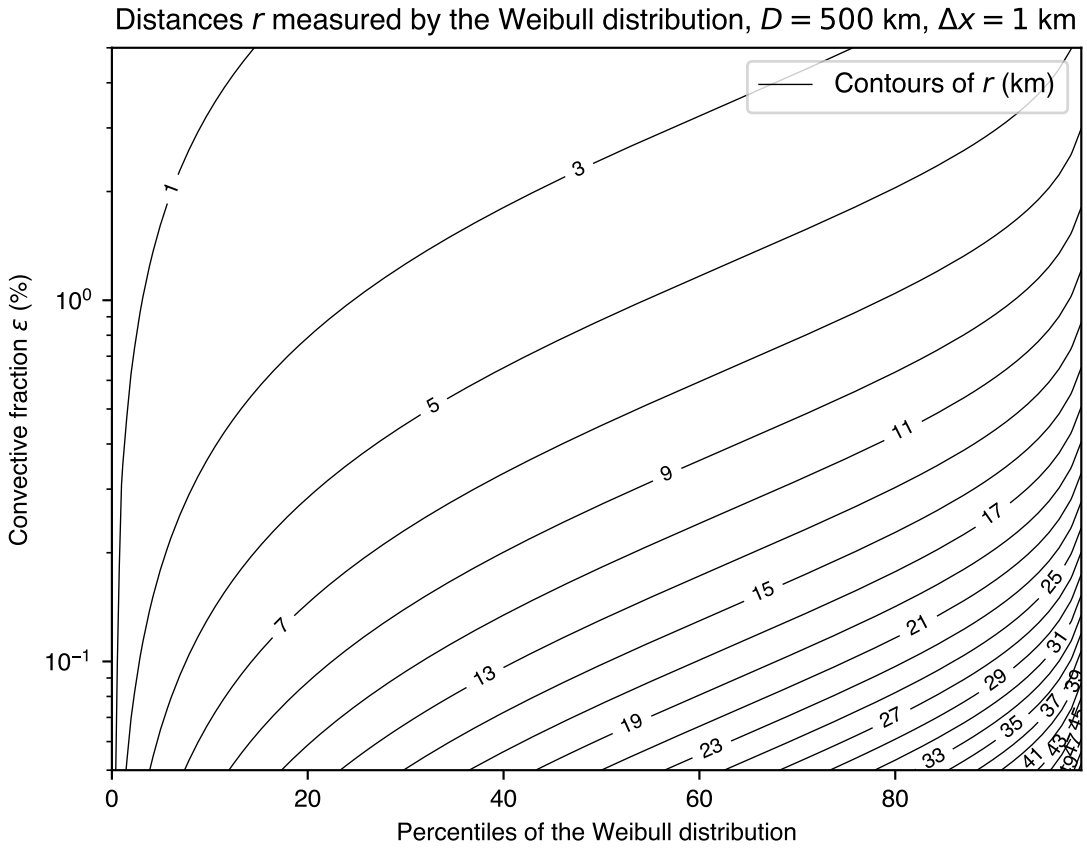

Figure 5.3: *Contours of the spatial scales over which the Weibull distribution measures organization, shown as multiples of the grid spacing $\Delta x = 1$ km for a case with $D = 500$ km and convective fractions ϵ as reported on the y-axis.*

where erf is the error function, $\text{erf}(z) = \frac{2}{\sqrt{\pi}} \int_0^z e^{-t^2}\, dt$. In principle, with the Poisson law, unbounded regions are considered, hence as $r_{\max} \to \infty$ and we recover the well known $\frac{1}{2\sqrt{\lambda}}$ limit for the Weibull distribution. In practical cases, however, it is sufficient that $r_{\max} \gg (\pi\lambda)^{-\frac{1}{2}}$ for the limit to be a good approximation, usually the case for cloud resolving model simulations of radiative-convective equilibrium where the updraft core fractions is $\epsilon < 1\%$ (Craig, 1996; Tompkins and Craig, 1998a).

Eqn. (5.1) proves that the mean spatial scale associated with the analysis of the nearest-neighbor distance distribution is related to the inverse of the density of convective events/entities. Also, all the spatial scales that much exceed $(\lambda\pi)^{-\frac{1}{2}}$ have very little influence on the values of the Weibull CDF (hence on RI_{org}), which is instead controlled by mesoscale organization of convection and neglects long-range interactions between the constituent objects of the pattern. It is already well known that the nearest-neighbor and the point-to-neighbor statistics are dominated by short-range inter-point spacings

and say little about the elements over scales beyond (Illian et al., 2008). This is confirmed by Fig. 5.4, which shows two configurations, both consisting of the presence of four clusters, but characterized by different large-scale arrangements of those clusters. In Fig. 5.4(a) the inter-cluster distance is less that that in panel (b), but the organization index does not capture this difference (i.e., $RI_{\text{org}} = 0.33$ in both cases) because it is only impacted by sub-cluster distances and the cloud field is designed so that each pair of neighboring points belongs to the same cluster. For the number of events and the domain size employed here, the mean spatial scale associated with the value of RI_{org} is $\lambda_{RI_{\text{org}}} \sim 15$ km.

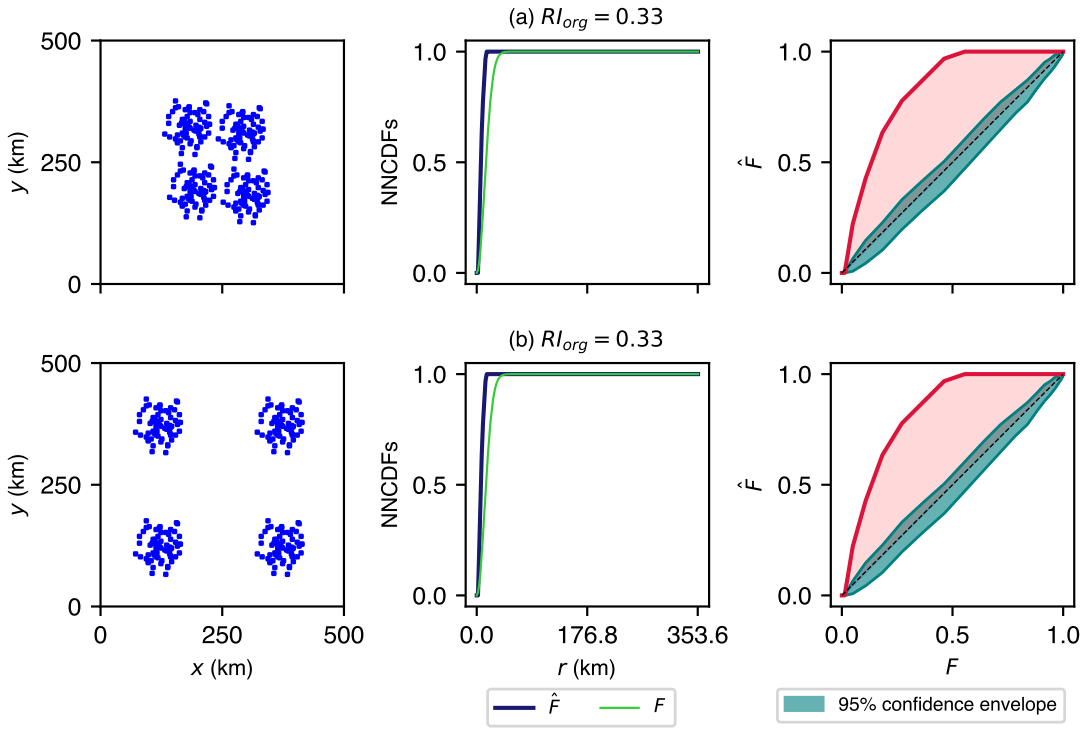

Figure 5.4: *(left) Sets of points featuring small-scale clustering (a,b) and large-scale clustering (a) and regularity (b), over a doubly-periodic* 500*km square domain with resolution* $\Delta x = 2$ *km; (center) observed NNCDF of cloud centers compared to the theoretical expectation for a random distribution of the same number of points; (right) plots of the Poisson vs simulated NNCDFs, with the cyan and red shadings representing a* 95% *confidence interval for CSR and the integral deviation* $\hat{F} - F$ *that gives* RI_{org}.

5.2.5 RI_{org} scales in tropical rainfall fields

The mean spatial scale of RI_{org} can be investigated more systematically as a function of the scene scale (namely, the size of the observation window). This can be carried out by

analyzing observational data, provided that a proxy for the amount of deep convective activity is selected. Here we make use of rainfall values obtained from the GPM data, which have a spatial resolution of $0.1^\circ \times 0.1^\circ$ and a temporal resolution of 30 minutes. To detect convective areas, we set a precipitation threshold of 8 mm h^{-1}: only the pixels whose rainfall rate exceeds the minimum value are flagged as convective.

There is no broad consensus in the literature about the partitioning criteria between stratiform and convective precipitation, as relatively different rain-rate thresholds have been imposed in past studies, ranging from 6 mm h^{-1} (Johnson and Hamilton, 1988) to 20 mm h^{-1} (Houze jr., 1973; Churchill and Houze, 1984), 22 mm h^{-1} (Tao et al., 2000), 25 mm h^{-1} (Tao et al., 1993; Xu, 1995), with the threshold likely a function of dataset resolution. In some cases, the threshold is not fixed, but allowed to vary, e.g., between 10 and 25 mm h^{-1} (Lang et al., 2003). Moreover, Yang and Nesbitt (2014) found convective rain pixels with intensities far below those discussed above (in some cases as low as 2 mm h^{-1}) in their analysis of Tropical Rainfall Measuring Mission (TRMM) precipitation radar data, but specified that, in general, the convective rain intensity is larger than 5 mm h^{-1}, partly consistent with previous results (e.g., Schumacher and Houze, 2003).

Our analysis is conducted for a single scene (Fig. 5.5a) by gradually enlarging some given square observation regions in the tropics (yellow boxes) to cover an area of $60^\circ \times 60^\circ$ (red). Shown in Fig. 5.5b is the mean RI_{org} lengthscale, $\lambda_{RI_{\text{org}}}$, as a function of the window size D for the three domains D1, D2 and D3. In some regions there is a weak trend of the RI_{org} scale with increasing domain size, but in all cases $\lambda_{RI_{\text{org}}} \ll D$. The typical range of $\lambda_{RI_{\text{org}}}$ values for these scenes ranges from 40-125 km and belongs to the β-mesoscale (20-200 km, Orlanski, 1975), confirming the conclusions of Bony et al. (2020) based on observed NNDs. These findings provide further evidence for the need to "broaden the horizons" of organizational indices and develop a new metric that can measure aggregation quantitatively beyond the β-mesoscale.

5.3 A new organization index L_{org}

5.3.1 Continuous case

Instead of using nearest-neighbor distances, the new indices derived in the present thesis adopt an all-neighbor connectivity approach. The spatial structure of cloud fields as a whole and the related scales can be determined through the *Ripley's K-function*, which is essentially based on the counting of neighbors within a certain distance of a convective event of the scene (Ripley, 1976, 1977, 1981). Although widely employed in plant ecology and forestry (e.g., Haase, 1995), this method has already been used in the context of meteorological applications (e.g., Chan et al., 2013). Similar techniques were also adopted by Nair et al. (1998); Cohen and Craig (2006) to evaluate the spatial trends of a cloud field scene. In particular, they considered the mean local cloud number density in annular regions centered at each cloud centroid, as a function of the radial distance r from the centroid itself, and then compared the resulting profile to that expected from

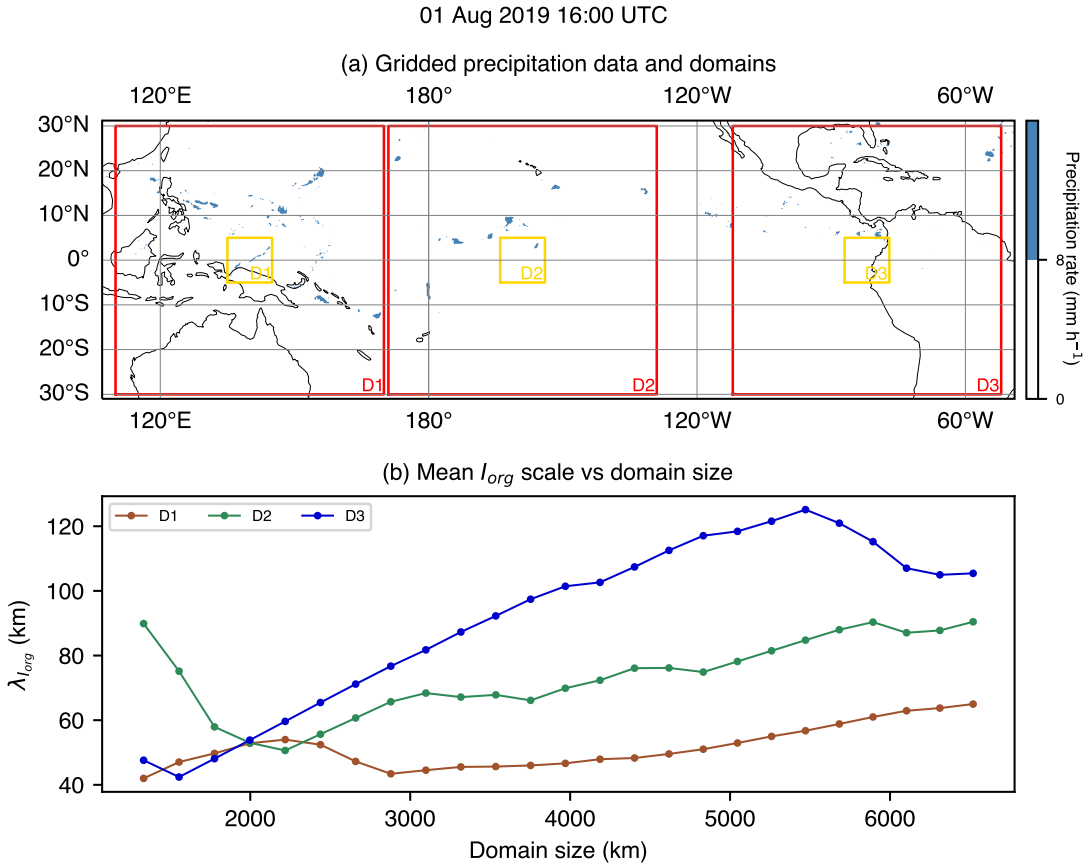

Figure 5.5: *Determination of the mean spatial scale associated with RI_{org}, $\lambda_{RI_{org}}$, in terms of the size of the study area (b) for a set of observations taken from a snapshot (a) from the GPM data set. The analysis is carried out over increasingly large regions (from the yellow to the red ones) whose size D has been incremented by 2° at a time. The convective points are those with rain rate exceeding a minimum threshold (8 mm h^{-1}).*

a Poisson process.

Formally the Ripley's function, $K = K(r)$, is defined so that the quantity $\lambda K(r)$ represents the mean number of neighbors of a typical point $\mathbf{x}$ lying in the disc $b(\mathbf{x}, r)$ of radius r centered at $\mathbf{x}$ (Fig. 5.6a), i.e.,

$$\lambda K(r) = \mathbb{E}\left(N\left(b\left(\mathbf{x}, r\right) \setminus \{\mathbf{x}\}\right)\right), \tag{5.2}$$

with $\mathbb{E}(\cdot)$ denoting the expectation and $N(\cdot)$ the random number of points of the process in a bounded set. Note that self-exclusion is assumed when counting the neighbors of $\mathbf{x}$.

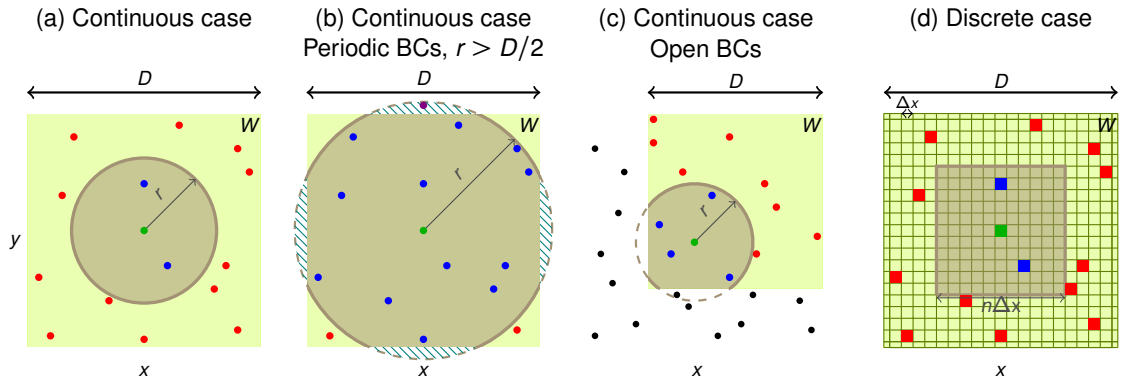

Figure 5.6: *Neighbor counting over continuous domains (a,b,c) and discrete grids (d). The base event* $\mathbf{x}_i$ *is marked as a green dot/cell; the cloud centers belonging to the search disc/box (grey shading) are shown as blue, while the other elements of the pattern contained in the observation window* W *(light green shading) are red. If the search radius* $r > D/2$ *(b), the purple point in the hatched circular segments has to be excluded from the counting, as it has already been included when cyclic boundaries are imposed. The case of open domains (c) is that of a pattern that can be assumed infinite (black dots), but with observations only available over* W*. The grey shading in (c) also represents the fractional area of* $b(\mathbf{x}_i, r)$ *inside* W *that appears in eqn.* (5.9)*. In the discretized domain (d), the doubly-periodic nature is accounted for.*

For the homogeneous Poisson process, by definition,

$$\begin{aligned}\mathbb{E}\left(N\left(b\left(\mathbf{x},r\right)\setminus\{\mathbf{x}\}\right)\right) &= \sum_{k=0}^{\infty} k e^{-\lambda\pi r^2}\frac{\left(\lambda\pi r^2\right)^k}{k!} = e^{-\lambda\pi r^2}\sum_{k=1}^{\infty} k\frac{\left(\lambda\pi r^2\right)^k}{k!}\\ &= \lambda\pi r^2 e^{-\lambda\pi r^2}\sum_{k=1}^{\infty}\frac{\left(\lambda\pi r^2\right)^{k-1}}{(k-1)!} = \lambda\pi r^2 e^{-\lambda\pi r^2}\sum_{k=0}^{\infty}\frac{\left(\lambda\pi r^2\right)^k}{k!}\\ &= \lambda\pi r^2 e^{-\lambda\pi r^2}e^{\lambda\pi r^2} = \lambda\pi r^2,\end{aligned}$$

hence

$$K(r) = \pi r^2. \tag{5.3}$$

We also introduce the area-normalized K-function, known as the *Besag's L-function* (Besag, 1977) and given by

$$L(r) = \sqrt{\frac{K(r)}{\pi}}. \tag{5.4}$$

In view of (5.3), in the homogeneous Poisson case, eqn. (5.4) reduces to

$$L(r) = \sqrt{\frac{\pi r^2}{\pi}} = r. \tag{5.5}$$

Unlike metrics based on the NNCDF or PCCDF, the Ripley's and Besag's functions are not "short-sighted" as they are based on all-point interactions.

Similar to the procedure for computing RI_{org}, given any scene we can compare two different L-functions, i.e., the one derived from the distribution of the objects within that scene, which will be referred to as the observed or simulated L-function, $\hat{L}(r)$, and the theoretical random one eqn. (5.5). If the convective events occur in space as a Poisson process, then $\hat{L}(r)$ is approximately equal to r. For clustered situations $\hat{L}(r) > r$, which is ultimately due to the fact that, on average, for a given distance r from any typical point, more objects are found than expected with the Poisson process. The reverse is true for regular fields, in which case $\hat{L}(r) < r$. We must ascertain, however, whether any observed indication of clustering/regularity is statistically significant. Ripley (1979) and Getis and Franklin (1987) provided approximations of the 0.05 and 0.01 point levels of significance for rejection of the homogeneous Poisson process null hypothesis; nevertheless here, following Haase (1995), we determine the 95% confidence envelopes by generating a large number (400) of random patterns with the same number of objects as the observed scene and then computing the 2.5^{th} and 97.5^{th} percentiles of $\hat{L}(r)$ for each r within the range of possible distances.

While the theoretical null eqn. (5.5) assumes an infinite point pattern, in practice model output and observations are only available over finite regions W containing a finite number N_c of cloud elements. For a given realization of a point pattern, the estimator for the Besag's function is defined as

$$\hat{L}(r) = \sqrt{\frac{1}{\pi\hat{\lambda}}\frac{1}{N_c}\sum_{i=1}^{N_c} w_i(r)\sum_{\substack{j=1,\\ j\neq i}}^{N_c}\delta_{ij}(r)} = \sqrt{\frac{\nu(W)}{\pi N_c\,(N_c-1)}\sum_{i=1}^{N_c} w_i(r)\sum_{\substack{j=1,\\ j\neq i}}^{N_c}\delta_{ij}(r)}, \tag{5.6}$$

where $\delta_{ij}(r)$ is an indicator function, $\delta_{ij}(r) = 1$ if the separation distance d_{ij} between points $\mathbf{x}_i$ and $\mathbf{x}_j$ is such that $d_{ij} \leq r$, zero otherwise; $\hat{\lambda}$ is the unbiased estimator of the average spatial density of events, $\hat{\lambda} = (N_c - 1)/\nu(W)$. To allow for the correction of edge effects in case of open domains, $w_i(r)$ are weighting factors applied to the event count $\sum_{j\neq i}\delta_{ij}(r)$, cf. Section 5.3.2. For periodic domains with cyclic boundaries, $w_i(r) = 1$.

Eqn. (5.6) allows to summarize the spatial trends of a point pattern over W or given subregions of W. This approach is in fact estremely flexible as one can choose the desired range of distances $0 \leq r \leq r_{\max}$ over which to compute the L-functions, $r_{\max}$ being the maximal distance between points within the selected region. It is possible to normalize both the distance r and the Besag's functions by $r_{\max}$ and we label $z = r_{\max}^{-1} r$, $\bar{L}$ and $\bar{\hat{L}}$ the rescaled coordinate and L-functions, respectively. We first consider the case of square domains of size D, both cyclic and open; applications to rectangular regions will be dealt with in Section 5.3.4.

The estimate (5.6), normalized by $r_{\max}$, is compared to the rescaled function $\bar{L}(z) = z$ theoretically expected in case of CSR. We can then introduce a new index L_{org}, which is now linear in z (hence r) and is defined as the integral of $\bar{\hat{L}} - \bar{L}$ with respect to z, i.e., the area under $\bar{\hat{L}} - \bar{L}$:

$$L_{\text{org}} = \int_0^1 \left(\bar{\hat{L}}(z) - \bar{L}(z)\right)\, dz. \tag{5.7}$$

We perform the integration numerically, by means of the trapezoidal rule. Values of L_{org} equal to, larger or lower than zero correspond to random, clustered or regular configurations, respectively. As with RI_{org}, the value of L_{org} is an average over spatial scales and there may occur cancellation between clustering and regularity (cf. Fig. 5.7c). To discern between pure randomness and composite cases, we therefore again consider the organization irregularity index, which is now defined as the RMSE of $\bar{\hat{L}}$ with respect to $\bar{L}$:

$$OII = \sqrt{\int_0^1 \left(\bar{\hat{L}}(z) - \bar{L}(z)\right)^2 dz}. \tag{5.8}$$

To illustrate L_{org} in operation, several arrangements of points are shown in Fig. 5.7, along with the observed normalized L-function and the corresponding value of the index (5.7). Periodic boundary conditions are assumed. When the objects are randomly distributed (a), the simulated Besag's function lies on the diagonal as expected from the theory (eqn. 5.5). Contrary to RI_{org}, **the new metric L_{org} is able to distinguish situations with different levels of large-scale organization**, as suggested by comparing Figs. 5.4 and 5.7b,c. In (b), clustering is apparent at all spatial scales and is reproduced by the observed Besag's function being always above the diagonal. In (c), the crossover of the identity line indicates a robust transition towards regularity in the long-range.

In panel (c) we also notice that, for large distances, there is a prominent deviation of $\bar{\hat{L}}$ from the expected trend, which appears not to be due to particular features of the point process but is quite artificial. Although smaller, the same behavior is also visible in (a) and in the 95% confidence envelopes for complete spatial randomness. In fact, when counting the number of events within discs of increasing radii, a tendency towards regularity emerges if $r > D/2$, because the circles exceed the boundary of the domain but the objects cannot be double-counted (Fig. 5.6b). This apparently reduces the actual number of neighbors within r as compared to the expectation, thus explaining the observed profiles. In the following Section 5.3.3, we will show two ways of correcting this effect.

5.3.2 Open boundary conditions

A major issue arises when considering open rather than periodic domains. This situation is particularly relevant to the analysis of distance distributions in the deep convective cloud fields as inferred from, e.g., satellite or radar observations (Radtke et al., 2022). In such configurations, the discs $b(\mathbf{x}, r)$ centered at elements located close to the boundary of W may exceed it and this eventually leads to an underestimation of the actual number of neighbors within distance r (Fig. 5.6c). This is not the case when cyclic boundary conditions are prescribed as the domain is periodically continued. To avoid undercount biases when estimating the Besag's functions, edge effects have to be accounted for.

Several edge-correction strategies can be implemented. An exhaustive review of techniques is presented in Haase (1995); Illian et al. (2008). If observations were avail-

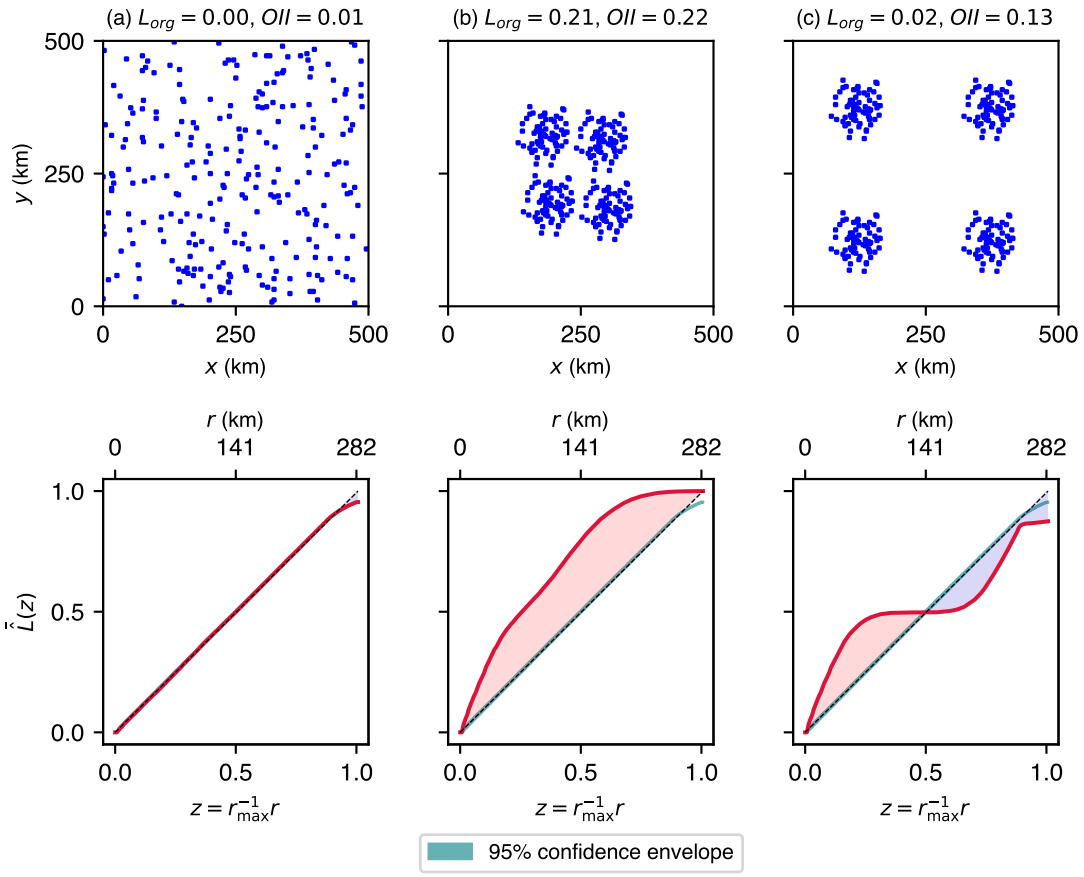

Figure 5.7: *Synthetic point patterns featuring randomness (a), small- and large-scale clustering (b, cf. Fig. 5.4a), small-scale clustering and large-scale regularity (c, cf. Fig. 5.4b), along with the corresponding L-functions* $\bar{\bar{L}}(z)$ *(red lines in the lower row). The dashed lines in the bottom panels represent the Besag's functions* $\bar{L}(z) = z$ *expected for a random arrangement of the* $N_c = 252$ *objects. 95% confidence bands for CSR are also shown (cyan shading), while red and blue shadings respectively indicate areas counting as positive and negative in the calculation of* L_{org}*. The value of the OII* (5.8) *is also provided. The domain size is* $D = 500$ *km, with biperiodic boundaries and resolution* $\Delta x = 2$ *km, while* $r_{\max} = D/\sqrt{\pi}$ *in order for circles of radius* $r_{\max}$ *to cover the same area as the domain.*

able also outside the study region W, one could define a buffer zone surrounding the window of interest. This approach is the one that most accurately mirrors the actual point pattern. Nevertheless, Haase (1995) pointed out that it requires the density of points in the buffer zone be the same as in the interior, which might not be the case, and also that a much more relevant computational effort is needed.

Here we balance the potential loss of information introduced by considering open domains by weighting the event counts at all distances r from any given element of the

pattern. This technique, referred to as the *area-based correction* by Besag (1977), weights the number of points in $b(\mathbf{x}_i, r)$ by a factor $w_i(r)$ that accounts for the proportion of the area of $b(\mathbf{x}_i, r)$ that lies within the domain (cf. Fig. 5.6c):

$$w_i(r) = \frac{\pi r^2}{\nu\left(b\left(\mathbf{x}_i, r\right) \cap W\right)}. \tag{5.9}$$

We note that this calculation in principle is not limited by any maximum search radius (i.e., when the disc $b(\mathbf{x}_i, r)$ is completely outside the domain, $\nu\left(b\left(\mathbf{x}_i, r\right) \cap W\right) = \nu(W)$).[1]

5.3.3 The discrete binomial process: $dL_{\mathbf{org}}$

For practical purposes, modeling the spatial distribution of convective events as a homogeneous Poisson point process may be inadequate for two reasons. One has already been mentioned in Section 5.2.3, namely, representing updraft locations as a point process (not necessarily Poisson) neglects inhibition effects due to finite cloud sizes. Secondly, one of the potential drawbacks of RI_{org} and L_{org} is that the theoretical model they are based upon assumes a continuous metric over an infinite plane, while numerical studies or observational data sets demand to consider finite, discrete grids. The above results are thus strictly valid only if unbounded regions are taken, as the Poisson model itself may not be appropriate to represent a point pattern in limited-area domains (cf. Figs. 5.7 and 5.6b).

To solve this latter issue, we make use of arguments borrowed from the stochastic geometry. We already saw in Section 3.3.3 that any finite random point pattern resulting from the restriction to a compact set of a homogeneous Poisson process would follow a binomial law. In particular, given N_c objects independently and uniformly distributed (iud) within a finite domain W, for each bounded subset Ω containing a typical point $\mathbf{x}$, eqn. (5.2) translates into

$$\mathbb{E}\left(N\left(\Omega \setminus \{\mathbf{x}\}\right)\right) = \left(N_c - 1\right) \frac{\nu(\Omega)}{\nu(W)}$$

[1] The most widely employed method in the analysis of spatial point patterns is by far the so-called *Ripley's local correcting factor method* (Haase, 1995). It consists in weighting all pair separation distances and holds under the assumptions of stationarity and isotropy of the point process. In this case, eqn. (5.6) has to be modified as

$$\hat{L}(r) = \sqrt{\frac{\nu(W)}{\pi N_c \left(N_c - 1\right)} \sum_i \sum_{j \neq i} w_{ij} \delta_{ij}(r)},$$

where the weight w_{ij} accounts for the proportion of the circumference centered at $\mathbf{x}_i$ and passing through $\mathbf{x}_j$ contained in W, i.e.,

$$w_{ij} = \frac{2\pi d_{ij}}{|\partial b(\mathbf{x}_i, d_{ij}) \cap W|}, \tag{5.10}$$

$\partial \cdot$ denoting the boundary of a set and $|\cdot|$ the length. For rectangular study areas in the planar case, explicit formulas are given by Goreaud and Pélissier (1999). However, unlike the area-based correction method (5.9), the calculation is limited by a maximum search radius as, for square domains of size D, the procedure (5.10) provides unbiased estimates for $\hat{\bar{L}}$ only up to distances equal to $\sqrt{2}D/2$ (Diggle, 1983; Haase, 1995).

hence

$$\lambda^{-1}\mathbb{E}\left(N\left(\Omega \setminus \{\mathbf{x}\}\right)\right) = \frac{N_c - 1}{N_c}\nu(\Omega). \tag{5.11}$$

since by definition $\lambda = N_c/\nu(W)$. When circles of radius r are considered, i.e., $\nu(\Omega) = \pi r^2$, and infinite point patterns are assumed, $N_c \to \infty$ and we recover eqn. (5.3). In any case, for reasonable sample sizes (e.g., $N_c > 15$), we can still approximate

$$\lambda^{-1}\mathbb{E}\left(N\left(\Omega \setminus \{\mathbf{x}\}\right)\right) \approx \nu(\Omega).$$

Taking circles of radius r as study areas in a random process over periodic square regions of size D, the definition (5.4) now reads

$$L(r) = \begin{cases} \sqrt{\dfrac{N_c - 1}{N_c}}r & \text{for } 0 \leq r \leq \dfrac{D}{2}, \\ \sqrt{\dfrac{1}{\pi}\dfrac{N_c - 1}{N_c}\left(\pi r^2 - 4\left(r^2 \arccos\dfrac{D}{2r} - \dfrac{D}{2}\sqrt{r^2 - \dfrac{D^2}{4}}\right)\right)} & \text{for } \dfrac{D}{2} < r < \dfrac{D}{\sqrt{2}}, \end{cases} \tag{5.12}$$

which incorporates the correction necessary when $r > D/2$, whose importance has been highlighted in Fig. 5.6b. The function (5.12) explains the profiles observed in the random point pattern realizations (Fig. 5.8a) but we note that it is no longer linear when $r > D/2$. Similar issues emerge when treating the case of elongated-channel domains, which will be discussed in Section 5.3.4.

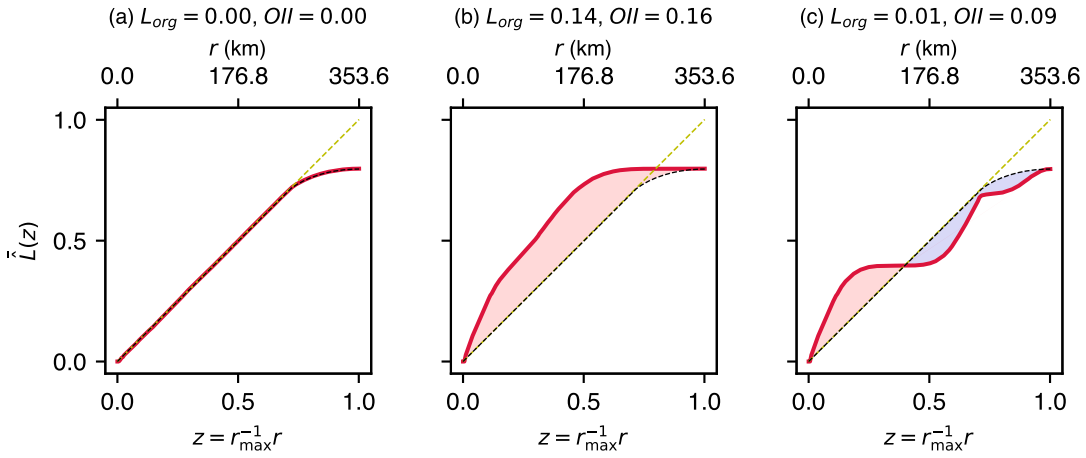

Figure 5.8: *As in Fig. 5.7 but with* $r_{\max} = D/\sqrt{2}$ *and the theoretical profile for a random arrangement of points corrected for the boundedness of the domain (black dashed line). The yellow dashed line corresponds to the theoretical expectation assumed for infinite domains,* $\bar{L}(z) = z$.

An alternative solution comes from the first point discussed above. In fact, we might directly consider the discrete grid, also because the zonal and meridional components

of the inter-point distances are quantized in practical applications (for regular grids, they are multiples of the horizontal spacing Δx). This would prevent any deviation from the expected profiles for distances lower than the minimum inter-convective spacing. It must be noted, however, that the impact of inhibition effects would be much weaker with the all-neighbor connectivity approach than with the nearest-neighbor one. In the discrete grid, instead of considering circles of radius r as in eqn. (5.2), it seems reasonable to count the events within square observation boxes of size $\ell = n\Delta x$ (i.e., consisting of $n^2 - 1$ cells) surrounding one of the convective pixels in turn (Figure 5.6d). We assume $n \in \mathbb{N}$, $1 \leq n \leq D/\Delta x$, where $\mathbb{N}$ denotes the set of non-negative integers.

Given eqn. (5.11) with a square of size $n\Delta x$ as Ω, we can define the discrete binomial counterpart of the Besag's function as

$$L(n\Delta x) \equiv \sqrt{K(n\Delta x)} = \sqrt{\frac{N_c - 1}{N_c}\left(n^2 - 1\right)\Delta x^2} \approx n\Delta x, \tag{5.13}$$

which is the L-function that would be theoretically expected if the updraft centers were independently and uniformly distributed within the domain. The approximation holds under the assumption of reasonable sample sizes. The function (5.13) will be compared against the one diagnosed from a realization of a point process, $\hat{L}(n\Delta x)$, given by

$$\hat{L}(n\Delta x) = \sqrt{\frac{\nu(W)}{N_c\left(N_c - 1\right)}\sum_{i=1}^{N_c} w_i(n\Delta x)\sum_{\substack{j=1 \\ j\neq i}}^{N_c}\delta_{ij}(n\Delta x)}, \tag{5.14}$$

where $\delta_{ij}(n\Delta x) = 1$ if the size of the box centered at the i-th object and delimited by the j-th is less than $n\Delta x$, otherwise $\delta_{ij}(n\Delta x) = 0$; $w_i(n\Delta x)$ are weights assigned to the count $\sum_{j\neq i}\delta_{ij}(n\Delta x)$ of events over boxes of size $n\Delta x$ to correct for edge effects in case of open domains (for periodic ones, $w_i(n\Delta x) = 1$). The edge correction technique designed here is similar to the one in eqn. (5.9), i.e., $w_i(n\Delta x)$ represents the fractional area of a square of size $n\Delta x$ surrounding the i-th point of the process contained within the domain. An application of this method is presented in Section 5.4.

One may want to investigate the prevailing organizational regimes of a pattern over the whole domain or restrict to given subsets of W. It would just suffice to select a proper range of search box sizes $0 \leq \ell = n\Delta x \leq \ell_{\max}$ over which to evaluate the L-functions, $\ell_{\max}$ being the maximum size within the region under consideration. If the analysis is to be performed over the entirety of a square domain of size D, $\ell_{\max} = D$ if the domain is periodic, $\ell_{\max} = 2D$ if it is open. Similar to the derivation of L_{org}, both ℓ and and the functions (5.13) and (5.14) are rescaled by $\ell_{\max}$. Let $z_n = \ell_{\max}^{-1}\ell = \ell_{\max}^{-1}n\Delta x$, $\bar{L}$ and $\bar{\hat{L}}$ be the results of the normalization.

We can then introduce the discrete version of the L-function-based index, dL_{org}, as the Riemann sum

$$dL_{\text{org}} = \sum_{n=1}^{\frac{D}{\Delta x}}(z_n - z_{n-1})\left(\bar{\hat{L}}(z_n) - \bar{L}(z_n)\right). \tag{5.15}$$

Similar conclusions to the above apply to the new index (5.15) and the spatial regimes corresponding to its values, with positive and negative deviations revealing overall clustering and regularity trends, respectively. However, contrary to the derivation in eqn. (5.12), no corrections due to the boundedness of the domain have to be imposed for square study regions.

These considerations are supported by the following Figure 5.9, which shows the normalized Besag's function as measured from numerical routines for the same configurations of Fig. 5.7. Note that the profile of the observed L-function in panel (a) allows an interpretation of random organization to be safely made at all spatial scales, since the tendencies towards randomness are recovered also in the far-field. We do not see significant differences in Fig. 5.9b compared to Fig. 5.7b, as the spatial scales potentially affected by the limited-area correction (5.12) are not attained by the grid point distances here. The converse is true for panel (c), which now shows exactly what we expected, short-range clustering and long-range regularity, whose effects mutually cancel, as $dL_{\mathrm{org}} = 0$. Note that the scenes in (a) and (c) can be distinguished using the organization irregularity index (eqn. 5.8 in discrete form).

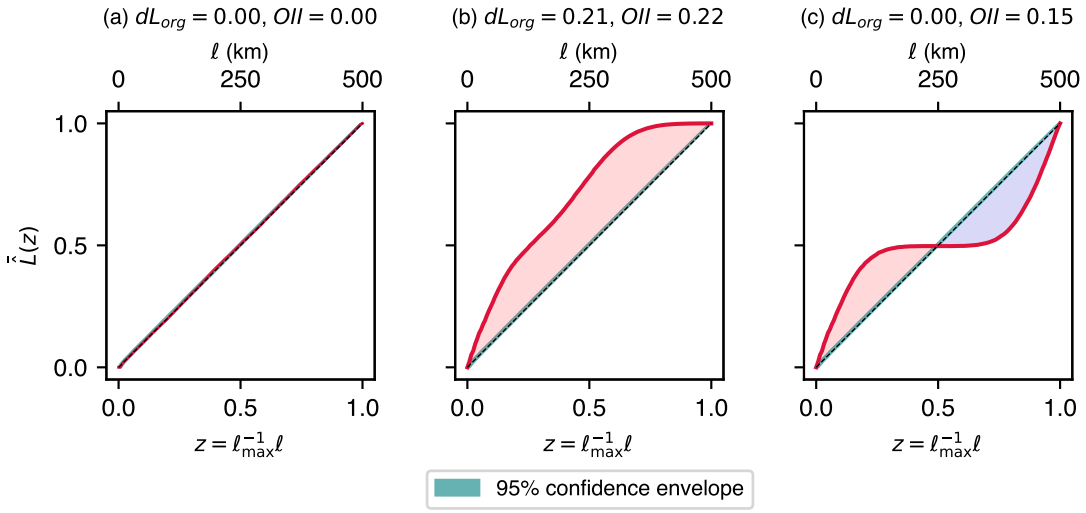

Figure 5.9: *As in Figs. 5.7, 5.8 but with the discrete binomial model* (5.13) *used as a standard of randomness. The normalizing factor is* $\ell_{\max} = D$. *Red and blue shadings respectively refer to areas counting as positive and negative in the calculation of* dL_{org}.

5.3.4 The case of non-square domains

So far we have examined square domains only, but the index should be generalized to rectangle domains used in modeling studies (Tompkins, 2001c; Stephens et al., 2008; Wing and Cronin, 2016) and which are also suitable for observational studies of the tropics (e.g. Bony et al., 2020). Past numerical studies have pointed out that long chan-

nel geometries do not artificially constrain the large-scale circulations while also retaining any salient three-dimensional dynamical features (Tompkins, 2001a), allow a diagnosis of the typical aggregation length scales (Wing and Cronin, 2016; Wing et al., 2017) and, as compared to square-domain experiments, also produce humidity distributions that are in a much closer agreement with observations (Holloway et al., 2017).

Rectangular domains of width D_x and height D_y are considered here, assuming $D_y < D_x$ without loss of generality. The definition of the indices (5.7) and (5.15) is still valid. The observed L-functions $\hat{L}$ are again given by eqns. (5.6) and (5.14) with $\nu(W) = D_x D_y$, while the theoretical functions are given by eqn. (5.5) and (5.13) in case of open domains; for cyclic domains, they are to be modified. In this case, arguments similar to the finite-domain correction (5.12) apply, since, when periodically duplicating the domain, multiple counting must be avoided. We thus have, for the derivation of L_{org},

$$L(r) = \begin{cases} \sqrt{\frac{N_c - 1}{N_c}} r & 0 \le r \le \frac{D_y}{2}, \\ \sqrt{\frac{1}{\pi} \frac{N_c - 1}{N_c} \left(\pi r^2 - 2 \left(r^2 \arccos\left(\frac{D_y}{2r} \right) - \frac{D_y}{2} \sqrt{r^2 - \frac{D_y^2}{4}} \right) \right)} & \frac{D_y}{2} < r \le \frac{D_x}{2}, \\ \sqrt{\frac{1}{\pi} \frac{N_c - 1}{N_c} \left(\pi r^2 - 2 \left(r^2 \arccos\left(\frac{D_y}{2r} \right) - \frac{D_y}{2} \sqrt{r^2 - \frac{D_y^2}{4}} \right) \right) - 2 \left(r^2 \arccos\left(\frac{D_x}{2r} \right) - \frac{D_x}{2} \sqrt{r^2 - \frac{D_x^2}{4}} \right)} & \frac{D_x}{2} < r \le \frac{D_x}{\sqrt{2}} \end{cases} \tag{5.16}$$

and, for that of dL_{org},

$$L(n\Delta x) = \begin{cases} \sqrt{\frac{N_c - 1}{N_c} \left(n^2 - 1 \right) \Delta x^2} & \text{for } 0 \le n\Delta x \le D_y, \\ \sqrt{\frac{N_c - 1}{N_c} \left(\left(n^2 - 1 \right) \Delta x^2 - n \left(n - \frac{D_y}{\Delta x} \right) \Delta x^2 \right)} & \text{for } D_y < n\Delta x \le D_x. \end{cases} \tag{5.17}$$

We note that the theoretical L-functions are no longer linear across scales in this case. Eqns. (5.16) and (5.17) can be generalized by replacing D_y by $\min\{D_x, D_y\}$ and D_x by $\max\{D_x, D_y\}$. Concerning the normalizations that have to be performed for the calculation of the indices, if organization is to be assessed over the whole domain the maximum search radius and box size would become $r_{\max} = \sqrt{D_x^2 + D_y^2}/2$ and $\ell_{\max} = \max\{D_x, D_y\}$, respectively, for periodic domains, twice those values in case of open boundaries.

Figure 5.10 shows some synthetic scenes along with the corresponding values of dL_{org}. Panel (a) confirms that the theoretical model (5.17) provides the L-function expected in case of spatial randomness for the discrete binomial process, whereas the situation in (b) displays a relevant clustering signal at all scales. For open domains, weighting procedures are defined that are similar to the ones discussed earlier. For the same scene of Fig. 5.10b, if the domain is assigned open and cyclic boundaries in the meridional and zonal directions, respectively, the clustering tendency is still notable because the leftmost and rightmost bands are again close to each other (c). This is no

longer the case with open conditions (d), which features a weak clustering tendency in the short-range and a nearly imperceptible regularity signal in the long-range.

We again emphasize that the theoretical L-functions in (a,b) differ from those in (c,d). In the first case, when $n\Delta x > D_y$ (i.e., $z > D_y/D_x = 0.25$), periodic continuation of the domain along the y axis must be considered but multiple counting of points is not allowed, which explains the actual reduction in the number of neighbors for $z > 0.25$ (the situation is similar to that shown in Fig. 5.6b). This is no longer the case when the domain is open in the meridional direction: even though the theoretical L-function is to be computed with respect to a pattern of independently and uniformly distributed objects over the finite domain under consideration, the pattern itself can be implicitly thought of as infinite along the y axis. This does not pose any restriction in terms of avoiding multiple counting and square search boxes can be taken that also exceed the domain and for which the theoretical L-function follows eqn. (5.13), because the distribution of events outside the domain is assumed to be same as in the interior (iud objects). In particular, the theoretical function $L(n\Delta x) = n\Delta x$ is represented by the identity line in (c,d).

5.4 Applications

5.4.1 Application to model data

The discrete approach proposed in Section 5.3.3 is particularly suited to analyzing numerical model output. We compare the performance of dL_{org} vs RI_{org} for a large-domain (3000×3000 km^2) CRM-like experiment conducted with the stochastic model introduced in Chapter 2. The time evolution of the indices is charted in Fig. 5.11. Snapshots are superimposed that show maps of the spatial column-integrated relative humidity field R sampled at different stages of the simulation. The aggregated state consists of several mesoscale convective systems that reduce in number over time until a single dominant convective cluster remains (cf. Section 3.2.2). Output every six hours is considered to calculate the organization indices.

RI_{org} abruptly increases at the start of the integration, taking on very high values that indicate strong clustering with $RI_{\text{org}} > 0.2$ by day 7 and stabilizing by around day 40 (Fig. 5.11e). However, as expected from its nearest-neighbor construct (cf. Fig. 5.4), it is almost totally insensitive to the number (and the position) of MCSs in the scene, as it only increases from 0.39 to 0.43 between day 25 (d) and day 100 (h). The new index agrees with RI_{org} in that it always classifies the field as clustered, nevertheless, it evolves smoothly across different degrees of aggregation. The new metric can also discern the impact of cluster number and size, increasing linearly between day 32 and day 45, when the same six clumps are active and with changes in slope marking the elimination of clusters. dL_{org} finally stabilizes around day 86, when the penultimate cluster expires leaving one dominant mesoscale convective system. The general evolution of the R field and the simulated NNCDF and L-function are reported in a movie available at `http://clima-dods.ictp.it/Users/gbiagiol/indices.mp4`.

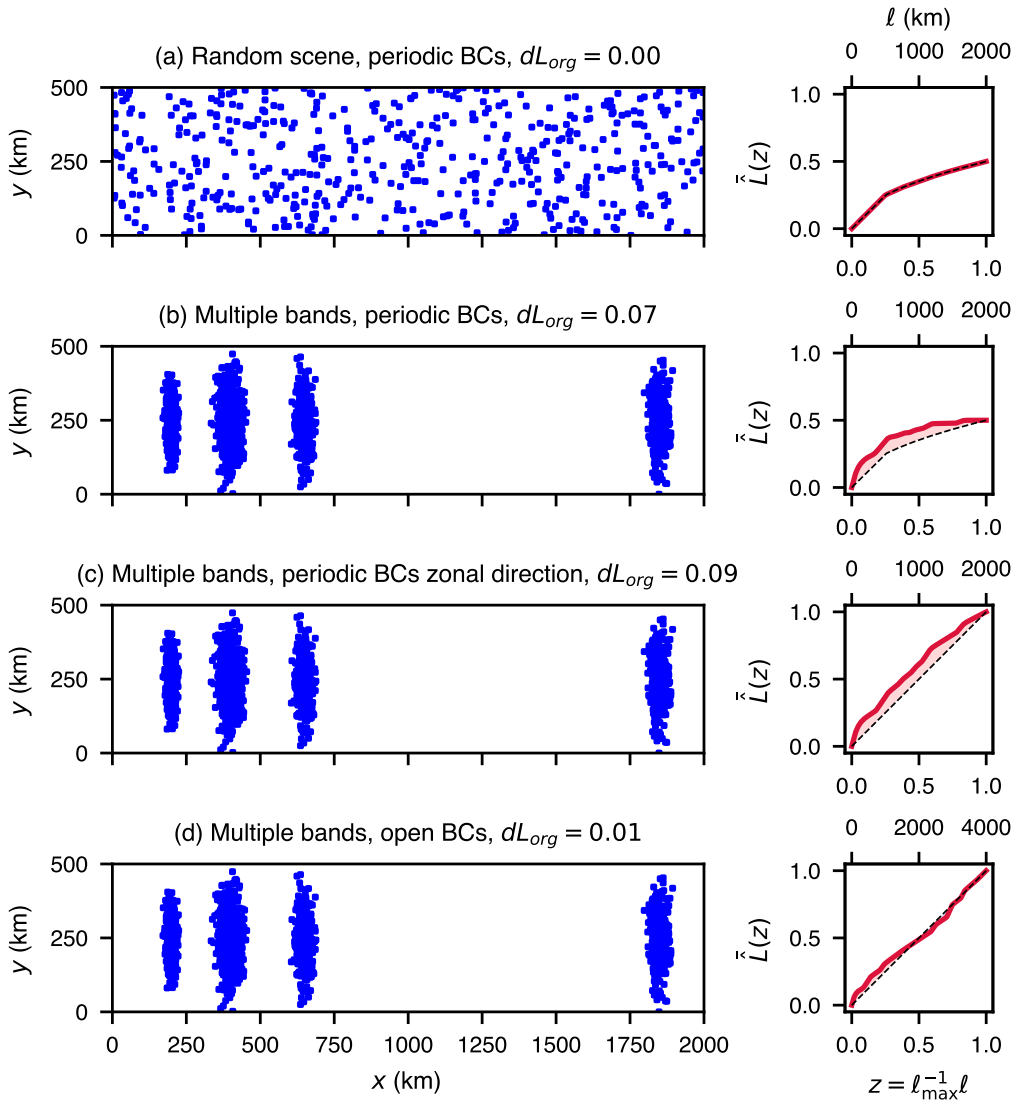

Figure 5.10: *Synthetic scenes featuring a random distribution of points (a) and the coexistence of banded structures (b,c,d) in a long-channel domain with* $D_x = 2000$ *km and* $D_y = 500$ *km. Different boundary conditions are imposed: biperiodicity in (a) and (b), periodicity in the zonal direction only (c), while in (d) the domain is open in both directions. The corresponding theoretical and simulated L-functions are shown (black dashed and red solid lines), along with the red and blue shadings that represent positive and negative deviations* $\hat{\bar{L}}(z) - \bar{L}(z)$ *and count as such in the derivation of* dL_{org}.

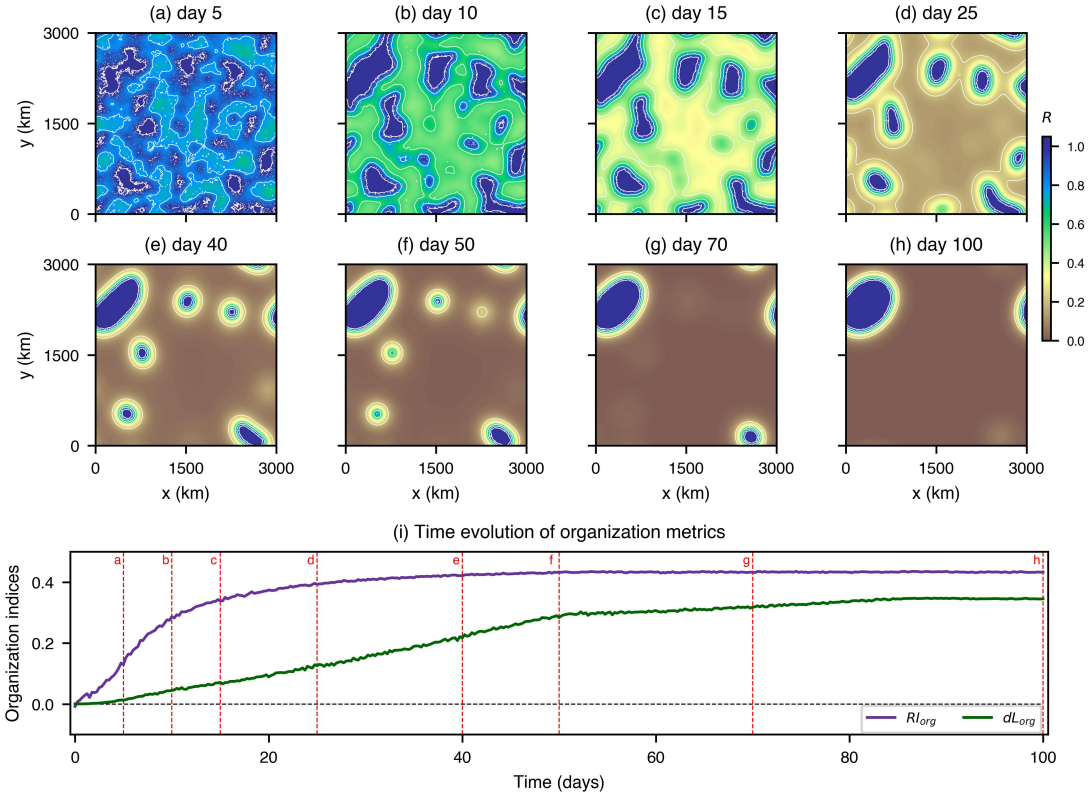

Figure 5.11: *(a-h) Maps of the spatial column relative humidity field (color shading and contours, with intervals of* 0.2*) for a simulation performed with the model introduced in this thesis. (i) Temporal evolution of the indices* RI_{org} *(purple) and* dL_{org} *(green). The horizontal dashed line marks the zero level, which is the value for a random distribution of convective cells for both* RI_{org} *and* dL_{org}*. The vertical dashed lines refer to the samples (a-h).*

5.4.2 Application to precipitation observations

Here we analyze organization in GPM rainfall observations and consider a box of $10^\circ \times 10^\circ$ (135E-145E, 5N-15N) in the Western Pacific warm pool region, imposing a threshold of 8 mm h^{-1} on the rain rate field to identify convective pixels. As the resolution is coarser than that of convective updrafts no recursive algorithm is applied to adjoint adjacent points to single events.

In order to test the robustness of both indices to calculation method, two approaches to identifying convective locations are compared. In the first all pixels exceeding the threshold are counted as convective. Instead in the second method, only those convective cells exceeding the threshold that are also a local maximum in their immediate (3×3) neighborhood are retained, similar to Bony et al. (2020). This technique will be referred to as the *local maximum method*.

We examine rain maps for five days in October 2016 (Fig. 5.12); the entire sequence

of 30 minutes temporal resolution scenes is contained in an animation available at `http://clima-dods.ictp.it/Users/gbiagiol/obs_indices.mp4`. For each scene, the indices RI_{org} and dL_{org} are calculated (Fig. 5.13). Scenes with $N_c < 15$ are discarded. The values of the indices as reported in the text will only refer to the application of the local maximum method. In the computation of dL_{org}, the area-based edge correction is employed.

Visual inspection of the situation of Fig. 5.12 panel (a) would suggest that it is less organized than that in (b). Both cases show the presence of a very large aggregate in the south-east corner, which is slightly larger at 19:30, but at 19:00, two smaller aggregates can be identified at the south-west corner. The new index classifies the 19:30 scene as more organized ($dL_{\text{org}} = 0.21$) than that at 19:00 ($dL_{\text{org}} = 0.11$), but the nearest-neighbor connectivity metric RI_{org} indicates the opposite, as $RI_{\text{org}} = 0.44$ in (a) and 0.40 in (b). The reason for this behaviour of RI_{org} lies in the presence of the isolated event in the south-west part of the scene (b): indeed, we calculated that if this event is arbitrarily eliminated, RI_{org} would increase back to a value of 0.45 for this scene. Something analogous happens in the situations (h-i), in which, as soon as the individual object at the center of the window at 08:00 is flanked by an other one at 08:30, the value of RI_{org} increases while the new index remains roughly constant. Finally, the scenes in (d) and (e) look nearly identical in terms of their degree of aggregation, and indeed the new metric stays constant (0.08), but RI_{org}, by virtue of its strong sensitivity to the relative positions of the clouds, increases by 0.12 from (d) to (e).

These examples already hint at the weakness of indices based on nearest-neighbor statistics, namely that they are quite sensitive to the appearance or addition of single events to a scene, despite its considerable $\mathcal{O}(1000\text{ km})$ dimension, mainly due to sampling issues. This is evident in the considerable temporal variability in RI_{org}. Even though both indices overall indicate clustering of the deep convective cloud field during the period under consideration (Fig. 5.13), RI_{org} is strongly impacted by the relative positions between the objects, whereas dL_{org} is not (or, at least, to a lesser extent).

It is also seen that RI_{org} is dramatically influenced by the number of points in the scene. In particular, RI_{org} is very sensitive to the calculation method, with little agreement between the methods with and without the local maximum algorithm applied. Conversely, **the new metric evolves more smoothly in time and is far more robust to calculation method** since the two timeseries (green solid and dashed lines in Fig. 5.13) are in good agreement with each other and feature a very limited offset, which never impairs our assessment of the organization level of a scene. The level of clustering given by dL_{org} is considerably lower than RI_{org} due to the fact that the new index is able to measure inter-cluster spacing of rain up to the domain scale of 1000 km.

Code availability and performance

The numerical routine used for the analysis presented in this chapter is freely available on github at `https://github.com/giobiagioli/organization_indices`, along with a detailed code documentation. The procedure to calculate $L_{\text{org}}/dL_{\text{org}}$, although more

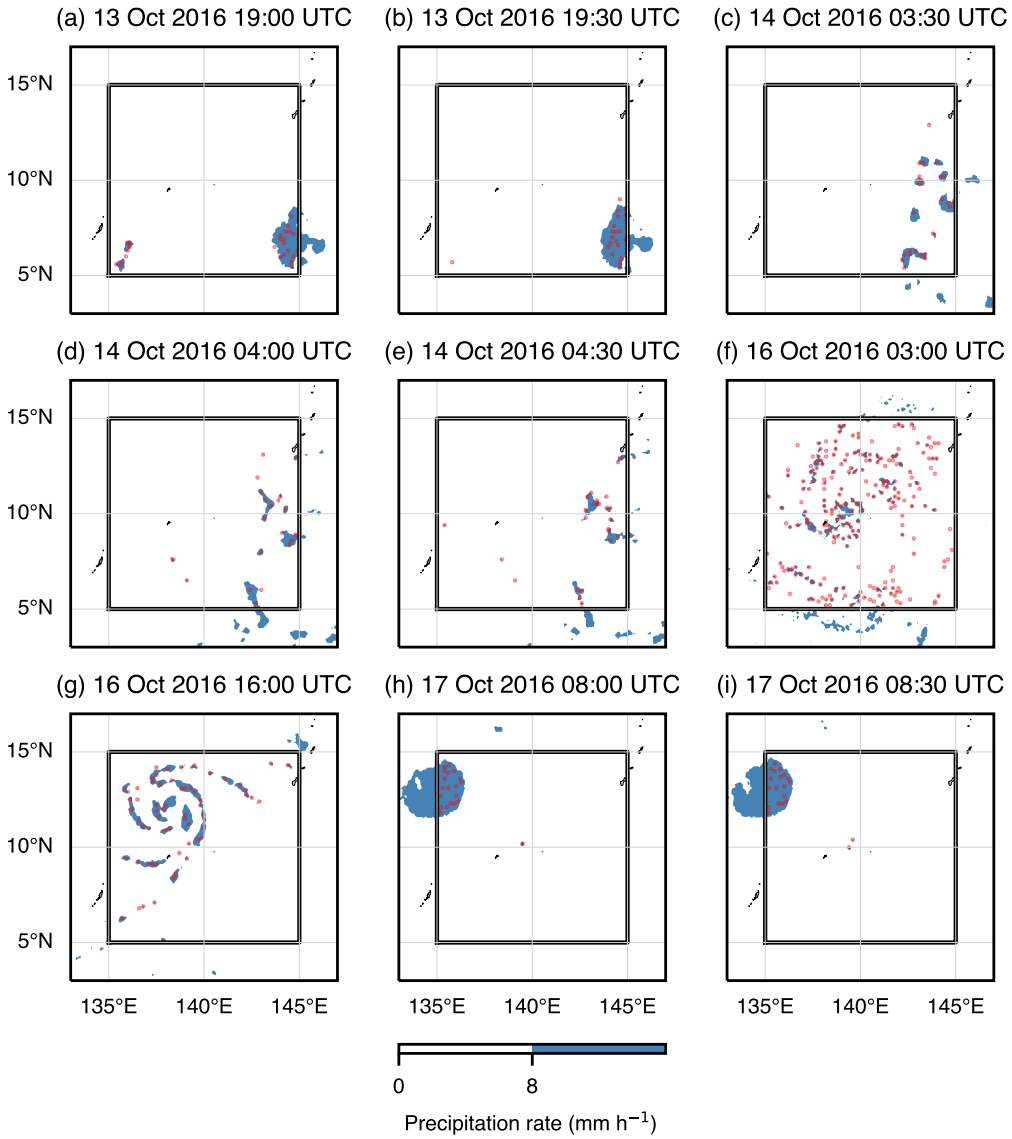

Figure 5.12: *Example snapshots from GPM observations in the period 13-17 October 2017. The study area is the central* $10^\circ \times 10^\circ$ *box bounded by the thick solid line (135E-145E, 5N-15N). The blue patches represent the pixels that exceed the* 8 *mm* h^{-1} *rain rate threshold, while the red points are the convective centers identified through the local maximum method.*

computationally burdensome than that for RI_{org}, is efficient for practical cases. The computation time on a Intel-Core i7−4790 4-core (3.60 GHz) PC is $\sim$ 12 s for a 500×500 input data with periodic boundary conditions and a 0.5% convective fraction, $\sim$ 16 s for the open boundary case.

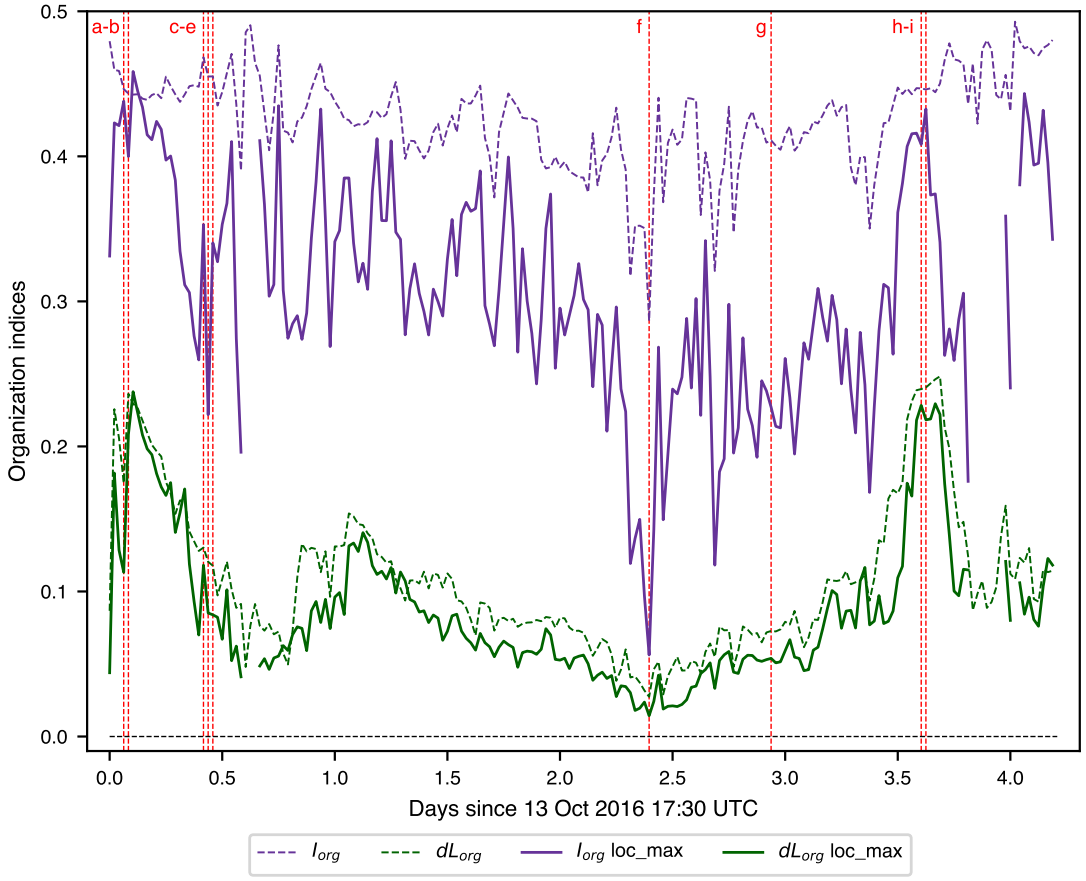

Figure 5.13: *Time evolution of the metrics RI_{org} (purple) and dL_{org} (green) for the analysis of GPM rainfall data in the 135E-145E, 5N-15N region (cf. Fig. 5.12) for the period from 13 October 2016 17.30 UTC to 17 October 2016 22 UTC. The metrics are calculated based on the half-hour GPM retrievals, considering as convective points all those pixels that exceed the 8 mm h^{-1} rain rate threshold (dashed lines) or the pixels in the thresholded field that are further identified as local maxima (solid lines). Missing values correspond to scenes with number of convective objects $N_c < 15$. The vertical dashed lines refer to the samples (a-h) of Fig. 5.12.*

Chapter 6

Conclusions

Deep convective clouds can be observed in a variety of organizational states, from spatially random distributions to more coherent patterns spanning a wide range of spatial scales. The clustering of convection is usually associated with high-impact precipitation extremes and future changes in the frequency of occurrence of organized deep convection have the potential to affect climate sensitivity. However the possible feedbacks on climate provided by convective clustering are still poorly represented in present-generation climate models. These are among the reasons that motivated the scientific community to devote increasing attention to modes of deep convective organization over the last decades, whether in idealized numerical studies or realistic situations involving squall lines, mesoscale convective systems, tropical cyclones, up to the Madden Julian Oscillation.

The increased availability of computing resources to conduct complex modeling studies has brought to attention the intriguing paradigm of convective self-aggregation, in which, under certain circumstances, tropical convection shows a *spontaneous* transition from a random distribution in space to a state where the clouds are clumped together. This phenomenon occurs in spite of homogeneous initial and boundary conditions and large-scale forcing in a state of radiative-convective equilibrium and has been detected in a variety of modeling frameworks, with convection either explicitly resolved or parameterized. The prominent domain-mean tropospheric drying found in association with self-aggregation in both models and seminal observational studies leads to a more efficient cooling by infrared emission and therefore has ramifications for tropical climate and its variability. It has been suggested that self-aggregation can act as a safety valve to regulate tropical climate and that there may be a propensity for more aggregated convective conditions in warmer scenarios, producing a negative feedback to global warming.

Nonetheless, discrepancies exist in the literature about the models' representation of self-aggregation and its robustness across models is far from being established. Recent intercomparison studies have shown that sometimes the models display little or no consensus even about whether organization is attained or not at all for a fixed ex-

perimental configuration. The onset and nature of the aggregated equilibrium state and the sensitivity to lower boundary conditions (e.g., SST) are among the aspects that differ most between models with varying dynamical cores and representations of moist physics, radiation, turbulence, etc. The fact that the occurrence of aggregation is sensitive to the details of the experimental setup, such as domain size and resolution, raises questions as to whether this phenomenon is real or just an artifact of the models.

Another major problem arises when it comes to assessing the strength of aggregation and convective organization in general. There is no agreement in the literature on how to define, and hence quantitatively measure, organization not only in models but also in observations. This has motivated the derivation of a wide variety of *aggregation metrics/organization indices*, whose scope is to quantify how and to which extent deep convective clouds occupy space. These indices explore different aspects of the organization processes and, because of this, often disagree between each other in the assessment of the degree of organization of a scene, as shown in the introduction.

This thesis has attempted to address these issues. In the introduction, we specified two interconnected tracks along which we aimed to move and which we briefly recap here.

- First track: aid understanding of self-aggregation in terms of the physical processes involved, in order to explain the sensitivities detected in cloud-resolving models.
- Second track: aid measuring of the organization level of cloud field scenes through improved metrics, suitable for use in the analysis of wide ranges of model output and observational data.

First track

Regarding the first research direction, in the introduction we proposed to shed light on the controversial aspects between models by introducing a very idealized, minimally simple model of the tropical atmosphere which retains the fundamental features of the more complex ones but allows robust conclusions to be drawn due to its simplicity. In doing so, we have entered a rich research avenue which uses toy models as diagnostic tools to gain a deeper understanding of the processes related to convective self-aggregation. Within the framework of such approaches, the self-aggregation behaviour has been regarded as a phase transition in moist convective systems and its onset as caused by an instability of the spatially homogeneous RCE state of tropical convection.

In Chapter 2 we presented a stochastic reaction-diffusion model for the column total water relative humidity R in the tropics, whose representation of physics is based on Craig and Mack (2013) but which uses CRM-like domain sizes and horizontal resolutions in an attempt to explain the sensitivities detected in full-physics models. The model incorporates the effects of moistening due to convection, horizontal transport of moisture by advection and diffusion processes, and drying due to compensating subsidence. It contains the correlation between convection and water vapor that has been

documented in observations and also shown to be key for the localization of convection in previous numerical studies. In particular, convection towers are located according to a weighted random selection process, which makes convection more likely in moist areas using a functional form derived from TRMM observations. The towers then rapidly moisten their local environment for the entirety of their life span, which averages 30 minutes and local moistening is spread laterally by a local diffusive transport term. Subsidence drying balances the moistening uniformly throughout the domain, mimicking the action of fast spreading gravity waves in a highly idealized way as they are effectively assumed to have infinite group velocity. The model thus has three key parameters that describe the sensitivity of convection to humidity, a_d, the efficiency of the transport, K, and the strength of the subsidence drying, τ_{sub}, in addition to the domain size D and the horizontal resolution Δx.

The local delta function perturbations introduced into the R field by the triggering of convection made the numerical solution procedure quite challenging, with sharp gradients between convective non-convective grid boxes. An efficient numerical solver extending the classical ADI scheme (Peaceman and Rachford, 1955) was designed for the treatment of the model governing equation, that is fully implicit in time and therefore ensures stability.

In Chapter 3, we showed that, depending on the chosen parameter settings and experimental framework, the model can produce either random or aggregated convective states, which well resemble those yielded by more complex CRMs. Clustering is favoured by more vigorous subsidence, weaker transport and stronger convection-moisture feedback. Interestingly, the model is found to produce a transition to aggregation at parameter values that are a reasonable approximation of the present-day tropical atmosphere and sensitivities to domain size and grid spacing similar to CRM studies, with aggregation more likely using larger domains and coarser resolutions. While over large domains two or more convective clusters can survive for a limited period in runs that aggregate, they always ultimately collapse to a single center, due to the fact that compensating subsidence occurs uniformly throughout the domain, that is, there is no explicit deformation radius.

Concerning the sensitivity of self-aggregation to subsidence and diffusion, we argued that the horizontal transport efficiency and subsidence rate can be dimensionally combined to give an *area of influence* of convection on the moisture budget. This quantity serves as a measure of the distance through which the effects of a single deep convective core are felt, with large areas of influence inhibiting aggregation by enlarging the humidity "halo" around convective events.

Concerning the domain size and resolution sensitivities, we heuristically argued that the important factor is a measure of the maximum convective-free distance prior to clustering onset, as this would determine the size of the humidity fluctuations in the pre-aggregated state. Indeed, since aggregation begins as a dry patch that expands and then amplifies, larger convection-free distances would enhance the spatial heterogeneities of the column humidity field and promote the formation of drier-than-average regions with suppressed convective activity, which may further develop and eventually

lead to organization. Using the maximum inter-convective nearest-neighbor distances interchangeably, we showed that these are constrained to decrease with smaller domains or higher resolutions for a given convective fraction, thereby making aggregation less likely. For example, finer resolutions lead to more but smaller convective centers, reducing the inter-convective spacing. We note that this is different from the suggestion of Tompkins and Semie (2017), who instead attributed resolution dependence to the reduction of explicit entrainment. Our simple model therefore permits a reinterpretation of the sensitivity of aggregation to diffusion scheme found in Tompkins and Semie (2017) not as the effect of humidity entrainment into updrafts, but instead as the impact on mean updraft size, and therefore inter-convective distance.

Expanding on these arguments and using fits from experimental data to investigate the dependence of aggregation on a_d, we combined the five model parameters into a single dimensionless quantity, the *aggregation number* N_{ag}, that predicts whether a specific model and experiment setup will result in an aggregated convective state. The reliability of N_{ag} was assessed on the basis of large ensembles of $\mathcal{O}(1000)$ simulations that explore the five-dimensional parameter space, which demonstrate that the transition to aggregation occurs at a specific threshold value of the dimensionless quantity. In particular, clustering occurs when N_{ag} falls below the critical threshold. This is subject to a small amount of uncertainty due to the stochastic nature of the model. We suggest that N_{ag} could be of practical benefit for the community to help explain the differences in aggregation states seen in model intercomparison projects such as RCEMIP (Wing et al., 2020).

Some important physical processes and sensitivities missing from the aggregation number in its present formulation have been explored in Chapter 4. We showed some examples of the documented sensitivity of self-aggregation to initial conditions, with the simple model exhibiting a weak hysteresis, consistently with the findings of CRM simulations. The chapter also includes a first, very basic attempt to account for inhibition effects due to cold pools, which suppress convection in their stable interiors. Their impacts on the convection-water vapor feedback, hence on aggregation, were discussed.

Second track

Regarding the second research direction, in Chapter 5, to give a bit of context, we attempted the first comprehensive review to collate all documented convective organization metrics, briefly highlighting the drawbacks of some of these. We emphasized that the vast majority of metrics only measure the *relative* (rather than absolute) clustering comparing two scenes and are thus qualitative in nature, and that some of them are biased towards specific spatial scales or very sensitive to details of the calculation procedure. It is also possible that the indices can suffer from non-linearities, which means that they can not be employed to assess the strength of aggregation on a gradual continuum but only to differentiate aggregated from random convective states.

We then revisited the metric I_{org} (Tompkins and Semie, 2017), which has been widely

used since its introduction in many observational studies and model intercomparison projects, and also as a benchmark against which to compare the performance of other organization indices. The main reasons for its popularity lie in that it has a theoretical null to compare against and is quantitative in nature, i.e., it permits an absolute categorization of scenes into random, clustered or regular. We derived an analytical formula for the mean spatial scale over which I_{org} measures organization as a function of the convective density, and showed that its foundation on nearest-neighbor distances means that it measures clustering over the β-mesoscale of 20-200 km. We showed that, despite its usefulness, the metric is almost blind to inter-cluster organization on scales exceeding 200 km and can also suffer from sampling issues which make the assessed organization measure very sensitive to calculation details.

The aim of the second track has been achieved through the derivation of a new and complementary metric L_{org} to quantify the organization level of scenes, which is based on all-neighbor (rather than nearest-neighbor) connectivity approach and thus measures organization robustly over but also beyond the β-mesoscale. The metric exploits the theory behind the Ripley's K-function and the related Besag's L-function, which are commonly used tools in the context of spatial point processes and are based on the counting of events in the neighborhood of any element of the pattern for different neighborhood sizes. These functions have proven to be effective and powerful tools to capture the dominant spatial trends of a point pattern over a range of scales.

L_{org} is similar to I_{org} in its theoretical foundations - it assumes a continuous metric over an infinite plane and compares the observed L-function against a theoretical null used a reference (homogeneous Poisson process) - and also in that it is intended to provide an absolute classification of scenes into regular, random and clustered. However, unlike I_{org}, it measures organization *linearly* across different spatial scales, with the only possible exception of scales where periodic continuation of the domain is to be accounted for in the presence of cyclic boundaries. This is a consequence of the fact that the Poisson law strictly holds in the only case of unbounded domains.

The practical need of analyzing gridded model output and observational data also led us to derive a discrete version of L_{org}, called dL_{org}. It is based on the comparison of the discrete counterparts of two Besag's functions, one derived from the distribution of the events in a scene and a theoretical random one, assuming a discrete version of the binomial point process, with neighbor searches performed over square boxes rather than over circles. This follows directly from the theory of stochastic geometry, which indicates that the restriction of a homogeneous Poisson process to a compact set (the domain) is distributed according to a binomial law. Suitable corrections were proposed to account for periodic and finite open boundary domains also of non-equal aspect ratio.

The new index has proven satisfactory at reproducing the expected spatial trends of organization at different scales, with the spacing of MCSs beyond the mesoscale well detected. Like I_{org}, the new metric is an integral index of organization over a range of scales. Visual inspection of the underlying observed Besag's functions can reveal how organization changes as a function of scale, but we also introduced a second moment

based index, the organization irregularity index (OII) which is an integrated measure of the departure of convection from randomness across all spatial scales. Thus L_{org} and I_{org} give two integrated assessments of the mean organization, while the OII is an integrated measure of the variance of organization.

Application to idealized synthetic configurations and real-world situations, such as model output and satellite rainfall retrievals in the tropics, revealed that L_{org} improves on several deficiencies of I_{org}. The fact that the new metric is based on all-pair distances implies that it is much less temporally noisy than I_{org} and is also very robust to the details of the implementation methodology. L_{org} is indeed much less sensitive than I_{org} to the number and relative positions of the aggregates.

We believe that these improvements address many shortcomings of the existing measures and also imply that the new metric is more appropriate to quantifying the degree of aggregation in suites of experiments within the framework of model intercomparison projects, and also can usefully supplement existing methodologies of measuring convective organization in a wide variety of observations.

As suggested by Muller et al. (2022), the introduction of new indices is a fundamental step forward to bridge the gaps between idealized models and observations. In spite of being object-based, the new indices introduced in this thesis can also lend themselves to assessing the role of some underlying physical processes. For instance, if the inspection of the L-functions reveals some tendency towards regularity in the short range, this could be due to the inhibition effect of cold pools, especially if the scales of this regularity signal are comparable to the typical cold pool diameter. To ultimately strengthen the connection between our two research directions, we notice that the new indices are able to distinguish self-aggregation from other modes of organization. The use of dL_{org} in a run with the stochastic model captured different stages of the aggregation process, with the index steadily increasing and then stabilizing as soon as the smaller mesoscale systems succumb. In this final state, the value of the index is very high, because the updraft cores exist in close proximity to each other. This is not the case for other organized regimes: for example, the mesoscale organization also present in homogeneous RCE states of tropical convection is expected to correspond to lower values of the new metrics, while a nearest-neighbor index would likely saturate in both situations.

6.1 Final remarks and future research directions

There are multiple possible directions for future research, which are outlined below.

1. The next step in the work on the aggregation number is ideally to devise a methodology to take consecutive cloud-resolving model snapshots and calculate N_{ag}. This can be carried out by identifying the locations selected for new convective events and by estimating the values of the parameters from the initial random state fields through, e.g., the autocorrelation of water vapor. It should be sufficient in fact to estimate the aggregation number in the initial phase of a simula-

tion in order to predict if the corresponding random state is unstable and would eventually undergo aggregation.

2. If a given model is found to have a more complicated convective autocorrelation function, perhaps due to the mutual exclusivity of cold pools operating at scales smaller than 15 or 20 km, then a systematic analysis similar to the one conducted in this thesis could be performed with cold pools incorporated into the simple model as in Chapter 4, to explore the impact on aggregation in a wider parameter space.

3. In order to help investigate the unexplored features of the simple model, such as the sensitivity to initial conditions and the hysteresis behaviour, which is also relevant to CRMs, one might perform a stability analysis of the system's variance equation. The latter could be derived by introducing a reasonable analytical approximation of the stochastic formulation presented in this dissertation. More generally, it would be desirable to introduce a more theoretical framework to predict when the instability of the RCE state that leads to self-aggregation is expected to occur.

4. The next step in the work on the new aggregation metric is to evaluate its performance in a wider range of model output and observational data, and possibly investigate the relationships of convective organization as measured by L_{org} with some relevant variables. These would include land and ocean surface (or near-surface) temperatures in various regions of the tropics to see if there are differences in organizational states between them, or the OLR, in an attempt to capture signs of self-aggregation in the real atmosphere.

Bibliography

Abbot, D. S. (2014). Resolved Snowball Earth Clouds. *Journal of Climate*, 27(12):4391–4402.

Ahmed, F. and Neelin, J. D. (2019). Explaining Scales and Statistics of Tropical Precipitation Clusters with a Stochastic Model. *Journal of the Atmospheric Sciences*, 76(10):3063–3087.

Arnold, N. P. and Putman, W. M. (2018). Nonrotating Convective Self-Aggregation in a Limited Area AGCM. *Journal of Advances in Modeling Earth Systems*, 10(4):1029–1046.

Arnold, N. P. and Randall, D. A. (2015). Global-scale convective aggregation: Implications for the Madden-Julian Oscillation. *Journal of Advances in Modeling Earth Systems*, 7(4):1499–1518.

Bao, J., Sherwood, S. C., Colin, M., and Dixit, V. (2017). The Robust Relationship Between Extreme Precipitation and Convective Organization in Idealized Numerical Modeling Simulations. *Journal of Advances in Modeling Earth Systems*, 9(6):2291–2303.

Beljaars, A., Balsamo, G., Bechtold, P., Bozzo, A., Forbes, R., Hogan, R. J., Köhler, M., Morcrette, J.-J., Tompkins, A. M., Viterbo, P., and Wedi, N. (2018). The Numerics of Physical Parametrization in the ECMWF Model. *Frontiers in Earth Science*, 6:137.

Benjamin, T. B. (1968). Gravity currents and related phenomena. *Journal of Fluid Mechanics*, 31(2):209–248.

Benner, T. C. and Curry, J. A. (1998). Characteristics of small tropical cumulus clouds and their impact on the environment. *Journal of Geophysical Research*, 103:28753–28767.

Besag, J. (1977). Contribution to the Discussion on Dr. Ripley's Paper. *Journal of the Royal Statistical Society: Series B (Methodological)*, 39(2):193–195.

Beucler, T. and Cronin, T. (2019). A budget for the size of convective self-aggregation. *Quarterly Journal of the Royal Meteorological Society*, 145(720):947–966.

Beucler, T. and Cronin, T. W. (2016). Moisture-radiative cooling instability. *Journal of Advances in Modeling Earth Systems*, 8(4):1620–1640.

Beucler, T., Leutwyler, D., and Windmiller, J. M. (2020). Quantifying Convective Aggregation Using the Tropical Moist Margin's Length. *Journal of Advances in Modeling Earth Systems*, 12(10):e2020MS002092.

Biagioli, G. and Tompkins, A. M. (2023a). A Dimensionless Parameter for Predicting Convective Self-Aggregation Onset in a Stochastic Reaction-Diffusion Model of Tropical Radiative-Convective Equilibrium. *Journal of Advances in Modeling Earth Systems*, 15(5):e2022MS003231.

Biagioli, G. and Tompkins, A. M. (2023b). Measuring convective organization [submitted]. *Journal of the Atmospheric Sciences*.

Bini, D., Capovani, M., and Menchi, O. (1988). *Metodi numerici per l'algebra lineare*. Zanichelli.

Bohren, C. F. and Albrecht, B. A. (1998). *Atmospheric thermodynamics*. Oxford University Press.

Böing, S. J. (2016). An Object-Based Model for Convective Cold Pool Dynamics. *Mathematics of Climate and Weather Forecasting*, 2(1):43–60.

Bony, S., Semie, A., Kramer, R. J., Soden, B., Tompkins, A. M., and Emanuel, K. A. (2020). Observed Modulation of the Tropical Radiation Budget by Deep Convective Organization and Lower-Tropospheric Stability. *AGU Advances*, 1(3):e2019AV000155. e2019AV000155 10.1029/2019AV000155.

Bony, S., Stevens, B., Frierson, D. M. W., Jakob, C., Kageyama, M., Pincus, R., Shepherd, T. G., Sherwood, S. C., Siebesma, A. P., Sobel, A. H., Watanabe, M., and Webb, M. J. (2015). Clouds, circulation and climate sensitivity. *Nature Geoscience*, 8(4):261–268.

Bretherton, C. S., Blossey, P. N., and Khairoutdinov, M. (2005). An Energy-Balance Analysis of Deep Convective Self-Aggregation above Uniform SST. *Journal of the Atmospheric Sciences*, 62(12):4273–4292.

Bretherton, C. S. and Khairoutdinov, M. F. (2015). Convective self-aggregation feedbacks in near-global cloud-resolving simulations of an aquaplanet. *Journal of Advances in Modeling Earth Systems*, 7(4):1765–1787.

Bretherton, C. S., Peters, M. E., and Back, L. E. (2004). Relationships between Water Vapor Path and Precipitation over the Tropical Oceans. *Journal of Climate*, 17(7):1517–1528.

Bretherton, C. S. and Smolarkiewicz, P. K. (1989). Gravity Waves, Compensating Subsidence and Detrainment around Cumulus Clouds. *Journal of Atmospheric Sciences*, 46(6):740–759.

Brugnano, L. and Trigiante, D. (1998). *Solving Differential Problems by Multistep Initial and Boundary Value Methods*. Gordon and Breach Science Publishers.

Brune, S., Buschow, S., and Friederichs, P. (2020). Observations and high-resolution simulations of convective precipitation organization over the tropical Atlantic. *Quarterly Journal of the Royal Meteorological Society*, 146(729):1545–1563.

Brune, S., Buschow, S., and Friederichs, P. (2021). The local wavelet-based organization index – Quantification, localization and classification of convective organization from radar and satellite data. *Quarterly Journal of the Royal Meteorological Society*, 147(736):1853–1872.

Brune, S., Kapp, F., and Friederichs, P. (2018). A wavelet-based analysis of convective organization in icon large-eddy simulations. *Quarterly Journal of the Royal Meteorological Society*, 144(717):2812–2829.

Chan, S. C., Kendon, E. J., Fowler, H. J., Blenkinsop, S., Ferro, C. A. T., and Stephenson, D. B. (2013). Does increasing the spatial resolution of a regional climate model improve the simulated daily precipitation? *Climate Dynamics*, 41(5):1475–1495.

Chen, M. (1987). On the Solution of Circulant Linear Systems. *SIAM Journal on Numerical Analysis*, 24(3):668–683.

Churchill, D. D. and Houze, R. A. (1984). Development and Structure of Winter Monsoon Cloud Clusters On 10 December 1978. *Journal of Atmospheric Sciences*, 41(6):933–960.

Cohen, B. G. and Craig, G. C. (2004). The response time of a convective cloud ensemble to a change in forcing. *Quarterly Journal of the Royal Meteorological Society*, 130(598):933–944.

Cohen, B. G. and Craig, G. C. (2006). Fluctuations in an Equilibrium Convective Ensemble. Part II: Numerical Experiments. *Journal of the Atmospheric Sciences*, 63(8):2005–2015.

Cooley, J. and Tukey, J. (1965). An Algorithm for the Machine Calculation of Complex Fourier Series. *Mathematics of Computation*, 19(90):297–301.

Coppin, D. and Bony, S. (2015). Physical mechanisms controlling the initiation of convective self-aggregation in a General Circulation Model. *Journal of Advances in Modeling Earth Systems*, 7(4):2060–2078.

Craig, G. C. (1996). Dimensional analysis of a convecting atmosphere in equilibrium with external forcing. *Quarterly Journal of the Royal Meteorological Society*, 122(536):1963–1967.

Craig, G. C. and Cohen, B. G. (2006). Fluctuations in an Equilibrium Convective Ensemble. Part I: Theoretical Formulation. *Journal of the Atmospheric Sciences*, 63(8):1996–2004.

Craig, G. C. and Mack, J. M. (2013). A coarsening model for self-organization of tropical convection. *Journal of Geophysical Research: Atmospheres*, 118(16):8761–8769.

Cronin, T. W. and Emanuel, K. A. (2013). The climate time scale in the approach to radiative-convective equilibrium. *Journal of Advances in Modeling Earth Systems*, 5(4):843–849.

Cronin, T. W. and Wing, A. A. (2017). Clouds, Circulation, and Climate Sensitivity in a Radiative-Convective Equilibrium Channel Model. *Journal of Advances in Modeling Earth Systems*, 9(8):2883–2905.

Davis, P. J. (1979). *Circulant matrices*. John Wiley & Sons.

Derbyshire, S. H., Beau, I., Bechtold, P., Grandpeix, J.-Y., Piriou, J.-M., Redelsperger, J.-L., and Soares, P. M. M. (2004). Sensitivity of moist convection to environmental humidity. *Quarterly Journal of the Royal Meteorological Society*, 130(604):3055–3079.

Diggle, P. J. (1983). *Statistical Analysis of Spatial Point Patterns*. Academic Press.

Douglas, J. and Gunn, J. E. (1964). A general formulation of alternating direction methods. part i. parabolic and hyperbolic problems. *Numerische Mathematik*, 6(1):428–453.

Douglas, J. and Kim, S. (2001). Improved accuracy for locally one-dimensional methods for parabolic equations. *Mathematical Models and Methods in Applied Sciences*, 11(09):1563–1579.

Emanuel, K. A. (1987). An Air-Sea Interaction Model of Intraseasonal Oscillations in the Tropics. *Journal of Atmospheric Sciences*, 44(16):2324–2340.

Emanuel, K. A. (1994). *Atmospheric Convection*. Oxford University Press.

Emanuel, K. A., Wing, A. A., and Vincent, E. M. (2014). Radiative-convective instability. *Journal of Advances in Modeling Earth Systems*, 6(1):75–90.

Ferziger, J. H. and Perić, M. (2002). *Computational Methods for Fluid Dynamics*. Springer, 3rd edition.

Fu, H. and O'Neill, M. (2021). The Role of Random Vorticity Stretching in Tropical Depression Genesis. *Journal of the Atmospheric Sciences*, 78(12):4143–4168.

Getis, A. and Franklin, J. (1987). Second-Order Neighborhood Analysis of Mapped Point Patterns. *Ecology*, 68(3):473–477.

Golub, G. H. and van Loan, C. F. (2013). *Matrix Computations*. Johns Hopkins University Press, 4th edition.

Goreaud, F. and Pélissier, R. (1999). On Explicit Formulas of Edge Effect Correction for Ripley's K-Function. *Journal of Vegetation Science*, 10(3):433–438.

Grabowski, W. W. and Moncrieff, M. W. (2004). Moisture–convection feedback in the tropics. *Quarterly Journal of the Royal Meteorological Society*, 130(604):3081–3104.

Gray, M. E. B. and Marshall, C. (1998). Mesoscale convective systems over the UK, 1981–97. *Weather*, 53(11):388–396.

Haase, P. (1995). Spatial pattern analysis in ecology based on Ripley's K-function: Introduction and methods of edge correction. *Journal of Vegetation Science*, 6(4):575–582.

Haerter, J. O. (2019). Convective Self-Aggregation As a Cold Pool-Driven Critical Phenomenon. *Geophysical Research Letters*, 46(7):4017–4028.

Haerter, J. O., Böing, S. J., Henneberg, O., and Nissen, S. B. (2019). Circling in on Convective Organization. *Geophysical Research Letters*, 46(12):7024–7034.

Hartmann, D. L. (2015). *Global physical climatology*. Elsevier, 2nd edition.

Hartmann, D. L., Hendon, H. H., and Houze jr., R. A. (1984). Some Implications of the Mesoscale Circulations in Tropical Cloud Clusters for Large-Scale Dynamics and Climate. *Journal of Atmospheric Sciences*, 41(1):113–121.

Held, I. M., Hemler, R. S., and Ramaswamy, V. (1993). Radiative-Convective Equilibrium with Explicit Two-Dimensional Moist Convection. *Journal of Atmospheric Sciences*, 50(23):3909–3927.

Held, I. M., Zhao, M., and Wyman, B. (2007). Dynamic Radiative–Convective Equilibria Using GCM Column Physics. *Journal of the Atmospheric Sciences*, 64(1):228–238.

Higham, N. J. (2002). *Accuracy and Stability of Numerical Algorithms*. Society for Industrial and Applied Mathematics, 2nd edition.

Hohenegger, C. and Jakob, C. (2020). A Relationship Between ITCZ Organization and Subtropical Humidity. *Geophysical Research Letters*, 47(16):e2020GL088515.

Hohenegger, C. and Stevens, B. (2016). Coupled radiative convective equilibrium simulations with explicit and parameterized convection. *Journal of Advances in Modeling Earth Systems*, 8(3):1468–1482.

Holloway, C. E. (2017). Convective aggregation in realistic convective-scale simulations. *Journal of Advances in Modeling Earth Systems*, 9(2):1450–1472.

Holloway, C. E. and Neelin, J. D. (2010). Temporal Relations of Column Water Vapor and Tropical Precipitation. *Journal of the Atmospheric Sciences*, 67(4):1091–1105.

Holloway, C. E., Wing, A. A., Bony, S., Muller, C. J., Masunaga, H., L'Ecuyer, T. S., Turner, D. D., and Zuidema, P. (2017). Observing Convective Aggregation. *Surveys in Geophysics*, 38(6):1199–1236.

Holloway, C. E. and Woolnough, S. J. (2016). The sensitivity of convective aggregation to diabatic processes in idealized radiative-convective equilibrium simulations. *Journal of Advances in Modeling Earth Systems*, 8(1):166–195.

Hottovy, S. and Stechmann, S. N. (2015a). A Spatiotemporal Stochastic Model for Tropical Precipitation and Water Vapor Dynamics. *Journal of the Atmospheric Sciences*, 72(12):4721–4738.

Hottovy, S. and Stechmann, S. N. (2015b). Threshold Models for Rainfall and Convection: Deterministic versus Stochastic Triggers. *SIAM Journal on Applied Mathematics*, 75(2):861–884.

Houze jr., R. A. (1973). A Climatological Study of Vertical Transports by Cumulus-Scale Convection. *Journal of Atmospheric Sciences*, 30(6):1112–1123.

Houze jr., R. A. (1977). Structure and Dynamics of a Tropical Squall–Line System. *Monthly Weather Review*, 105(12):1540–1567.

Houze jr., R. A. (1982). Cloud Clusters and Large-Scale Vertical Motions in the Tropics. *Journal of the Meteorological Society of Japan. Ser. II*, 60(1):396–410.

Houze jr., R. A. (2004). Mesoscale convective systems. *Reviews of Geophysics*, 42(4).

Houze jr., R. A. (2014). *Cloud Dynamics*. Elsevier, 2nd edition.

Huang, J.-D. and Wu, C.-M. (2022). A Framework to Evaluate Convective Aggregation: Examples With Different Microphysics Schemes. *Journal of Geophysical Research: Atmospheres*, 127(5):e2021JD035886.

Huffman, G. J., Bolvin, D. T., Braithwaite, D., Hsu, K.-L., Joyce, R. J., Kidd, C., Nelkin, E. J., Sorooshian, S., Stocker, E. F., Tan, J., Wolff, D. B., and Xie, P. (2020). *Integrated Multi-satellite Retrievals for the Global Precipitation Measurement (GPM) Mission (IMERG)*, pages 343–353. Springer International Publishing, Cham.

Hundsdorfer, W. and Verwer, J. (2003). *Numerical Solution of Time-Dependent Advection-Diffusion-Reaction Equations*. Springer.

Huppert, H. E. and Simpson, J. E. (1980). The slumping of gravity currents. *Journal of Fluid Mechanics*, 99(4):785–799.

Illian, J., Penttinen, A., Stoyan, H., and Stoyan, D. (2008). *Statistical Analysis and Modelling of Spatial Point Patterns*. Wiley.

Jakob, C., Singh, M. S., and Jungandreas, L. (2019). Radiative Convective Equilibrium and Organized Convection: An Observational Perspective. *Journal of Geophysical Research: Atmospheres*, 124(10):5418–5430.

Jeevanjee, N. and Romps, D. M. (2013). Convective self-aggregation, cold pools, and domain size. *Geophysical Research Letters*, 40(5):994–998.

Jin, D., Oreopoulos, L., Lee, D., Tan, J., and Kim, K.-m. (2022). A New Organization Metric for Synoptic Scale Tropical Convective Aggregation. *Journal of Geophysical Research: Atmospheres*, 127(13):e2022JD036665.

Johnson, R. H. and Hamilton, P. J. (1988). The Relationship of Surface Pressure Features to the Precipitation and Airflow Structure of an Intense Midlatitude Squall Line. *Monthly Weather Review*, 116(7):1444–1473.

Johnson, R. H., Rickenbach, T. M., Rutledge, S. A., Ciesielski, P. E., and Schubert, W. H. (1999). Trimodal Characteristics of Tropical Convection. *Journal of Climate*, 12(8):2397–2418.

Kadoya, T. and Masunaga, H. (2018). New Observational Metrics of Convective Self-Aggregation: Methodology and a Case Study. *Journal of the Meteorological Society of Japan. Ser. II*, 96(6):535–548.

Khairoutdinov, M. and Emanuel, K. (2013). Rotating radiative-convective equilibrium simulated by a cloud-resolving model. *Journal of Advances in Modeling Earth Systems*, 5(4):816–825.

Khairoutdinov, M. F. and Emanuel, K. A. (2010). Aggregated Convection and the Regulation of Tropical Climate. Extended Abstracts, 29th Conference on Hurricanes and Tropical Meteorology, Tucson, AZ, Amer. Meteor. Soc., P2.69.

Khouider, B. (2014). A Coarse Grained Stochastic Multi-Type Particle Interacting Model for Tropical Convection: Nearest Neighbour Interactions. *Communications in Mathematical Sciences*, 12(8):1379–1407.

Khouider, B., Biello, J., and Majda, A. J. (2010). A Stochastic Multicloud Model for Tropical Convection. *Communications in Mathematical Sciences*, 8(1):187–216.

Khouider, B., Majda, A. J., and Katsoulakis, M. A. (2003). Coarse-grained stochastic models for tropical convection and climate. *Proceedings of the National Academy of Sciences*, 100(21):11941–11946.

Kruse, I. L., Haerter, J. O., and Meyer, B. (2022). Cold pools over the Netherlands: A statistical study from tower and radar observations. *Quarterly Journal of the Royal Meteorological Society*, 148(743):711–726.

Lang, S., Tao, W.-K., Simpson, J., and Ferrier, B. (2003). Modeling of Convective–Stratiform Precipitation Processes: Sensitivity to Partitioning Methods. *Journal of Applied Meteorology*, 42(4):505–527.

Lebsock, M., L'Ecuyer, T., and Pincus, R. (2017). An Observational View of Relationships Between Moisture Aggregation, Cloud, and Radiative Heating Profiles. *Surveys in Geophysics*, 38(6):1237–1254.

Lee, J., Chou, J., Weger, R. C., and Welch, R. M. (1994). Clustering, randomness, and regularity in cloud fields: 4. Stratocumulus cloud fields. *Journal of Geophysical Research: Atmospheres*, 99(D7):14461–14480.

LeVeque, R. J. (2007). *Finite Difference Methods for Ordinary and Partial Differential Equations*. Society for Industrial and Applied Mathematics.

Li, Z. (2021). *Understanding the Characteristics of Precipitation and Their Response to Climate Change*. PhD thesis, MIT.

Lin, J. W. B. and Neelin, J. D. (2000). Influence of a stochastic moist convective parameterization on tropical climate variability. *Geophysical Research Letters*, 27(22):3691–3694.

Lin, J. W. B. and Neelin, J. D. (2002). Considerations for Stochastic Convective Parameterization. *Journal of the Atmopheric Sciences*, 59(5):959–975.

Lindzen, R. S., Chou, M.-D., and Hou, A. Y. (2001). Does the Earth Have an Adaptive Infrared Iris? *Bulletin of the American Meteorological Society*, 82(3):417–432.

Lohmann, U., Lüönd, F., and Mahrt, F. (2016). *An Introduction to Clouds: From the Microscale to Climate*. Cambridge University Press.

Lorenz, E. N. (1968). Climatic determinism. *Meteorological Monographs*, 8(30):1–3.

Machado, L. A. T. and Rossow, W. B. (1993). Structural Characteristics and Radiative Properties of Tropical Cloud Clusters. *Monthly Weather Review*, 121(12):3234–3260.

Madden, R. A. and Julian, P. R. (1971). Detection of a 40–50 Day Oscillation in the Zonal Wind in the Tropical Pacific. *Journal of Atmospheric Sciences*, 28(5):702–708.

Maddox, R. A. (1980). Mesoscale convective complexes. *Bulletin of the American Meteorological Society*, 61(11):1374–1387.

Majda, A. J. and Khouider, B. (2002). Stochastic and mesoscopic models for tropical convection. *Proceedings of the National Academy of Sciences*, 99(3):1123–1128.

Manabe, S. and Strickler, R. F. (1964). Thermal Equilibrium of the Atmosphere with a Convective Adjustment. *Journal of Atmospheric Sciences*, 21(4):361–385.

Mapes, B. and Neale, R. (2011). Parameterizing Convective Organization to Escape the Entrainment Dilemma. *Journal of Advances in Modeling Earth Systems*, 3(2).

Mapes, B. E. (1993). –Gregarious Tropical Convection. *Journal of Atmospheric Sciences*, 50(13):2026–2037.

Mapes, B. E., Chung, E. S., Hannah, W. M., Masunaga, H., Wimmers, A. J., and Velden, C. S. (2018). The Meandering Margin of the Meteorological Moist Tropics. *Geophysical Research Letters*, 45(2):1177–1184.

Mapes, B. E. and Houze jr., R. A. (1993). Cloud Clusters and Superclusters over the Oceanic Warm Pool. *Monthly Weather Review*, 121(5):1398–1416.

Mapes, B. E. and Zuidema, P. (1996). Radiative-Dynamical Consequences of Dry Tongues in the Tropical Troposphere. *Journal of Atmospheric Sciences*, 53(4):620–638.

Mathon, V., Laurent, H., and Lebel, T. (2002). Mesoscale Convective System Rainfall in the Sahel. *Journal of Applied Meteorology*, 41(11):1081–1092.

Mauritsen, T. and Stevens, B. (2015). Missing Iris Effect as a Possible Cause of Muted Hydrological Change and High Climate Sensitivity in Models. *Nature Geoscience*, 8(5):346–351.

Mitchell, A. and Griffiths, D. (1980). *The Finite Difference Method in Partial Differential Equations*. John Wiley & Sons.

Moltchanov, D. (2012). Distance distributions in random networks. *Ad Hoc Networks*, 10(6):1146–1166.

Muller, C. J. and Bony, S. (2015). What favors convective aggregation and why? *Geophysical Research Letters*, 42(13):5626–5634.

Muller, C. J. and Held, I. M. (2012). Detailed Investigation of the Self-Aggregation of Convection in Cloud-Resolving Simulations. *Journal of the Atmospheric Sciences*, 69(8):2551–2565.

Muller, C. J., Yang, D., Craig, G. C., Cronin, T. W., Fildier, B., Haerter, J. O., Hohenegger, C., Mapes, B. E., Randall, D. A., Shamekh, S., and Sherwood, S. C. (2022). Spontaneous Aggregation of Convective Storms. *Annual Review of Fluid Mechanics*, 54(1):133–157.

Nair, U. S., Weger, R. C., Kuo, K. S., and Welch, R. M. (1998). Clustering, randomness, and regularity in cloud fields: 5. The nature of regular cumulus cloud fields. *Journal of Geophysical Research: Atmospheres*, 103(D10):11363–11380.

Narsey, S., Jakob, C., Singh, M. S., Bergemann, M., Louf, V., Protat, A., and Williams, C. (2019). Convective Precipitation Efficiency Observed in the Tropics. *Geophysical Research Letters*, 46(22):13574–13583.

Neelin, J. D., Held, I. M., and Cook, K. H. (1987). Evaporation-Wind Feedback and Low-Frequency Variability in the Tropical Atmosphere. *Journal of Atmospheric Sciences*, 44(16):2341–2348.

Nesbitt, S. W., Zipser, E. J., and Cecil, D. J. (2000). A Census of Precipitation Features in the Tropics Using TRMM: Radar, Ice Scattering, and Lightning Observations. *Journal of Climate*, 13(23):4087–4106.

Nilsson, J. and Emanuel, K. A. (1999). Equilibrium atmospheres of a two-column radiative-convective model. *Quarterly Journal of the Royal Meteorological Society*, 125(558):2239–2264.

Nolan, D. S., Rappin, E. D., and Emanuel, K. A. (2007). Tropical cyclogenesis sensitivity to environmental parameters in radiative–convective equilibrium. *Quarterly Journal of the Royal Meteorological Society*, 133(629):2085–2107.

Orlanski, I. (1975). A Rational Subdivision of Scales for Atmospheric Processes. *Bulletin of the American Meteorological Society*, 56(5):527–530.

Østerby, O. (2003). Five Ways of Reducing the Crank–Nicolson Oscillations. *BIT Numerical Mathematics*, 43(4):811–822.

Parsons, D. B., Redelsperger, J.-L., and Yoneyama, K. (2000). The evolution of the tropical western Pacific atmosphere-ocean system following the arrival of a dry intrusion. *Quarterly Journal of the Royal Meteorological Society*, 126(563):517–548.

Patrizio, C. R. and Randall, D. A. (2019). Sensitivity of Convective Self-Aggregation to Domain Size. *Journal of Advances in Modeling Earth Systems*, 11(7):1995–2019.

Peaceman, D. W. and Rachford, H. H. (1955). The numerical solution of parabolic and elliptic differential equations. *Journal of the Society for Industrial and Applied Mathematics*, 3(1):28–41.

Pendergrass, A. G., Reed, K. A., and Medeiros, B. (2016). The link between extreme precipitation and convective organization in a warming climate: Global radiative-convective equilibrium simulations. *Geophysical Research Letters*, 43(21):11,445–11,452.

Peters, O. and Neelin, J. D. (2006). Critical phenomena in atmospheric precipitation. *Nature Physics*, 2(6):393–396.

Pierrehumbert, R. T. (1995). Thermostats, Radiator Fins, and the Local Runaway Greenhouse. *Journal of Atmospheric Sciences*, 52(10):1784–1806.

Plank, V. G. (1969). The Size Distribution of Cumulus Clouds in Representative Florida Populations. *Journal of Applied Meteorology and Climatology*, 8(1):46–67.

Plant, R. S. and Craig, G. C. (2008). A Stochastic Parameterization for Deep Convection Based on Equilibrium Statistics. *Journal of the Atmospheric Sciences*, 65(1):87–105.

Popke, D., Stevens, B., and Voigt, A. (2013). Climate and climate change in a radiative-convective equilibrium version of ECHAM6. *Journal of Advances in Modeling Earth Systems*, 5(1):1–14.

Popp, M. and Bony, S. (2019). Stronger zonal convective clustering associated with a wider tropical rain belt. *Nature Communications*, 10(1):4261.

Posselt, D. J., van den Heever, S., Stephens, G., and Igel, M. R. (2012). Changes in the Interaction between Tropical Convection, Radiation, and the Large-Scale Circulation in a Warming Environment. *Journal of Climate*, 25(2):557–571.

Prein, A. F., Rasmussen, R. M., Wang, D., and Giangrande, S. E. (2021). Sensitivity of organized convective storms to model grid spacing in current and future climates. *Philosophical Transactions of the Royal Society A: Mathematical, Physical and Engineering Sciences*, 379(2195):20190546.

Pscheidt, I., Senf, F., Heinze, R., Deneke, H., Trömel, S., and Hohenegger, C. (2019). How organized is deep convection over Germany? *Quarterly Journal of the Royal Meteorological Society*, 145(723):2366–2384.

Radtke, J., Naumann, A. K., Hagen, M., and Ament, F. (2022). The relationship between precipitation and its spatial pattern in the trades observed during EUREC4A. *Quarterly Journal of the Royal Meteorological Society*, 148(745):1913–1928.

Randall, D. A. and Huffman, G. J. (1980). A Stochastic Model of Cumulus Clumping. *Journal of the Atmospheric Sciences*, 37(9):2068–2078.

Raymond, D. J. (2000a). The Hadley Circulation as a Radiative–Convective Instability. *Journal of the Atmospheric Sciences*, 57(9):1286–1297.

Raymond, D. J. (2000b). Thermodynamic control of tropical rainfall. *Quarterly Journal of the Royal Meteorological Society*, 126(564):889–898.

Raymond, D. J. and Zeng, X. (2000). Instability and large-scale circulations in a two-column model of the tropical troposphere. *Quarterly Journal of the Royal Meteorological Society*, 126(570):3117–3135.

Redelsperger, J.-L., Parsons, D. B., and Guichard, F. (2002). Recovery Processes and Factors Limiting Cloud-Top Height following the Arrival of a Dry Intrusion Observed during TOGA COARE. *Journal of the Atmospheric Sciences*, 59(16):2438–2457.

Reed, K. A., Medeiros, B., Bacmeister, J. T., and Lauritzen, P. H. (2015). Global Radiative–Convective Equilibrium in the Community Atmosphere Model, Version 5. *Journal of the Atmospheric Sciences*, 72(5):2183–2197.

Retsch, M. H., Jakob, C., and Singh, M. (2020). Assessing Convective Organization in Tropical Radar Observations. *Journal of Geophysical Research: Atmospheres*, 125(7):e2019JD031801.

Rigo, T., Berenguer, M., and del Carmen Llasat, M. (2019). An improved analysis of mesoscale convective systems in the western Mediterranean using weather radar. *Atmospheric Research*, 227:147–156.

Ripley, B. D. (1976). The second-order analysis of stationary point processes. *Journal of Applied Probability*, 13(2):255–266.

Ripley, B. D. (1977). Modelling Spatial Patterns. *Journal of the Royal Statistical Society: Series B (Methodological)*, 39(2):172–192.

Ripley, B. D. (1979). Tests of 'Randomness' for Spatial Point Patterns. *Journal of the Royal Statistical Society: Series B (Methodological)*, 41(3):368–374.

Ripley, B. D. (1981). *Spatial Statistics*. Wiley Series in Probability and Statistics. Wiley.

Robe, F. R. and Emanuel, K. A. (2001). The Effect of Vertical Wind Shear on Radiative–Convective Equilibrium States. *Journal of the Atmospheric Sciences*, 58(11):1427–1445.

Roca, R., Fiolleau, T., and Bouniol, D. (2017). A Simple Model of the Life Cycle of Mesoscale Convective Systems Cloud Shield in the Tropics. *Journal of Climate*, 30(11):4283–4298.

Ross, A. N., Tompkins, A. M., and Parker, D. J. (2004). Simple Models of the Role of Surface Fluxes in Convective Cold Pool Evolution. *Journal of the Atmospheric Sciences*, 61(13):1582–1595.

Rotunno, R., Klemp, J. B., and Weisman, M. L. (1988). A Theory for Strong, Long-Lived Squall Lines. *Journal of Atmospheric Sciences*, 45(3):463–485.

Rushley, S. S., Kim, D., Bretherton, C. S., and Ahn, M.-S. (2018). Reexamining the Nonlinear Moisture-Precipitation Relationship Over the Tropical Oceans. *Geophysical Research Letters*, 45(2):1133–1140.

Schumacher, C. and Houze, R. A. (2003). Stratiform Rain in the Tropics as Seen by the TRMM Precipitation Radar. *Journal of Climate*, 16(11):1739–1756.

Seifert, A. and Heus, T. (2013). Large-eddy simulation of organized precipitating trade wind cumulus clouds. *Atmospheric Chemistry and Physics*, 13(11):5631–5645.

Sengupta, S. K., Welch, R. M., Navar, M. S., Berendes, T. A., and Chen, D. W. (1990). Cumulus Cloud Field Morphology and Spatial Patterns Derived from High Spatial Resolution Landsat Imagery. *Journal of Applied Meteorology and Climatology*, 29(12):1245–1267.

Sessions, S. L., Herman, M. J., and Sentić, S. (2015). Convective response to changes in the thermodynamic environment in idealized weak temperature gradient simulations. *Journal of Advances in Modeling Earth Systems*, 7(2):712–738.

Sessions, S. L., Sentić, S., and Herman, M. J. (2016). The role of radiation in organizing convection in weak temperature gradient simulations. *Journal of Advances in Modeling Earth Systems*, 8(1):244–271.

Sessions, S. L., Sugaya, S., Raymond, D. J., and Sobel, A. H. (2010). Multiple equilibria in a cloud-resolving model using the weak temperature gradient approximation. *Journal of Geophysical Research: Atmospheres*, 115(D12).

Sgura, I., Bozzini, B., and Lacitignola, D. (2012). Numerical approximation of Turing patterns in electrodeposition by ADI methods. *Journal of Computational and Applied Mathematics*, 236(16):4132–4147.

Shamekh, S., Muller, C., Duvel, J.-P., and D'Andrea, F. (2020). Self-Aggregation of Convective Clouds With Interactive Sea Surface Temperature. *Journal of Advances in Modeling Earth Systems*, 12(11):e2020MS002164. e2020MS002164 10.1029/2020MS002164.

Sherwood, S. C. (1999). Convective Precursors and Predictability in the Tropical Western Pacific. *Monthly Weather Review*, 127(12):2977–2991.

Shi, X. and Fan, Y. (2021). Modulation of the Bifurcation in Radiative-Convective Equilibrium by Gray-Zone Cloud and Turbulence Parameterizations. *Journal of Advances in Modeling Earth Systems*, 13(10):e2021MS002632.

Showman, A. P. (2007). Numerical Simulations of Forced Shallow-Water Turbulence: Effects of Moist Convection on the Large-Scale Circulation of Jupiter and Saturn. *Journal of the Atmospheric Sciences*, 64(9):3132–3157.

Sobel, A. H., Bellon, G., and Bacmeister, J. (2007). Multiple equilibria in a single-column model of the tropical atmosphere. *Geophysical Research Letters*, 34(22).

Sobel, A. H., Nilsson, J., and Polvani, L. M. (2001). The Weak Temperature Gradient Approximation and Balanced Tropical Moisture Waves. *Journal of the Atmospheric Sciences*, 58(23):3650–3665.

Stechmann, S. N. and Neelin, J. D. (2011). A Stochastic Model for the Transition to Strong Convection. *Journal of the Atmospheric Sciences*, 68(12):2955–2970.

Stechmann, S. N. and Neelin, J. D. (2014). First-Passage-Time Prototypes for Precipitation Statistics. *Journal of the Atmospheric Sciences*, 71(9):3269–3291.

Stein, T. H. M., Holloway, C. E., Tobin, I., and Bony, S. (2017). Observed Relationships between Cloud Vertical Structure and Convective Aggregation over Tropical Ocean. *Journal of Climate*, 30(6):2187–2207.

Steiner, M., Houze, R. A., and Yuter, S. E. (1995). Climatological Characterization of Three-Dimensional Storm Structure from Operational Radar and Rain Gauge Data. *Journal of Applied Meteorology and Climatology*, 34(9):1978–2007.

Stephens, G. L., van den Heever, S., and Pakula, L. (2008). Radiative–Convective Feedbacks in Idealized States of Radiative–Convective Equilibrium. *Journal of the Atmospheric Sciences*, 65(12):3899–3916.

Stevens, B. (2005). Atmospheric moist convection. *Annual Review of Earth and Planetary Sciences*, 33(1):605–643.

Stoyan, D., Kendall, W., Chiu, S., and Mecke, J. (2013). *Stochastic Geometry and Its Applications*. Wiley Series in Probability and Statistics. Wiley, 3rd edition.

Strang, G. (1968). On the Construction and Comparison of Difference Schemes. *SIAM Journal on Numerical Analysis*, 5(3):506–517.

Sueki, K., Yamaura, T., Yashiro, H., Nishizawa, S., Yoshida, R., Kajikawa, Y., and Tomita, H. (2019). Convergence of Convective Updraft Ensembles With Respect to the Grid Spacing of Atmospheric Models. *Geophysical Research Letters*, 46(24):14817–14825.

Sullivan, S. C., Schiro, K. A., Stubenrauch, C., and Gentine, P. (2019). The Response of Tropical Organized Convection to El Niño Warming. *Journal of Geophysical Research: Atmospheres*, 124(15):8481–8500.

Tan, J., Jakob, C., and Lane, T. P. (2013). On the Identification of the Large-Scale Properties of Tropical Convection Using Cloud Regimes. *Journal of Climate*, 26(17):6618–6632.

Tan, J., Jakob, C., Rossow, W. B., and Tselioudis, G. (2015). Increases in tropical rainfall driven by changes in frequency of organized deep convection. *Nature*, 519:451–454.

Tao, W. K., Lang, S., Simpson, J., Olson, W. S., Johnson, D., Ferrier, B., Kummerow, C., and Adler, R. (2000). Vertical Profiles of Latent Heat Release and Their Retrieval for TOGA COARE Convective Systems using a Cloud Resolving Model, SSM/I, and Ship-borne Radar Data. *Journal of the Meteorological Society of Japan. Ser. II*, 78(4):333–355.

Tao, W. K., Simpson, J., Sui, C. H., Ferrier, B., Lang, S., Scala, J., Chou, M. D., and Pickering, K. (1993). Heating, Moisture, and Water Budgets of Tropical and Midlatitude Squall Lines: Comparisons and Sensitivity to Longwave Radiation. *Journal of Atmospheric Sciences*, 50(5):673–690.

Thomas, J. W. (1995). *Numerical Partial Differential Equations: Finite Difference Methods*. Springer.

Thorpe, A. J., Miller, M. J., and Moncrieff, M. W. (1982). Two-dimensional convection in non-constant shear: A model of mid-latitude squall lines. *Quarterly Journal of the Royal Meteorological Society*, 108(458):739–762.

Tobin, I., Bony, S., Holloway, C. E., Grandpeix, J.-Y., Sèze, G., Coppin, D., Woolnough, S. J., and Roca, R. (2013). Does convective aggregation need to be represented in cumulus parameterizations? *Journal of Advances in Modeling Earth Systems*, 5(4):692–703.

Tobin, I., Bony, S., and Roca, R. (2012). Observational Evidence for Relationships between the Degree of Aggregation of Deep Convection, Water Vapor, Surface Fluxes, and Radiation. *Journal of Climate*, 25(20):6885–6904.

Tompkins, A. M. (2001a). On the Relationship between Tropical Convection and Sea Surface Temperature. *Journal of Climate*, 14(5):633–637.

Tompkins, A. M. (2001b). Organization of Tropical Convection in Low Vertical Wind Shears: The Role of Cold Pools. *Journal of the Atmospheric Sciences*, 58(13):1650–1672.

Tompkins, A. M. (2001c). Organization of Tropical Convection in Low Vertical Wind Shears: The Role of Water Vapor. *Journal of the Atmospheric Sciences*, 58(6):529–545.

Tompkins, A. M. and Craig, G. C. (1998a). Radiative–convective equilibrium in a three-dimensional cloud-ensemble model. *Quarterly Journal of the Royal Meteorological Society*, 124(550):2073–2097.

Tompkins, A. M. and Craig, G. C. (1998b). Time-scales of adjustment to radiative-convective equilibrium in the tropical atmosphere. *Quarterly Journal of the Royal Meteorological Society*, 124(552):2693–2713.

Tompkins, A. M. and Semie, A. G. (2017). Organization of tropical convection in low vertical wind shears: Role of updraft entrainment. *Journal of Advances in Modeling Earth Systems*, 9(2):1046–1068.

Tompkins, A. M. and Semie, A. G. (2021). Impact of a Mixed Ocean Layer and the Diurnal Cycle on Convective Aggregation. *Journal of Advances in Modeling Earth Systems*, 13(12):e2020MS002186. e2020MS002186 2020MS002186.

Torri, G., Kuang, Z., and Tian, Y. (2015). Mechanisms for convection triggering by cold pools. *Geophysical Research Letters*, 42(6):1943–1950.

Waliser, D. E. and Graham, N. E. (1993). Convective cloud systems and warm-pool sea surface temperatures: Coupled interactions and self-regulation. *Journal of Geophysical Research: Atmospheres*, 98(D7):12881–12893.

Weger, R. C., Lee, J., and Welch, R. M. (1993). Clustering, Randomness, and Regularity in Cloud Fields: 3. The Nature and Distribution of Clusters. *Journal of Geophysical Research: Atmospheres*, 98(D10):18449–18463.

Weger, R. C., Lee, J., Zhu, T., and Welch, R. M. (1992). Clustering, Randomness and Regularity in Cloud Fields: 1. Theoretical Considerations. *Journal of Geophysical Research: Atmospheres*, 97(D18):20519–20536.

White, B. A., Buchanan, A. M., Birch, C. E., Stier, P., and Pearson, K. J. (2018). Quantifying the Effects of Horizontal Grid Length and Parameterized Convection on the Degree of Convective Organization Using a Metric of the Potential for Convective Interaction. *Journal of the Atmospheric Sciences*, 75(2):425–450.

Wielicki, B. A. and Welch, R. M. (1986). Cumulus Cloud Properties Derived Using Landsat Satellite Data. *Journal of Applied Meteorology and Climatology*, 25(3):261–276.

Windmiller, J. M. (2017). *Organization of Tropical Convection*. PhD thesis, Ludwig-Maximilians-Universität München.

Windmiller, J. M. and Craig, G. C. (2019). Universality in the Spatial Evolution of Self-Aggregation of Tropical Convection. *Journal of the Atmospheric Sciences*, 76(6):1677–1696.

Wing, A. A. and Cronin, T. W. (2016). Self-aggregation of convection in long channel geometry. *Quarterly Journal of the Royal Meteorological Society*, 142:1–15.

Wing, A. A. and Emanuel, K. A. (2014). Physical mechanisms controlling self-aggregation of convection in idealized numerical modeling simulations. *Journal of Advances in Modeling Earth Systems*, 6(1):59–74.

Wing, A. A., Emanuel, K. A., Holloway, C. E., and Muller, C. J. (2017). Convective Self-Aggregation in Numerical Simulations: A Review. *Surveys in Geophysics*, 38(6):1173–1197.

Wing, A. A., Reed, K. A., Satoh, M., Stevens, B., Bony, S., and Ohno, T. (2018). Radiative–convective equilibrium model intercomparison project. *Geoscientific Model Development*, 11(2):793–813.

Wing, A. A., Stauffer, C. L., Becker, T., Reed, K. A., Ahn, M.-S., Arnold, N. P., Bony, S., Branson, M., Bryan, G. H., Chaboureau, J.-P., De Roode, S. R., Gayatri, K., Hohenegger, C., Hu, I.-K., Jansson, F., Jones, T. R., Khairoutdinov, M., Kim, D., Martin, Z. K., Matsugishi, S., Medeiros, B., Miura, H., Moon, Y., Müller, S. K., Ohno, T., Popp, M., Prabhakaran, T., Randall, D., Rios-Berrios, R., Rochetin, N., Roehrig, R., Romps, D. M., Ruppert Jr., J. H., Satoh, M., Silvers, L. G., Singh, M. S., Stevens, B., Tomassini, L., van Heerwaarden, C. C., Wang, S., and Zhao, M. (2020). Clouds and Convective Self-Aggregation in a Multimodel Ensemble of Radiative-Convective Equilibrium Simulations. *Journal of Advances in Modeling Earth Systems*, 12(9):e2020MS002138. e2020MS002138 10.1029/2020MS002138.

Xu, K.-M. (1995). Partitioning Mass, Heat, and Moisture Budgets of Explicitly Simulated Cumulus Ensembles into Convective and Stratiform Components. *Journal of Atmospheric Sciences*, 52(5):551–573.

Xu, K.-M., Hu, Y., and Wong, T. (2019). Convective Aggregation and Indices Examined from CERES Cloud Object Data. *Journal of Geophysical Research: Atmospheres*, 124(24):13604–13624.

Yanai, M., Esbensen, S., and Chu, J.-H. (1973). Determination of Bulk Properties of Tropical Cloud Clusters from Large-Scale Heat and Moisture Budgets. *Journal of the Atmospheric Sciences*, 30(4):611–627.

Yang, D. (2018). Boundary Layer Height and Buoyancy Determine the Horizontal Scale of Convective Self-Aggregation. *Journal of the Atmospheric Sciences*, 75(2):469–478.

Yang, D. (2019). Convective Heating Leads to Self-Aggregation by Generating Available Potential Energy. *Geophysical Research Letters*, 46(17-18):10687–10696.

Yang, D. (2021). A Shallow-Water Model for Convective Self-Aggregation. *Journal of the Atmospheric Sciences*, 78(2):571–582.

Yang, S. and Nesbitt, S. W. (2014). Statistical properties of precipitation as observed by the TRMM precipitation radar. *Geophysical Research Letters*, 41(15):5636–5643.

Yano, J.-I. and Manzato, A. (2022). Does More Moisture in the Atmosphere Lead to More Intense Rains? *Journal of the Atmospheric Sciences*, 79(3):663–681.

Zhang, C., Gottschalck, J., Maloney, E. D., Moncrieff, M. W., Vitart, F., Waliser, D. E., Wang, B., and Wheeler, M. C. (2013). Cracking the MJO nut. *Geophysical Research Letters*, 40(6):1223–1230.

Zhang, C., Mapes, B. E., and Soden, B. J. (2003). Bimodality in tropical water vapour. *Quarterly Journal of the Royal Meteorological Society*, 129(594):2847–2866.

Zhao, G. and Di Girolamo, L. (2007). Statistics on the macrophysical properties of trade wind cumuli over the tropical western Atlantic. *Journal of Geophysical Research: Atmospheres*, 112(D10).

Zhu, T., Lee, J., Weger, R. C., and Welch, R. M. (1992). Clustering, Randomness, and Regularity in Cloud Fields: 2. Cumulus Cloud Fields. *Journal of Geophysical Research: Atmospheres*, 97(D18):20537–20558.